

**Three dimensional nonlinear simulation, sensitivity analysis and increasing the maximum frequency to 2.5 Hz using a physics-based method for basins in Ottawa, Canada**

by

Amin Esmailzadeh

A thesis submitted to the Faculty of Graduate and Postdoctoral Affairs in partial fulfillment of the requirements for the degree of

**Doctor of Philosophy in Earth Sciences**

Department of Earth Sciences

Carleton University

Ottawa, Ontario

April 5, 2019

©Copyright

Amin Esmailzadeh, 2019

## **Abstract**

We performed 3-D nonlinear-viscoelastic ground motion simulations using a finite difference modeling method in a frequency range of 0.1 to 1 Hz in the Kinburn basin, Ottawa, Canada, for large earthquakes. Comparing the records and simulated velocity time series showed that regular viscoelastic simulations could model the ground motions at the rock and soil sites in the Kinburn basin for the Ladysmith earthquake ( $M_w=4.7$ ). Using nonlinear-viscoelastic ground motion simulations for the scaled Ladysmith earthquake ( $M_w=7.5$ ) significantly reduced the amplitude of the horizontal components of the Fourier spectrum and the predicted PGA and PGV values compared to regular linear viscoelastic simulations. Further, using a finite fault source ( $M_w=7$ ) for the nonlinear-viscoelastic simulation decreased PGAs of the horizontal components.

Our sensitivity analysis of simulations for different seismic moments showed that the PGV values exponentially increased with moment magnitude. Using a Gaussian source function with a short half duration increased the PGVs and the amplitude of velocity Fourier spectrum.

Relaxation times and relaxation coefficients for viscoelastic simulation significantly increased PGV, the amplitude of the PSA ratio, and the velocity Fourier spectrum for a small earthquake. Employing a small soil Q model reduced PGV, PSA of soil/rock ratios, and the amplitude of velocity Fourier spectrum. Using finite fault model for a large earthquake ( $M_w = 7$ ) significantly reduced the PGV values relative to a point source model.

We increased the maximum frequency to 2.5 Hz in FD modeling using a dual grid size method for two basins (Kinburn and Orleans basins in Ottawa, Canada). The simulated velocity time series from the dual grid size method provided better results compared to the results of the single grid size, although there were large differences between the amplitude of the velocity Fourier spectrum of the simulations and the amplitude of the records, particularly at low frequencies ( $<1$

Hz). However, the velocity Fourier spectrums of the records and simulations showed a similar variation versus frequency. Further, using the dual grid size method increased the PGVs and amplitudes of the velocity Fourier spectrum for both the Kinburn and Orleans basins compared to the results of the single grid size simulation.

## **Acknowledgments**

Firstly, I would like to express my sincere gratitude to my supervisor Prof. Dariush Motazedian for the continuous support of my Ph.D study and related research, for his patience, motivation, and immense knowledge. His guidance helped me in all the time of research and writing of this thesis. I could not have imagined having a better advisor and mentor for my Ph.D study.

I would also wish to express my gratitude to Dr. James Hunter for extended discussions and valuable suggestions which have contributed greatly to the improvement of the thesis.

I would also like to thank the research team, Steve, Sylvia, Sherry, Parisa, and Shutian who I learned a lot from them, through their personal and scholarly interactions, their suggestions at various points of my research.

Thank you to my fellow grad students and the staff and faculty of the Department of Earth Sciences for the discussions on this topic and others.

This research was supported by the Natural Sciences and Engineering Research Council of Canada under the Discovery Grant program and Collaborative Research and Development grants. This research used computational resources provided by the High Performance Computing Virtual Laboratory (HPCVL) and Calcul Québec, both under Compute Canada. I gratefully acknowledge the constructive comments, suggestions, and text revisions from reviewers. I used the AWP-ODC [Anelastic Wave Propagation, developed by Olsen-Day-Cui) program package, and we would like to show our gratitude to Professor Kim Olsen for providing us with the package. I appreciate Dr. Daniel Roten's guidance in using the AWP-ODC program. Special gratitude is given to the Geological Survey of Canada for providing me with helpful

comments, suggestions, and the necessary materials, including seismograms and geological information, for this research.

Lastly, I would like to thank my family for all their love and encouragement. For my parents who raised me with love and supported me in all my pursuits. For my brothers and sisters for supporting me spiritually throughout writing this thesis and my life in general. And most of all for my loving, supportive, encouraging, and patient wife whose faithful support during this Ph.D. is so appreciated.

## **Preface**

This is a paper-based thesis, thus there are some unavoidable repetitions in the thesis.

- The abstract is a modified combination of abstracts of papers.
- There are some repetitions in the introductions of papers about the Ladysmith earthquake, seismological, geological, and geophysical information of the study area and basins.
- In all papers, we used the original or modified version (please see paper 1 and paper 3) of the finite difference (FD) modeling method, developed by Olsen-Day-Cui; thus, there are some repetitions about the method.
- I have submitted paper 1 (chapter 3) to BSSA, and we have gone through the first round of modifications recommended by the reviewers; the modified version was submitted on January 24, 2019 to BSSA.
- We submitted paper 2 (chapter 4) to BSSA on February 8, 2019.
- We submit Paper 3 (chapter 5) to BSSA on February 18, 2019.

Each article has been modified to comply with input from the thesis examination committee.

Table and figure numbers have been standardized and updated to be consistent within the thesis, and a list of references has been compiled at the end.

In the first paper (third chapter), we determined the 3D basin effects on the amplification of ground motion for nonlinear soil in the Ottawa area.

In the second paper (forth chapter) submitted to the Bulletin of the Seismological Society of America, we studied the sensitivities of a physics-based ground motion simulation to source characteristics and the material models for modeling the Ladysmith earthquake in the Kinburn basin, Ottawa, Canada.

In the third paper (fifth chapter), we considered a hybrid non-uniform method to model the Ladysmith earthquake for a frequency range of 0.1-2.5 Hz for the Kinburn and Orleans basins.

## Table of contents

Abstract .....	ii
Acknowledgments.....	iv
Preface.....	vi
Table of contents.....	viii
List of Tables .....	xii
List of Figure Captions .....	xiv
1. Introduction .....	1
2. Methodology and literature review.....	5
3. Three dimensional nonlinear ground motion simulation using a physics-based method for the Kinburn basin.....	17
Abstract.....	18
3.1. Introduction.....	19
3.2. Geographical location and geological features .....	21
3.3. Finite difference modeling.....	22
3.4. Proposed nonlinear-viscoelastic simulation method.....	24
3.5. Seismic characteristics of the Kinburn basin .....	28
3.6. The Ladysmith earthquake.....	30
3.7. Simulation characteristics .....	31
3.8. Viscoelastic simulation for the Ladysmith earthquake $M_w=4.7$ , $R=43$ km .....	33
3.9. Scaling the Ladysmith earthquake to a magnitude of 7.5.....	37
3.10. Viscoelastic ground motion simulation for $M_w=7.5$ , $R=5.6$ km .....	38
3.11. Nonlinear-viscoelastic ground motion simulation for $M_w=7.5$ , $R=5.6$ km.....	39

3.12.	Viscoelastic and nonlinear-viscoelastic simulations for $M_w=7.5$ , $R=43$ km.....	43
3.13.	Finite fault model for $M_w=7$ .....	47
3.14.	Discussion and Conclusion .....	50
	Data and Resources.....	53
	Acknowledgements.....	53
	Tables and Figures .....	55
	Appendix.....	95
4.	Sensitivity analysis for finite difference seismic basin modeling: a case study for Kinburn basin, Ottawa, Canada.....	106
	Abstract.....	107
4.1.	Introduction.....	109
4.2.	The Ladysmith earthquake.....	110
4.3.	Geographical location and geological features .....	111
4.4.	Kinburn basin model.....	112
4.5.	Physics-based finite difference modeling .....	113
4.6.	Sensitivity of the viscoelastic simulation to source parameters.....	115
4.6.1.	Sensitivity to $M_0$ , using a point source model .....	118
4.6.2.	Sensitivity to strike and dip angles.....	120
4.6.3.	Sensitivity to the source functions .....	121
4.6.4.	Sensitivity to the slip duration.....	123
4.6.5.	Sensitivity to geometry of source (point source versus finite fault source).....	124
4.7.	Sensitivity to the regional path parameters.....	126
4.7.1.	Sensitivity to crustal $V_s$ , $V_p$ and density model of rock.....	126

4.7.2.	Sensitivity to crustal damping .....	128
4.7.3.	Sensitivity to relaxation coefficients, and relaxation of modulus .....	129
4.8.	Sensitivity to local soil/site conditions .....	132
4.8.1.	Sensitivity to soil Q model .....	132
4.8.2.	Sensitivity to Vs contrast (Vs_soil/Vs_rock) .....	133
4.8.3.	Sensitivity to level of shaking and nonlinearity .....	136
4.9.	Discussion and conclusion .....	137
	Data and Resources .....	141
	Acknowledgements .....	142
	Tables and Figures .....	143
5.	Increasing the maximum frequency to 2.5 Hz in finite difference modeling using a dual grid size method for basins in Ottawa, Canada .....	190
	Abstract .....	191
5.1.	Introduction .....	192
5.2.	Study sites .....	194
5.2.1.	The Kinburn Basin .....	195
5.2.2.	The Orleans Basin .....	196
5.3.	Uniform grid size finite difference simulations for a frequency range of 0.1-1 Hz .....	198
5.3.1.	Main input parameters for simulations .....	198
5.3.2.	Application of single grid size method for a frequency range of 0.1-1 Hz for the Kinburn basin .....	202
5.3.3.	Application of single grid size method for a frequency range of 0.1-1 Hz for the Orleans basin	203

5.4.	Dual grid size method for a frequency range of 0.1-2.5 Hz .....	204
5.4.1.	Implementation of the dual grid size method.....	205
5.5.	Application of the dual grid size method for a frequency range of 0.1-2.5 Hz .....	206
5.5.1.	Application of the dual grid size method to the Kinburn basin .....	208
5.5.2.	Application of the dual grid size method to the Orleans basin .....	209
5.6.	Discussion and conclusion.....	211
	Data and Resources.....	214
	Acknowledgements.....	215
	Tables and Figures .....	216
6.	Conclusion.....	252
6.1.	Summary .....	252
6.2.	Future work.....	254
7.	References .....	256

## List of Tables

Table 3-1. Properties of the seismic velocity model (Burger et al., 1987; Eaton et al., 2006; Hunter et al., 2010; Crow et al., 2011; Bent et al., 2015) .....	55
Table 3-2. The focal mechanism proposed for the Ladysmith earthquake (Ma and Audet; 2014) .....	56
Table 4-1. Properties of modelled soil and rock (Burger et al., 1987; Hunter et al., 2010; Crow et al., 2011; Motazedian et al., 2011; Bent et al., 2015) 143	
Table 4-2. The focal mechanisms proposed for the Ladysmith earthquake .....	144
Table 4-3. Calculated seismic moments associated with different moment magnitudes .....	145
Table 4-4. Crustal Vs, Vp and density models; Model 1 (Burger et al., 1987; Hunter et al., 2010)and Model 2 (Burger et al., 1987; Motazedian et al., 2013).....	146
Table 4-5. Crustal damping factor models; Crustal damping factor (Q) model 1 (Burger et al., 1987; Hunter et al., 2010.) and Crustal damping factor (Q) model 2 (Burger et al., 1987; Hunter et al., 2010) used for rock site.....	147
Table 4-6. Damping factor models; Soil damping factor(Q) model 1 (Burger et al., 1987; Hunter et al., 2010; Crow et al., 2011) and Soil damping factor(Q) model 2 (Burger et al., 1987; Hunter et al., 2010; Crow et al., 2011) used for soil site .....	148
Table 4-7. Vs models used for soil site; Soil Vs model 1 (Burger et al., 1987; Hunter et al., 2010; Crow et al., 2011) and Soil Vs model 2 (Burger et al., 1987; Hunter et al., 2010; Crow et al., 2011; Motazedian et al., 2011) .....	149
Table 5-1. Crustal velocity models used for rock sites in the Ottawa area (Burger et al., 1987; Motazedian et al., 2013).....	216

Table 5-2. Properties of the seismic velocity model of the Kinburn basin (Burger et al., 1987; Hunter et al., 2010; Crow et al., 2011; Motazedian et al., 2011).....	217
Table 5-3. Properties of the seismic velocity model of the Orleans basin (Motazedian and Hunter, 2008; Hunter et al., 2010; Crow et al., 2011) .....	218
Table 5-4. Two focal mechanisms proposed for the Ladysmith earthquake .....	219
Table 5-5. Velocity model used for the low velocity zone in the Kinburn basin simulation (Burger et al., 1987; Hunter et al., 2010; Crow et al., 2011; Motazedian et al., 2011) .....	220
Table 5-6. Velocity model used for the low velocity zone in the Orleans basin simulation (Burger et al., 1987; Motazedian and Hunter, 2008; Hunter et al., 2010; Crow et al., 2011; Motazedian et al., 2013) .....	221

## List of Figure Captions

Figure 3-1. Vs30 map of the Ottawa region (Motazedian et al., 2011; Hunter et al., 2012). The location of the Kinburn basin is indicated by the black circle .....	57
Figure 3-2. Top: Air photo A31837-105 taken 22/05/2002 1:15,000 of the Kinburn area, Ottawa valley, showing the location of the borehole (the red star) and the location of the seismic section (the red dashed line). Bottom: seismic section, as prepared and interpreted by Pugin et al. (2013) showing the location of the borehole and the interpreted lithologies and structures (Medioli et al., 2012) .....	58
Figure 3-3. Velocity profile of the Kinburn basin .....	59
Figure 3-4. Contour map of the Kinburn basin depth showing the location of the GSC borehole, seismic stations (JSBS and JSSS), receivers, and section location.....	60
Figure 3-5. Cross-section along the northwest-southeast side of the basin and the location of the receivers (the values are in m) .....	61
Figure 3-6. The Ladysmith earthquake (NRCan webpage) .....	62
Figure 3-7. a) Recorded velocity time series associated with the Ladysmith earthquake at the rock site (JSBS) and soil site (JSSS) in the Kinburn basin. b) The unfiltered velocity Fourier spectral ratio of records of the soil site (JSSS) to the rock site (JSBS) in the Kinburn basin. ....	63
Figure 3-8. Comparison of a) simulated velocity time series versus recorded velocity time series and b) the velocity Fourier spectrum of the simulation versus the velocity Fourier spectrum of the record at the rock site for the proposed focal mechanism of Ma and Audet (2014); epicentral distance $R=43$ km, depth=14.5 km, $M_w=4.7$ , $M_0=1.32e+16$ Nt-m. ....	64
Figure 3-9. Comparison of a) simulated velocity time series versus recorded velocity time series and b) the velocity Fourier spectrum of the simulation versus the velocity Fourier spectrum of	

the record at the soil site for the proposed focal mechanism of Ma and Audet (2014); epicentral distance $R=43$ km, depth= $14.5$ km, $M_w=4.7$ , $M_0=1.32e+16$ Nt-m. ....	65
Figure 3-10. Comparison of a) simulated velocity time series versus recorded velocity time series and b) the velocity Fourier spectrum of the simulation versus the velocity Fourier spectrum of the record at the soil site for $M_w=4.7$ using a half duration of 1.6 for the Gaussian source function .....	66
Figure 3-11. Comparison of the velocity Fourier spectral ratios of soil site to rock site for a) the simulation and b) the record .....	67
Figure 3-12. Stress-strain and modulus reduction curves for the a) E-W component, b) N-S component, and c) vertical component at the soil site at a depth of 25 m for the viscoelastic simulation using $M_w=7.5$ ( $R=5.6$ km, X= east-west, Y= north-south, Z= vertical) .....	68
Figure 3-13. Acceleration time series and Fourier spectrums of the viscoelastic simulation for $M_w=7.5$ for the receiver at the soil site ( $R=5.6$ km).....	69
Figure 3-14. PSA ratio of soil site to rock site for the viscoelastic simulation [PSA (soil site)/PSA (rock site)].....	70
Figure 3-15. Stress-strain and modulus reduction curves of the a) X-Y component, b) X-Z component, and c) Y-Z component at the soil site for the viscoelastic and nonlinear-viscoelastic simulations for $M_w=7.5$ ( $R=5.6$ km, X= east-west, Y= north-south, Z= vertical).....	71
Figure 3-16. The strain time series of the a) X-Y component, b) X-Z component, and c) Y-Z component at the soil site for the viscoelastic and nonlinear-viscoelastic simulations for $M_w=7.5$ ( $R=5.6$ km, X= east-west, Y= north-south, Z= vertical). ....	72

Figure 3-17. Acceleration time series and associated Fourier spectrums of the viscoelastic (Original) and nonlinear-viscoelastic (Modified) simulations for $M_w=7.5$ for the receiver at the soil site ( $R=5.6$ km) .....	73
Figure 3-18. PSA ratio of soil site to rock site for the viscoelastic simulation and the nonlinear-viscoelastic simulation [PSA (soil site)/ PSA (rock site)] .....	74
Figure 3-19. a) Comparison of the nonlinear-viscoelastic simulated velocity time series at the rock site and soil site ( $M_w =7.5$ , $R=5.6$ km). b) Comparison of the simulated velocity time series of the viscoelastic and the nonlinear-viscoelastic simulations at the soil site ( $M_w=7.5$ , $R=5.6$ km) .....	75
Figure 3-20. Particle motion of the nonlinear-viscoelastic simulation at the rock site.....	76
Figure 3-21. Particle motion of the nonlinear-viscoelastic simulation at the soil site for a) the whole modeled time series and b) the first 20 s of the modeled time series.....	77
Figure 3-22. Velocity and acceleration time series and associated Fourier spectrums of the viscoelastic simulation for the receiver at the soil site ( $R=43$ km).....	79
Figure 3-23. Velocity Fourier spectral ratio of soil site to rock site associated with the viscoelastic simulation only.....	80
Figure 3-24. PSA ratio of soil site to rock site for the viscoelastic simulation [PSA (soil site)/ PSA (rock site)].....	81
Figure 3-25. Modulus reduction and stress-strain curves of the a) X-Y component, b) X-Z component, and c) Y-Z component for the receiver at the soil site in the nonlinear-viscoelastic simulation ( $R=43$ km, X= east-west, Y= north-south, Z= vertical).....	82
Figure 3-26. Velocity and acceleration time series and associated Fourier spectrums of the nonlinear-viscoelastic simulation for the receiver at the soil site ( $R=43$ km) .....	84

Figure 3-27. Velocity Fourier spectral ratio of soil site to rock site for the nonlinear-viscoelastic simulation.....	85
Figure 3-28. PSA ratio of soil site to rock site for the nonlinear-viscoelastic simulation [PSA (soil site)/ PSA (rock site)] .....	86
Figure 3-29. Comparison of the PSA ratios of the viscoelastic simulation to the nonlinear-viscoelastic simulation for a) R=5.6 km and b) R=43 km .....	88
Figure 3-30. Sub-faults of finite fault plane used for the simulation a) 3D view and b) top view	89
Figure 3-31. Stress-strain and modulus reduction curves of the a) X-Y component, b) X-Z component, and c) Y-Z component at the soil site for the viscoelastic and nonlinear-viscoelastic simulations for Mw=7 using a finite fault model (R=43 km, X= east-west, Y= north-south, Z= vertical) .....	90
Figure 3-32. Comparison of the velocity and acceleration time series and associated Fourier spectrums of the nonlinear-viscoelastic and viscoelastic simulations for the receiver at the soil site (R=43 km) .....	92
Figure 3-33. Comparison of the velocity Fourier spectral ratios of soil site to rock site for the a) nonlinear-viscoelastic simulation and b) viscoelastic simulation.....	93
Figure 3-34. PSA ratio of soil site to rock site for the a) nonlinear-viscoelastic simulation and b) viscoelastic simulation [PSA (soil site)/ PSA (rock site)] .....	94
Figure 4-1.a) Location of the May 2013 Ladysmith, Quebec, earthquake (star with 2013), within the outline of the western Quebec seismic zone (WQSZ; Basham et al., 1982). The earthquakes recorded between January 1980 and May 2014 are also denoted by circles, m $N \geq 3.0$ ; squares, m $N \geq 4.0$ ; stars, m $N \geq 5$ events with the year of occurrence. The other abbreviations show the approximate area of the Ottawa–Bonnehère Graben (OBG) and St. Lawrence rift system, the	

assumed position of the Great Meteor hotspot track (GMHST; Bleeker et al., 2011), and TOR, Toronto; OTT, Ottawa; MTL, Montréal; and T, Temiscaming. b) The open star shows the epicenter of the Ladysmith earthquake. Other symbols represent seismograph stations (diamonds: three-component broadband stations installed for research purposes; squares: permanent instruments of the Canadian National Seismograph Network; upside-down triangles: the U.S. Transportable Array stations; and JSBS–JSSS: the locations of the Kinburn basin array for approximately the same region as (a) (Bent et al., 2015)..... 150

Figure 4-2. Topographic map of the Kinburn basin, as prepared by J. A. Hunter (2012). Approximate locations of seismic stations are marked with yellow stars, and the study area is outlined by a black box (Hayek, 2016). ..... 151

Figure 4-3. Contour map of the Kinburn basin depth showing the location of soil site (JSSS) and rock site (JSBS) and the gridded (mesh size 25 m) 3D variation of depth within the Kinburn basin. .... 152

Figure 4-4. Velocity profile of the Kinburn basin. .... 153

Figure 4-5. Contour map of the Kinburn basin depth and the location of the receivers at soil (JSSS) and rock sites (JSBS) and the GSC borehole in the basin. .... 154

Figure 4-6. Simulated velocity time series and related Fourier spectrum versus recorded velocity time series and associated Fourier spectrum at rock site for the three proposed focal mechanisms: a) Bent et al. (2015); epicentral distance  $R=39.3$  km, depth=12 km,  $M_w=4.55$ ,  $M_0=8.372e+15$  Nt-m, b) Ma and Audet (2014); epicentral distance  $R=39.3$  km; depth=14.5 km,  $M_w=4.7$ ,  $M_0=1.32e+16$  Nt-m, and c) CMT (last modified 2011); epicentral distance  $R=39.3$  km, depth=22.1 km,  $M_w=4.7$ ,  $M_0=1.52e+16$  Nt-m ..... 156

Figure 4-7. Simulated velocity time series and related Fourier spectrum versus recorded velocity time series and associated Fourier spectrum at soil site for the three proposed focal mechanisms: a) Bent et al. (2015); epicentral distance  $R=43$  km, depth= $12$  km,  $M_w=4.55$ ,  $M_0=8.372e+15$  Nt-m, b) Ma and Audet (2014); epicentral distance  $R=43$  km, depth= $14.5$  km,  $M_w=4.7$ ,  $M_0=1.32e+16$  Nt-m, and c) CMT (last modified 2011); epicentral distance  $R=43$  km, depth= $22.1$  km,  $M_w=4.7$ ,  $M_0=1.52e+16$  Nt-m ..... 158

Figure 4-8. PGVs of the viscoelastic simulations associated with seismic moment and seismic magnitude, using a point source model.  $PGV_{rock} = 1E-11e3.4747*M_w$  and  $PGV_{soil} = 7E-11e3.4695M_w$  represents the equations related to plots. .... 159

Figure 4-9. Amplitude of Velocity Fourier spectrum of the modeled velocity time series for the rock site and soil site associated with different moment magnitudes. .... 160

Figure 4-10. PSA ratio of soil site to rock site associated with different moment magnitudes.. 161

Figure 4-11. Simulated a) velocity time series and b) Fourier spectrum of rock site for  $M_w=4.7$  using fault plane 1: 306 (strike), 41 (dip), 94 (slip); and fault plane 2: 122 (strike), 50 (dip), 87 (slip). .... 162

Figure 4-12. Simulated a) velocity time series and b) Fourier spectrum of soil site for  $M_w=4.7$  using fault plane 1: 306 (strike), 41 (dip), 94 (slip); and fault plane 2: 122 (strike), 50 (dip), 87 (slip). .... 163

Figure 4-13. Comparison of PSA ratios of soil site to rock site for  $M_w=4.7$  using fault plane 1: 306 (strike), 41 (dip), 94 (slip); and fault plane 2: 122 (strike), 50 (dip), 87 (slip). .... 164

Figure 4-14. Simulated a) velocity time series and b) Fourier spectrum of rock site for  $M_w=4.7$  using Gaussian and semi-triangular source functions..... 165

Figure 4-15. Simulated a) velocity time series and b) Fourier spectrum of soil site for $M_w=4.7$ using Gaussian and semi-triangular source functions.....	166
Figure 4-16. Comparison of PSA ratios of soil site to rock site for $M_w=4.7$ using Gaussian and semi-triangular source functions.....	167
Figure 4-17. Simulated a) velocity time series and b) Fourier spectrum of rock site for $M_w=4.7$ using half durations of 0.6 s and 1.6 s for Gaussian source function. ....	168
Figure 4-18. Simulated a) velocity time series and b) Fourier spectrum of soil site for $M_w=4.7$ using half durations of 0.6 s and 1.6 s for Gaussian source function. ....	169
Figure 4-19. Comparison of PSA ratios of soil site to rock site for $M_w=4.7$ using half durations of 0.6 s and 1.6 s for Gaussian source function. ....	170
Figure 4-20. 3D view of sub-faults of the finite fault plane used for simulation. ....	171
Figure 4-21. Simulated a) velocity time series and b) Fourier spectrum of rock site for $M_w=7$ using point source model and finite fault model.....	172
Figure 4-22. Simulated a) velocity time series and b) Fourier spectrum of soil site for $M_w=7$ using point source model and finite fault model.....	173
Figure 4-23. Comparison of PSA ratios of soil site to rock site for $M_w=7$ using point source model and finite fault model.....	174
Figure 4-24. Simulated a) velocity time series and b) Fourier spectrum of rock site for $M_w=4.7$ using crustal model 1 and crustal model 2.....	175
Figure 4-25. Simulated a) velocity time series and b) Fourier spectrum of soil site for $M_w=4.7$ using crustal model 1 and crustal model 2.....	176
Figure 4-26. Comparison of PSA ratios of soil site to rock site for $M_w=4.7$ using crustal model 1 and crustal model 2. ....	177

Figure 4-27. Simulated a) velocity time series and b) Fourier spectrum of rock site for Mw=4.7 using crustal Q model 1 and crustal Q model 2.....	178
Figure 4-28. Simulated a) velocity time series and b) Fourier spectrum of soil site for Mw=4.7 using crustal Q model 1 and crustal Q model 2.....	179
Figure 4-29. Comparison of PSA ratios of soil site to rock site for Mw=4.7 using crustal Q model 1 and crustal Q model 2.....	180
Figure 4-30. Simulated a) velocity time series and b) Fourier spectrum of rock site for Mw=4.7 using the memory variables model 1 and the memory variables model 2.....	181
Figure 4-31. Simulated a) velocity time series and b) Fourier spectrum of soil site for Mw=4.7 using the memory variables model 1 and the memory variables model 2.....	182
Figure 4-32. Comparison of PSA ratios of soil site to rock site for Mw=4.7 using the memory variables model 1 and the memory variables model 2.....	183
Figure 4-33. Simulated a) velocity time series and b) Fourier spectrum of soil site for Mw=4.7 using soil Q model 1 and soil Q model 2.....	184
Figure 4-34. Comparison of PSA ratios of soil site to rock site for Mw=4.7 using soil Q model 1 and soil Q model 2.....	185
Figure 4-35. Simulated a) velocity time series and b) Fourier spectrum of soil site for Mw=4.7 using soil Vs model 1 and soil Vs model 2.....	186
Figure 4-36. Comparison of PSA ratios of soil site to rock site for Mw=4.7 using soil Vs model 1 and soil Vs model 2.....	187
Figure 4-37. Simulated a) velocity time series and b) Fourier spectrum of soil site for Mw=7 using viscoelastic simulation and nonlinear-viscoelastic simulation.....	188

Figure 4-38. Comparison of PSA ratios of soil site to rock site for $M_w=7$ using viscoelastic simulation and nonlinear-viscoelastic simulation.....	189
Figure 5-1. Recorded earthquakes by the Canadian seismograph network since the beginning of the century in the Western Quebec Seismic Zone. The approximate study region is outlined by a black rectangle. The studied basins are located in the black box ( <a href="http://www.earthquakescanada.nrcan.gc.ca">www.earthquakescanada.nrcan.gc.ca</a> ).....	222
Figure 5-2. $V_s30$ map of the Ottawa region (Motazedian et al., 2011; Hunter et al., 2012). The locations of the Kinburn basin and Orleans basin are indicated by the black circle and black box, respectively. ....	223
Figure 5-3. Location of the Ladysmith earthquake (the star) and the locations of Kinburn and Orleans basins (NRCan webpage). ....	224
Figure 5-4. Kinburn basin depth model and locations of seismic stations and GSC boreholes. ....	225
Figure 5-5. Orleans basin depth model and seismic stations. ....	226
Figure 5-6. Recorded velocity time series associated with the Ladysmith earthquake at a) rock site (JSBS) and soil site (JSSS) in the Kinburn basin and b) rock site (ORHO) and soil site (ORIO) in the Orleans basin. ....	227
Figure 5-7. Simulated velocity time series and related Fourier spectrum versus recorded velocity time series and associated Fourier spectrum at rock site for the two proposed focal mechanisms: a) Bent et al. (2015); epicentral distance $R=39.3$ km, depth=12 km, $M_w=4.55$ , $M_0=8.372e+15$ Nt-m, frequency range=0.1-1 Hz and b) Ma and Audet (2014); epicentral distance $R=39.3$ km, depth=14.5 km, $M_w=4.7$ , $M_0=1.32e+16$ Nt-m, frequency range=0.1-1 Hz. ....	229
Figure 5-8. Simulated velocity time series and related Fourier spectrum versus recorded velocity time series and associated Fourier spectrum at soil site for the two proposed focal mechanisms:	

a) Bent et al. (2015); epicentral distance  $R=43$  km, depth=12 km,  $M_w=4.55$ ,  $M_0=8.372e+15$  Nt-m, frequency range=0.1-1 Hz and b) Ma and Audet (2014); epicentral distance  $R=43$  km, depth=14.5 km,  $M_w=4.7$ ,  $M_0=1.32e+16$  Nt-m, frequency range=0.1-1 Hz. .... 231

Figure 5-9. PSA ratios of soil site to rock site for recorded velocity time series versus PSA ratios of the simulated velocity time series for the Kinburn basin for the two proposed focal mechanisms: a) Bent et al. (2015); epicentral distance=43 km, depth=12 km,  $MW=4.55$ ,  $M_0=8.372e+15$  Nt-m, frequency range=0.1-1 Hz and b) Ma and Audet (2014); epicentral distance=43 km, depth=14.5 km,  $MW=4.7$ ,  $M_0=1.32e+16$  Nt-m, frequency range=0.1-1 Hz.. 232

Figure 5-10. Simulated velocity time series and associated velocity Fourier spectrum versus recorded velocity time series and related velocity Fourier spectrum for the Orleans basin at rock site for the two proposed focal mechanisms: a) Bent et al. (2015); epicentral distance=72.2 km, depth=12 km,  $MW=4.55$ ,  $M_0=8.372e+15$  Nt-m, frequency range=0.1-1 Hz and b) Ma and Audet (2014); epicentral distance=72.2 km, depth=14.5 km,  $MW=4.7$ ,  $M_0=1.32e+16$  Nt-m, frequency range=0.1-1 Hz. .... 234

Figure 5-11. Simulated velocity time series and associated velocity Fourier spectrum versus recorded velocity time series and related velocity Fourier spectrum for the Orleans basin at soil site for the two proposed focal mechanisms: a) Bent et al. (2015); epicentral distance=70.4 km, depth=12 km,  $MW=4.55$ ,  $M_0=8.372e+15$  Nt-m, frequency range=0.1-1 Hz and b) Ma and Audet (2014); epicentral distance=70.4 km, depth=14.5 km,  $MW=4.7$ ,  $M_0=1.32e+16$  Nt-m, frequency range=0.1-1 Hz. .... 236

Figure 5-12. PSA ratios of soil site to rock site for recorded velocity time series versus PSA ratios of the simulated velocity time series for the Orleans basin for the two proposed focal mechanisms: a) Bent et al. (2015); epicentral distance=70.4 km, depth=12 km,  $MW=4.55$ ,

M0=8.372e+15 Nt-m, frequency range=0.1-1 Hz and b) Ma and Audet (2014); epicentral distance=70.4 km, depth=14.5 km, MW=4.7, M0=1.32e+16 Nt-m, frequency range=0.1-1 Hz. .... 237

Figure 5-13. Schematic figure of 3D grid system that shows the boundary between the high velocity zone (large grids) and low velocity zone (small grids) (Aoi and Fujiwara, 1999). ..... 238

Figure 5-14. Grid point locations on a plane for interpolation, where the large white hexagons show grid points in the large grid (high velocity zone) simulation, and the small black hexagons are grid points in the small grid (low velocity zone) simulation (Aoi and Fujiwara, 1999). ..... 239

Figure 5-15. Simulated velocity time series and associated velocity Fourier spectrum versus recorded velocity time series and related velocity Fourier spectrum for the Kinburn basin at rock site for the Ma and Audet (2014); epicentral distance=39.3 km, depth=14.5 km, MW=4.7, M0=1.32e+16 Nt-m, frequency range=0.1-2.5 Hz. .... 240

Figure 5-16. Simulated velocity time series and associated velocity Fourier spectrum for the single grid size simulation (frequency range of 0.1-1 Hz) versus modeled velocity time series and related velocity Fourier spectrum for the dual grid size simulation (frequency range of 0.1-2.5 Hz) for the Kinburn basin at rock site for the Ma and Audet (2014); epicentral distance=39.3 km, depth=14.5 km, MW=4.7, M0=1.32e+16 Nt-m. .... 241

Figure 5-17. Simulated velocity time series and associated velocity Fourier spectrum versus recorded velocity time series and related velocity Fourier spectrum for the Kinburn basin at soil site for the Ma and Audet (2014); epicentral distance=43 km, depth=14.5 km, MW=4.7, M0=1.32e+16 Nt-m, frequency range=0.1-2.5 Hz. .... 242

Figure 5-18. Simulated velocity time series and associated velocity Fourier spectrum for the single grid size simulation (frequency range of 0.1-1 Hz) versus modeled velocity time series and

related velocity Fourier spectrum for the dual grid size simulation (frequency range of 0.1-2.5 Hz) for the Kinburn basin at soil site for the Ma and Audet (2014); epicentral distance=43 km, depth=14.5 km, MW=4.7, M0=1.32e+16 Nt-m. .... 243

Figure 5-19. PSA ratios of soil site to rock site for recorded velocity time series versus PSA ratios of the simulated velocity time series for the Kinburn basin for the Ma and Audet (2014); epicentral distance=43 km, depth=14.5 km, MW=4.7, M0=1.32e+16 Nt-m, frequency range=0.1-2.5 Hz. .... 244

Figure 5-20. PSA ratios of soil site to rock site for the simulated velocity time series of the single grid size simulation (frequency range of 0.1-1 Hz) and the dual grid size simulation (frequency range of 0.1-2.5 Hz) for the Kinburn basin for the Ma and Audet (2014); epicentral distance=43 km, depth=14.5 km, MW=4.7, M0=1.32e+16 Nt-m. .... 245

Figure 5-21. Simulated velocity time series and associated velocity Fourier spectrum versus recorded velocity time series and related velocity Fourier spectrum for the Orleans basin at rock site for the Ma and Audet (2014); epicentral distance=72.2 km, depth=14.5 km, MW=4.7, M0=1.32e+16 Nt-m, frequency range=0.1-2.5 Hz. .... 246

Figure 5-22. Simulated velocity time series and associated velocity Fourier spectrum for the single grid size simulation (frequency range of 0.1-1 Hz) versus modeled velocity time series and related velocity Fourier spectrum for the dual grid size simulation (frequency range of 0.1-2.5 Hz) for the Orleans basin at rock site for the Ma and Audet (2014); epicentral distance=72.2 km, depth=14.5 km, MW=4.7, M0=1.32e+16 Nt-m. .... 247

Figure 5-23. Simulated velocity time series and associated velocity Fourier spectrum versus recorded velocity time series and related velocity Fourier spectrum for the Orleans basin at soil

site for the Ma and Audet (2014); epicentral distance=70.4 km, depth=14.5 km, MW=4.7, M0=1.32e+16 Nt-m, frequency range=0.1-2.5 Hz. .... 248

Figure 5-24. Simulated velocity time series and associated velocity Fourier spectrum for the single grid size simulation (frequency range of 0.1-1 Hz) versus modeled velocity time series and related velocity Fourier spectrum for the dual grid size simulation (frequency range of 0.1-2.5 Hz) for the Orleans basin at soil site for the Ma and Audet (2014); epicentral distance=70.4 km, depth=14.5 km, MW=4.7, M0=1.32e+16 Nt-m. .... 249

Figure 5-25. PSA ratios of soil site to rock site for recorded velocity time series versus PSA ratios of the simulated velocity time series for the Orleans basin for the Ma and Audet (2014); epicentral distance=70.4 km, depth=14.5 km, MW=4.7, M0=1.32e+16 Nt-m, frequency range=0.1-2.5 Hz. .... 250

Figure 5-26. PSA ratios of soil site to rock site for the simulated velocity time series of the single grid size simulation (frequency range of 0.1-1 Hz) and the dual grid size simulation (frequency range of 0.1-2.5 Hz) for the Orleans basin for Ma and Audet (2014); epicentral distance=70.4 km, depth=14.5 km, MW=4.7, M0=1.32e+16 Nt-m. .... 251

## **1. Introduction**

Over the last three decades, seismologists have introduced several analytical and numerical techniques to compute synthetic seismograms. These ground motion simulation approaches are increasingly applied to estimate reliably the ground shaking levels for past and future events (Graves et al., 2008; Imperatori and Mai, 2012).

There are different parameters that influence ground motion for broadband frequency ground motion simulation in earthquake hazard analysis. The effects of these parameters can be generally divided into three groups: earthquake source effects (seismic moment, slip distribution, stress drop distribution, fault geometry, rupture velocity, etc.), path effects (distance, depth, crustal velocity structure, near source effects, etc.) and site effects (soil type, thickness and heterogeneity, 3D basin effect, etc.).

Montreal and Ottawa are ranked second and third, respectively, behind Vancouver in terms of the population and seismic hazard. Major cities in eastern Canada, such as Montreal and Ottawa, are mainly located on loose postglacial sediments with very low shear wave velocities ( $< 200$  m/s) overlying very firm bedrock with high shear wave velocities ( $> 2000$  m/sec). Hence, the boundary between unconsolidated overburden and the bedrock generally constitutes a large change in stiffness or seismic impedance, which is unique (Hunter et al., 2007; Hunter et al., 2012).

Due to the strong dependency of the characteristics of the shaking at the ground surface (amplitude, frequency, and duration) on the materials through which the waves travel over the last few hundred meters (or less), local soil/site conditions play a key role in determining the damage caused by seismic waves generated by earthquakes. In additions, there is a strong correlation between the level of earthquake ground shaking and some characteristics of the basin,

including the geometrical shape of the basin (3D depth, width, and length), the geotechnical properties of the deposited soil (shear wave velocity-depth profile, shear modulus, damping reduction, etc.) and the contrast between the geotechnical properties of the bedrock and the overlying soil. In addition, most urban areas in eastern North America are located along river valleys (i.e., basins) where there are deep alluvial deposits. Therefore, basin effects can be important controlling parameters that should be considered in the determination of ground motion amplification in an area (Anderson et al., 1986; Holzer, 1994; Hisada and Yamamoto, 1996; Choi and Stewart, 2003; Hunter and Crow, 2012; Panzera, 2012).

Throughout the world, there are numerous examples of the importance of soil effects in sedimentary basins. Several studies focused on large sedimentary basins in the United States, Japan, and New Zealand (Olsen and Archuleta, 1995; Satoh et al., 2001; Benites and Olsen, 2005); other studies focused on wave propagation studies in smaller sedimentary basins, such as the Nice basin (Semblat et al., 2000), the Grenoble basin (Bonilla et al., 2006), and the Sion basin in Europe (Roten et al., 2009; Gélis et al., 2011).

Mechanisms that can be included in seismic basin effects are the reverberation of seismic waves, which can lead to longer durations and larger amplitudes of waves, seismic wave amplification in soft soil due to changes in seismic wave velocity, seismic wave attenuation due to damping in soft soil, generation of surface waves by the interaction of body waves on a steep bed of a basin's edge, impedance contrast between sediment and bed, scattering of waves in the layers interface or surface topography, focusing and defocusing of waves, and directivity (Olsen, 1994; Olsen and Schuster, 1995; Kawase, 2003).

In general, a seismic response in a basin is, therefore, dependent on its geometry, the impedance contrast between sediments and bedrock, the properties of sediments and constitutive models that

describe soil behavior, and the characteristics of the seismic source (complexity and intensity). Some of the above-mentioned mechanisms are 3D effects due to the complexities of the geological structures in basins (Kramer 1996). Thus, for a more accurate simulation that allows for greater understanding and assessment of the influence of different parameters that govern basin effects, 3D simulation methods need to be employed and improved. Improvements are now possible due to the advancements in computer capabilities (Yang, 2008; Gélis et al., 2011). It should be noted that in this research we modeled 3D ground motion for basins using earthquake source characteristics.

Three-dimensional basin modeling methods for linear soil have been performed by seismologists; however, including nonlinear soil is still a challenge. The main aim of the first paper submitted (third chapter) to the Bulletin of the Seismological Society of America is to determine the 3D basin effects on the amplification of ground motion for nonlinear soil in the Ottawa area. The parameters that were considered in the proposed basin modeling in the Ottawa area were an unusually 3D high impedance contrast and a unique nonlinear attenuation of soil (Hunter and Crow, 2012). These two parameters have not been considered in previous studies. It should be mentioned that we used the ratio of the pseudo-spectral acceleration (PSA) of the soil site to the PSA of the rock site for single degree of freedom system with 5% damping to calculate the amplification level in the soil site relative to the rock site. Further we used velocity and acceleration Fourier spectrum to consider the simulation results in frequency domain. Earthquake-related ground motions have been modeled for eastern Canada using different algorithms (e.g., Atkinson and Boore, 2007; Khasheshi Banab et al., 2012; Atkinson and Adams, 2013; Crane and Motazedian, 2014; Crane et al., 2015; Hayek, 2016; Crane, 2016). However, the uncertainties that influence the results of the models and are related to the defined source

parameters of a scenario earthquake and material model have not been well resolved for the study area. Therefore, in the second paper (forth chapter) submitted to the Bulletin of the Seismological Society of America, we studied the sensitivities of a physics-based ground motion simulation to source characteristics and the material models for modeling the Ladysmith earthquake in the Kinburn basin, Ottawa, Canada. For this study, we used a 3D staggered-grid finite difference method that employs fourth-order solutions in space and second-order solutions in time for simulations of the ground motion (Olsen, 1994; Day and Bradley, 2001; Olsen et al., 2006; Cui et al., 2010).

The improvement in computer capacities has made it possible to carry out a 3D wave propagation for a broadband frequency range with realistic velocity models on a large scale. Mostly, the modeled media for the time-domain finite-difference (FD) simulation is discretized on a numerical grid with equidistant grid spacing. Since the required spatial grid spacing is determined using the minimum (shear-wave) velocity, areas with higher velocities are spatially over sampled, which leads to an extensive oversampling of the high velocity zone in large-scale simulations. Different techniques have been used to implement variable grids in time-domain FD methods. In the third submitted paper (fifth chapter), we implemented a hybrid non-uniform method to model the Ladysmith earthquake for a frequency range of 0.1-2.5 Hz for the Kinburn and Orleans basins.

## 2. Methodology and literature review

We used a finite difference (FD) modeling method, developed by Olsen-Day-Cui, to simulate the visco-elastic propagation of seismic waves in the Kinburn basin and Orleans basin, Ottawa, Canada, for the Ladysmith earthquake ( $M_w=4.7$ ). This program solves 3D velocity-stress wave equations with an explicit staggered-grid FD scheme. This method, which is fourth-order in space and second-order in time, can be used for elastic, viscoelastic, elastoplastic, and visco-elasto-plastic behavior.

To analyze the deformation of a medium, whether it is solid or fluid, elastic or inelastic, the program uses the infinitesimal strain tensor defined in a Cartesian coordinate system ( $x_1, x_2, x_3$ ) as follows (Stein and Wysession, 2003):

$$\gamma_{ij} = \frac{1}{2}(\partial u_i / \partial x_j + \partial u_j / \partial x_i) \quad (1)$$

where  $\gamma_{ij}$  is the  $ij^{\text{th}}$  component of the strain tensor, and  $u_i$  is the  $i^{\text{th}}$  component of displacement.

The spatial derivative of displacement is then represented by  $u_{i,j} = \partial u_i / \partial x_j$  and  $u_{j,i} = \partial u_j / \partial x_i$ .

The internal forces acting mutually between adjacent particles within a continuum are related to the stress tensor as follows:

$$T_i = \tau_{ij} n_j \quad (2)$$

where  $T_i$  is the  $i^{\text{th}}$  component of the traction vector acting on the plane of normal  $n$ ,  $\tau_{ij}$  is the  $ij^{\text{th}}$  component of the stress tensor, and  $n_j$  is the  $j^{\text{th}}$  component of the unit vector normal to the surface where it interacts with traction  $T$ .

There are generally two types of forces that can act on an object. The first is a body force ( $f_i$ ), which acts everywhere within an object, resulting in a net force proportional to the volume of the

object. The second type of force is a surface force, which acts on the surface of object, causing a net force proportional to the surface area of the object. To obtain the equation of motion of a general particle, according to Newton's second ( $F=ma$ ) law, we use the following equation:

$$\frac{\partial}{\partial t} \iiint_V \rho \frac{\partial u}{\partial t} dV = \iiint_V f_i + \iint_S T dS \quad (3)$$

where  $\rho$  is the bulk density of the media. The application of Gauss's divergence theorem gives the following:

$$\iint_S T_i dS = \iint_S \tau_{ij} n_j dS = \iiint_V \tau_{ij,j} dV \quad (4)$$

For a general volume and wherever it is continuous, the integral must be zero; thus, we can conclude the following:

$$\rho \ddot{u}_i = f_i + \tau_{ij,j} \quad (5)$$

where  $\ddot{u}$  shows the second derivative of displacement, equation (5) is called the equation of motion. To simplify the calculations in the AWP-ODC program, we omit the body force ( $f_i$ ) and only use the surface forces ( $\tau_{ij,j}$ ). The body force term ( $f_i$ ) generally consists of a gravity term  $f_g$  and a source term  $f_s$ . The gravity term is an important factor at very low frequencies in normal mode seismology, but it can generally be neglected for body and surface wave calculations at typically observed wavelengths. The source term is important to model earthquake in seismic source regions (Shearer 2009), however the source term was not considered for finite fault model because the AWP-ODC program omit the body force in wave propagation simulation.

To find the relation between stress and strain, we can use a generalization of Hooke's law to express the stress tensor as a linear combination of all components of the strain tensor if the medium is linear elastic:

$$\tau_{ij} = c_{ijkl}\gamma_{kl} \quad (6)$$

where stress  $\tau_{ij}$  and strain  $\gamma_{kl}$  are second-order tensors, and  $c_{ijkl}$  is a fourth-order tensor. The most general isotropic fourth-order tensor is represented as follows:

$$c_{ijkl} = \lambda\delta_{ij}\delta_{kl} + \mu(\delta_{ik}\delta_{jl} + \delta_{il}\delta_{jk}) \quad (7)$$

with  $\lambda$  and  $\mu$  as the Lamé moduli, the stress-strain relation is as follows:

$$\tau_{ij} = \lambda\delta_{ij}\gamma_{kk} + 2\mu\gamma_{ij} \quad (8)$$

The equation of motion:

$$\rho\ddot{u}_i = (\lambda + \mu)u_{j,ij} + \mu u_{i,jj} \quad (9)$$

It should be noted that the linear elastic stress-strain relation in equation (8) is an idealized behavior. The stresses and strains occurring within a propagating wave can lead to irreversible changes in the microscopic structures of the medium, and dissipative energy may also occur on grain boundaries (Aki and Richards, 2002; Stein and Wyssession, 2003; Martin, 2010). Due to these phenomena, the AWP-ODC program solves a modified Hooke's law stress-strain equation to incorporate the effects of viscosity into time-stepped numerical simulations of wave propagation:

$$\sigma(t) = Mu[\varepsilon(t) - \sum_{i=1}^N \xi_i(t)] \quad (10)$$

where  $\xi_i$ ,  $i=1 \dots N$  are internal or memory variables that evolve with time,  $N$  is the number of relaxation terms in the approximation,  $M_u$  is the unrelaxed shear modulus,  $\sigma(t)$  is stress as a function of time, and  $\varepsilon(t)$  is strain as a function of time (Day and Minster, 1984; Day, 1998; Day and Bradly, 2001; Graves and Day, 2003; Liu and Archuleta, 2006).

The memory variables are approximated by solving the  $N$  first order of the following differential equation:

$$\tau_i \frac{d\xi_i(t)}{dt} + \xi_i(t) = \lambda_i \frac{\delta M}{M_u} \varepsilon(t) \quad (11)$$

To solve the differential equation, we calculate  $\tau_i$ ,  $\lambda_i$ , and  $\delta M$ , which are the relaxation times, relaxation coefficients, and the relaxation of the modulus, respectively. In the conventional memory variables approach for a 3D simulation,  $\lambda_i \frac{\delta M}{M_u}$  is assumed as the relaxation coefficient ( $\lambda_i$ ).  $2N$  values of  $\tau_i$  and  $\lambda_i$  are chosen in such a way that equation (12) is a good approximation of the target  $Q^{-1}(\omega)$ :

$$Q^{-1}(\omega) \approx \frac{\delta M}{M_u} \sum_{i=0}^N \frac{\lambda_i \omega \tau_i}{\omega \tau_i + 1} \quad (12)$$

Day (1998) set the relaxation coefficient to 1 and uniformly distributed the relaxation times over the logarithmic axis between the lower and upper absorption-band cutoffs using the below equation:

$$\ln \tau_k = \ln \tau_m + \frac{2k-1}{16} (\ln \tau_M - \ln \tau_m) \quad (13)$$

The lower and upper absorption-band cutoffs are represented by  $\tau_m$  and  $\tau_M$ , respectively, and are calculated as  $\tau_m = \omega_n^{-1}$  and  $\tau_M = 5N_t \omega_n^{-1}$ , where  $N_t$  is the total number of time steps in the computation (Day and Minster, 1984; Day, 1998; Day and Bradly, 2001; Graves and Day, 2003;

Liu and Archuleta, 2006 ). This method could approximately, but not optimally, model the visco-elastic behavior of seismic waves (Day and Bradly, 2001).

There are many studies (e.g., Lanzo et al., 1997; Zekkos et al., 2006; Díaz-Rodríguez et al., 2008; El Mosallamy, 2016) that show even small strains can cause a small modulus reduction. Furthermore, our simulations show that the resulting strains from the Ladysmith earthquake slightly exceed the yielding strain level of clay ( $10^{-6}$ ) at some points in the soil sites.

Thus, to improve the approximation that we used in the visco-elastic simulation, we adopted the approximation by calculating the modulus deficit ( $\delta M/Mu$ ) and relaxation coefficients ( $\lambda i$ ) at each time step in the simulation. We calculated the relaxation times using the same method as that of the regular visco-elastic simulation, and we defined the relaxation coefficients as a function of the modulus deficit so that equation (12) was a good approximation of the target  $Q^{-1}(w)$ . In addition, we calculated the modulus deficit using a modulus reduction curve. In this research, we used the modulus reduction equation proposed by Seed et al. (1970), described as follows (Rollins et al., 1998):

$$\frac{M}{Mu} = \frac{1}{1+20\varepsilon(1+10^{-10}\varepsilon)} \quad (14)$$

where  $M$  is the modified shear modulus calculated at each time step,  $Mu$  is the preliminary value of the shear modulus ( $Mu=V_s*\rho$ ), and  $\varepsilon$  is strain. Thus, the relaxation coefficient and modulus deficit ( $\delta M/Mu$ ) are updated at each time step. The calculated relaxation times, relaxation coefficients, and modulus deficit are used to calculate the memory variables at each time step in the simulation.

Due to the deficiency of elastic and viscous bodies in the description of linear rheological behavior, the linear description of soil behavior requires the consideration of time effects and/or a combination of different rheological responses. Three common linear rheological models are a)

a firmoviscous (or Kelvin) body showing anelasticity or elastic afterworking, i.e., the elastic strain takes a finite time to be achieved and recovered; b) a viscoelastic (or Maxwell) body showing an instantaneous elastic response followed by a linear viscous flow; and c) a general linear (or Burgers) body, where an instantaneous elastic strain is followed by a time-dependent strain and then by viscous strain (Ranalli, 1995, Banks et al., 2011).

If an input motion to soft-surface layers becomes so intense that the shear strain built up inside the layer reaches a certain threshold level, soil behaves nonlinearly. It has been commonly assumed that the nonlinear effects of wave propagation on strong and soft materials are the same. However, nonlinear effects (a nonlinear stress-strain relationship) significantly affect soft materials with slower velocities and more rapidly attenuate large amplitude waves. Further, according to observational evidence, this phenomenon is common for many accelerograms.

Soil nonlinearity is characterized by reduced shear rigidity, which causes a reduction in the shear wave velocity and an increase in the damping factor. Thus, the main effects of nonlinearity are a decreased effective shear velocity in sediments, increased damping, which lead to shifting resonant peaks to lower frequencies and lower amplitudes. Other effects include permanent displacements not associated with source dislocation, reductions in peak ground velocity and peak ground acceleration, and soil liquefaction. It should be mentioned that, before the 1989 Loma Prieta and 1994 Northridge earthquakes, the influence of soil nonlinearities on ground motion was only assumed to happen for areas that involved liquefaction. In terms of site effects, these effects result in prolonged predominant periods and reduced amplification.

An understanding of nonlinearity is, therefore, a current and important issue for strong-motion seismology, specifically for wave propagation analyses and assessing quantitative physical

parameters (Chin and Aki, 1991; Field et al., 1997; Kawas, 2003; Martin, 2010; Taborda et al., 2012; Restrepo et al., 2012).

The unusual impedance contrast in eastern Canada can introduce surface waves at a basin edge. It has been suggested that the large strains induced by energetic long period surface waves give rise to nonlinear behavior in shallow sedimentary soils. The nonlinear behavior of sediments influences ground motion by creating permanent displacement and reducing peak ground velocity (PGV) and amplitude. Thus, predicting soil nonlinearity is very important to determine seismic soil amplification at stronger levels of shaking in seismic hazard assessments.

Past observations have shown that both viscoelasticity and nonlinearity strongly modify ground motion for a range of broadband frequencies, but they compete in different frequency bands.

This observation means that realistic simulations should consider both viscoelasticity and nonlinear soil behavior. Although the effects of nonlinear attenuation were initially considered controversial among seismologists and engineers, it is now well accepted that soil may behave nonlinearly during moderate to large magnitude earthquakes (Beresnev and Wen, 1996; Restrepo, 2012).

It should be mentioned that it has been customary to present a reduced shear modulus and increased damping as functions of increasing shear strain, which represented a measure of material nonlinearity. Considering soil nonlinear behavior, we need to verify the shear modulus reduction and increased damping (Hardin and Dmevich, 1972a; Bonilla, 2000).

There are different methods for predicting soil nonlinear behavior, including a) equivalent linear models based on a viscoelastic constitutive model, b) cyclic nonlinear models, and c) advanced constitutive models (Kramer, 1996; Dupros et al., 2010). Equivalent linear models are only an

approximation of the actual nonlinear behavior of the soil; thus, the models use a very simple class of computational models for earthquake engineering (Kramer, 1996; Dupros, 2010).

In contrast, the calculations used in advanced constitutive models involve descriptions of soil behavior for general initial stress conditions, a wide variety of stress paths, rotating principal axes, cyclic or monotonic loading, low and high strain rates, and drained or undrained conditions. In advanced models, parameters should be chosen such that they are closely related to the rheology that describes the material properties at various strain levels. In some cases, these rheological models do not necessarily have physical parameters; sometimes the parameters are indirect and cannot be measured in a laboratory. Thus, one obstacle in using advanced models is the difficulty in identifying the parameters. In addition, a lack of knowledge of soil properties is common in seismic studies, and a complete geotechnical description of a site is very rare (Kramer, 1996; Dupros, 2010; Martin, 2010).

Therefore, we used cyclic nonlinear models to take into account soil nonlinear effects using a hysteresis loop notion. The hysteresis loop states that a stress-strain relationship can be described in two ways: a) by parameters (inclination and the area of hysteresis loop) that describe its general shape, as described in the equivalent linear method, and b) by the actual path of the loop itself. Cyclic nonlinear models, which mainly consider an elasto-plastic constitutive behavior for soil deposits, determine the nonlinear stress-strain behavior of soil by following the actual stress-strain path during cyclic loading. These models are able to reproduce the intrinsic complex features of soil behavior, such as stiffness degradation, irrecoverable displacement, and volumetric strain generation, under seismic loading in a wide range of shear strains, i.e., from  $10^{-6}$  to  $10^{-2}$  (Kramer, 1996; Dupros, 2010).

Based on laboratory tests, soil stiffness is influenced by the cyclic strain amplitude, void ratio, mean principal effective stress, plasticity index, overconsolidation ratio, and number of loading cycles. The secant shear modulus of an element of soil varies with the cyclic shear strain amplitude. Thus, a variety of nonlinear models have been developed to describe soil behavior, which can be characterized by the initial loading or backbone curve and a series of rules that govern unloading-reloading behavior. The initial (low-strain) stiffness and the (high-strain) shear strength of soil are parameters that control the shape of any backbone curve (Kramer, 1996; Dupros, 2010).

Two types of materials have been used to describe the nonlinear stress-strain relationship [ $\tau = F_{bb}(\gamma)$ ] of soils. The first and simpler model, the backbone function,  $F_{bb}(\gamma)$ , is a two-parameter model that can be described by a hyperbola (Kramer, 1996):

$$F_{bb}(\gamma) = \frac{G_{max}\gamma}{1 + \left(\frac{G_{max}}{\tau_{max}}\right)|\gamma|} \quad (15)$$

where  $G_{max}$  is the maximum shear modulus,  $\tau_{max}$  is the maximum shear stress, and  $\gamma$  is the shear strain. The values of  $G_{max}$  and  $\tau_{max}$  can be calculated directly, computed, or obtained by empirical correlation. The use of measured shear wave velocities is generally the most reliable means of evaluating  $G_{max}$  (Kramer, 1996; Ishihara, 1996):

$$G_{max} = \rho v_s^2 \quad (16)$$

The second model is a four-parameter model known as the Ramberg-Osgood model (R-O model). The original form of the stress-strain relationship for the backbone curve is as follows:

$$\frac{\gamma}{\gamma_y} = \frac{\tau}{\tau_y} \left[ 1 + \alpha \left| \frac{\tau}{\tau_y} \right|^{r-1} \right] \quad (17)$$

where  $\tau_y$  and  $\gamma_y$  are the shear stress and shear strain, respectively, which are selected appropriately, and  $\alpha$  and  $r$  are constants (Kramer, 1996; Ishihara, 1996).

It should be mentioned that hysteresis loops follow the Masing (1926) criteria, which is a constitutive law that specifies the stress-strain relation at each step of loading, unloading, and reloading phases as follows:

1. For initial loading, the stress-strain curve follows the backbone curve.
2. If a stress reversal occurs at a point defined by  $(\gamma_r, \tau_r)$ , according to the original Masing rules, the initial loading or backbone curve is defined by a functional relationship between the stress,  $\tau$ , and the strain,  $\gamma$ , as  $\tau = f(\gamma)$ . Subsequently, the unloading stress-strain relationship keeps the same shape as that of the initial loading curve in the negative domain, but is magnified by a factor of two, whereas the reloading stress-strain relationship has the same shape as that of the initial loading in the positive domain and is also magnified by a factor of two. Both unloading and reloading stress-strain relationships follow the path below:

$$\left(\frac{1}{K_H}\right) (\tau - \tau_r) = f\left[\left(\frac{1}{K_H}\right) (\gamma - \gamma_r)\right] \quad (18)$$

where  $K_H$  is the hysteresis scale factor, which for Masing's original formulation is equal to 2.

Due to the insufficiency of these two rules in describing soil response under general cyclic loading, some additional rules were added to prevent the computed stress from exceeding the maximum strength of a material,  $\tau_{\max}$ . According to these rules, after the reloading/unloading curve again meets the backbone curve, further reloading/unloading continues along this

backbone curve. Generally, every time a stress-strain curve meets a curve from a previous cycle, it follows the previous curve. These four criteria are known as the extended Masing rules. There are other unloading-reloading models available (Iwan, 1967; Finn et al., 1977; Pyke, 1979; Vucetic, 1990; Kramer, 1996; Bonilla, 2000; Hartzel et al., 2004; Yi et al., 2010; Puzrin, 2012).

The ability to represent the development of permanent strains is the most important advantage of these other models, but they are not able to determine the shear-induced volumetric strains that can lead to hardening under drained conditions or to a pore pressure development under undrained conditions. Thus, a more complex cyclic nonlinear model should incorporate many other parameters (Kramer, 1996).

If uniform grids are used, the grid size of a model is determined by the shortest wavelength that needs to be calculated. In a realistic geological structure with a large impedance contrast in seismic wave velocity between soils and rocks, simulating seismic wave propagation using a spatially uniform grid can be computationally demanding due to over sampling high-speed materials. Thus, numerical methods that allow for coarser discretization of the faster regions have the potential to be much more efficient. Further, using non-uniform mesh size lets us model the ground motion for a broadband frequency range (Aoi and Fujiwara, 1999; Nie et al., 2017).

We developed the AWP-ODC program to use discontinuous grids, which are a kind of hybrid, multi-grid method. In discontinuous grids, the grid system consists of two regions; each region has a uniform grid that consists of grids with fine spacing near the surface (soil site) where the wave velocity is low and coarser spacing in the deeper region (rock site). This kind of multi-grid technique is already used in the field of fluid mechanics (e.g., McBryan et al, 1991). In each region, the wave field is calculated independently using a velocity-stress formulation. Thus, first

we model the ground motion simulation for a rock site, and then we use the output of the simulation of the rock site as input for the ground motion simulation in the basin. The stress between two mesh sizes is calculated using linear interpolations.

**3. Three dimensional nonlinear ground motion simulation using a physics-based method for the Kinburn basin**

## **Abstract**

We used a finite difference (FD) modeling method, developed by Olsen-Day-Cui, to simulate nonlinear-viscoelastic basin effects in a spectral frequency range of 0.1 to 1 Hz in the Kinburn bedrock topographic basin, Ottawa, Canada, for large earthquakes. The geotechnical and geological features of the study area are unique: loose, postglacial sediments with very low shear wave velocities ( $< 200$  m/s) overlying very firm bedrock with high shear wave velocities ( $> 2000$  m/s). Comparing records and simulated velocity time series showed that regular viscoelastic simulations could model the ground motions at the rock and soil sites in the Kinburn basin for the Ladysmith earthquake, a local earthquake that occurred on 17 May 2013 with  $M_w$  4.7 ( $M_N$  5.2). The Ladysmith earthquake was scaled to provide a strong level of shaking for investigating the nonlinear behavior of soil; therefore, a new nonlinear-viscoelastic subroutine was introduced to the program. A modeled stress-strain relationship associated with ground motion modeling in the Kinburn basin using a scaled Ladysmith earthquake event of  $M_w=7.5$  followed Masing rules. Using nonlinear-viscoelastic ground motion simulations significantly reduced the amplitude of the horizontal component of the Fourier spectrum at low frequencies and the predicted PGA and PGV values compared to regular linear viscoelastic simulations; hence, the lower soil amplification of seismic waves and the frequency and amplitude spectral content were altered by the nonlinear soil behavior. In addition, using a finite fault model to simulate an earthquake with  $M_w=7.5$  was necessary to predict the higher levels of stresses and strains that were generated in the basin. Using a finite fault source for the nonlinear-viscoelastic simulation caused the amplification of vertical component while it caused de-amplification of horizontal components because of the shear modulus reduction and increase of damping.

### **3.1. Introduction**

Several parameters influence the seismic ground motion of a broadband frequency range in earthquake hazard analysis. The effects of these parameters can be generally divided into three groups: earthquake source effects (seismic moment, slip distribution, stress drop distribution, fault geometry, rupture velocity, etc.), path effects (distance, depth, crustal velocity structure, near source effects, etc.), and site effects (soil type, thickness and heterogeneity, 3D basin effect, soil nonlinearity, etc.).

The characteristics of ground shaking (amplitude, frequency content, and duration) are highly dependent on the soft basin materials through which the waves travel over the last few hundred meters (or so). Consequently, the extent of the damage caused by seismic waves generated by earthquakes is dependent on the local soil/site conditions in many urban areas located along river valleys (i.e., basins) where there are deep alluvial deposits. Therefore, basin geotechnical and geometrical features are important controlling parameters that should be considered to determine ground motion amplification in such areas (Anderson et al., 1986; Holzer, 1994; Olsen, 1994; Hisada and Yamamoto, 1996; Olsen, 2000; Choi and Stewart, 2003; Hunter and Crow, 2012; Panzera, 2012; Gélis and Bonilla, 2012; Molnar et al., 2014).

In general, a basin's seismic response is dependent on its shape/geometry, the seismic impedance (shear wave velocity times density) contrast between sediments and bedrock, and the geotechnical properties of the sediments such as shear modulus and damping behavior of soil. Some of the above-mentioned mechanisms are 3D effects (Olsen, 1994; Olsen and Schuster, 1995; Kramer, 1996; Kawase, 2003; Gélis et al., 2011; Gélis and Bonilla, 2012; Gélis and Bonilla, 2014). Thus, for a more realistic simulation that provides a better understanding of different parameters that govern basin effects, 3D simulation methods need to be employed and

improved; these methods and improvements are now possible due to advancements in computer capabilities (Olsen, 2000; Yang, 2008; Cui et al., 2010; Gélis et al., 2011; Cui et al., 2013; Olsen et al., 2016).

Seismologists have performed large scale 3D ground motion simulations for linear soil since 1990s; however, the large scale modeling of the nonlinear soil behavior is still a challenge. Since the early 1960s, laboratory studies have shown that nonlinear soil behavior can cause the shear modulus and shear wave velocities reduction, and consequently de-amplification (Wen, 1994; Beresnev et al., 1995; Field et al., 1997; Taborda et al., 2012), in addition to permanent deformations in soil (Wen, 1994; Beresnev et al., 1995; Field et al., 1997; Li, 2010; Taborda et al., 2012). Thus, a realistic simulation should take into account the nonlinear soil effects (Wen, 1994; Beresnev et al., 1995; Field et al., 1997; Gélis and Bonilla, 2012; Gélis and Bonilla, 2014).

The nonlinear behavior of soil is more important in frequency ranges greater than about 0.5 Hz (Taborda 2012), where PGA values exceed 0.1 g and the shear strain is larger than  $10^{-6}$  (Darragh and Shakal, 1991; Field et al., 1997; Beresnev, 2002; Chang et al., 1989; Chin and Aki, 1991; Beresnev and Wen, 1996; Trifunac and Todorovska, 1996; Taborda et al., 2012; Régnier et al., 2013; Chandra et al., 2015 and 2016; Guéguen, 2016). Therefore, nonlinear soil behavior should be considered in simulation of strong ground motions for broadband frequency ranges.

Past geological studies in the Ottawa area have proven the presence of soft soil that has very high shear wave contrasts (15-20) with bedrock compared to typical soil/bedrock contrasts of 3–5 in western North America. This unusually high contrast along with nonlinear behaviour of local soil in Ottawa area (Leda clay's shear modulus curve) can lead to unusual soil amplification/de-amplification because of the reverberation of waves within the basin (Hunter et al., 2007; Motazedian et al., 2010; Hunter and Crow, 2012). Thus, we need to take into account

the high shear wave contrast and nonlinear soil effect for ground motion simulations in the Ottawa area. The important feature of the Leda clay's shear modulus curve is because of the linear behavior of curve up to higher strain ( $\sim 10E-4$ ) and a sharp decrease at larger strains.

It should be mentioned which, although, there is not any recorded large earthquake in Ottawa area but there are several paleo-seismology studies which have identified large paleoearthquakes in eastern Canada by studying the landslides within the basins (e.g. Adams 1982; Shilts and Clague 1992; Ouellet 1997; Doughty et al., 2014; Brooks 2015; Lajeunesse et al., 2016; Esmailzadeh et al., 2017).

There are several constitutive models, such as the Duncan-Chang model or Hyperbolic model, and the (modified) Cam-Clay model, that can be used to simulate the material behavior to formulate the relationship between stress (or stress increment) and strain (or strain increment) (Brinkgreve, 2005). However, The AWP-ODC program, which has been used in this study, solves a modified Hooke's law stress-strain equation to incorporate the effects of viscosity into time-stepped numerical simulations of wave propagation. In this paper, the seismic response of the Kinburn basin in Ottawa, Canada, was simulated using AWP-ODC [Anelastic Wave Propagation developed by the Olsen-Day-Cui program (Olsen, 1994; Olsen et al., 1995, 2003, 2006; Cui et al., 2009)] and a subroutine was developed and employed to consider nonlinear soil behavior to investigate the effects of the soil and basin characteristics on the seismic amplification/de-amplification in a basin.

### **3.2. Geographical location and geological features**

Because of the regional population and seismic hazards, Montreal and Ottawa are ranked second and third, respectively, behind Vancouver, in terms of seismic risk in Canada. Major

cities in eastern Canada, such as Montreal and Ottawa, are mainly located on loose, postglacial sediments (Leda clay) that have very low shear wave velocities, on average around 150 m/s, overlying very firm bedrock that has high shear wave velocities, on average around 2700 m/s (Hunter et al., 2010; Motazedian et al., 2011; Hunter et al., 2012; Khareshi Banab et al., 2012). Hence, the boundary between the unconsolidated overburden and the bedrock generally marks a large change seismic impedance.

Figure 3-1 shows the updated Vs30 classification for the cities of Ottawa and Gatineau (Hunter et al., 2010; Motazedian et al., 2011; Hunter et al., 2012). The Kinburn basin (lat. 45°22'59.5"N, long. 76°09'16.5"W) is located 2.8 km southeast of the hamlet of Kinburn, Ontario, and is oriented in a northwest-southeast direction (Fulton, 1987). This basin is one of the smaller interconnected basins in the region. Based on seismic and borehole data, a Paleozoic carbonate bedrock ridge bounds the depression to the south and west, and a Precambrian Shield ridge bounds the depression to the north and east (Richard, 1984). The maximum depth from the surface to the bedrock is approximately 140 m. It is bounded on the northeastern side by steep faults, whereas the southwestern edge is more gently sloped. The basin is filled with low Vs fine-grained sediments called Leda clay (non-sensitive); this clay overlies a till layer, which directly overlies the bedrock in many locations (Hayek, 2016; Hunter et al., 2012). The seismic characteristics of the Kinburn basin that are used in the simulation are described in the following sections.

### **3.3. Finite difference modeling**

For this simulation, we used a finite difference (FD) code (Anelastic Wave Propagation - AWP), developed and maintained by Kim B. Olsen, Steven M. Day, and Yifeng Cui (ODC)

(Olsen, 1994; Olsen et al., 1995, 2003, 2006; Cui et al., 2009), that simulated the 3D propagation of a spontaneous rock rupture. Using an explicit staggered grid FD scheme, the program solves modified Hooke's law to model the relationship between stress and strain increment and to incorporate the effects of viscosity into time-stepped numerical simulations of wave propagation:

$$\sigma(t) = \mu[\varepsilon(t) - \sum_{i=1}^N \xi_i(t)] \quad (1)$$

where  $\xi_i$ ,  $i=1 \dots N$  are internal or memory variables that evolve with time,  $N$  is the number of relaxation terms in the approximation,  $\mu$  is the unrelaxed shear modulus,  $\sigma(t)$  is stress as a function of time, and  $\varepsilon(t)$  is strain as a function of time (Day and Minster, 1984; Day, 1998; Day and Bradley, 2001; Graves and Day, 2003; Liu and Archuleta, 2006).

Although Hooke's law is the simplest available stress-strain relationship and cannot directly capture essential features of soil behavior, it still plays an important role in advance constitutive modeling as it forms the elastic part of advanced models (Brinkgreve, 2005). In addition, using a cyclic nonlinear model, we can take into account nonlinear soil behavior using Hooke's law (more detail is provided later) (Kramer, 1996; Dupros, 2010).

This method, which is fourth-order in space and second-order in time, can be used for elastic, viscoelastic, elastoplastic, and visco-elasto-plastic behavior. In the staggered-grid technique, normal stress components and Lamé parameters are defined on the grids. The shear stress component and the modulus of rigidity are defined at the center of each grid. The horizontal and vertical components of particle displacement and density are defined midway between two adjacent grid points in the horizontal and vertical directions, respectively (Cui et al., 2010; Narayan, 2010).

Based on previous studies (for example Olsen et al., 1995, 2003, 2006; Cui et al., 2009; Roten et al., 2016), the staggered-grid FD scheme reproduces features at both fault rupture

modeling and wave propagation in basins away from the earthquake sources. Thus, it can simulate normal incidence reflections and multiples, converted shear waves, head waves, reflected head waves, and surface waves (Olsen et al., 1995, 2003, 2006; Cui et al., 2009; Roten et al., 2016). The advantages of the staggered-grid method include its stability and accuracy in modeling large Poisson's ratio materials (e.g., low  $V_s$  velocities) and mixed acoustic-elastic media and the ease with which sources can be inserted at or near the free surface. This code is particularly useful for modeling near-surface problems and for the studies of seismic wave changes with the distance in laterally varying media (Levander, 1988; Yao and Margrave, 1999).

Hooke's law mainly models linear elastic stress-strain relationships, however, implementation of shear modulus reduction curve at each time step, as described in the following sections, provides an appropriate approximation of nonlinear soil behavior. We used a cyclic nonlinear model to incorporate the nonlinear soil effects in the ground motion simulation.

### **3.4. Proposed nonlinear-viscoelastic simulation method**

To model the nonlinear soil effects, we need a hysteresis loop that describes the stress-strain relationship. The hysteresis loop follows the actual stress-strain path during cyclic loading. Masing criteria (1926) specify the stress-strain relationships at each step of the loading, unloading, and reloading phases as follows:

- 1) For initial loading, the stress-strain curve follows the backbone curve.
- 2) If a stress reversal occurs at a point defined by  $(\gamma_r, \tau_r)$ , according to the original Masing's rules, the initial loading or backbone curve is defined by a functional relationship between the stress,  $\tau$ , and the strain,  $\gamma$ , as  $\tau = f(\gamma)$ . Subsequently, the unloading stress-strain relationship keeps the same shape as that of the initial loading

curve in the negative domain, but it is magnified by a factor of two; thus, the reloading stress-strain relationship has the same shape as that of the initial loading in the positive domain, but it is also magnified by a factor of two. Both unloading and reloading stress-strain relationships follow a path given by the following:

$$\left(\frac{1}{K_H}\right)(\tau - \tau_r) = f\left[\left(\frac{1}{K_H}\right)(\gamma - \gamma_r)\right] \quad (2)$$

where  $K_H$  is the hysteresis scale factor, which is equal to 2 according to Masing's original formulation.

Due to the inadequacy of these two rules in describing the soil response under general cyclic loading, two additional rules are added to prevent the computed stress from exceeding the maximum strength of the material,  $\tau_{\max}$ :

3) When the maximum past strain is exceeded during unloading or reloading, and thus the backbone curve is intersected, the unloading or reloading curve will follow the backbone curve until the next stress reversal.

4) If the reloading/unloading curve again meets the backbone curve, further reloading/unloading continues along the backbone curve.

These two additional rules were formulated by Iwan (1966, 1967), and therefore, they are called Iwan's models or extended Masing's rules.

The Davidenkov-class model describes a stress-strain relation as follows:

$$\tau = \tau_c + G_{\max}(\gamma - \gamma_c)\left[1 - H\left(\frac{|\gamma - \gamma_c|}{n}\right)\right] \quad (3)$$

where  $\tau_c$  and  $\gamma_c$  are the stress and strain values at the last reversal, and the coefficient  $n$  is equal to 1 for initial loading and 2 for unloading and reloading.

One of the most well-known models that proves the above model uses a hyperbola, represented by  $H(\gamma)$ , to model soil behavior (Konder and Zelasko 1963):

$$H(\gamma) = \frac{\gamma}{\gamma_y} / (1 + (\frac{\gamma}{\gamma_y})) \quad (4)$$

where  $\gamma_y$  is the reference strain, which is defined in terms of the maximum shear modulus  $G_{max}$ .

Using the hyperbolic model in equation 2 with a minor rearrangement gives the following (Pyke, 1980; Kramer, 1996; Bonilla, 2000; Hartzel, 2004; Puzrin, 2012):

$$\tau = \tau_c + G_{max}(\gamma - \gamma_c) [1 / (1 + \frac{\gamma - \gamma_c}{n\gamma_y})] \quad (5)$$

The right side of equation 5 contains 2 terms. The first term ( $\tau_c$ ) is the stress level at the reversal point, and the second term ( $G_{max}(\gamma - \gamma_c) [1 / (1 + \frac{\gamma - \gamma_c}{n\gamma_y})]$ ) includes a modulus reduction equation times the strain; the strain in the modulus reduction equation is initiated from zero at each reversal. Thus, we can rearrange equation 5 to describe the nonlinear stress-strain relationship of soils (Chandra et al., 2015):

$$\tau = \tau_c + G_{(\gamma - \gamma_i)} * \gamma \quad (6)$$

where  $G_{(\gamma - \gamma_i)}$  is the shear modulus as a function of strain, and  $\gamma_i$  is the shear strain, which is initiated at the beginning of each cycle. The value of  $G$  in this equation is calculated directly from the modulus reduction curve, which is described as follows:

$$G(\gamma) = G_{max} * f(\gamma - \gamma_i) \quad (7)$$

Where  $f(\gamma - \gamma_i)$  is the modulus reduction function and  $G_{max}$  is the maximum shear modulus, which is evaluated using measured shear wave velocities:

$$G_{max} = \rho v_s^2 \quad (8)$$

The AWP-ODC program calculates the particle motion velocity using the below governing elastodynamic equations for a 3D model:

$$\partial_t v = \frac{1}{\rho} \nabla \cdot \sigma \quad (9)$$

$$\partial_t \sigma = \lambda(\nabla \cdot v)I + \mu(\nabla v + \nabla v^T) \quad (10)$$

where  $v$  denote the particle velocity vector ( $v = v_x, v_y, v_z$ ),  $\sigma$  is the symmetric stress tensor

$$\sigma = \begin{pmatrix} \sigma_{xx} & \sigma_{xy} & \sigma_{xz} \\ \sigma_{yx} & \sigma_{yy} & \sigma_{yz} \\ \sigma_{zx} & \sigma_{zy} & \sigma_{zz} \end{pmatrix}, \lambda \text{ and } \mu \text{ are the Lamé coefficients, } \rho \text{ is the density (Cui et al., 2010). The}$$

AWP-ODC program solves the 3D elastic wave equation using a staggered-grid finite difference method driven by Virieux (1984, 1986) as an extension of a 2D approach to calculate the velocity of each cubic mesh in the model at each time step (for more detail, please refer to Olsen, 1994). The strain tensor describes the internal deformation and its components are calculated using spatial derivatives of the displacement vector components ( $u_x, u_y, u_z$ ) as follow:

$$e_{ij} = \begin{pmatrix} \partial_x u_x & \frac{1}{2}(\partial_y u_x + \partial_x u_y) & \frac{1}{2}(\partial_z u_x + \partial_x u_z) \\ \frac{1}{2}(\partial_x u_y + \partial_y u_x) & \partial_y u_y & \frac{1}{2}(\partial_z u_y + \partial_y u_z) \\ \frac{1}{2}(\partial_x u_z + \partial_z u_x) & \frac{1}{2}(\partial_z u_y + \partial_y u_z) & \partial_z u_z \end{pmatrix} \quad (11)$$

where  $e_{ij}$  is the shear strain. To implement the nonlinear formulation in AWP-ODC, we calculated the shear strain components on the faces of each cubic mesh from the associated calculated velocity components in each cubic mesh for each time step using the equation below:

$$e_{ij} = \frac{1}{2}(\partial_i v_j + \partial_j v_i)dt \quad (12)$$

where  $dt$  is the time step of the simulation. It should be mentioned that  $v_i = \partial_t u_i$  and we omitted the volume change (diagonal components of  $e_{ij}$  in equation 11) as we are interested in shear modules reduction. Thus there are 3 independent components that should be calculated (Stein and Wyssession, 2003). Then, if the calculated strain level in each face of each mesh exceeded the defined threshold strain, a new shear modulus was calculated for that face of the mesh to be used in the current calculation of the stress-strain relation (equation 10). The yielding strain in our simulation was defined as  $10^{-6}$  based on the unpublished geotechnical studies of the area, which were associated with the yielding shear strain of Leda clay in the Ottawa area. In our

modeling, we calculated a new shear modulus using a shear modulus reduction curve by Seed et al. (1970). The equation that best fit the average curve is as follows (Seed et al., 1970; Rollins et al., 1998):

$$G/G_{\max} = \frac{1}{[1+20\gamma(1+10^{(-10\gamma)})]} \quad (13)$$

Furthermore, based on the strain increment in each time step, unloading was differentiated from reloading. Therefore, we set the hysteresis factor in equation 2 equal to 1 for loading and 2 for unloading and reloading to follow Masing's rules. It should be mentioned which the Hooke's law used to describe the relation between stress and strain. Further, the nonlinearity was considered for shear components of stress tensor thus there is not nonlinearity on Bulk modulus.

The newly introduced subroutine, which uses the  $G/G_{\max}$  curve to include the nonlinear behavior of soil is in Appendix A.

### **3.5. Seismic characteristics of the Kinburn basin**

The high resolution seismic surveying (Pugin et al., 2013) and borehole logging studies conducted by the Geological Survey of Canada (GSC) on the Kinburn basin show that Leda clay deposits from bottom to top were formed with five main units (Figure 3-2): 1) interstratified silty clays and sand, 2) grey rhythmites, 3) massive marine clays, 4) red and grey rhythmites, and 5) upper clayey silts (Hunter et al., 2012). There have been extensive studies by Geological Survey of Canada and Carleton University (Hunter et al., 2010; Motazedian et al., 2011; Hunter et al., 2012) and the velocity inversion is very common in the study area due to an over-consolidated layer at the surface overlying lower level with lower shear wave velocity. The velocity profile of the Kinburn basin (Figure 3-3) was directly obtained from the high resolution measured velocities in borehole logging studies at a site near the deepest part of the basin was used to

model the basin. The borehole shear wave velocity-depth profile was arithmetically averaged within each mesh in the velocity model. Below soil layers, the bedrock was assigned measured velocities, estimated densities, and Q for modeling (Hunter et al., 2010; Motazedian et al., 2011; Hunter et al., 2012). Table 3-1 presents the properties used in our simulation of the seismic velocity model, which uses a grid size of 25 meters. In order to model the maximum frequency of 1 Hz in this FD simulation the grid size should be 25 m (see section 3.7 for the justifications) (Yang 2008). It should be noted that the variation of velocity at the top 25 m (Figure 3-3) can be properly modeled according to the grid size of 25 m used for simulations.

In addition, the 3D basin depth was modeled based on the high resolution seismic and horizontal to vertical spectral ratio (HVSr) data that was collected by GSC within the basin (Hunter et al., 2007; Hunter et al., 2010; and Pugin et al., 2013). As shown in the data, the basin was elongated along the northwest-southeast direction (Figure 3-2), and the maximum thickness of the Leda clay in the deepest part of the basin was 116 m. The maximum depth of the basin (Leda clay plus glacial till) was 140 m. Figure 3-4 shows the location of the broadband seismograph sites that were selected for this study including the bedrock outcrop and the deepest part of the basin. Thus, for modeling, two receiver sites were placed along these sites, one at the edge of the basin to capture the approximate input waves entering the basin and one at the deepest point in the basin to study the effects of the basin depth and shape in the ground motion simulation.

Figure 3-5 shows the defined cross-section of the site shown in Figure 3-4 and the grids (25 m) used for modeling. The maximum frequency modeled in the simulations is 1 Hz according to the grid size (25 m) and the minimum shear wave velocity (178 m/s) used in the velocity model. Because the Ladysmith earthquake was used as an input earthquake in this simulation, the cross-

section was along the radial direction of the Ladysmith earthquake waves, and the receiver sites were deployed on this cross-section. Figure 3-5 shows that the discretized model of the basin reasonably models the shape of the Kinburn basin although there are some second order discrepancies between the measured and modeled depths.

### **3.6. The Ladysmith earthquake**

At 09:43 EDT (13:43 UTC) on 17 May 2013, an Mw 4.7 ( $M_N$  5.2) earthquake occurred 18 km northeast of Shawville in southwestern Quebec and 4 km from the small community of Ladysmith (Figure 3-6). The earthquake occurred in the western Quebec seismic zone (WQSZ), a broad region of moderate earthquake activity extending northwest from Montreal to the Lake Timiskaming region in Quebec. Published studies that calculated the focal mechanism of this earthquake used a variety of methods based on the records from the Canadian National Seismograph Network (CNSN) and the U.S. Transportable Array (USTA) (Herrmann, 2013; Ma and Audet, 2014; Atkinson et al., 2014; Bent et al., 2015). The proposed focal mechanisms indicated oblique thrust faulting on a northwest striking plane. This kind of focal mechanism is typical of earthquakes in western Quebec (Ma and Audet, 2014).

Figure 3-7.a shows the recorded velocity time series associated with the Ladysmith earthquake at the rock site (JSBS) and soil site (JSSS) in the Kinburn basin (Figure 3-4). Further, Figure 3-7.b shows the velocity Fourier spectral ratio of soil site (JSSS) to rock site (JSBS). Figure 3-7.b shows that the maximum amplification happened at 0.7 Hz for Horizontal components which is consistent with previous studies in the Kinburn basin (e.g Hunter et al., 2010; Hayek, 2016). Thus, the ground motion simulation of the Ladysmith earthquake for the frequency range of 0.1-1 Hz is good enough to study soil effects in the Kinburn basin.

### 3.7. Simulation characteristics

*Grid size.* The FD method requires at least four samples per wavelength to model a wave. Thus, based on the minimum velocity that was chosen in the velocity model (178 m/s associated with the shear wave velocity at the top of the basin) and the maximum frequency of interest (1.0 Hz) which was chosen according to the available computational resources and the frequency associated with maximum amplification in the Kinburn basin (0.7 Hz), the grid size or spatial step (dh) was 25 m. Then, because of the maximum wave velocity,  $V_p=6200$  m/s, in the velocity model and the Courant number for the stability of the FD method, the time step for the simulation was calculated as follows:

$$dt < 0.5 * dh / V_{\max} \quad (14)$$

Thus, for this simulation  $dt=0.0016$  was used.

*Boundary conditions.* There were two options available for the boundary conditions of the simulation: the Cerjan et al. (1985) method (using the sponge zone of artificial attenuation) and the perfectly matched layer (PML) method (Berenger, 1994; Rappaport, 1995; Chew and Liu, 1996). Previous studies showed that the PML method was more effective than the Cerjan method for absorbing waves at the boundary of a model, particularly in 3D simulations; thus, PML was employed in this modeling (Marcinkovich and Olsen, 2003; Cui et al., 2010; Liu, 2013).

*Source parameters and Geometry of simulated area.* In this study we run two set of simulations including a small simulation (epicentral distance=5.6 km; Hypocenter depth = 4.5 Km;  $M_w=7.5$ ; input velocity model of  $7.5*10^5$  km for East-West\*North-South\*Vertical directions) and large simulations (epicentral distance=43 km [real epicentral distance of Ladysmith earthquake]; Hypocenter depth = 14.5 Km;  $M_w=4.7$  for studying the Ladysmith

earthquake proposed focal mechanism and  $M_w = 7$  and  $7.5$  for studying nonlinear soil effects in the Kinburn basin; input velocity model:  $21 \times 50 \times 17.5$  km for East-West\*North-South\*Vertical directions). We modeled the ground motions of the Kinburn basin for the focal mechanism which was proposed by Ma and Audet (2014) for the Ladysmith earthquake.

*Source function.* We used both semi-triangular and the Gaussian functions.

*Source Magnitude.*  $M_w 4.7$  and  $M_w 7.5$

*Seismic velocities of soil and rock.* The velocity models for bedrock and soil are given in Table 3-1. We used the same velocity models for both small and large simulations. The velocities in Table 3-1 are the velocities that were assigned to each horizontal layer in the velocity model (Figure 3-5).

*$Q_p$  and  $Q_s$ .* In this study, we used an average value of 185 for  $Q_p$  and  $Q_s$  for the whole basin. Also, it was reported that  $Q$  in fine grained soils (clays/silts) was primarily independent of the frequency over some bands (0.1–10 Hz). Further, we used the  $Q_p$  and  $Q_s$  of the regional studies for the rock site where  $Q_s$  was equal to half of  $Q_p$  (out of the basin) (Shibuya et al., 1995; Rix and Meng, 2005; Crow et al., 2011).

*Soil Nonlinearity.* Equation 13 shows  $G/G_{\max}$  which was in this study for nonlinear simulation of Leda clay.

*Frequency range.* The velocity time series for the simulations and the recorded values were filtered with a 12-pole causal Butterworth bandpass filter between 0.1 and 1.0 Hz, which was an acceptable frequency range for the simulation according to the available computational facilities and feasibility of simulation. This filter and tapering of signals were designed using the Signal Processing Toolbox for MATLAB (Simulink).

*Computation recourses.* We used 2 cores for the small simulations, and 200 cores for the large simulations. The computational time for every time step of the simulation was 2.687 s for the small area simulations and 1.427 s for the large area simulations.

### **3.8. Viscoelastic simulation for the Ladysmith earthquake Mw=4.7, R=43 km**

First of all, it should be mentioned that to compare the viscoelastic simulation with the real recordings, we modeled the ground motions of the Kinburn basin for the focal mechanism which was proposed by Ma and Audet (2014) for the Ladysmith earthquake. Table 3-2 presents the details associated with the proposed focal mechanism. Further, a semi-triangular source function was used to model the evolution of the slip over time on the point source fault for all three simulations. The semi-triangular source function is as follows:

$$m(t) = M_0 \left( \frac{t}{t_p} \right) \exp\left(-\frac{t}{t_p}\right) \quad (15)$$

where  $m(t)$  describes the variations of the seismic moment as a function of time,  $M_0$  is the total seismic moment of an earthquake,  $t$  is time, and  $t_p$  is the time associated with the maximum of the seismic moment (or the half duration of an earthquake) (Duputel et al., 2013).

In addition, the half duration of rupture used in the simulations is 0.6 s based on the proposed half duration of the Ladysmith earthquake used in the CMT method. Also, this value was verified using other empirical equations (Dziewonski et al., 1981; Duputel et al., 2012; Ekström et al., 2012; Duputel et al., 2013).

Comparisons of the modeled velocity time series and associated Fourier spectrum from the simulation and the real record at the rock site are shown in Figure 3-8. The PGV of the rock site in the real record was 1.14E-4 m/s for the east-west (E-W) component, while the PGVs of the simulation was 1.42E-4 m/s for the E-W component. The amplitude of the Fourier spectrum

of the velocity time series for the real record at the rock site was  $7.59E-2$  m at a frequency of 0.9 Hz, which occurred along the E-W component, while the amplitudes of the Fourier spectrum of the simulated time series were  $9.83E-2$  m. It should be noted that the rock site receiver (JSBS) is surrounded with 10 m thickness soil thus the ringing effects in the record (Figure 3-8) might be resulted from the surrounding soil, while the 10 m soil thickness cannot be modeled for the simulation due to the mesh size of the simulation (25 m). Further, the rock site of the simulation is located completely over rock velocity model and therefore there is no ringing within the simulated velocity time series. Furthermore, uniform rock velocity model that was used for the simulation might contribute in the discrepancy between record and simulation at rock site.

Figure 3-9 compares the filtered, modeled velocity time series and related Fourier spectrum to the filtered, recorded velocity time series and associated Fourier spectrum at the soil site. The difference between the modeled time series and recordings is large. Although the 3D geometry was carried out in the simulation, the input parameters came from the only borehole available in the basin, and that borehole only had 1D information. Consequently, there was no 3D information for  $V_s$ ,  $V_p$ ,  $Q_s$ ,  $Q_p$ , and density. Thus, the large differences between the real records and the simulation could be attributed to the 3D heterogeneities in the geotechnical and geophysical parameters (including seismic velocities, density,  $Q_p$ ,  $Q_s$ ) of the earth in comparison to the simplified geometry, and a grid size of 25 m that was used in the simulation that could not accurately model all of the details. These parameters cause different resonances of seismic waves in the basin, focusing/defocusing, and basin edge generated surface waves (Hunter et al., 2010). Furthermore, the comparison between velocity Fourier spectrum of records and simulations shows that the discrepancy mainly happened at low frequency thus the increase of seismic moment might improve the result of simulations in comparison to records. Also, our studies

showed that the source function could influence the accuracy of simulations relative to records (it will be described below).

The PGV of the recording at the soil site was 0.0016 m/s for the north-south (N-S) component. However, the PGV of the simulation at the soil site was 8.4E-4 m/s for the E-W component. Comparing the Fourier spectrum of the real record to the simulated velocity time series at the soil site showed that the amplitude of the velocity Fourier spectrum of the record was 2.47 m, while the amplitude of the Fourier spectrum of the simulation was 1.53 m.

Comparing the simulations of the soil site and rock site showed that a significant seismic wave motion continued within the basin at the soil site for a much longer time duration than at the rock site. These effects were also seen in the site recordings of the Ladysmith earthquake at the Kinburn basin (Figure 3-7.a). Thus, the reverberation of seismic waves within the basin was also modeled.

Our study shows that the source function and the half duration are the main reasons for the discrepancy between the records and simulations. Thus, for the closest PGVs relative to the records in the above simulations, we used the focal mechanism of Ma and Audet (2014) to run another simulation using a Gaussian source function. The Gaussian function is defined as follows:

$$M(t) = \frac{M_0}{\sqrt{2\pi\sigma^2}} e^{-\frac{(t-\mu)^2}{2\sigma^2}} \quad (16)$$

where  $M(t)$  is the seismic moment as a function of time,  $M_0$  is the total seismic moment,  $\mu$  is the mean of the distribution, and  $\sigma$  is the standard deviation of the distribution. A half duration of 1.6 s is used for this simulation because it provides the best results relative to the records.

Comparing the simulated velocity time series and filtered record velocity time series (Figure 3-10.a) at the soil site shows that there is consistency between the records and simulation for all

three components even though there are some discrepancies, particularly for later arrivals. The PGV of the simulation is  $1.68E-3$  for the E-W component, and the PGV of the filtered record is  $1.69E-3$  for the N-S component. Also, comparing the Fourier spectrum of the filtered record velocity and the Fourier spectrum of the simulated velocity time series (Figure 3-10.b) at the soil site shows that the amplitude of the Fourier spectrum of the records is 2.48 m, which occurred at 0.73 Hz, and the simulation predicted an amplitude of 3.3 m, which occurred at 0.7 Hz. Further, the amplitude of the Fourier spectrum happened along the E-W component for both the records and simulation. Thus, the simulation properly modeled the natural frequency and amplitude of the Fourier spectrum at the soil site. Comparing the velocity Fourier spectral ratio of the soil site to the rock site for the simulation and records (Figure 3-11) shows that while the velocity Fourier spectral ratios of the simulation are 231, 84, and 4.9 for the E-W, N-S, and vertical components, respectively, the velocity Fourier spectral ratios of the records are 90, 67, and 15 for the E-W, N-S, and vertical components. In addition, the amplitudes the velocity Fourier spectral ratios for both the records and simulation occurred at a frequency of 0.8 Hz along the N-S component; however, there is a large difference between the amplitudes.

Thus, for the below simulations related to point source, we used a Gaussian source function and a half duration of 0.6 s to consider the worst-case scenario for ground motion simulation for a large earthquake ( $M_w=7.5$ ). However, to obtain a more accurate simulation, we used a Gaussian source function and a half duration of 1.6 s to model a large earthquake ( $M_w=7$ ) using realistic finite fault model ( $=900 \text{ km}^2$ ).

### 3.9. Scaling the Ladysmith earthquake to a magnitude of 7.5

The nonlinear effects in soil is triggered by strong levels of shaking (strong incoming wave field) (Gueguen et al., 2018; Rubinstein and Beroza, 2004) and there is no recorded large earthquake in the Ottawa area to investigate the nonlinear soil behavior in the Kinburn basin. Thus, we need to scale the moment magnitude of the Ladysmith earthquake to larger magnitude with a short hypocentral distance. There are many different methods in time and frequency domains for scaling a small earthquake to a large one (for example, IASPEI, 2005; Hanks and Kanamori, 1979). For this study, we investigated the nonlinear soil behavior, and therefore, a standard method of scaling served our purposes (Bormann and Giacomo, 2011; IASPEI, 2005; Bormann et al., 2002). For the sake of simplicity, in this study we scaled the moment magnitude of the Ladysmith earthquake to a larger magnitude of 7.5 using equation 18, which described the relation between the moment magnitude and seismic moment (Bormann and Giacomo, 2011; IASPEI, 2005; Bormann et al., 2002):

$$M_w = (\log M_0 - 9.1)/1.5 \quad (17)$$

Furthermore, the calculated seismic moments using equation 18 were compared to the calculated seismic moments using the recordings of large earthquakes (such as Chi-Chi and earthquakes in Chile) to achieve a realistic value for the seismic moment of earthquakes with a magnitude of 7.5. Consequently, the seismic moment,  $M_0=2.2387E+20$  Nt-m, was used to model an earthquake with  $M_w$  7.5. It should be mentioned that PGAs and the amplitude of acceleration Fourier spectrum of simulations were compared to the recorded PGAs and the amplitude of acceleration Fourier spectrum of large earthquakes respectively to verify the simulation results.

### **3.10. Viscoelastic ground motion simulation for $M_w=7.5$ , $R=5.6$ km**

To determine the importance of the nonlinear soil behavior in the ground motion simulation, we used the scaled Ladysmith earthquake with a magnitude of 7.5 and placed the source 5.6 km away from the soil site in the Kinburn basin, creating a short epicentral distance.

Initially we used the original viscoelastic model built in the AWP-ODC program and studied the stress-strain behavior of the soil material to determine if the program is capable of modelling the soil nonlinearity, taking into account the material viscosity. The  $Q_p$  and  $Q_s$  were fixed values in the AWP-ODC program and were independent of the strain and stress levels, the original viscoelastic model built in the AWP-ODC program should not be able to simulate the soil nonlinearity. Thus, we introduced a new nonlinear soil subroutine (next section) to incorporate the nonlinearity using the shear modulus reduction curve (nonlinear-viscoelastic) instead of using a fixed shear modulus value to observe the nonlinearity of soil.

We used two cores and 90 G of memory for both simulations. The velocity model, time step, and mesh size, all used in both simulations, were the same. It should be added which we could use the same grid size and time step for both viscoelastic simulations and nonlinear-viscoelastic simulations because in the viscoelastic simulation the grid size is equal to  $1/7$  of wavelength and we had less than 50% modulus reduction in our nonlinear-viscoelastic simulations. Therefore, the minimum shear wave velocity of soil site (178 m/s) did not reduce to a value less than 100 m/s. Thus, there are at least four samples per wave length for nonlinear-viscoelastic simulations. The computing time for a viscoelastic simulation of 1 s of one node using one core was  $3.18E-5$  s, while the computing time for the nonlinear-viscoelastic simulation was  $4.72E-5$  s.

The stress-strain curve and modulus reduction curve (Figure 3-12) of the soil site at the second node from the surface (at a depth of 25 m) showed that the viscoelastic simulation did not model the nonlinear soil effects.

Three components of acceleration time series and their spectrums are presented for a receiver on the deepest part of the basin (soil site) in Figure 3-13. The predicted unreasonable PGA for the soil site is about 6 g. This level of PGA has not been recorded for any large earthquake in the world; further, no kind of soil can tolerate the force that results from 6 g acceleration. Thus, it is necessary to consider the nonlinear soil behavior to attenuate partially the increased amplitude within the basin.

We used the ratio of the pseudo-spectral acceleration (PSA) of the soil site to the PSA of the rock site at 5% damping (Figure 3-14) to calculate the amplification level in the soil site relative to the rock site. Using the PSA ratio of the soil site to the rock site (Figure 3-14) showed that the viscoelastic simulation predicted that the maximum PSA ratio was equal to 11.2 at a frequency of 0.62 Hz.

### **3.11. Nonlinear-viscoelastic ground motion simulation for $M_w=7.5$ , $R=5.6$ km**

Using the proposed nonlinear-viscoelastic simulation method, the nonlinear-viscoelastic ground motion was modeled in the Kinburn basin for the Ladysmith earthquake,  $M_w=7.5$ ,  $R=5.6$  km.

Figure 3-15 shows the modulus reduction curve and the stress-strain diagram for a receiver on the soil site related to both the viscoelastic (Original) and nonlinear-viscoelastic (Modified) simulations. These plots show that maximum nonlinearity occurs in the vertical components for

this simulation. In addition, Figure 3-16 shows that due to the nonlinear behavior in the soil, permanent strain happened in the X-Z and Y-Z components (Figure 3-16. b and c).

Furthermore, acceleration time series and associated Fourier spectrums (Figure 3-17) of the soil site validated the above results. The synthetic acceleration and velocity Fourier spectrum associated with the horizontal components showed that the dominant frequency at the deepest part of the basin was 0.77 Hz. Previous studies on the Kinburn basin showed 0.8 Hz as the fundamental frequency of the Kinburn basin (Hayek, 2016). The reduction of the fundamental frequency in the basin resulted from the modulus reduction that happened because of the nonlinear soil behavior.

A comparison of the modeled time series of the viscoelastic and nonlinear-viscoelastic (Figure 3-17) simulations for the soil site showed that considering the effects of nonlinearity in the soil site could shift the resonant frequencies of basin toward lower frequency and significantly reduce the ground motion amplification that happened in the basin for all three components (Further details are described below for Figure 3-18). The regular viscoelastic simulation predicted unreasonable PGAs of 5 g and 6 g for the E-W and N-S components, respectively; these PGA values were not reasonable according to the PGAs in real records of large earthquakes in the world (Yamada et al., 2010; Ma et al., 1999). Furthermore, soils cannot resist if they are subjected to high levels of stress; thus, most of the energy of the waves is dampened, and a PGA of 5 g or 6 g cannot be generated at soil sites. In contrast, the proposed nonlinear-viscoelastic formulation reduced the predicted reasonable PGAs to 3 g and 2 g at the soil site for the E-W and N-S components, respectively, according to the recorded large earthquakes (e.g. Yamada et al., 2010). The half duration of rupture that was used in the simulations was a short half duration (0.6 s) for a Mw 7.5 earthquake, and it was used based on

the half duration of the recorded small earthquake as there was not any recorded large earthquake for the Ottawa area. In addition, we could generate high stress in the basin to study the nonlinear soil effects using this small half duration. Therefore, the short half duration and using a point source for a large earthquake caused the high predicted PGA values in both the viscoelastic and nonlinear-viscoelastic simulations. Thus, using a finite fault source model is necessary (it is shown below). Further, the predicted PGAs using the nonlinear-viscoelastic simulation is large enough to generate plastic deformation in the soil site. Thus, incorporating plastic deformation in future ground motion simulations that use a point source for modeling large earthquakes is recommended.

Although the distance between the soil site and rock site was only about 2 km, the horizontal components of the modeled ground motion were amplified, and the level of this amplification was dependent on the nonlinear soil behavior along each component and the properties of the basin. If the strain level increased in one component, the shear modulus was reduced, and thus, the ground motion was dampened in that component as well.

The PSA ratio of soil site to rock site for the nonlinear-viscoelastic simulation (Figure 3-18) showed a maximum PSA ratio of 5.57 with a frequency of 0.56 Hz. A comparison of the PSA values of the viscoelastic simulation and the nonlinear-viscoelastic simulation (Figure 3-18) showed that the nonlinear soil effects reduced the amplification of seismic waves almost by half. Furthermore, as expected, because of the nonlinear soil behavior, the frequency of the maximum PSA ratio using the nonlinear-viscoelastic simulation was slightly smaller than the frequency of the maximum PSA ratio using the viscoelastic simulation.

Comparing the nonlinear-viscoelastic simulated velocity time series at the rock site and soil site (Figure 3-19.a) showed that the amplitude of the horizontal components increased at the soil

site relative to the rock site. However, for the vertical component, the amplitude decreased at the soil site relative to the rock site (discussed later in this section). In addition, the durations of all three components of the modeled seismic waves were longer at the soil site compared to the rock site.

Figure 3-19.b compares the simulated velocity time series of the soil site for the viscoelastic and nonlinear-viscoelastic simulations. This Figure proves that the nonlinear soil effects not only reduce the amplitude of seismic waves, but they also influence the phases of seismic waves. Modulus reduction caused by nonlinear soil behavior results in seismic waves that propagate with a lower velocity in the nonlinear-viscoelastic simulation compared to those in the viscoelastic simulation. Thus, the propagation of seismic waves with differing velocities causes phase differences in the simulated velocity time series at the soil site for the viscoelastic and nonlinear-viscoelastic simulations.

To understand the phenomenon that caused the amplification in the horizontal components and de-amplification in the vertical component in the basin, we need to consider the particle motion of the modeled time series for the nonlinear-viscoelastic simulation. Figure 3-20 shows the particle motion of the rock site. As expected, the particle motion in the whole time series is random in the rock site. The only dominant particle motion that we should consider is in the vertical-radial plot that is caused by P and S waves.

In contrast to the particle motion in the rock site, the particle motion in the soil site (Figure 3-21.a) for the whole modeled time series shows the presence of two dominant particle motions. The shapes of both dominant particle motions are typical particle motions of surface waves.

To recognize the reason for these dominant particle motions, we show the particle motion that occurred in the first 20 seconds of the synthetic time series for the soil site in Figure 3-21.b.

The EW-NS and radial-tangential plots in Figure 3-21.b show that the P and S arrivals, followed by the basin edge surface waves, are in the direction of the initially dominant arrivals along the northwest-southeast direction, which is the direction of the source relative to the receiver. Thus, another dominant particle motion, shown in Figure 3-21.a, has a smaller amplitude and is caused by the basin edge surface waves. As this dominant particle motion is mostly along the radial component in the radial-tangential plot (Figure 3-21.a), we can infer that the basin edge generated waves are mostly Rayleigh waves.

Further, in all plots associated with particle motions, there is no dominant particle motion along the vertical axis. Thus, it seems logical that the PGA of the vertical component at the soil site is smaller than the PGA of the horizontal components because most of the generated waves within the basin are along the horizontal components. Consequently, a larger amplification happened along the horizontal axis relative to the vertical axis.

### **3.12. Viscoelastic and nonlinear-viscoelastic simulations for $M_w=7.5$ , $R=43$ km**

The main contribution seismic zone to Ottawa area is located a few 10 km away from Ottawa. Thus, to consider a more realistic scenario of a large earthquake with a magnitude of 7.5 for the Kinburn basin, we scaled the Ladysmith earthquake to  $M_w = 7.5$  with the same epicentral distance, and then we simulated the earthquake for the Kinburn basin. The velocity model that was used in this simulation was the same as the ones used in previous simulations (Table 3-1); the results are shown for the soil site in Figure 3-4.

First, the ground motion from the scaled Ladysmith earthquake ( $M_w=7.5$ ) was modeled for the Kinburn basin using the regular viscoelastic formulation. The simulated time series and associated Fourier spectrums at the soil site (Figure 3-22) shows that the viscoelastic simulation

predicted a PGA of 0.86 g and PGV of 1.5 m/s for the soil site. Thus, the PGA at the soil site was amplified by a factor of 11.9 relative to the PGA at the rock site.

The ratio of the velocity Fourier spectrum of the soil site to the velocity Fourier spectrum of the rock site (Figure 3-23) was used to consider the soil effects on the frequency content in the viscoelastic simulation. Figure 3-23 shows that the N-S component has a maximum velocity Fourier spectral ratio of 81, which is associated with a frequency of 0.97 Hz. In addition, both horizontal components peak at a frequency that is slightly larger than 0.8 Hz, which is the natural frequency of the basin at the soil site. Furthermore, only the N-S velocity Fourier spectral ratio shows values of more than 10 in the frequency range of 0.1-0.7 Hz.

Using the PSA ratio of the soil site to the rock site (Figure 3-24) to calculate the amplification level in the soil site relative to the rock site shows that the viscoelastic simulation predicted a maximum PSA ratio equal to 19.4.

To demonstrate the impact of the introduced nonlinear soil behavior subroutine on the ground motion simulation, we modeled the ground motion of the Kinburn basin for the Ladysmith earthquake ( $M_w=7.5$ ,  $R=43$  km) using the same velocity model and earthquake parameters that were used for the viscoelastic simulation. As with other nonlinear-viscoelastic simulations, the nonlinear behavior was only modeled for the soil site.

Figure 3-25 shows the modulus reduction at the soil site, and therefore, the strain-stress curves represent nonlinear variations for the nonlinear-viscoelastic simulation at the soil site. Based on the calculated modulus reduction curves and stress-strain plots, the maximum nonlinear soil behavior happened in the X-Z component. The simulated time series and associated Fourier spectrum for the soil site (Figure 3-26) showed that the PGA and PGV at the soil site were equal to 0.62 g and 1.18 m/s, respectively.

The velocity Fourier spectral ratio of the soil site to the rock site for the nonlinear-viscoelastic simulation (Figure 3-27) showed that the maximum ratio was 41, which occurred at 0.79 Hz in the N-S component. Comparing the velocity Fourier spectral ratio of the viscoelastic simulation with the velocity Fourier spectral ratio of the nonlinear-viscoelastic simulation showed that the high frequency content of the modeled seismic waves was reduced in the nonlinear-viscoelastic simulation. Furthermore, the maximum velocity Fourier spectral ratio was reduced from 81 for the viscoelastic simulation to 41 for the nonlinear-viscoelastic simulation; the associated frequency of the amplitudes of the ratio decreased from 0.97 Hz for the viscoelastic modeling to 0.79 for the nonlinear-viscoelastic simulation. In addition, none of the 3 components showed a ratio greater than 10 within the frequency range of 0.1-06 Hz for the nonlinear-viscoelastic simulation. Thus, according to the velocity Fourier spectral ratio, as a measure of the amplification of seismic waves in the soil site relative to the rock site for both the viscoelastic and nonlinear-viscoelastic simulations, nonlinear soil effects reduced the amplification and the high frequency content of the seismic waves in the nonlinear-viscoelastic simulation.

The PSA ratio (Figure 3-28) showed that the predicted maximum PSA ratio of the soil site to the rock site in the nonlinear-viscoelastic simulation was equal to 14.5, which corresponded to the N-S component.

Finally, we considered the effects of the epicenter location relative to the basin on the predicted amplification for the viscoelastic and nonlinear-viscoelastic simulations. We compared the PSA ratios of the 3 components for the viscoelastic simulation (Original) to the PSA ratios for the nonlinear-viscoelastic simulation (Modified) for a moment magnitude of 7.5 and used epicentral distances of 5.6 km (Figure 3-29.a) and 43 km (Figure 3-29.b). Figure 3-29.a shows

that for the viscoelastic simulation of an earthquake with an epicentral distance of 5.6 km, the maximum amplification level of the horizontal components is about 11.2 for a frequency of 0.61 Hz and, for the vertical component, 1.4 for a frequency of 0.76 Hz. In contrast, the nonlinear-viscoelastic simulation predicts a maximum amplification of 6.1 for a frequency of 0.53 Hz. The ratio of the PSA ratios of the viscoelastic simulation to the nonlinear-viscoelastic simulation shows that the nonlinear effects reduce the predicted maximum amplification by a factor of about 4.3 for the N-S component and by a factor of 3 for the other components.

For the same earthquake with an epicentral distance of 43 km (Figure 3-29.b), the viscoelastic simulation shows a maximum amplification level of about 10.3, 19.4, and 17.3 for the E-W, N-S, and vertical components, respectively. The nonlinear-viscoelastic simulation predicts a maximum amplification of 9, 15.8, and 14 for the E-W, N-S, and vertical components, respectively. The amplification of the N-S and vertical components in Figure 3-29.b is larger compared to the amplification of the components in Figure 3-29.a; this result can be attributed to the location of the epicenter relative to the basin. First, with a short epicentral distance (5.6 km), the vertical component is not generated at the bottom of basin because of the short distance between the epicenter and basin; thus, the amplification of the components is smaller than that when the epicentral distance is greater. However, the characteristics of the source can influence the amplification of vertical component and thus we studied the finite fault effects as well. Second, the epicenter is placed on the west side of the basin for the simulation with an epicentral distance of 5.6 km, and most of the energy from the earthquake is along the E-W component. Therefore, this component shows the maximum amplification. In contrast, in the simulation with an epicentral distance of 43 km, the vertical component is properly generated, and thus, it is highly amplified. Also, the N-S component experiences high amplification because of the

location of the epicenter, which is in the northwest section of the basin. A comparison of the viscoelastic and the nonlinear-viscoelastic simulations for the model with an epicentral distance of 43 km (Figure 3-29.b) shows that the amplification can be reduced by a factor of up to 1.5 for the vertical component and about 2.8 for the horizontal components when nonlinear effects are considered.

### **3.13. Finite fault model for $M_w=7$**

Comparing the generated stress at the soil site in the viscoelastic and nonlinear-viscoelastic simulations of the earthquake with an epicentral distance=5.6 km (Figure 3-15) shows that the nonlinear-viscoelastic simulation reduced the generated stress to one third of the predicted stress at the soil site using the viscoelastic simulation. However, large earthquakes ( $M_w 7.0+$ ) occur on a large fault and cannot be treated as a point source, particularly for near field ground motion simulations which near source effects are important. Thus, the fault plane is discretized into small independently rupturing sub-faults to model a large earthquake using a finite fault model (Motazedian and Atkinson, 2005; Beresnev and Atkinson, 2002). We used a fault plane for the simulations; this fault plane was  $900 \text{ km}^2$  and the sub-fault size is  $5 \text{ km}^2$ . The strike, dip, and rake associated with the focal mechanism proposed by Ma and Audit (2014) for the Ladysmith earthquake (Table 3-2) were used for the simulations, while the magnitude was scaled to  $M_w=7$  (the necessary computational resources for  $M_w 7.5$ , as was used in the previous sections, was not available at this point). The fault was dipping and the closest distances to rock and soil stations are 33.8 km and 36.7 km, respectively. The hypocenter of the earthquake (center of the fault plane) was located at a depth of 14.5 km as proposed by the focal mechanism of Ma and Audit (2014) for the Ladysmith earthquake (Table 3-2). Since we were interested in the effects on the

soil, we used a simplified finite fault model that assumed all sub faults behave similarly and simultaneously rupture to simplify the finite fault model and consequently reduce the necessary computational memory; also, we assumed that the center of the fault plane was the hypocenter of the earthquake (Crouse, 1991). Figure 3-30.a and b show the 3D view and the top view, respectively, of the sub-faults of finite fault plane that was used for the simulations described below.

Figure 3-31 shows that using a finite fault model for viscoelastic and nonlinear-viscoelastic simulations reduced the generated stress and strain to reasonable values at the soil site. Since we were interested in soil nonlinear behavior, to have a noticeable modulus reduction at the soil site, we used  $10^{-6}$  as the yielding strain level for simulations using a finite fault model. This yielding strain level was chosen based on unpublished research on the behavior of Leda clay. Comparing the modulus reduction curve and stress-strain relationship (Figure 3-31) shows that nonlinear soil effects occur in all 3 components, and thus, a modulus reduction happened in all 3 components as well. The maximum modulus reduction happened in X-Z component that reduced the shear modulus to 42% of the  $G_{max}$ . This modulus reduction could reduce the shear wave velocity by factor of about 63%. Thus, the minimum shear wave velocity in the soil velocity model was decreased from 178 m/s to 112 m/s and therefore the mesh size of our simulation (25 m) is good enough to model the frequency of 1 Hz.

As shown in Figure 3-32, although both simulations have the same modeled velocity and acceleration for the first arrivals (in the first 20 s of the simulations), the nonlinear soil effects reduce the amplitude of the simulated velocity time series and acceleration time series by factors of about 3.4 and 4.1, respectively, in the nonlinear-viscoelastic simulation compared to the viscoelastic simulation for the later arrivals. It should be noted that using nonlinear-viscoelastic

simulation increased the amplitude of velocity time series and acceleration time series of vertical component by factor of 49% and 14%, respectively, in comparison to the amplitude of velocity time series and acceleration time series of vertical component of viscoelastic simulation.

Furthermore, the amplitudes of the velocity and acceleration Fourier spectrums of the nonlinear-viscoelastic simulation were reduced by factor of about 4.5 and 4.9, respectively, compared to the amplitudes of the velocity and acceleration Fourier spectrums of the viscoelastic simulation (Figure 3-32). In addition, the frequency content of the nonlinear-viscoelastic simulation was lowered relative to the frequency content of the viscoelastic simulation.

As shown in Figure 3-33, the amplitude of the velocity Fourier spectral ratio of the soil site to rock site was reduced from 397 in the viscoelastic simulation to 39 for the nonlinear-viscoelastic simulation. Also, the frequency of the amplitude of the velocity Fourier spectral ratio was slightly shifted from 0.95 for the viscoelastic simulation to 0.69 Hz for the nonlinear-viscoelastic simulation.

The maximum PSA ratio of soil site to rock site happened along the N-S component in both simulations (the nonlinear-viscoelastic simulation is shown in Figure 3-34.a, and the viscoelastic simulation is shown in Figure 3-34.b); the amplitude of PSA in the nonlinear-viscoelastic simulation was equal to 12 and, in the viscoelastic simulation, was equal to 51. Thus, the nonlinear soil effects attenuated the seismic wave's energy such that the amplitude of PSA was reduced significantly. Further, the amplitude of PSA ratio for E-W component reduced from 18 in viscoelastic simulation to 5.8 in nonlinear-viscoelastic simulation while the amplitude of PSA ratio for vertical component of viscoelastic simulation is slightly less than the amplitude of PSA ratio for vertical component of nonlinear-viscoelastic simulation.

### 3.14. Discussion and Conclusion

Using our newly introduced nonlinear-viscoelastic subroutine, our simulations of the ground motions of the Kinburn basin for a point source model show that when the strain level exceeds a defined yielding level ( $10^{-4}$ ) during a large earthquake, the amplification effects that occur in the basin are reduced compared to those effects obtained using the original program. In our nonlinear-viscoelastic simulation, the PGA and PGV of the horizontal components of the soil site were lower relative to the PGA of the horizontal components of the soil site in the linear viscoelastic modeling. Thus, ignoring nonlinear soil behavior in ground motion simulations can significantly increase the motion parameter values and using the modulus reduction equation or curve is necessary to have a more realistic simulation.

In our simulations using point source earthquakes, a smaller reduction in the PGA occurred in the vertical component of the nonlinear-viscoelastic simulation compared to the PGA in the vertical component of the viscoelastic simulation. According to the particle motion plots, most of the generated surface waves were along the radial axis; thus, a large amplification did not occur in the basin along the vertical axis (as per the conclusion of Konno and Omachi, 1998). Therefore, nonlinearity was not generated along the vertical axis to attenuate a significant amount of energy in the vertical component of the waves. However, the nonlinear soil behavior decreased the PGA of the vertical component of the seismic waves in the nonlinear-viscoelastic simulation more compared to the reduction of the PGA in the viscoelastic simulation at the soil site.

Comparing the frequency content of the soil site to the rock site shows that the nonlinear ground motion simulation of a point source large earthquake ( $M_w=7.5$ ) can significantly reduce the velocity Fourier spectral ratio of the soil site to the rock site (from 81 in the viscoelastic

simulation to 41 in the nonlinear-viscoelastic simulation). In addition, the resonant frequency amplitudes of the velocity Fourier spectral ratio decrease because of the nonlinear soil effects. Since the amplitude of the velocity Fourier spectral ratio of a record associated with  $M_w=4.7$  is 90, a high velocity Fourier spectrum ratio for the simulation of an earthquake with  $M_w=7.5$  is expected.

We used the PSA ratio of the soil site to the rock site to consider the amplification level at the soil site relative to the rock site. Our viscoelastic simulation of the Kinburn basin for a point source large earthquake ( $M_w=7.5$ ) (epicentral distance=43 km) showed that the PSA ratio was 19.4, but the nonlinear-viscoelastic simulation of the same earthquake predicted a PSA ratio of 15.8. Thus, using the nonlinear-viscoelastic simulation reduced the predicted PSA ratio of the viscoelastic simulation by a factor of about 1.5 and 2.8 for the horizontal and vertical components, respectively. The reduction of the PSA ratio in the nonlinear-viscoelastic simulation was due to the damping of the energy of seismic waves by the nonlinear soil effect.

In addition, the predicted PGA using the nonlinear-viscoelastic simulation (0.62 g) was 27 % smaller than the calculated PGA using the viscoelastic simulation (0.86g). Consequently, to predict a reliable PGA level for seismic hazard assessments, we must consider the nonlinear soil behavior in ground motion simulations for large earthquakes. Furthermore, considering nonlinear effects can reduce the predicted amplification within the basin by a factor of 5 and 3 for simulations with short (5.6 km) and long (43 km) epicentral distances, respectively.

Finally, the nonlinear-viscoelastic simulation using a point source earthquake properly modeled the reverberation of the seismic waves within the basin. The generated basin edge surface waves were the main cause of the amplification of seismic waves within the basin. Also, using the nonlinear-viscoelastic simulation, the dominant frequencies within the basin agreed

with the records of the Kinburn basin for smaller earthquakes, while the viscoelastic simulation did not accurately model the dominant frequency of seismic waves for the deep soil site.

Using a finite fault model, compare to a point source model, modifies the generated stress in the basin to a reasonable level for both the viscoelastic and nonlinear-viscoelastic simulations for a real scenario (epicentral distance=43 km) earthquake.

Considering the simulated velocity and acceleration time series related to the finite fault model with an epicentral distance of 43 km showed that the amplitude of the later arrivals in the nonlinear-viscoelastic simulation was about one forth that in the viscoelastic simulation. The amplitudes of the Fourier spectrums of the simulated velocity and acceleration time series in the nonlinear-viscoelastic simulation were about 4.5 times smaller than those in the viscoelastic simulation. Further, the frequency content of waves shifted toward low frequency for nonlinear-viscoelastic simulation compared to viscoelastic simulation. Also, the amplitude of the velocity Fourier spectral ratio (soil to rock) for the nonlinear-viscoelastic simulation was 10 times smaller than the those of viscoelastic simulation. Furthermore, the associated frequency of the amplitude of the velocity Fourier spectrum was lower in the nonlinear-viscoelastic simulation compared to the viscoelastic simulation. Finally, the PSA associated with the viscoelastic simulation was 4 times larger than the PSA ratio predicted by the nonlinear-viscoelastic simulation. Therefore, using a finite fault model in the nonlinear-viscoelastic simulation ( $M_w=7.5$ , epicentral distance=43 km), the energy of the seismic waves was properly attenuated within the basin because of the nonlinear soil effects.

In conclusion, considering nonlinear soil behavior in ground motion simulations has the following effects:

- Reduces the predicted PSA, PGA, and PGV values of the material with low strength that are subjected to high intensity incident wave-field ;
- Lowers the frequency content of waves;
- Reduces the resonant frequency amplitudes of the velocity Fourier spectral ratio;
- Damps the energy of waves and, consequently, decreases the predicted amplification;
- Using a finite fault source for nonlinear-viscoelastic simulation caused de-amplification in horizontal components (due to the increase of damping in the basin) compared to viscoelastic simulation.

## **Data and Resources**

The Global Centroid Moment Tensor Project database: [www.globalcmt.org/CMTsearch.html](http://www.globalcmt.org/CMTsearch.html) (last accessed August 2017).

The Earthquakes Canada, Natural Resources Canada (NRCAN) database: [www.earthquakescanada.nrcan.gc.ca](http://www.earthquakescanada.nrcan.gc.ca) (last accessed October 2017).

The Geological Survey of Canada provided the seismograms and information on the Kinburn basin depth; this information cannot be released to the public.

## **Acknowledgements**

This research was supported by the Natural Sciences and Engineering Research Council of Canada under the Discovery Grant program and Collaborative Research and Development grants. This research used computational resources provided by the High Performance Computing Virtual Laboratory (HPCVL) and Calcul Québec, both under Compute Canada. We gratefully acknowledge the constructive comments, suggestions, and text revisions from reviewers and Associate Editor, Dr. Arben Pitarka. We used the AWP-ODC [Anelastic Wave

Propagation, developed by Olsen-Day-Cui) program package, and we would like to show our gratitude to Professor Kim Olsen for providing us with the package. We appreciate Dr. Daniel Roten's guidance in using the AWP-ODC program. Special gratitude is given to the Geological Survey of Canada for providing us with helpful comments, suggestions, and the necessary materials, including seismograms and geological information, for this research.

## Tables and Figures

Table 3-1. Properties of the seismic velocity model (Burger et al., 1987; Eaton et al., 2006; Hunter et al., 2010; Crow et al., 2011; Bent et al., 2015)

Type of material	Soil	Soil	Soil	Soil	Rock
Depth (m)	0-25	25-50	50-75	75-100	> 100
Vs (m/s)	178	219	278	320	2783
Vp (m/s)	1380	1380	1380	1380	6200
Density (kg/m <sup>3</sup> )	1600	1600	1600	1600	2650
Qp	185	185	185	185	1000
Qs	185	185	185	185	500

Table 3-2. The focal mechanism proposed for the Ladysmith earthquake (Ma and Audet; 2014)

<b>Ma and Audet (2014)</b>			
Epicenter = 45.74, -76.34			
Depth = 14.5 Km			
$M_w = 4.7$			
$M_0 = 1.32e+16$ Nt-m			
	<b>Strike</b>	<b>Dip</b>	<b>Slip</b>
Plane 1	306	41	94
Plane 2	122	50	87

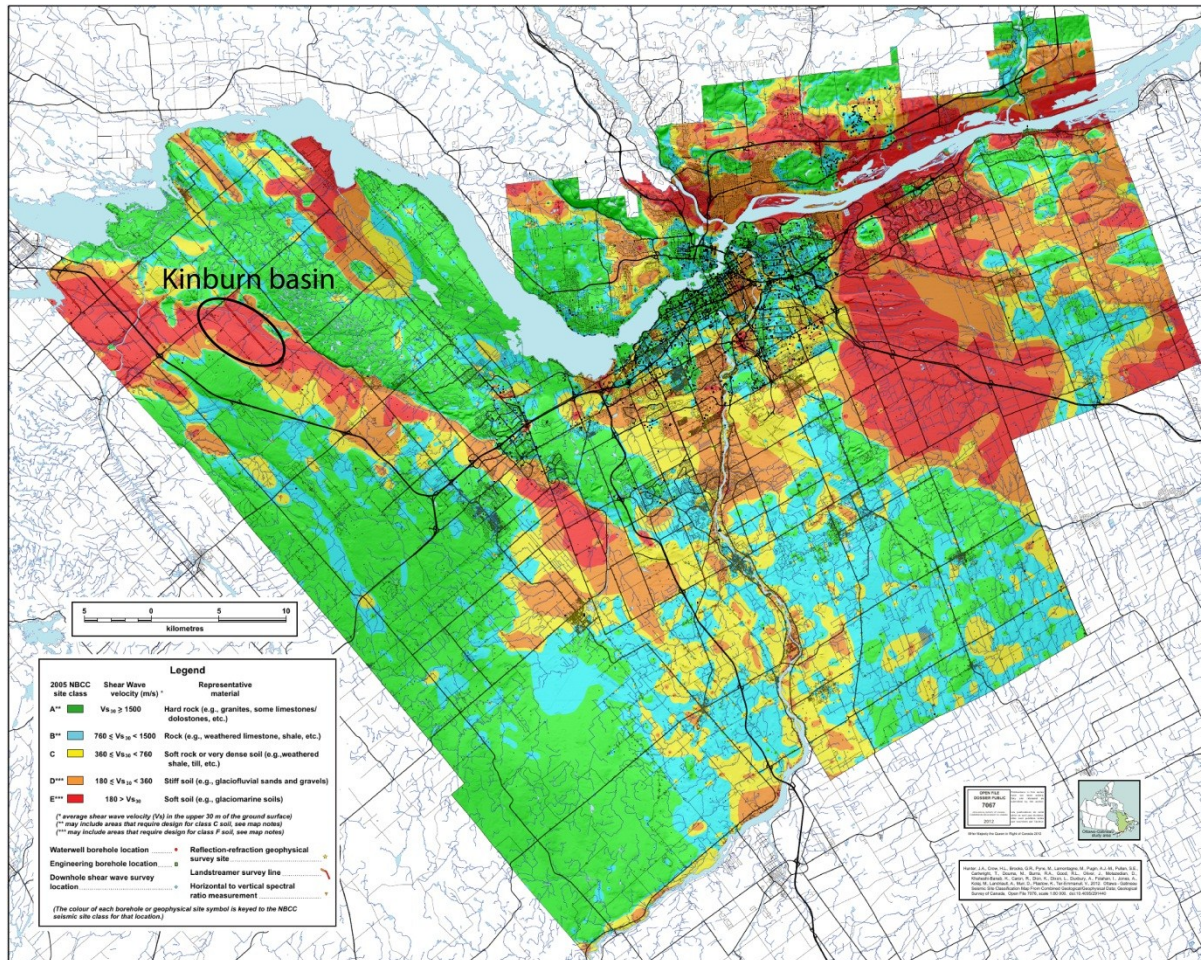


Figure 3-1. Vs30 map of the Ottawa region (Motazedian et al., 2011; Hunter et al., 2012). The location of the Kinburn basin is indicated by the black circle

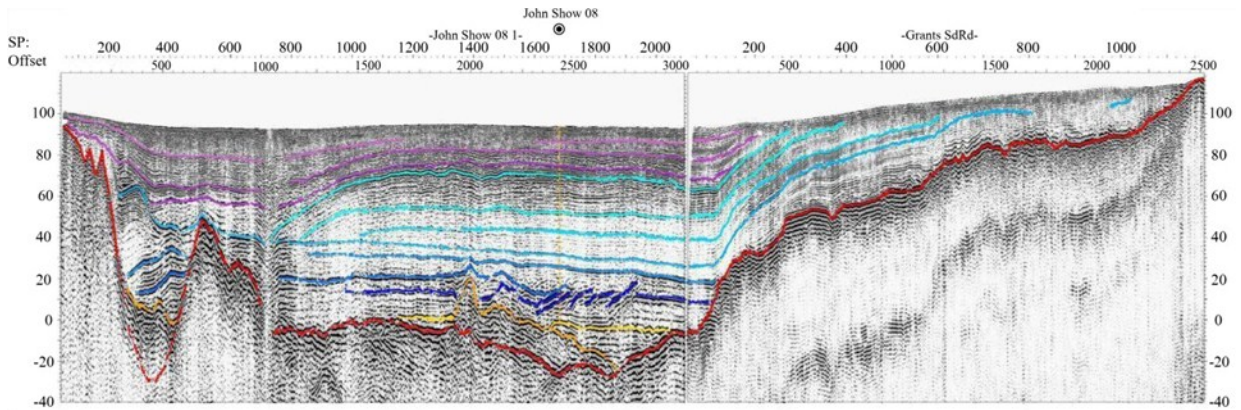


Figure 3-2. Top: Air photo A31837-105 taken 22/05/2002 1:15,000 of the Kinburn area, Ottawa valley, showing the location of the borehole (the red star) and the location of the seismic section (the red dashed line). Bottom: seismic section, as prepared and interpreted by Pugin et al. (2013) showing the location of the borehole and the interpreted lithologies and structures (Medioli et al., 2012)

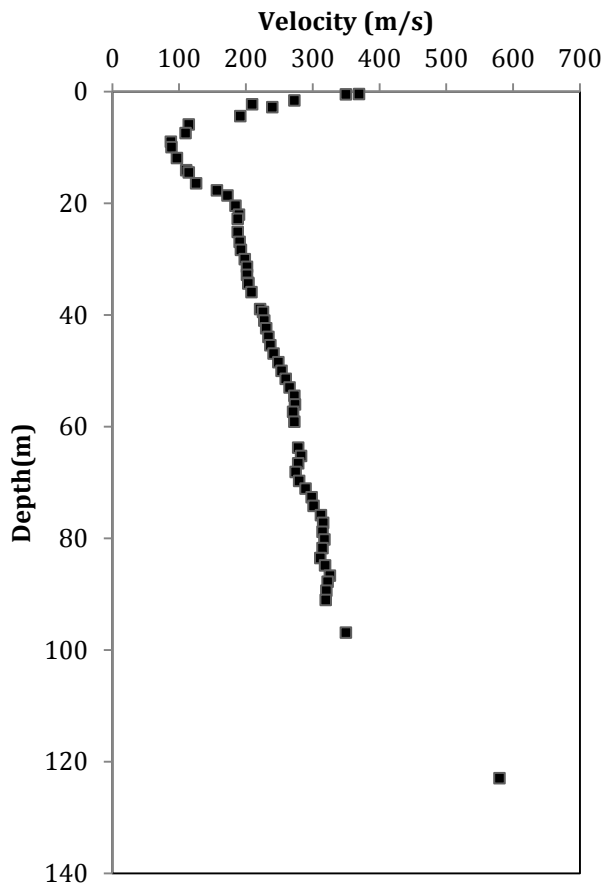


Figure 3-3. Velocity profile of the Kinburn basin

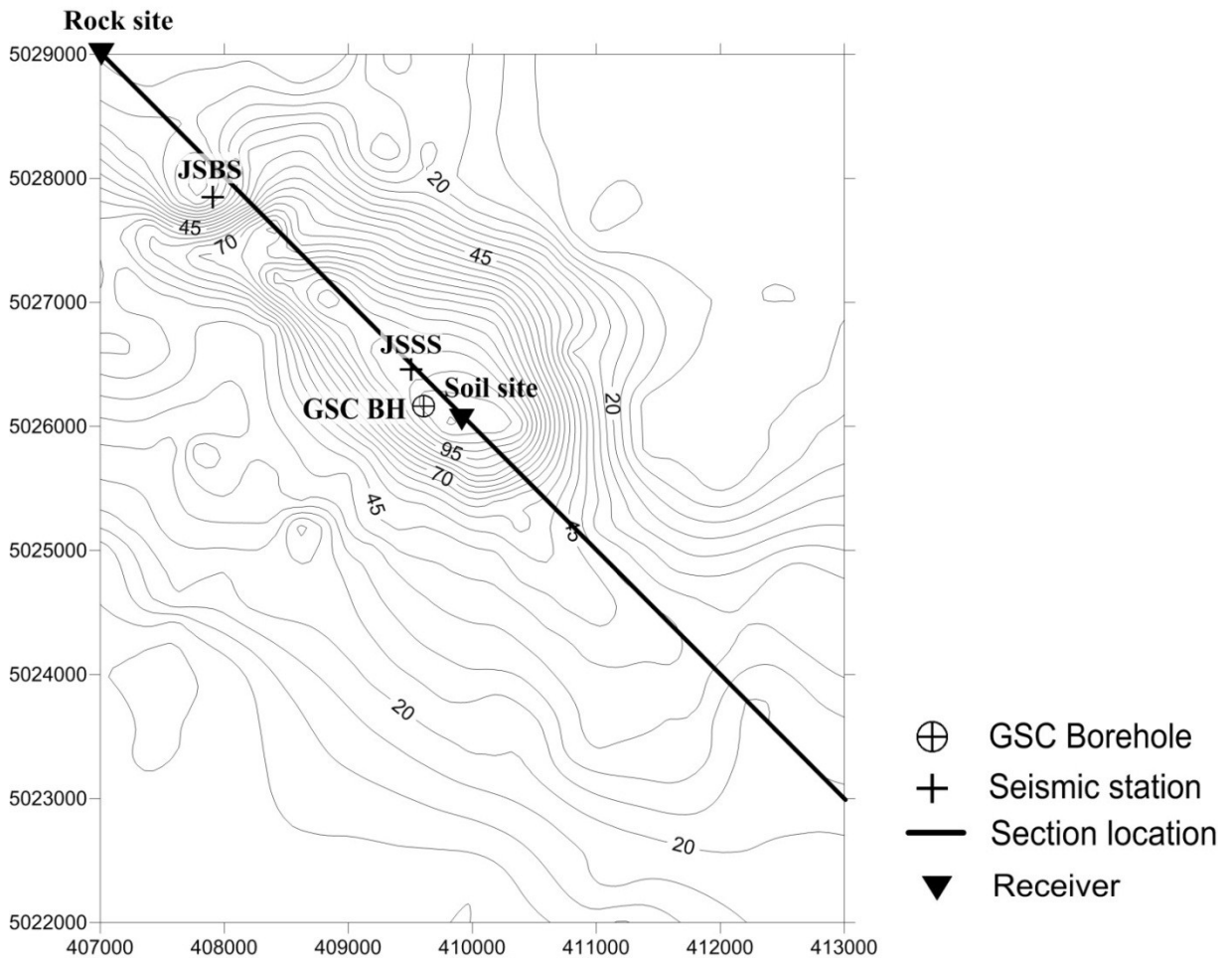


Figure 3-4. Contour map of the Kinburn basin depth showing the location of the GSC borehole, seismic stations (JSBS and JSS), receivers, and section location

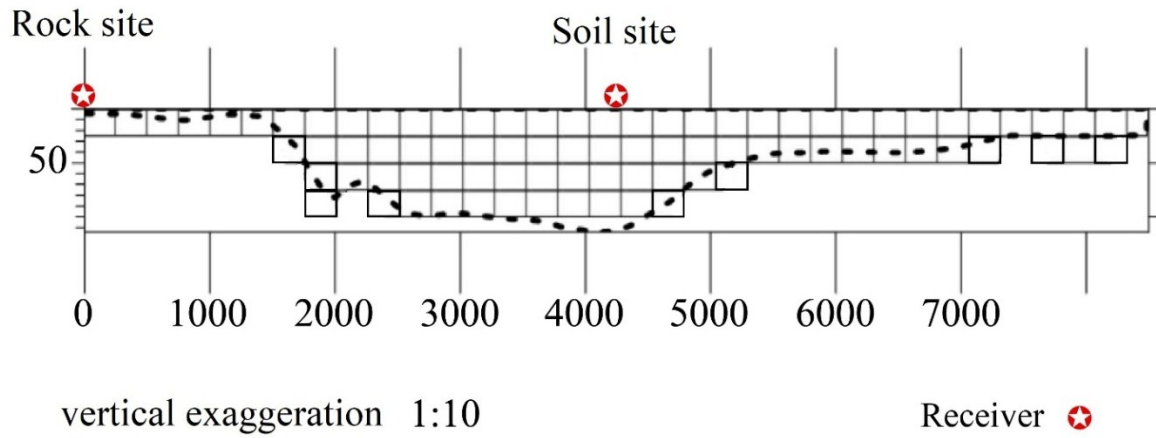


Figure 3-5. Cross-section along the northwest-southeast side of the basin and the location of the receivers (the values are in m)

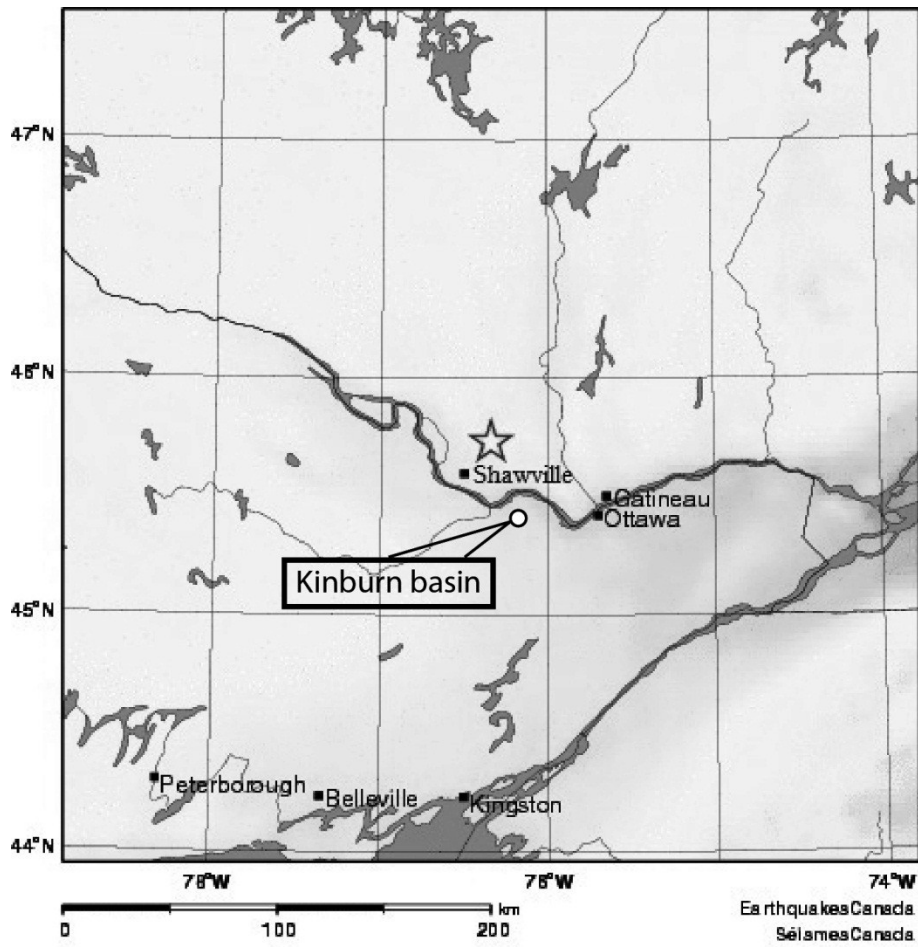


Figure 3-6. The Ladysmith earthquake (NRCAN webpage)

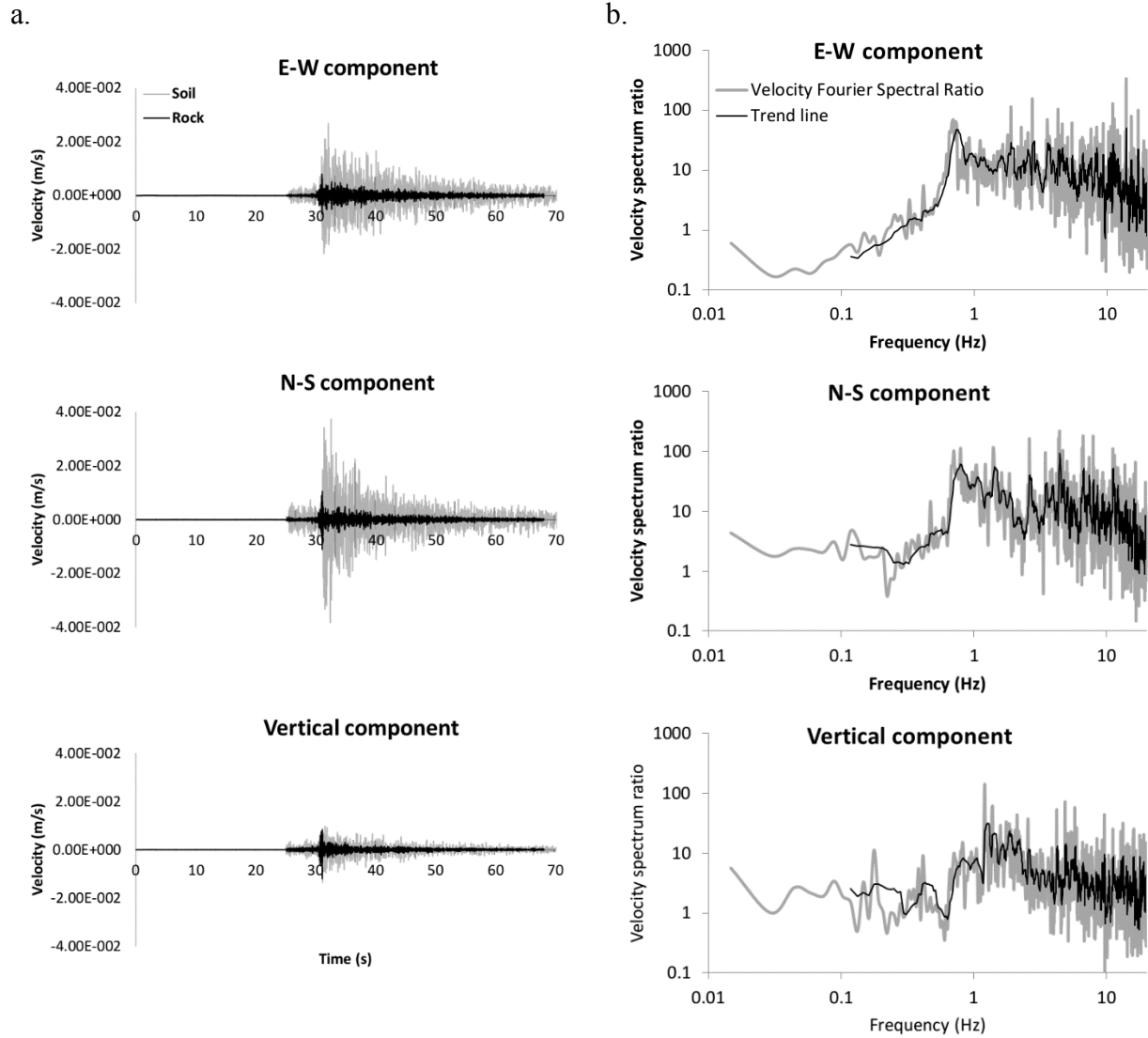


Figure 3-7. a) Recorded velocity time series associated with the Ladysmith earthquake at the rock site (JSBS) and soil site (JSSS) in the Kinburn basin. b) The unfiltered velocity Fourier spectral ratio of records of the soil site (JSSS) to the rock site (JSBS) in the Kinburn basin.

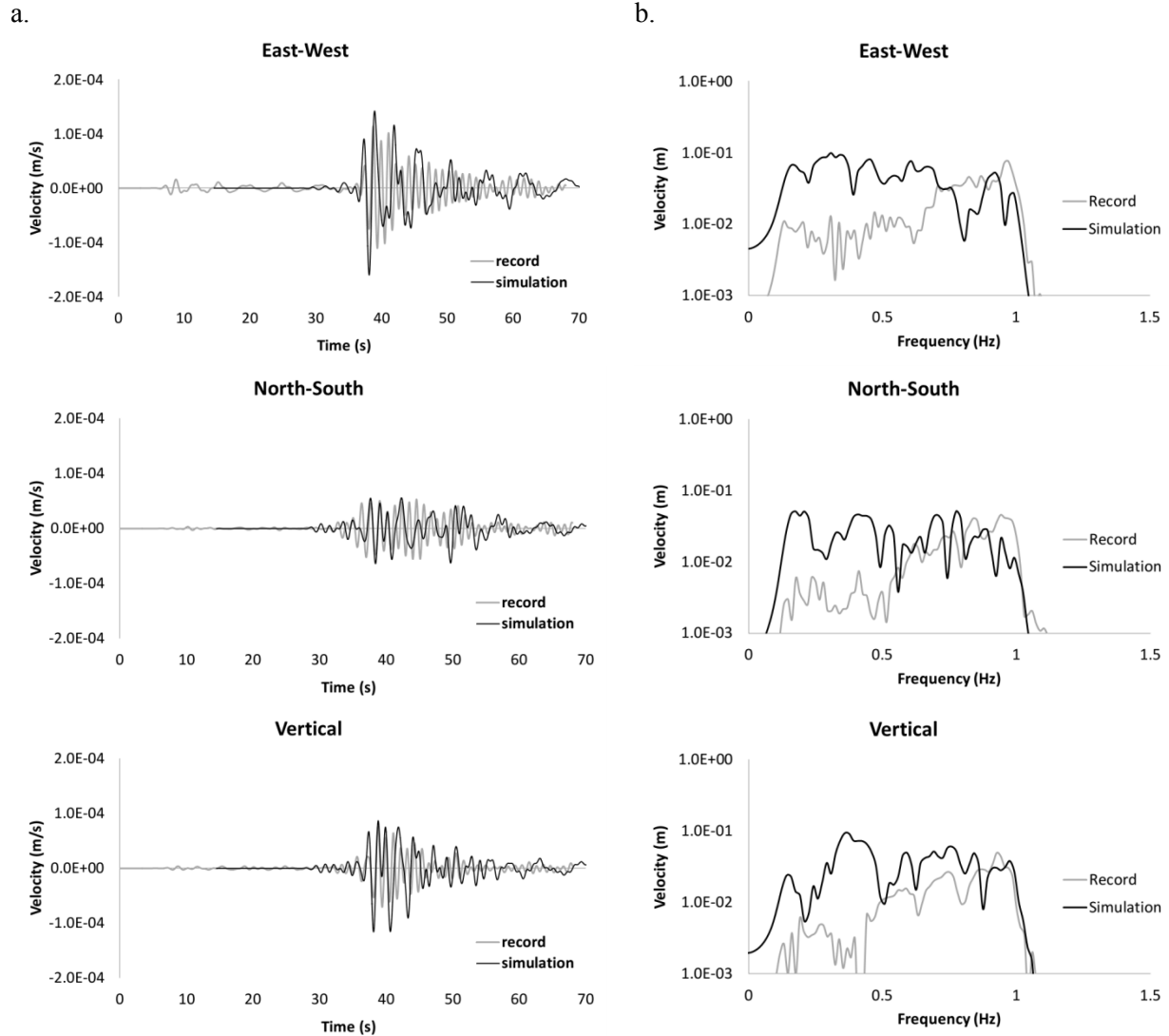


Figure 3-8. Comparison of a) simulated velocity time series versus recorded velocity time series and b) the velocity Fourier spectrum of the simulation versus the velocity Fourier spectrum of the record at the rock site for the proposed focal mechanism of Ma and Audet (2014); epicentral distance  $R=43$  km, depth=14.5 km,  $M_w=4.7$ ,  $M_0=1.32 \times 10^{16}$  Nt-m.

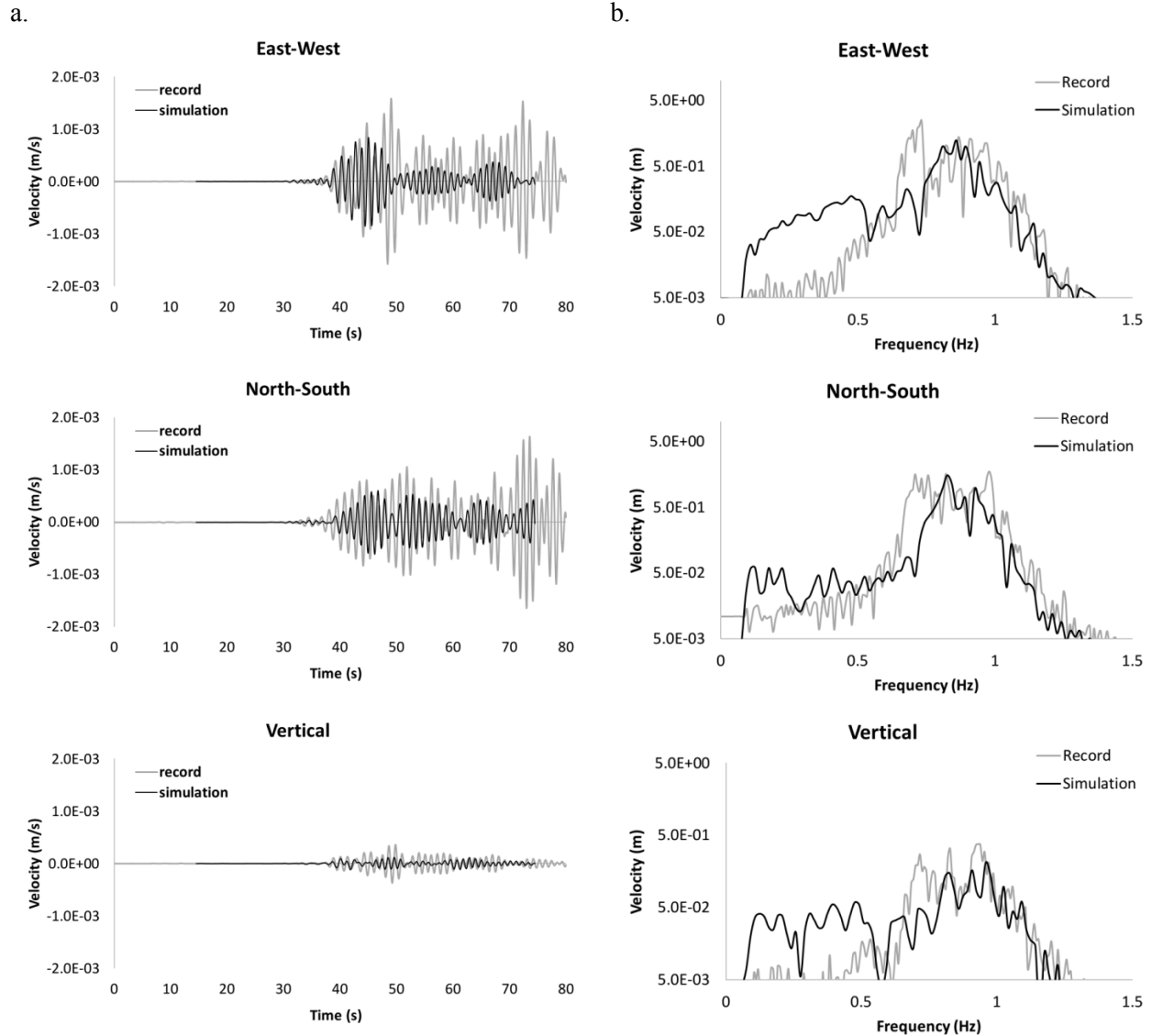


Figure 3-9. Comparison of a) simulated velocity time series versus recorded velocity time series and b) the velocity Fourier spectrum of the simulation versus the velocity Fourier spectrum of the record at the soil site for the proposed focal mechanism of Ma and Audet (2014); epicentral distance  $R=43$  km, depth=14.5 km,  $M_w=4.7$ ,  $M_0=1.32e+16$  Nt-m.

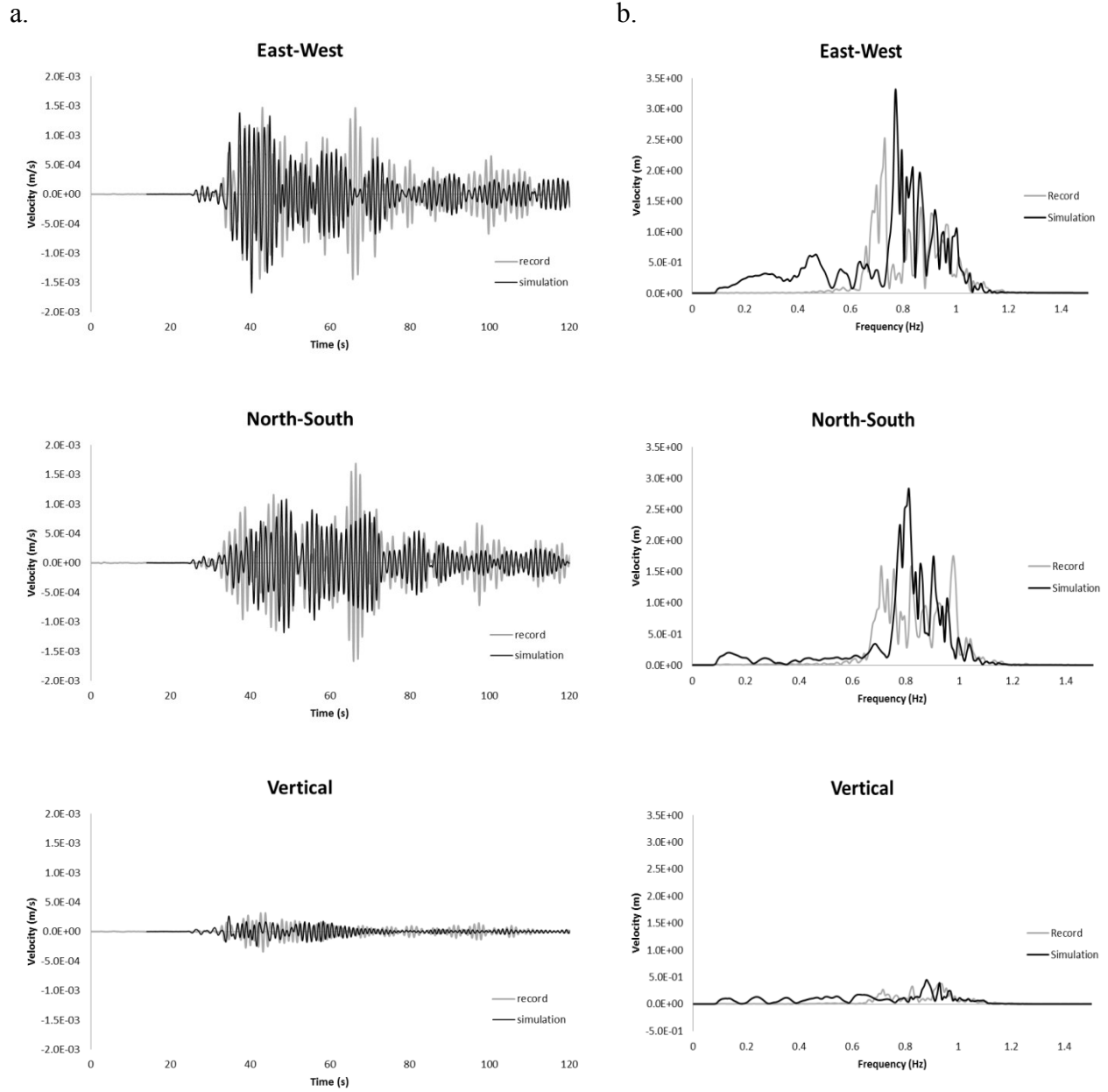
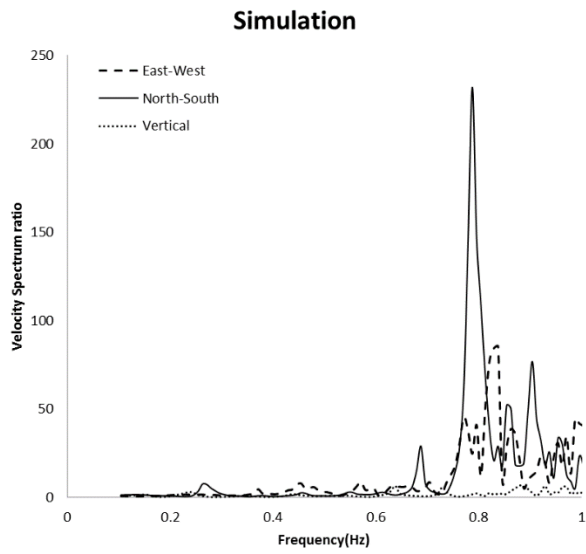


Figure 3-10. Comparison of a) simulated velocity time series versus recorded velocity time series and b) the velocity Fourier spectrum of the simulation versus the velocity Fourier spectrum of the record at the soil site for  $M_w=4.7$  using a half duration of 1.6 for the Gaussian source function

a.



b.

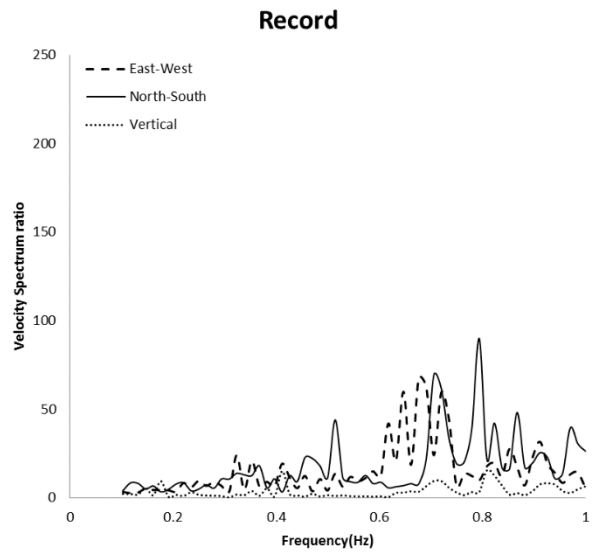
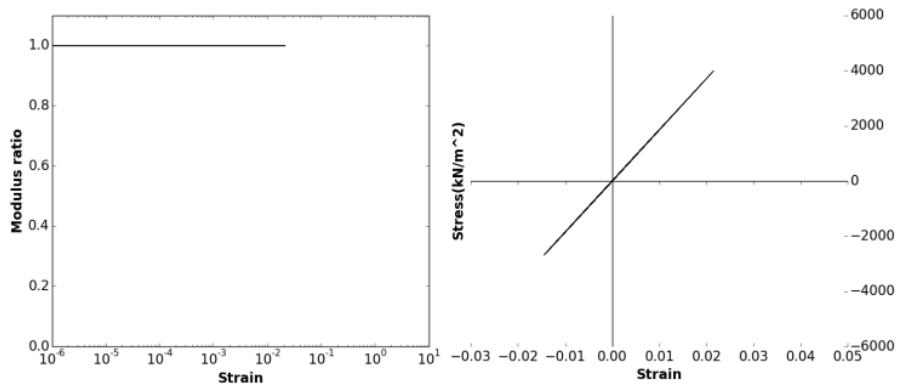
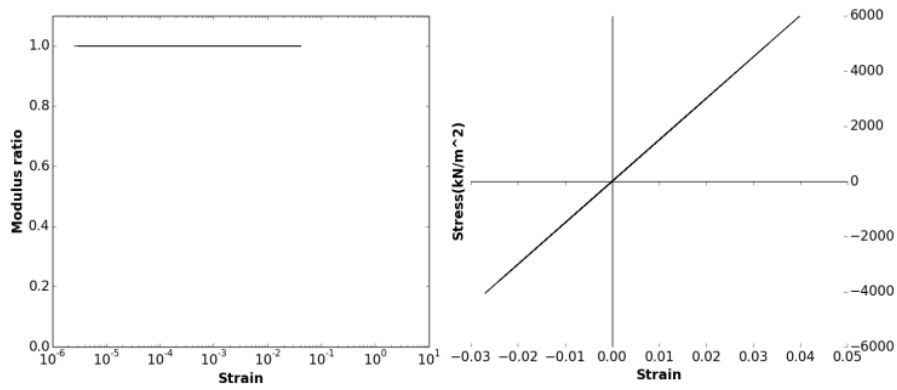


Figure 3-11. Comparison of the velocity Fourier spectral ratios of soil site to rock site for a) the simulation and b) the record

(a)



(b)



(c)

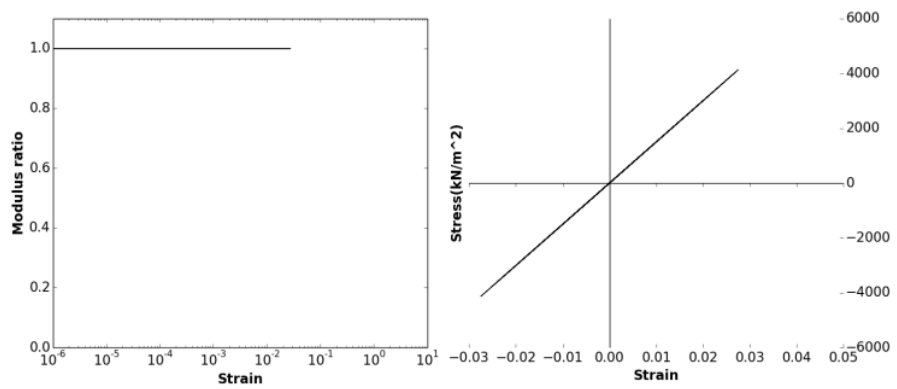


Figure 3-12. Stress-strain and modulus reduction curves for the a) E-W component, b) N-S component, and c) vertical component at the soil site at a depth of 25 m for the viscoelastic simulation using  $M_w=7.5$  ( $R=5.6$  km, X= east-west, Y= north-south, Z= vertical)

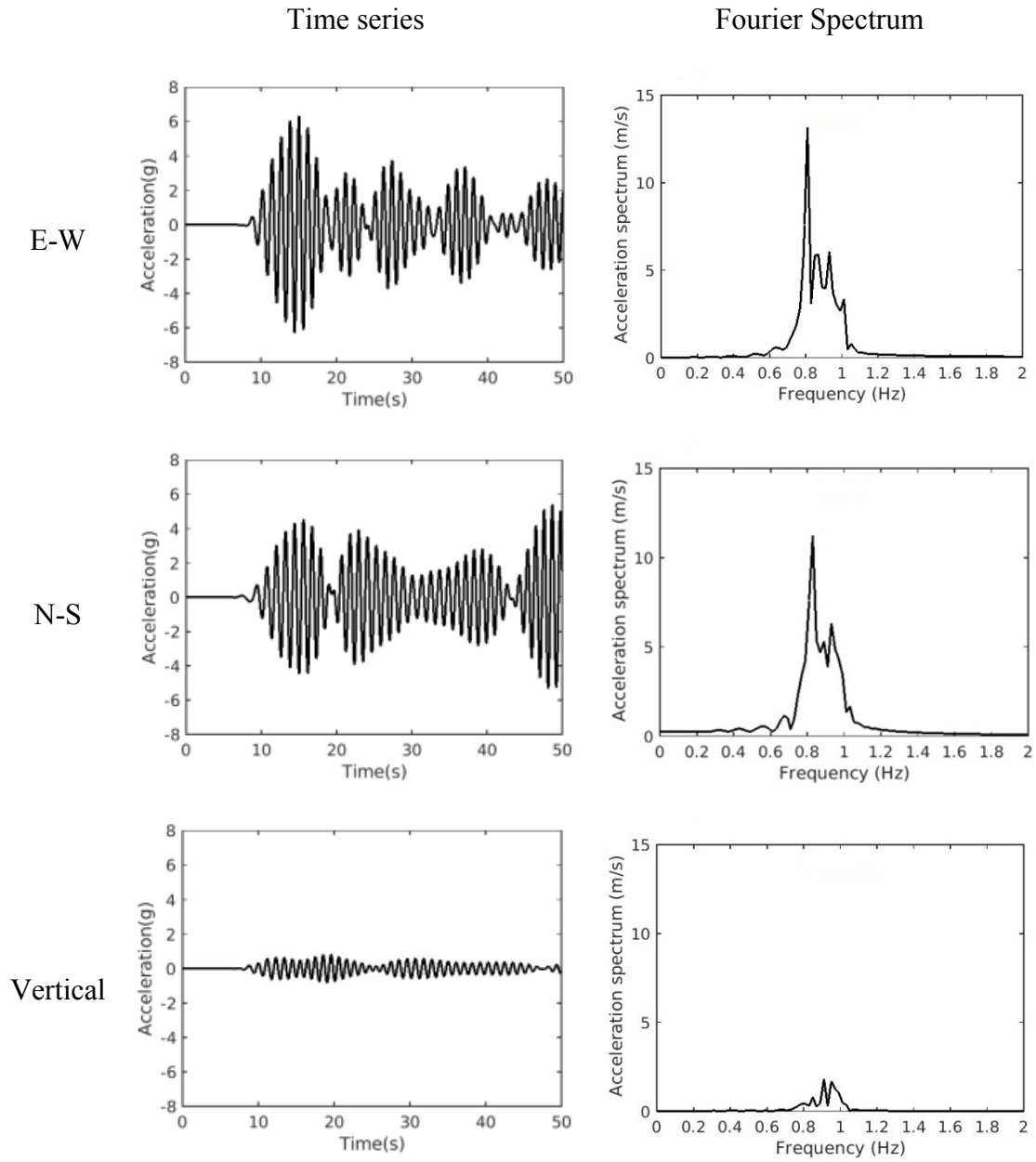


Figure 3-13. Acceleration time series and Fourier spectrums of the viscoelastic simulation for  $M_w=7.5$  for the receiver at the soil site ( $R=5.6$  km)

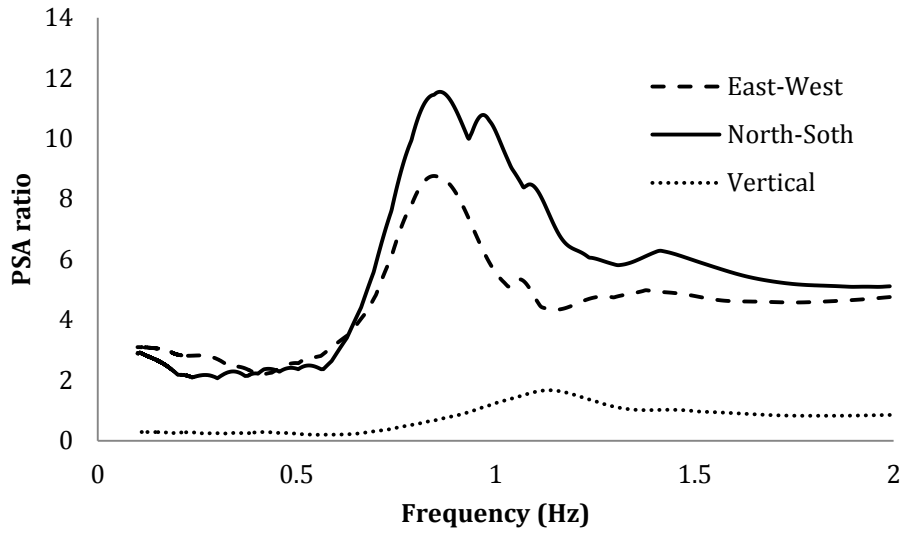


Figure 3-14. PSA ratio of soil site to rock site for the viscoelastic simulation [PSA (soil site)/ PSA (rock site)]

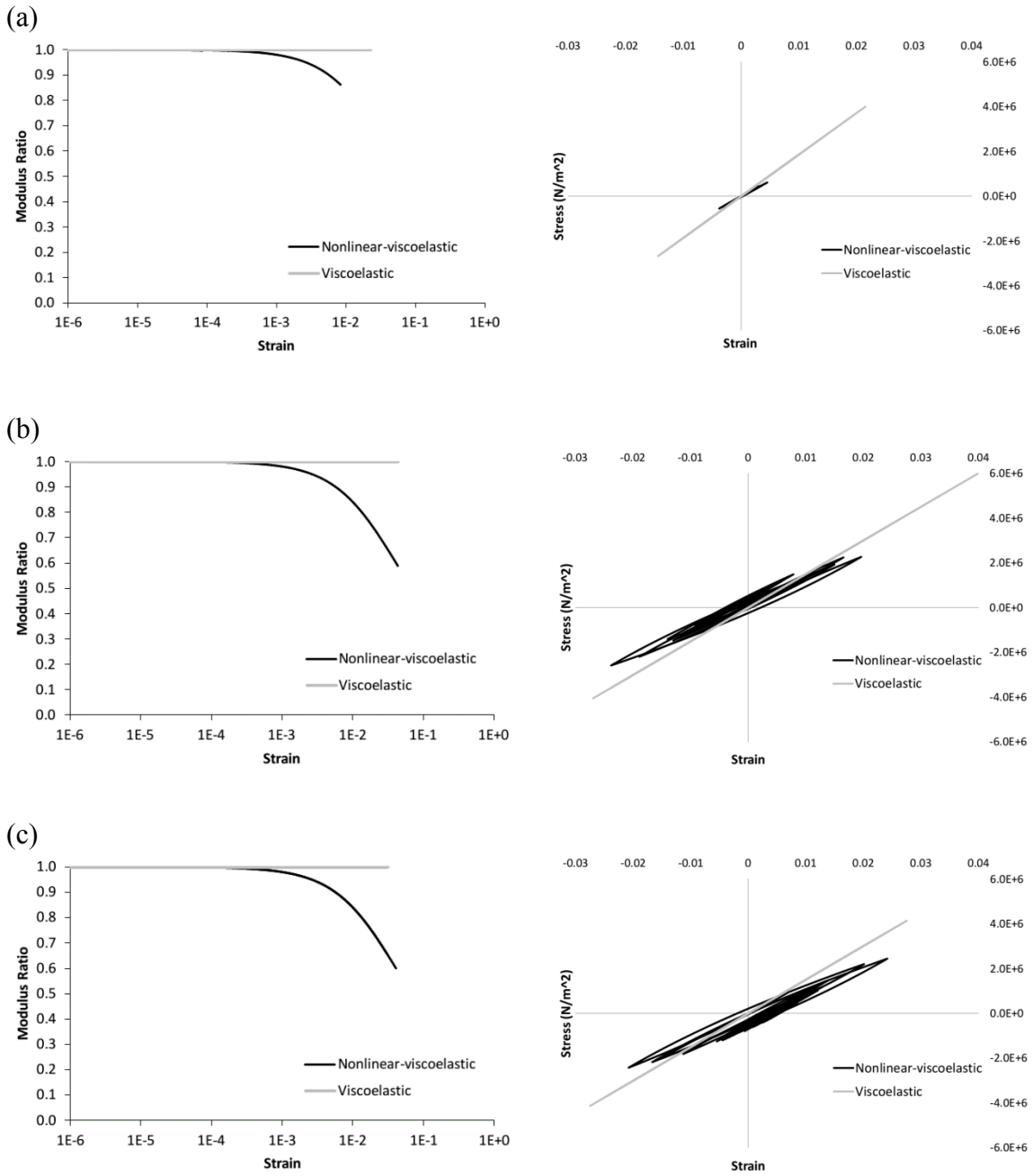


Figure 3-15. Stress-strain and modulus reduction curves of the a) X-Y component, b) X-Z component, and c) Y-Z component at the soil site for the viscoelastic and nonlinear-viscoelastic simulations for Mw=7.5 (R=5.6km, X= east-west, Y= north-south, Z= vertical)

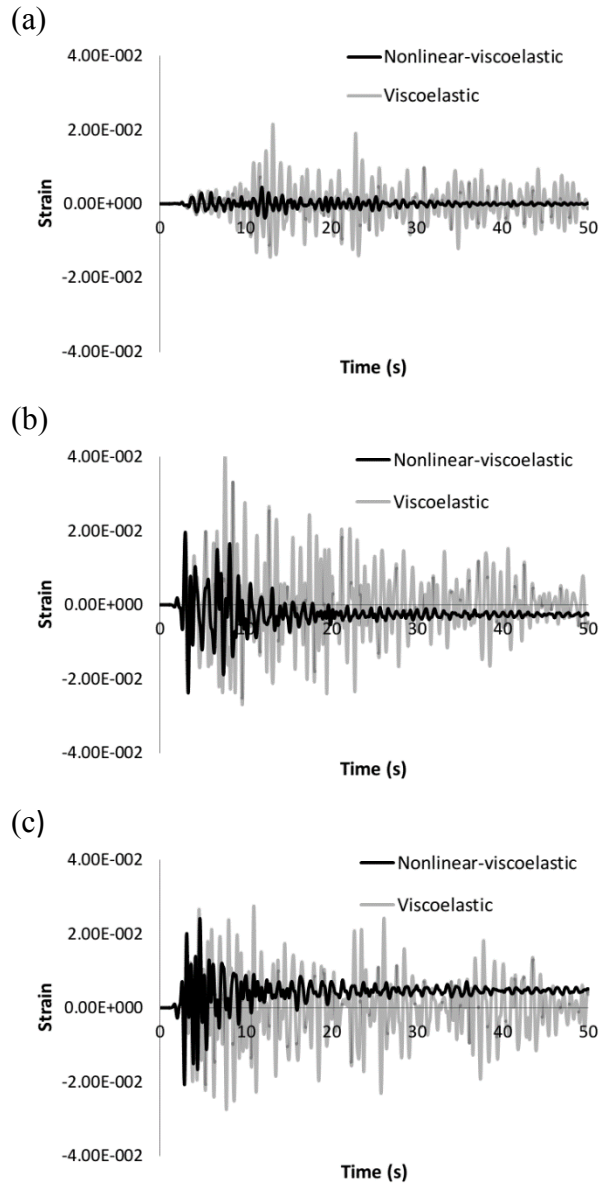


Figure 3-16. The strain time series of the a) X-Y component, b) X-Z component, and c) Y-Z component at the soil site for the viscoelastic and nonlinear-viscoelastic simulations for  $M_w=7.5$  ( $R=5.6\text{km}$ ,  $X=$  east-west,  $Y=$  north-south,  $Z=$  vertical).

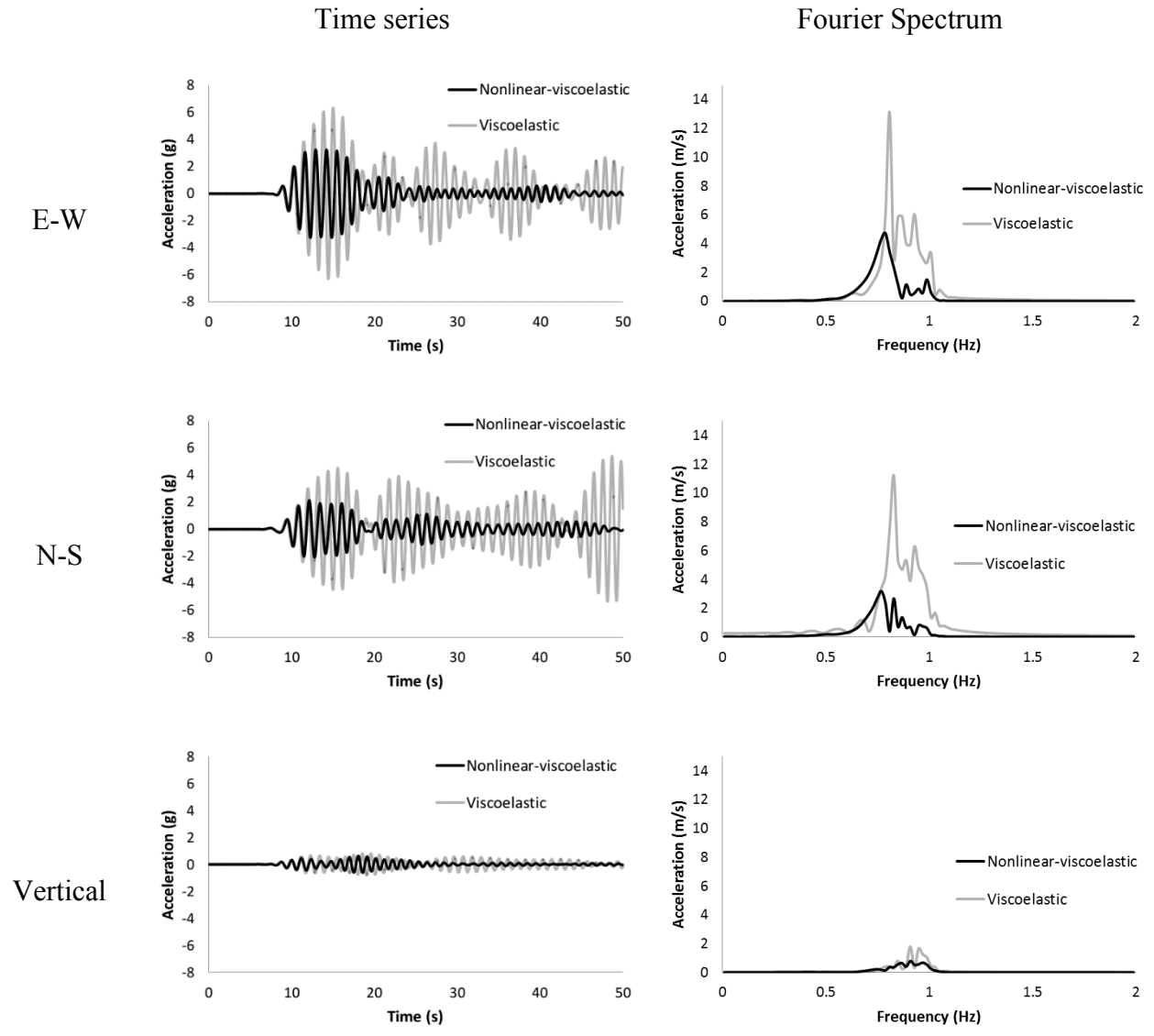


Figure 3-17. Acceleration time series and associated Fourier spectrums of the viscoelastic (Original) and nonlinear-viscoelastic (Modified) simulations for Mw=7.5 for the receiver at the soil site (R=5.6 km)

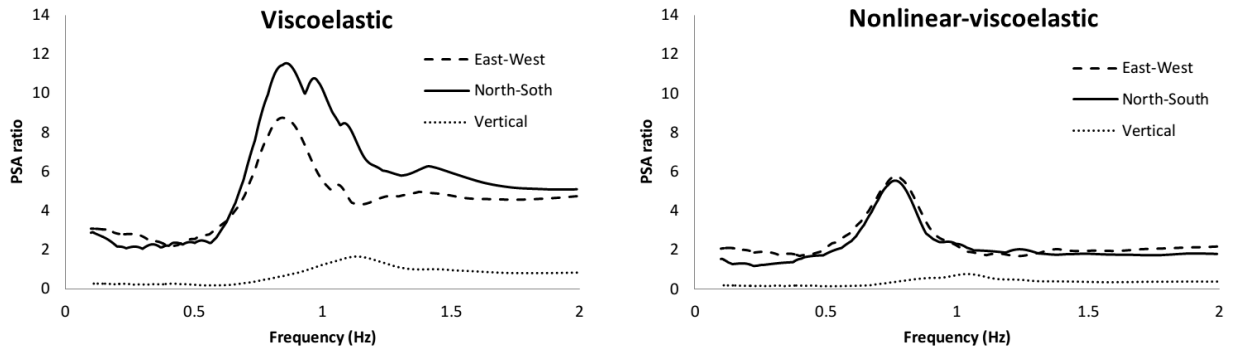


Figure 3-18. PSA ratio of soil site to rock site for the viscoelastic simulation and the nonlinear-viscoelastic simulation [PSA (soil site)/ PSA (rock site)]

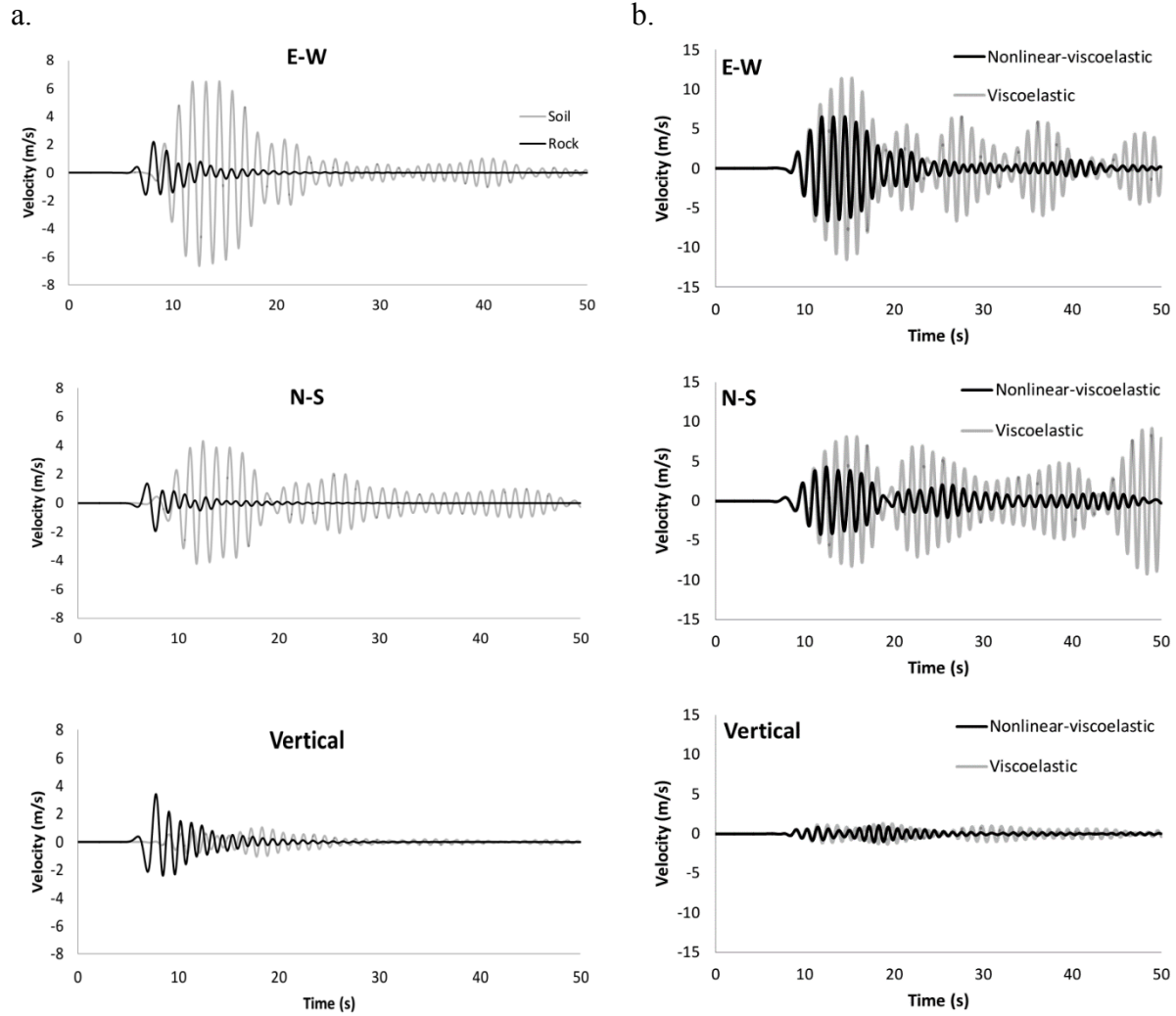


Figure 3-19. a) Comparison of the nonlinear-viscoelastic simulated velocity time series at the rock site and soil site ( $M_w = 7.5$ ,  $R = 5.6$  km). b) Comparison of the simulated velocity time series of the viscoelastic and the nonlinear-viscoelastic simulations at the soil site ( $M_w = 7.5$ ,  $R = 5.6$  km)

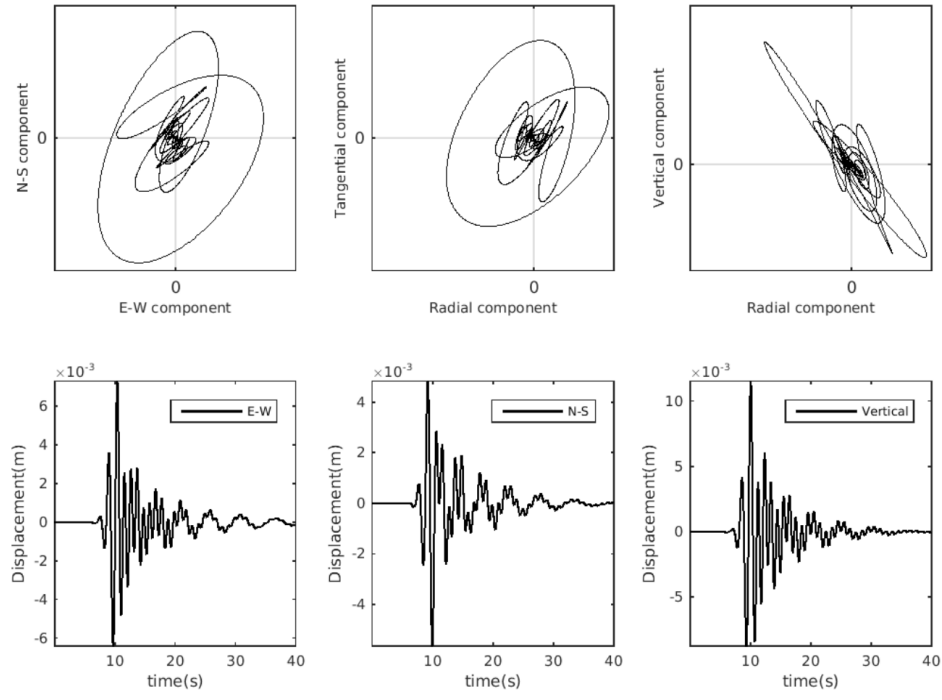


Figure 3-20. Particle motion of the nonlinear-viscoelastic simulation at the rock site

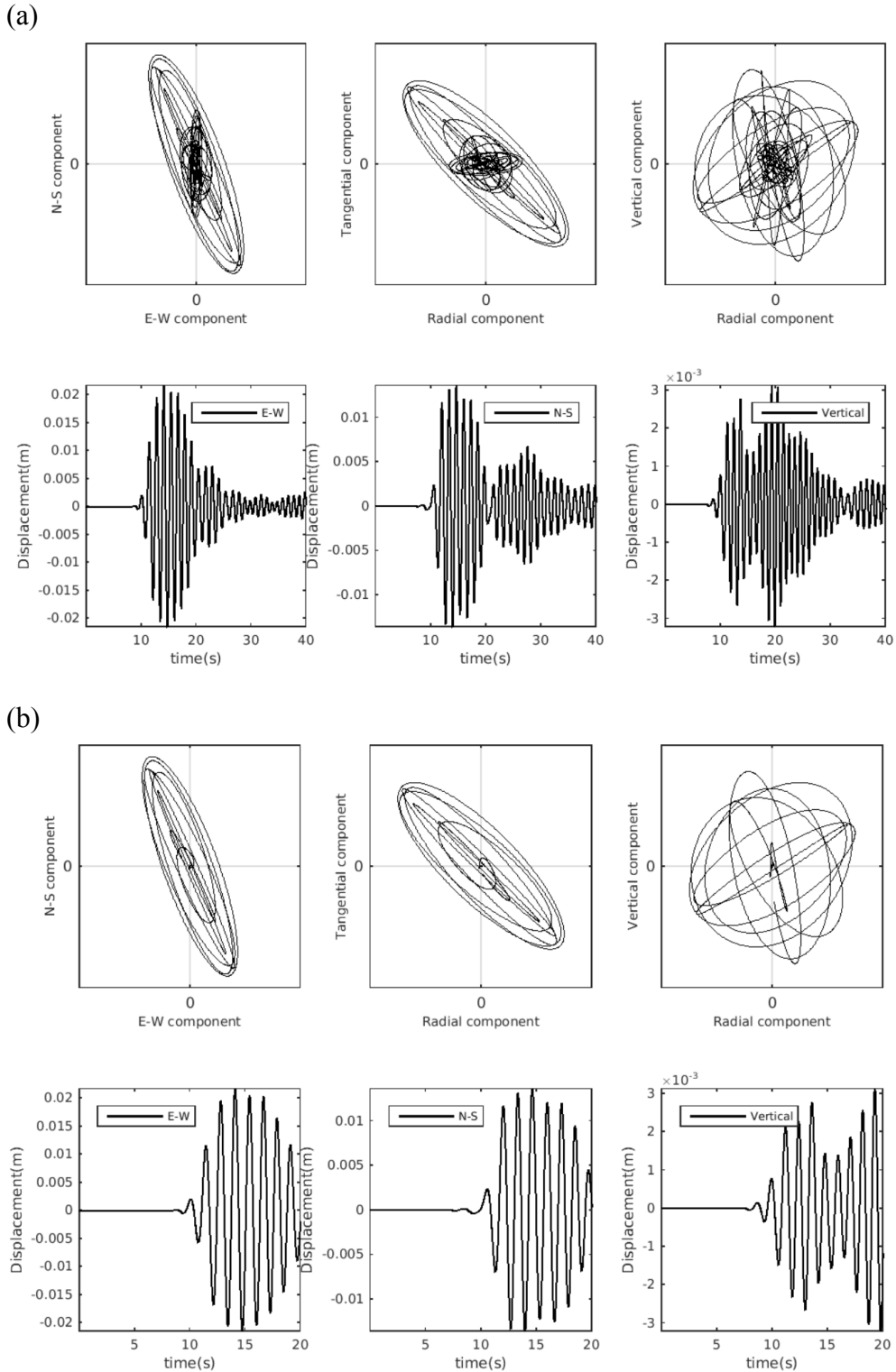
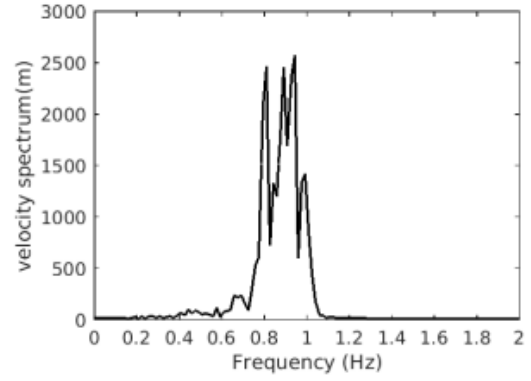
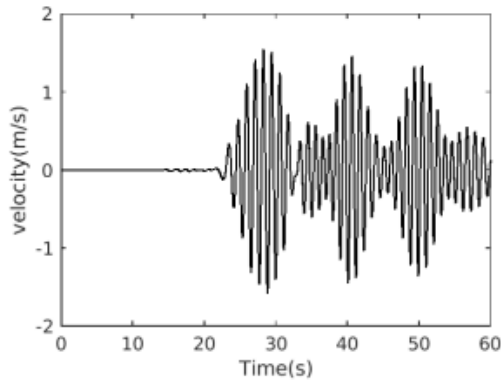


Figure 3-21. Particle motion of the nonlinear-viscoelastic simulation at the soil site for a) the whole modeled time series and b) the first 20 s of the modeled time series

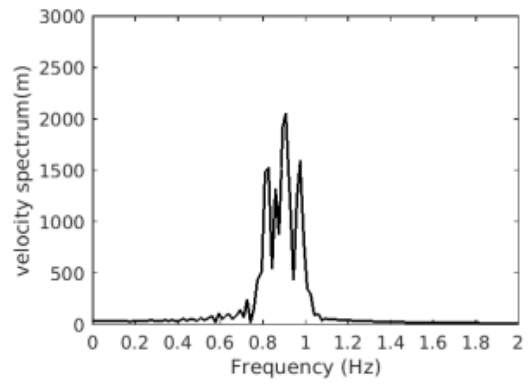
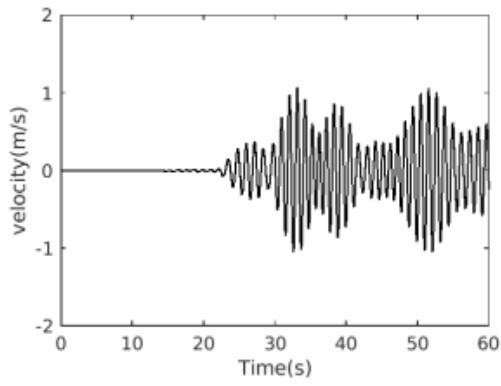
Time Series

Fourier Spectrum

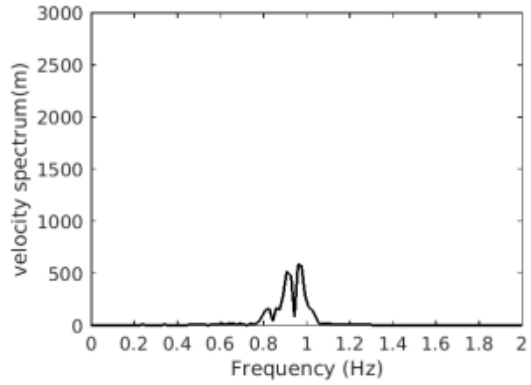
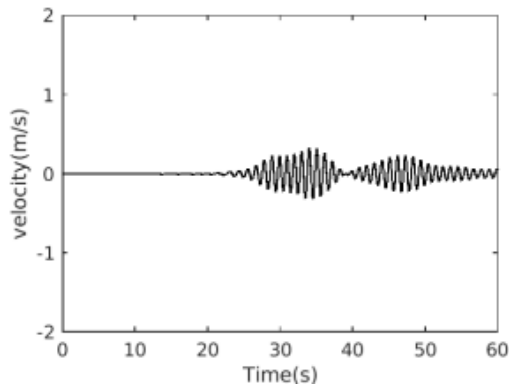
E-W



N-S



Vertical



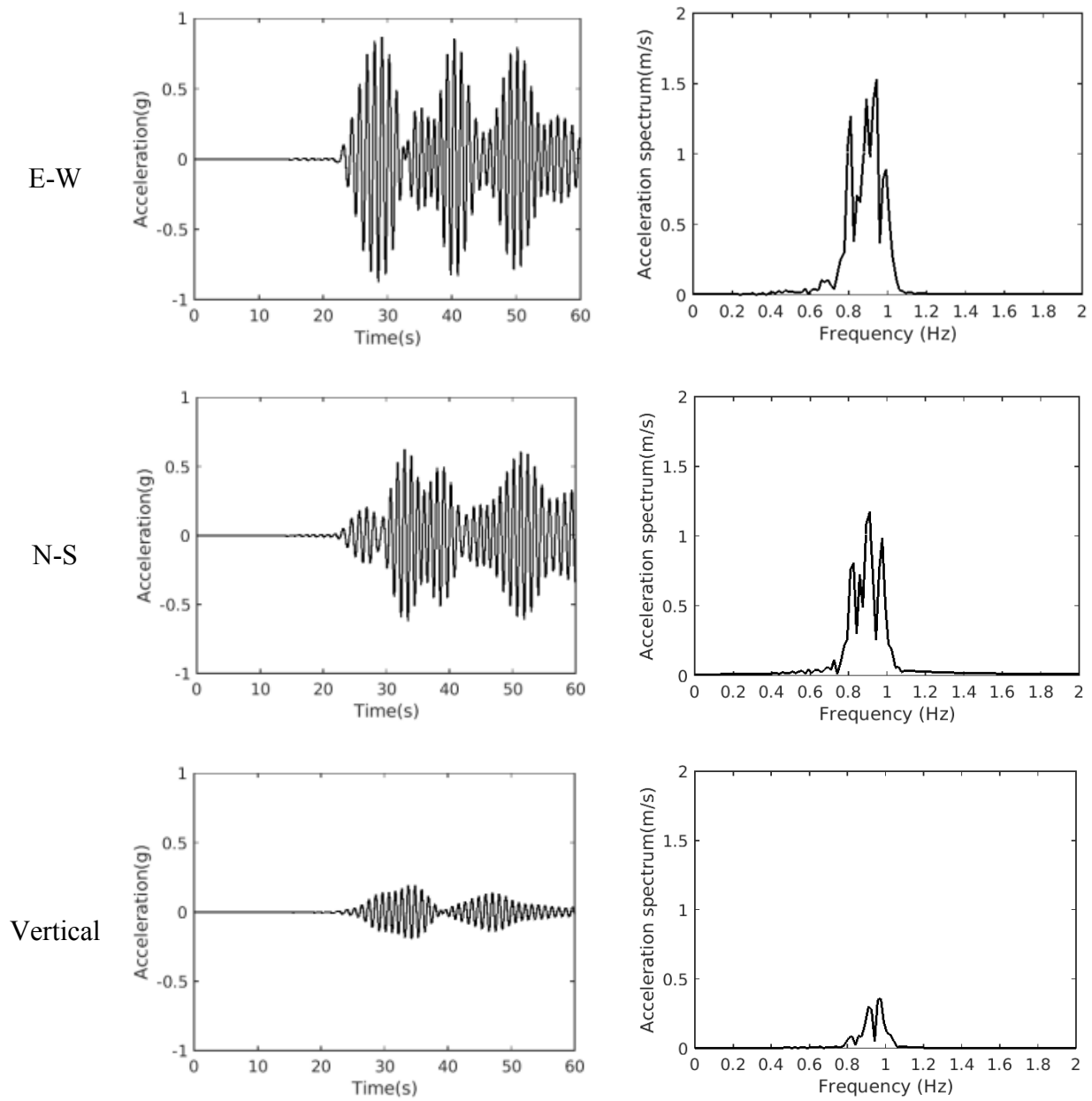


Figure 3-22. Velocity and acceleration time series and associated Fourier spectrums of the viscoelastic simulation for the receiver at the soil site (R=43 km)

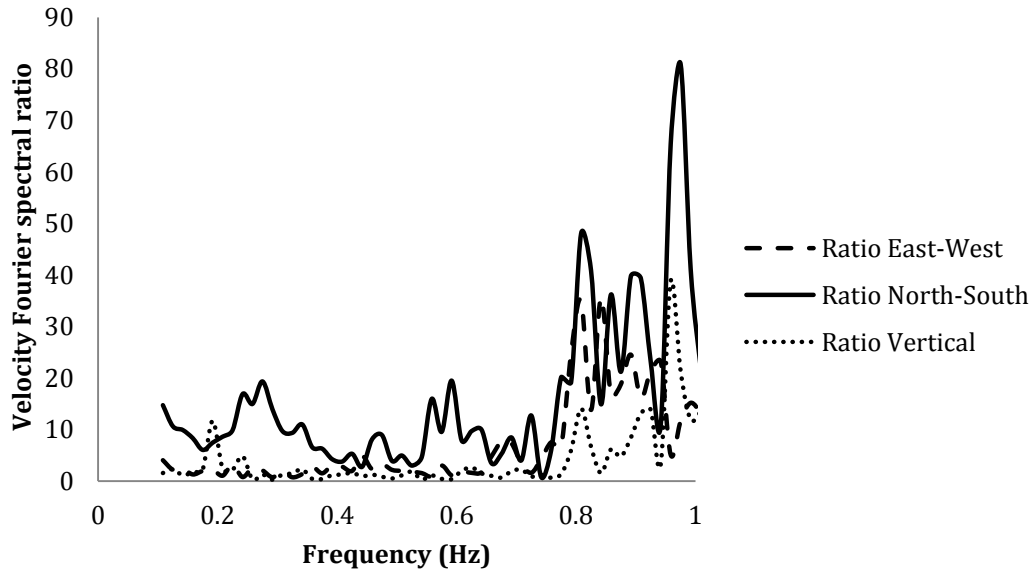


Figure 3-23. Velocity Fourier spectral ratio of soil site to rock site associated with the viscoelastic simulation only

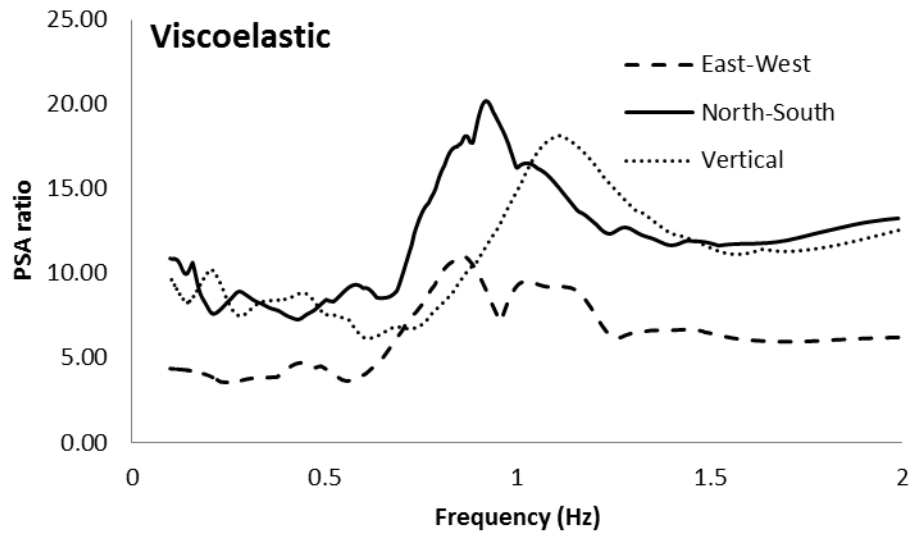


Figure 3-24. PSA ratio of soil site to rock site for the viscoelastic simulation [PSA (soil site)/ PSA (rock site)]

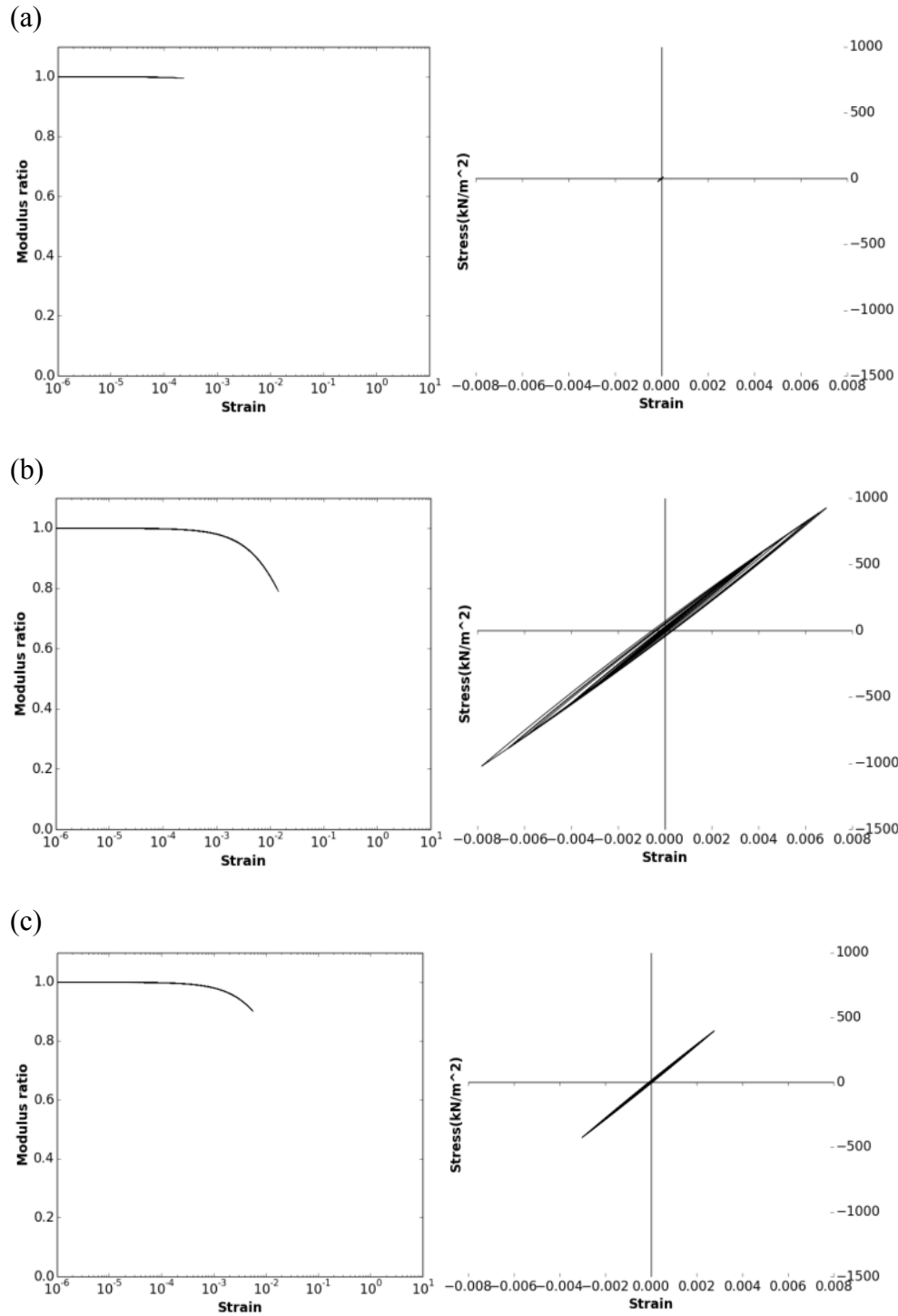
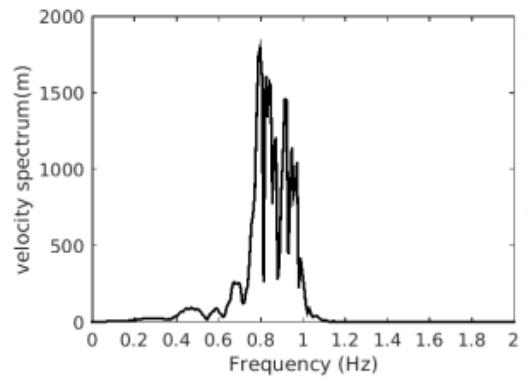
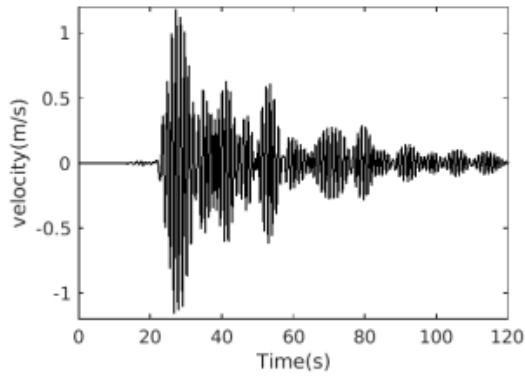


Figure 3-25. Modulus reduction and stress-strain curves of the a) X-Y component, b) X-Z component, and c) Y-Z component for the receiver at the soil site in the nonlinear-viscoelastic simulation (R=43 km, X= east-west, Y= north-south, Z= vertical)

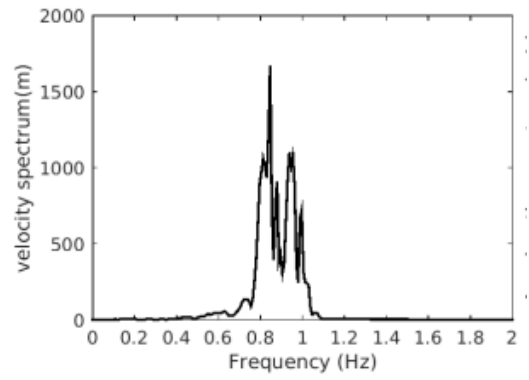
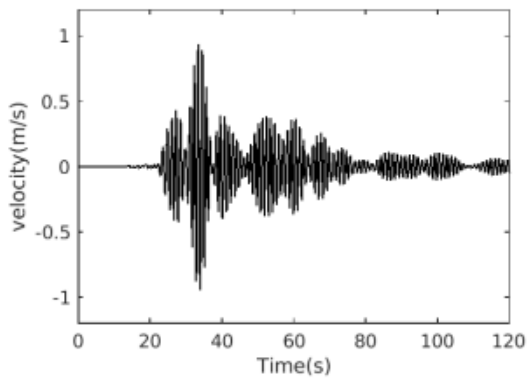
Time Series

Fourier Spectrum

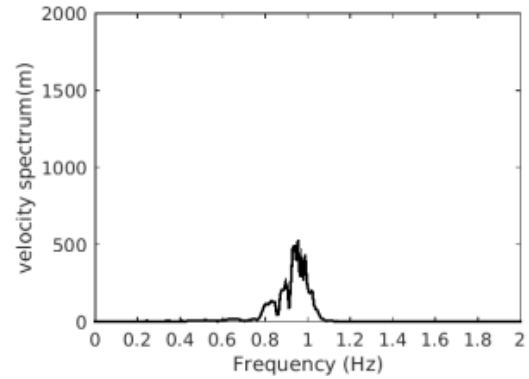
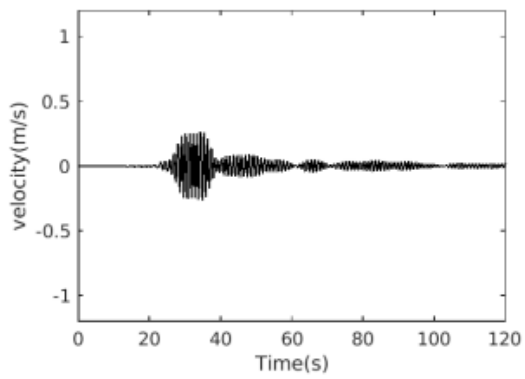
E-W



N-S



Vertical



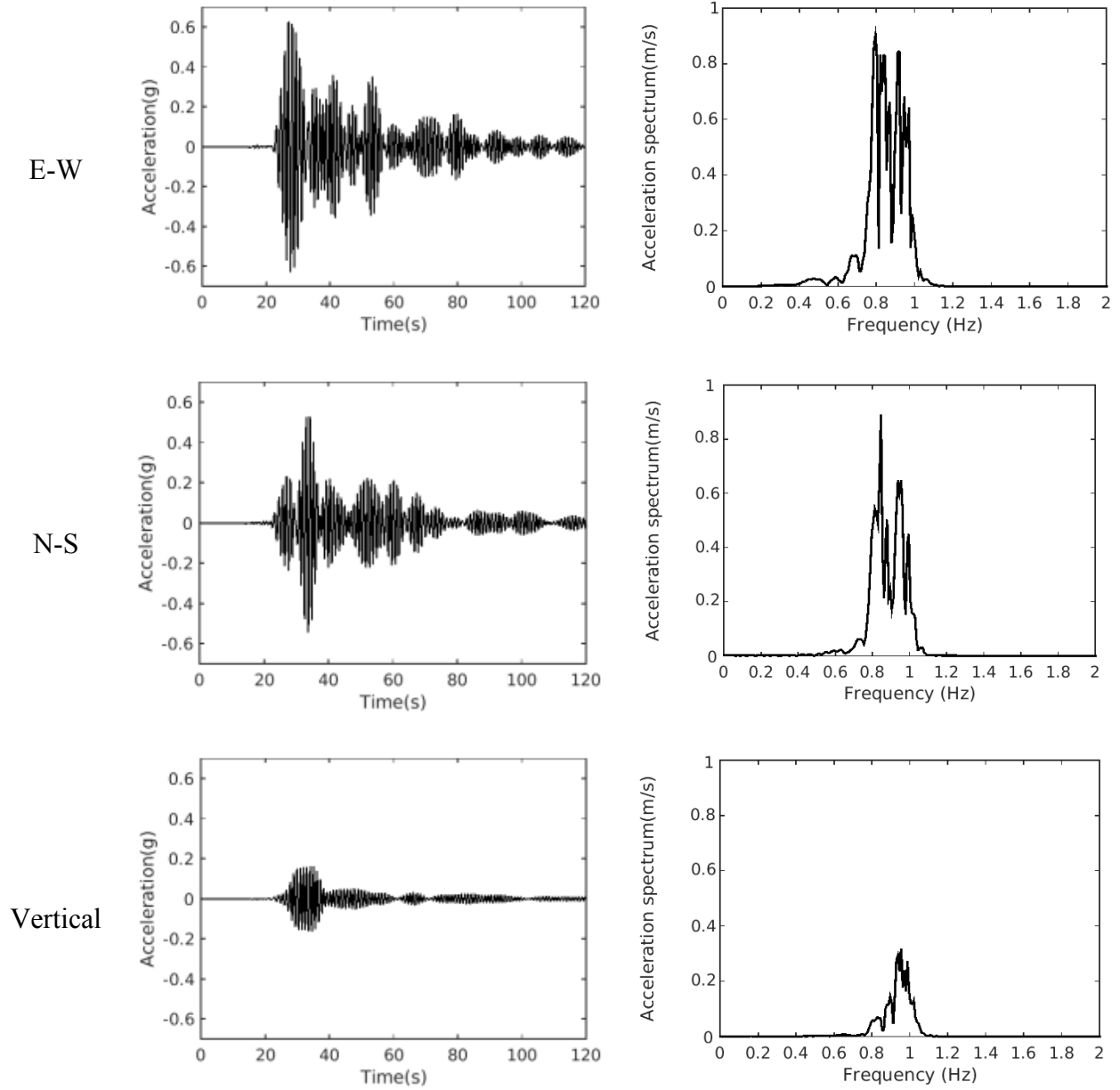


Figure 3-26. Velocity and acceleration time series and associated Fourier spectrums of the nonlinear-viscoelastic simulation for the receiver at the soil site (R=43 km)

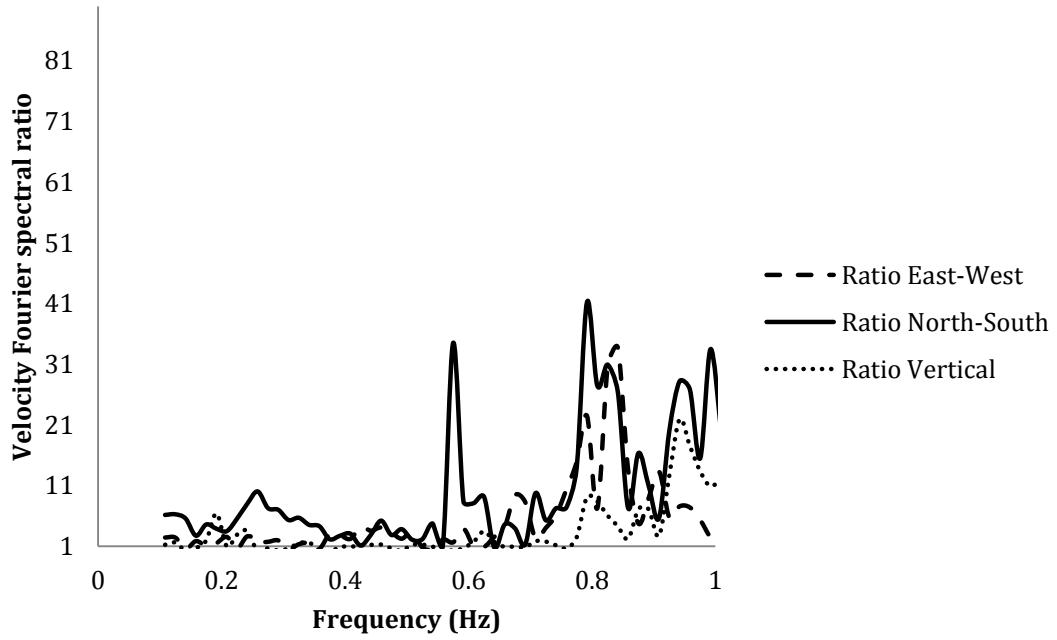


Figure 3-27. Velocity Fourier spectral ratio of soil site to rock site for the nonlinear-viscoelastic simulation

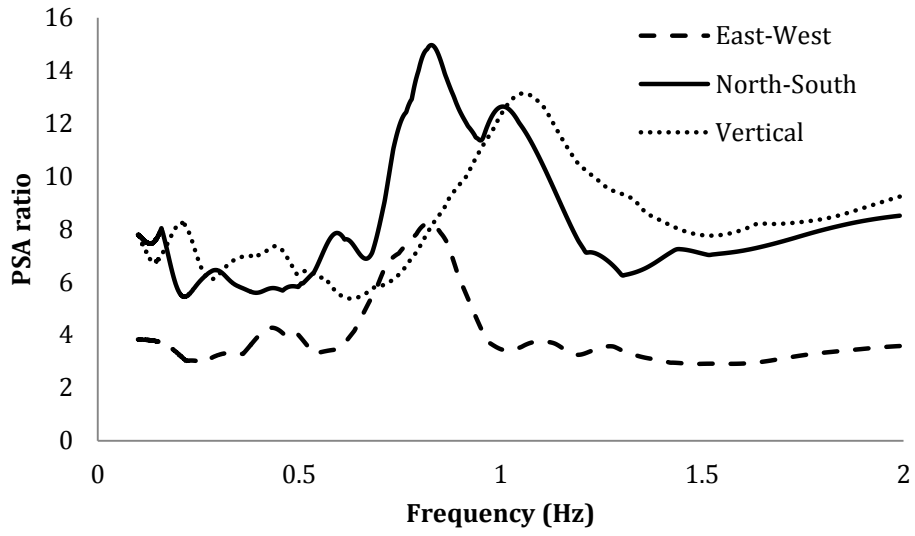
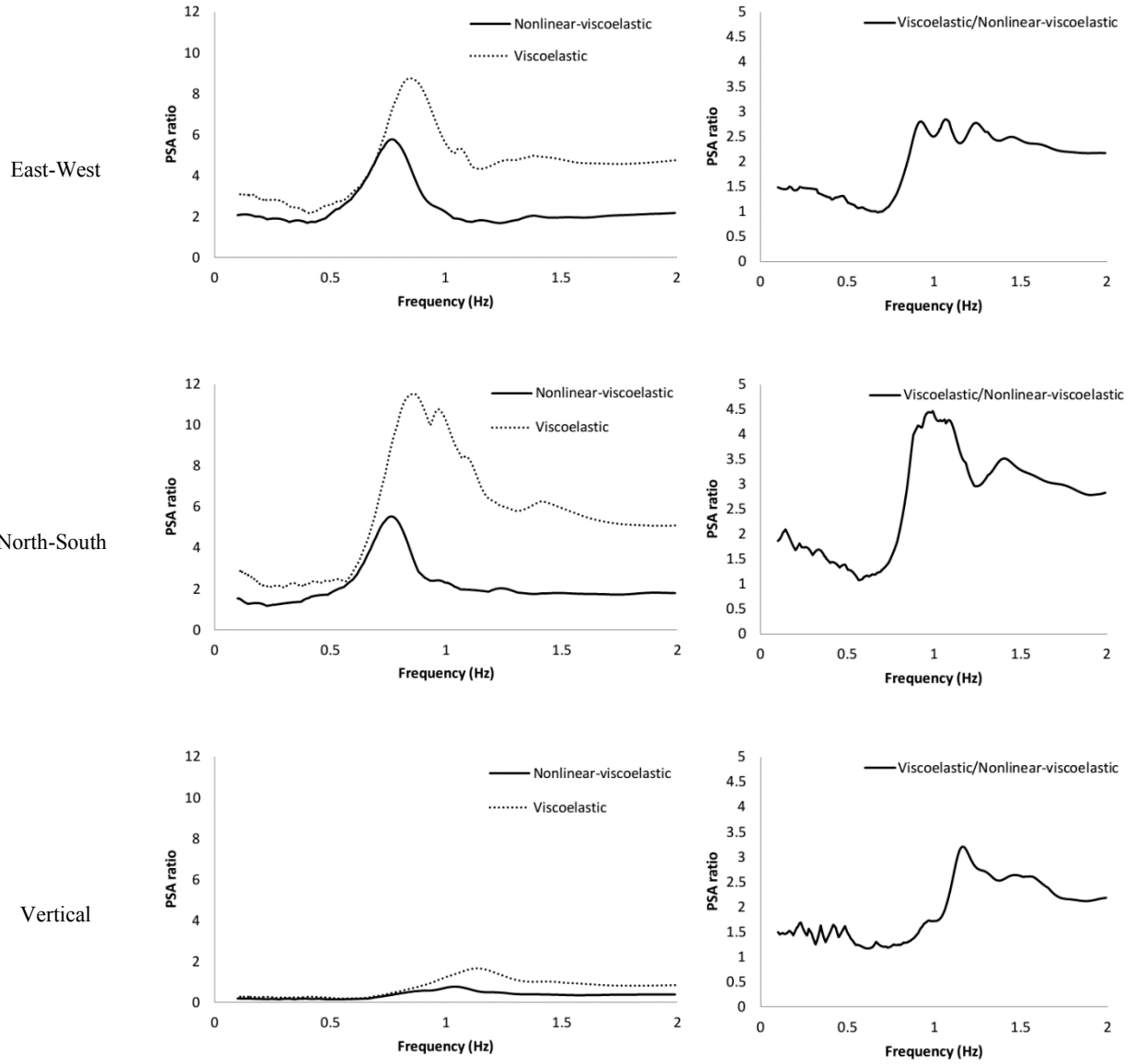


Figure 3-28. PSA ratio of soil site to rock site for the nonlinear-viscoelastic simulation [PSA (soil site)/ PSA (rock site)]

(a)



(b)

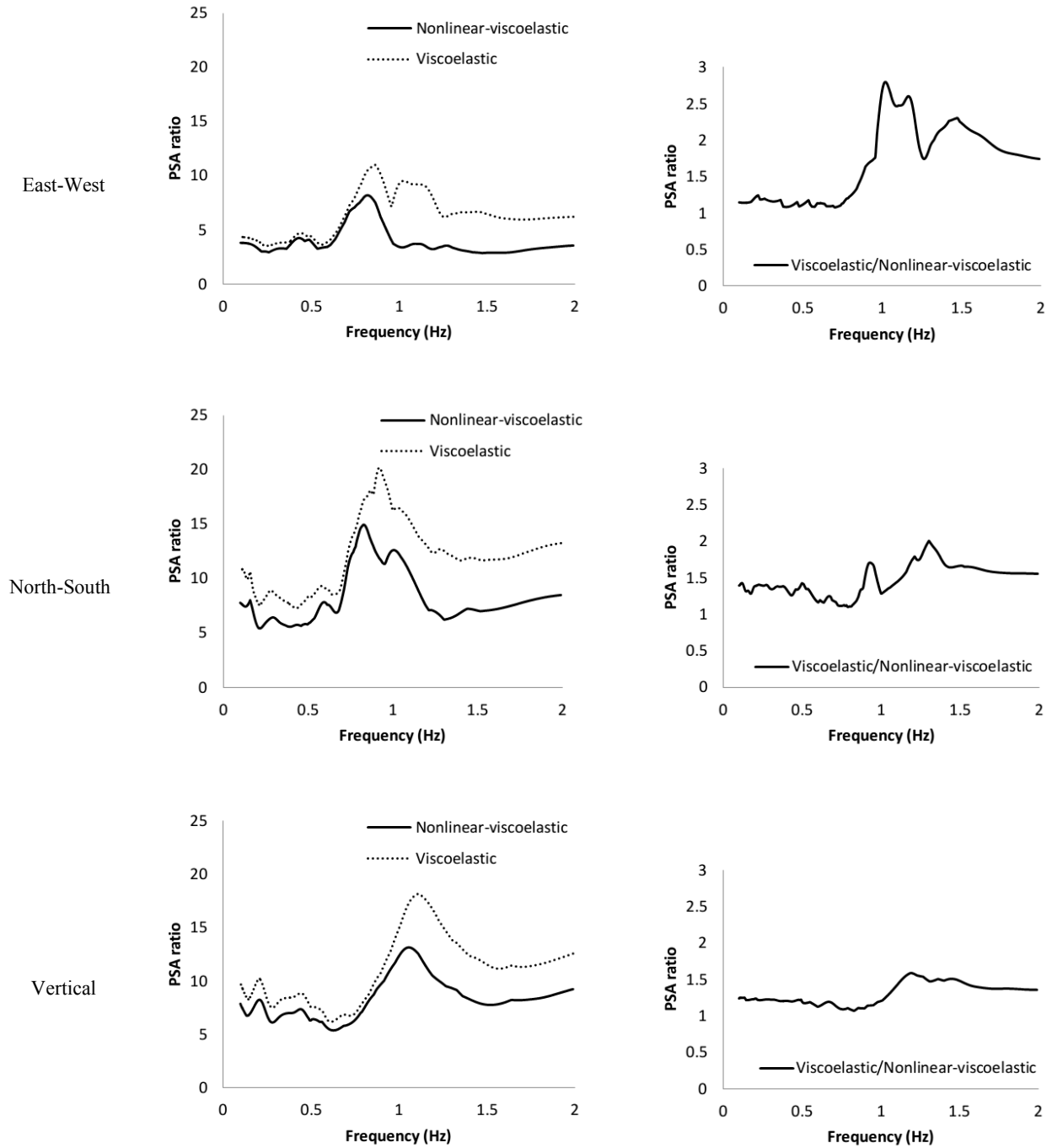
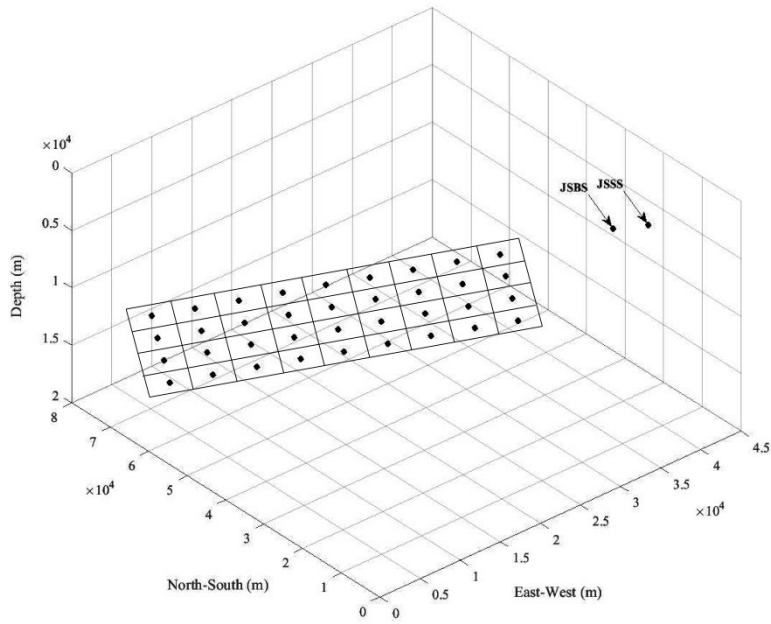


Figure 3-29. Comparison of the PSA ratios of the viscoelastic simulation to the nonlinear-viscoelastic simulation for a) R=5.6 km and b) R=43 km

a.



b.

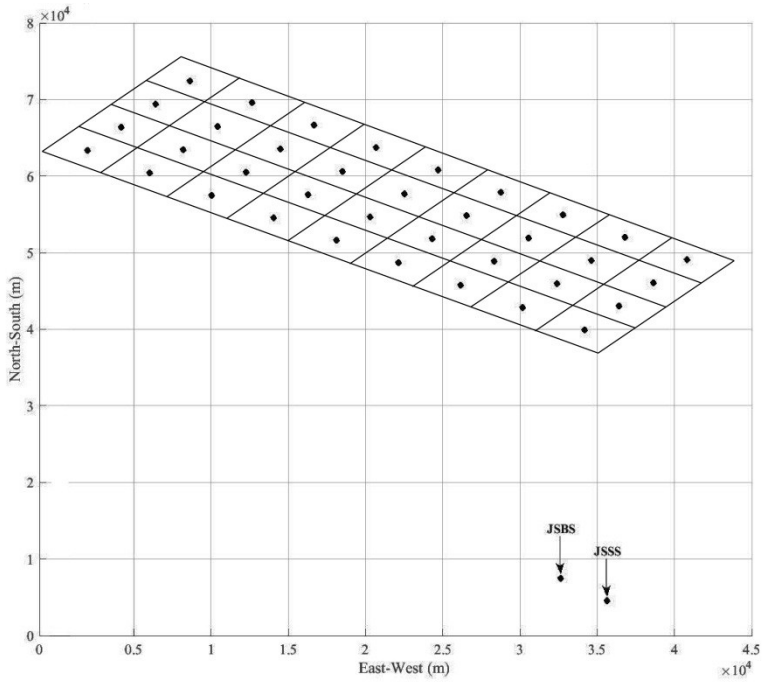


Figure 3-30. Sub-faults of finite fault plane used for the simulation a) 3D view and b) top view

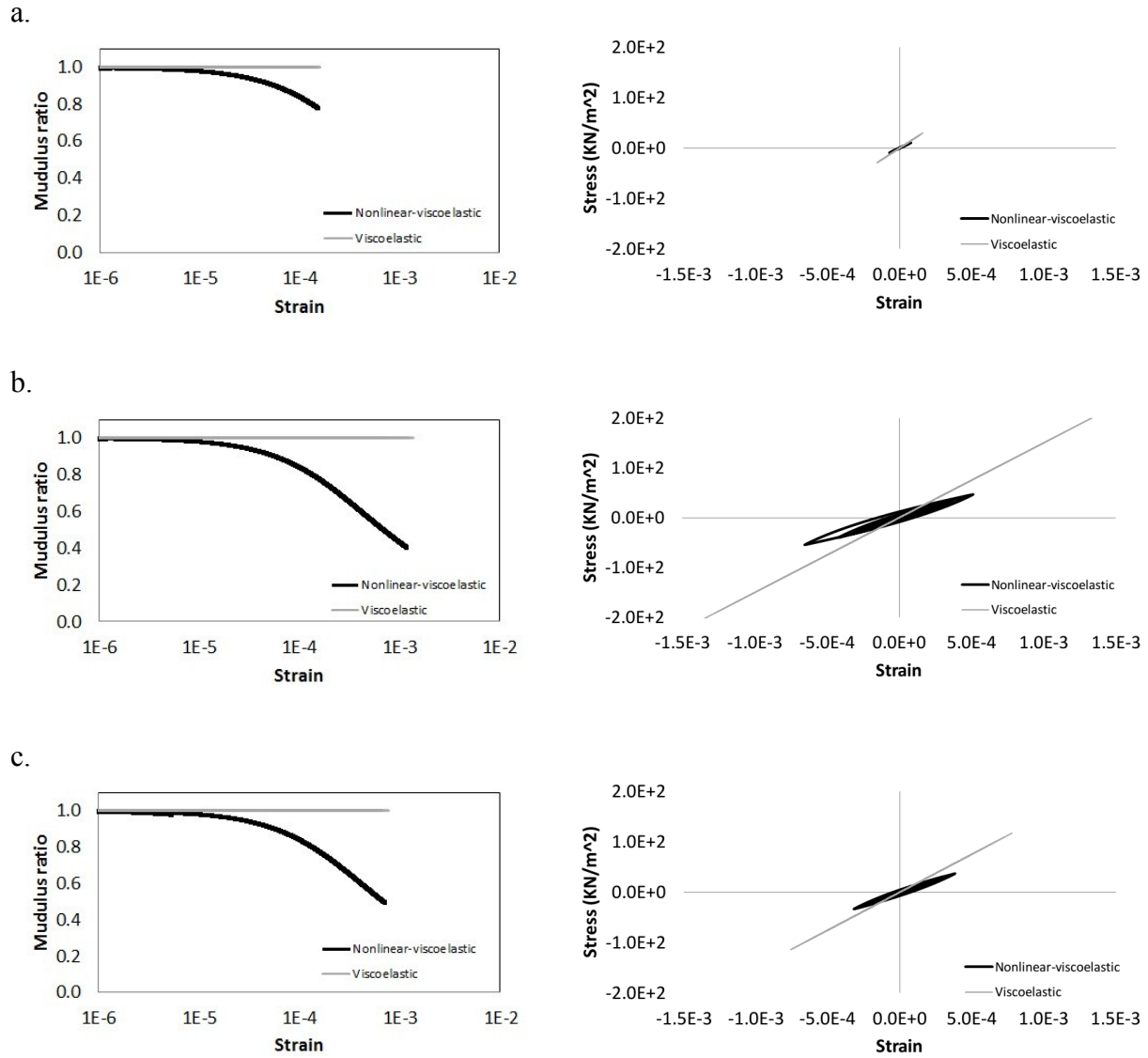
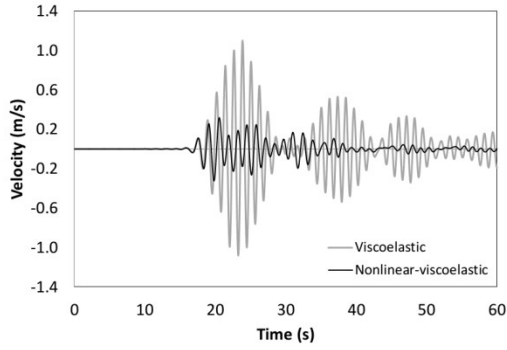
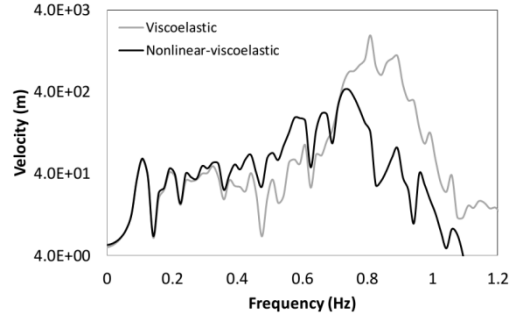


Figure 3-31. Stress-strain and modulus reduction curves of the a) X-Y component, b) X-Z component, and c) Y-Z component at the soil site for the viscoelastic and nonlinear-viscoelastic simulations for  $M_w=7$  using a finite fault model ( $R=43$  km, X= east-west, Y= north-south, Z= vertical)

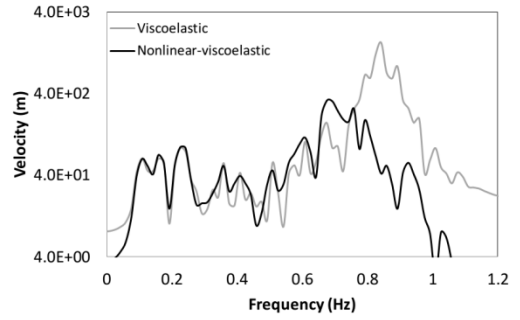
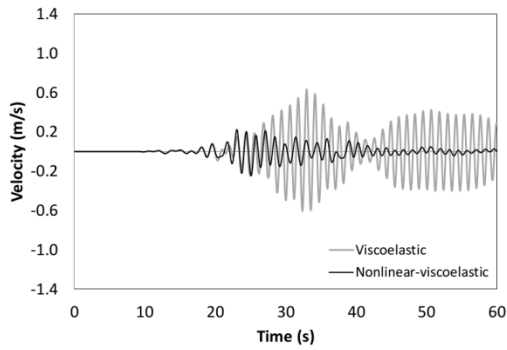
Time Series



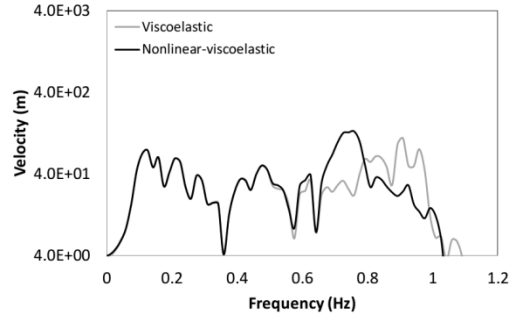
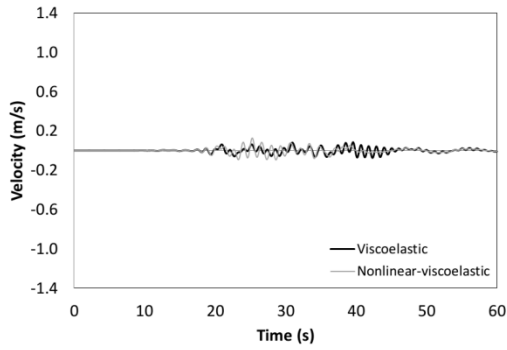
Fourier Spectrum



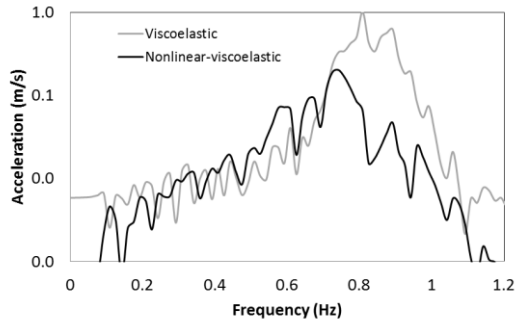
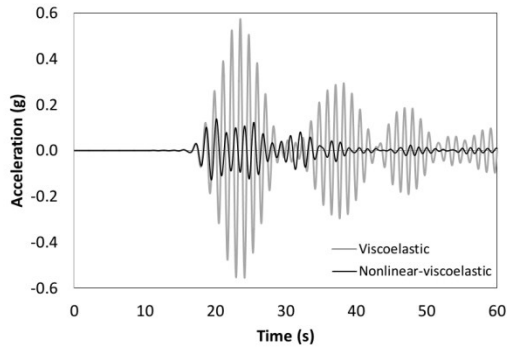
E-W



N-S

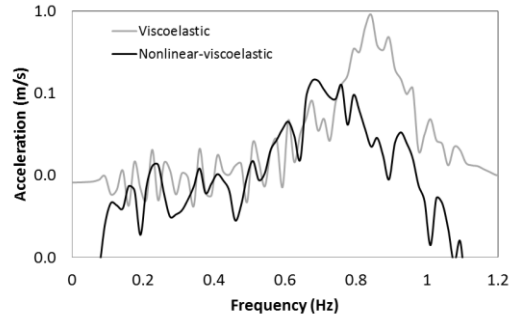
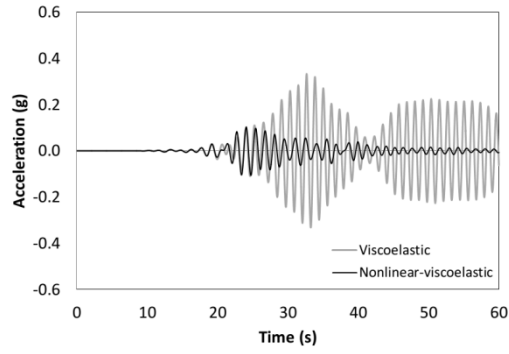


Vertical



E-W

N-S



Vertical

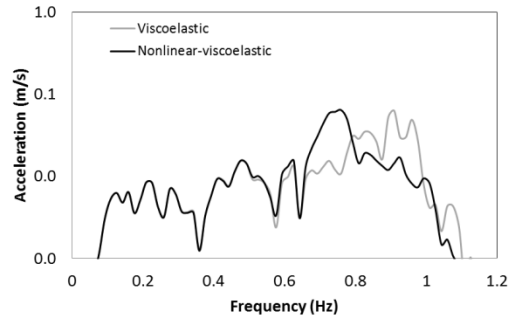
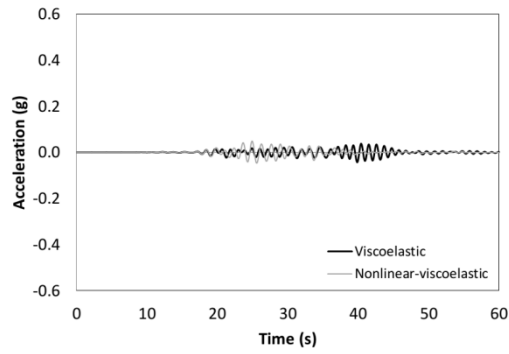
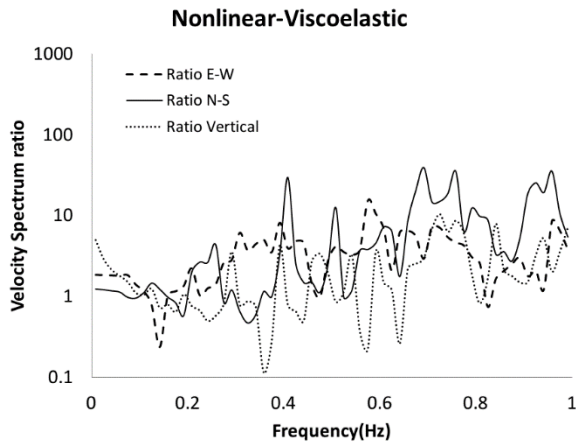


Figure 3-32. Comparison of the velocity and acceleration time series and associated Fourier spectrums of the nonlinear-viscoelastic and viscoelastic simulations for the receiver at the soil site (R=43 km)

a.



b.

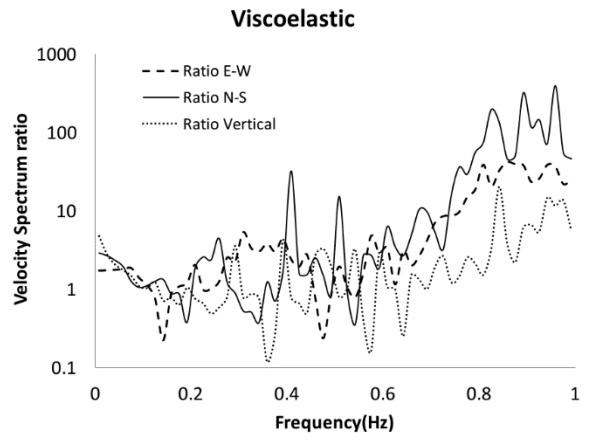


Figure 3-33. Comparison of the velocity Fourier spectral ratios of soil site to rock site for the a) nonlinear-viscoelastic simulation and b) viscoelastic simulation

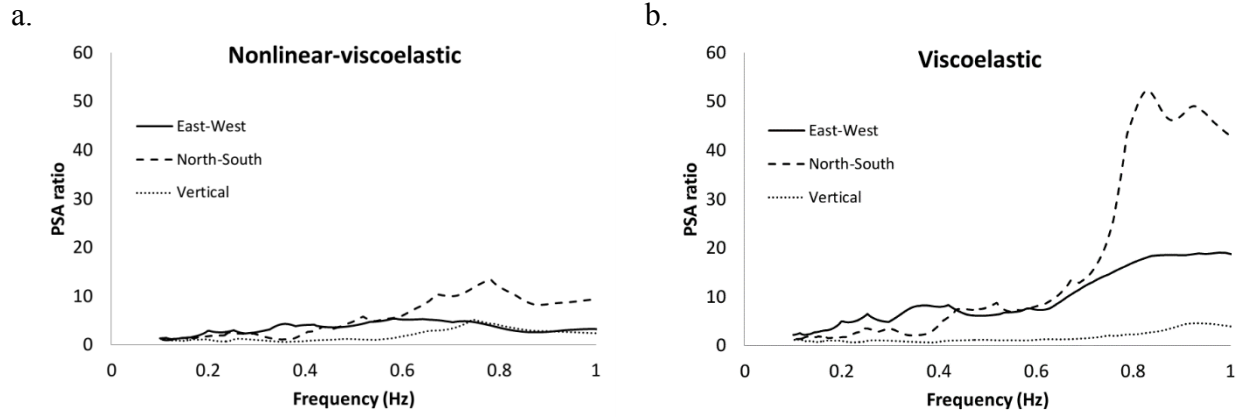


Figure 3-34. PSA ratio of soil site to rock site for the a) nonlinear-viscoelastic simulation and b) viscoelastic simulation [PSA (soil site)/ PSA (rock site)]

## Appendix

The nonlinear-viscoelastic subroutine that was added to the AWP-ODC program to take into account the nonlinear soil behavior in the viscoelastic ground motion simulation:

```
do kk= nzb,nze,kblock
do jj= nyb,nye,jblock
do 50 k= kk,min(kk+kblock-1,nze)
do 50 j= jj,min(jj+jblock-1,nye)

vt1(nxb:nxe)=c1*(u1(nxb+1:nxe+1,j,k)-
u1(nxb:nxe,j,k))+c2*(u1(nxb+2:nxe+2,j,k)-u1(nxb-1:nxe-1,j,k))
vt2(nxb:nxe)=c1*(v1(nxb:nxe,j,k)-v1(nxb:nxe,j-1,k))+c2*(v1(nxb:nxe,j+1,k)-
v1(nxb:nxe,j-2,k))
vt3(nxb:nxe)=c1*(w1(nxb:nxe,j,k)-w1(nxb:nxe,j,k-1))+c2*(w1(nxb:nxe,j,k+1)-
w1(nxb:nxe,j,k-2))
vt4(nxb:nxe)=c1*(u1(nxb:nxe,j+1,k)-u1(nxb:nxe,j,k))+c2*(u1(nxb:nxe,j+2,k)-
u1(nxb:nxe,j-1,k)) + &
c1*(v1(nxb:nxe,j,k)-v1(nxb-1:nxe-1,j,k))+c2*(v1(nxb+1:nxe+1,j,k)-v1(nxb-
2:nxe-2,j,k))
vt5(nxb:nxe)=c1*(u1(nxb:nxe,j,k+1)-u1(nxb:nxe,j,k))+c2*(u1(nxb:nxe,j,k+2)-
u1(nxb:nxe,j,k-1)) + &
c1*(w1(nxb:nxe,j,k)-w1(nxb-1:nxe-1,j,k))+c2*(w1(nxb+1:nxe+1,j,k)-w1(nxb-
2:nxe-2,j,k))
```

$$vt6(nxb:nxe)=c1*(v1(nxb:nxe,j,k+1)-v1(nxb:nxe,j,k))+c2*(v1(nxb:nxe,j,k+2)-v1(nxb:nxe,j,k-1))$$

$$vt7(nxb:nxe)=c1*(w1(nxb:nxe,j+1,k)-w1(nxb:nxe,j,k))+c2*(w1(nxb:nxe,j+2,k)-w1(nxb:nxe,j-1,k))$$

$$dv1(nxb:nxe,j,k)=vt1(nxb:nxe)$$

$$dv2(nxb:nxe,j,k)=vt2(nxb:nxe)$$

$$dv3(nxb:nxe,j,k)=vt3(nxb:nxe)$$

$$dv4(nxb:nxe,j,k)=vt4(nxb:nxe)$$

$$dv5(nxb:nxe,j,k)=vt5(nxb:nxe)$$

$$dv6(nxb:nxe,j,k)=vt6(nxb:nxe)$$

$$dv7(nxb:nxe,j,k)=vt7(nxb:nxe)$$

! Calculate strain at each time step

$$exy(nxb:nxe,j,k)= dth*0.5*dv4(nxb:nxe,j,k)$$

$$exz(nxb:nxe,j,k)= dth*0.5*dv5(nxb:nxe,j,k)$$

$$eyz(nxb:nxe,j,k)= (dth*0.5*dv6(nxb:nxe,j,k))+(dth*0.5*dv7(nxb:nxe,j,k))$$

! Calculate total strain

$$exy1(nxb:nxe,j,k)= exy1(nxb:nxe,j,k)+exy(nxb:nxe,j,k)$$

$$exz1(nxb:nxe,j,k)= exz1(nxb:nxe,j,k)+exz(nxb:nxe,j,k)$$

$$eyz1(nxb:nxe,j,k)= eyz1(nxb:nxe,j,k)+eyz(nxb:nxe,j,k)$$

! condition to check loading from unloading and reloading

con1(nxb:nxe,j,k)=exy(nxb:nxe,j,k)\*exy2(nxb:nxe,j,k)

con2(nxb:nxe,j,k)=exz(nxb:nxe,j,k)\*exz2(nxb:nxe,j,k)

con3(nxb:nxe,j,k)=eyz(nxb:nxe,j,k)\*eyz2(nxb:nxe,j,k)

con4(nxb:nxe,j,k)=exy1(nxb:nxe,j,k)\*xy(nxb:nxe,j,k)

con5(nxb:nxe,j,k)=exz1(nxb:nxe,j,k)\*xz(nxb:nxe,j,k)

con6(nxb:nxe,j,k)=eyz1(nxb:nxe,j,k)\*yz(nxb:nxe,j,k)

! calculate total strain in each loop

exy2(nxb:nxe,j,k)= exy2(nxb:nxe,j,k)+exy(nxb:nxe,j,k)

exz2(nxb:nxe,j,k)= exz2(nxb:nxe,j,k)+exz(nxb:nxe,j,k)

eyz2(nxb:nxe,j,k)= eyz2(nxb:nxe,j,k)+eyz(nxb:nxe,j,k)

! constant for loading

CH11(nxb:nxe,j,k)=1.

CH21(nxb:nxe,j,k)=1.

CH31(nxb:nxe,j,k)=1.

!constant for unloading and reloading

do i= nxb,nxe

CH1(i,j,k)=AMAX1(CH11(i,j,k),CH12(i,j,k))

CH2(i,j,k)=AMAX1(CH21(i,j,k),CH22(i,j,k))

CH3(i,j,k)=AMAX1(CH31(i,j,k),CH32(i,j,k))

! check if the calculation is in soil site ( $\mu(i,j,k) .gt. \mu\_lim$ ) and strain level exceeds the yielding strain ( $abs(exy2(i,j,k)) .gt. exyz\_lim$ ) then update shear modulus and constants in shear modulus reduction equation for 3 tangential components

if ( $abs(exy2(i,j,k)) .gt. exyz\_lim .and. \mu(i,j,k) .gt. \mu\_lim$ ) then

```

if (con1(i,j,k) .lt. 0.) then
    mu_new1(i,j,k)= mu(i,j,k)
    exy2(i,j,k)=0.
    CH12(i,j,k)=2.
else
    f_strain(i,j,k)=1./(1.+(20.*abs((exy2(i,j,k)*100.)/CH1(i,j,k)))*(1.+(10.**(-
10*abs((exy2(i,j,k)*100.)/CH1(i,j,k))))))
    mu_new1(i,j,k)= mu(i,j,k)/f_strain(i,j,k)
end if
else
    mu_new1(i,j,k)= mu(i,j,k)
end if

if (abs(exz2(i,j,k)) .gt. exyz_lim .and. mu(i,j,k) .gt. mu_lim) then
    if (con2(i,j,k) .lt. 0.) then
        mu_new2(i,j,k)= mu(i,j,k)
        exz2(i,j,k)=0.
        CH22(i,j,k)=2.
    else
        f_strain(i,j,k)=1./(1.+(20.*abs((exz2(i,j,k)*100.)/CH2(i,j,k)))*(1.+(10.**(-
10*abs((exz2(i,j,k)*100.)/CH2(i,j,k))))))
        mu_new2(i,j,k)= mu(i,j,k)/f_strain(i,j,k)
    end if
end if

```

```

else
    mu_new2(i,j,k)= mu(i,j,k)
end if

if (abs(eyz2(i,j,k)) .gt. exyz_lim .and. mu(i,j,k) .gt. mu_lim) then
    if (con3(i,j,k) .lt. 0.) then
        mu_new3(i,j,k)= mu(i,j,k)
        eyz2(i,j,k)=0.
        CH32(i,j,k)=2.
    else
        f_strain(i,j,k)=1./(1.+(20.*abs((eyz2(i,j,k)*100.)/CH3(i,j,k))*(1.+(10.**(-
10*abs((eyz2(i,j,k)*100.)/CH3(i,j,k)))))))
        mu_new3(i,j,k)= mu(i,j,k)/f_strain(i,j,k)
    end if
else
    mu_new3(i,j,k)= mu(i,j,k)
end if

enddo

50    continue

enddo

enddo

```

```

do k=1,2
  do j=1,2
    do i=1,2
      tauu=tau(i,j,k)
      tau1(i,j,k)=1/((tauu*dt1)+(1./2.))
      tau2(i,j,k)=(tauu*dt1)-(1./2.)
    enddo
  enddo
enddo

do kk= nzb,nze,kblock
  do jj= nyb,nye,jblock
    do 60 k= kk,min(kk+kblock-1,nze)
      itz = mod(((nz+1)-(coords(3)*nzt+k)),2)+1
      do 60 j= jj,min(jj+jblock-1,nye)
        ity = mod((coords(2)*nyt+j),2)+1
        itx = mod((coords(1)*nxt+nxb),2)+1
        do i=nxb,nxe
          vx1(i)=tau1(itx,ity,itz)
          vx2(i)=tau2(itx,ity,itz)
          itx = 3 - itx
        enddo
      enddo
    enddo
  enddo
enddo

```

end do

$$\begin{aligned} \text{vxl}(\text{nxb}:\text{nxe}) = & 8./(\text{lam}(\text{nxb}:\text{nxe},\text{j},\text{k}) + \text{lam}(\text{nxb}+1:\text{nxe}+1,\text{j},\text{k}) + \& \\ & \text{lam}(\text{nxb}:\text{nxe},\text{j}-1,\text{k}) + \text{lam}(\text{nxb}+1:\text{nxe}+1,\text{j}-1,\text{k}) + \& \\ & \text{lam}(\text{nxb}:\text{nxe},\text{j},\text{k}-1) + \text{lam}(\text{nxb}+1:\text{nxe}+1,\text{j},\text{k}-1) + \& \\ & \text{lam}(\text{nxb}:\text{nxe},\text{j}-1,\text{k}-1) + \text{lam}(\text{nxb}+1:\text{nxe}+1,\text{j}-1,\text{k}-1)) \end{aligned}$$
$$\text{vxm}(\text{nxb}:\text{nxe}) = 1./(\text{mu}(\text{nxb}:\text{nxe},\text{j},\text{k}))$$
$$\text{vxl}(\text{nxb}:\text{nxe}) = \text{vxl}(\text{nxb}:\text{nxe}) + 2.*\text{vxm}(\text{nxb}:\text{nxe})$$
$$\begin{aligned} \text{vqpa}(\text{nxb}:\text{nxe}) = & 0.125*(\text{qp}(\text{nxb}:\text{nxe},\text{j},\text{k}) + \text{qp}(\text{nxb}+1:\text{nxe}+1,\text{j},\text{k}) + \& \\ & \text{qp}(\text{nxb}:\text{nxe},\text{j}-1,\text{k}) + \text{qp}(\text{nxb}+1:\text{nxe}+1,\text{j}-1,\text{k}) + \& \\ & \text{qp}(\text{nxb}:\text{nxe},\text{j},\text{k}-1) + \text{qp}(\text{nxb}+1:\text{nxe}+1,\text{j},\text{k}-1) + \& \\ & \text{qp}(\text{nxb}:\text{nxe},\text{j}-1,\text{k}-1) + \text{qp}(\text{nxb}+1:\text{nxe}+1,\text{j}-1,\text{k}-1)) \end{aligned}$$
$$\begin{aligned} \text{vqsa}(\text{nxb}:\text{nxe}) = & 0.125*(\text{qs}(\text{nxb}:\text{nxe},\text{j},\text{k}) + \text{qs}(\text{nxb}+1:\text{nxe}+1,\text{j},\text{k}) + \& \\ & \text{qs}(\text{nxb}:\text{nxe},\text{j}-1,\text{k}) + \text{qs}(\text{nxb}+1:\text{nxe}+1,\text{j}-1,\text{k}) + \& \\ & \text{qs}(\text{nxb}:\text{nxe},\text{j},\text{k}-1) + \text{qs}(\text{nxb}+1:\text{nxe}+1,\text{j},\text{k}-1) + \& \\ & \text{qs}(\text{nxb}:\text{nxe},\text{j}-1,\text{k}-1) + \text{qs}(\text{nxb}+1:\text{nxe}+1,\text{j}-1,\text{k}-1)) \end{aligned}$$
$$\begin{aligned} \text{vtl}(\text{nxb}:\text{nxe}) = & \text{c1}*(\text{u1}(\text{nxb}+1:\text{nxe}+1,\text{j},\text{k}) - \\ & \text{u1}(\text{nxb}:\text{nxe},\text{j},\text{k})) + \text{c2}*(\text{u1}(\text{nxb}+2:\text{nxe}+2,\text{j},\text{k}) - \text{u1}(\text{nxb}-1:\text{nxe}-1,\text{j},\text{k})) \end{aligned}$$

$$vt2(nxb:nxe)=c1*(v1(nxb:nxe,j,k)-v1(nxb:nxe,j-1,k))+c2*(v1(nxb:nxe,j+1,k)-v1(nxb:nxe,j-2,k))$$

$$vt3(nxb:nxe)=c1*(w1(nxb:nxe,j,k)-w1(nxb:nxe,j,k-1))+c2*(w1(nxb:nxe,j,k+1)-w1(nxb:nxe,j,k-2))$$

$$vt4(nxb:nxe)=c1*(u1(nxb:nxe,j+1,k)-u1(nxb:nxe,j,k))+c2*(u1(nxb:nxe,j+2,k)-u1(nxb:nxe,j-1,k)) + \&$$

$$c1*(v1(nxb:nxe,j,k)-v1(nxb-1:nxe-1,j,k))+c2*(v1(nxb+1:nxe+1,j,k)-v1(nxb-2:nxe-2,j,k))$$

$$vt5(nxb:nxe)=c1*(u1(nxb:nxe,j,k+1)-u1(nxb:nxe,j,k))+c2*(u1(nxb:nxe,j,k+2)-u1(nxb:nxe,j,k-1)) + \&$$

$$c1*(w1(nxb:nxe,j,k)-w1(nxb-1:nxe-1,j,k))+c2*(w1(nxb+1:nxe+1,j,k)-w1(nxb-2:nxe-2,j,k))$$

$$vt6(nxb:nxe)=c1*(v1(nxb:nxe,j,k+1)-v1(nxb:nxe,j,k))+c2*(v1(nxb:nxe,j,k+2)-v1(nxb:nxe,j,k-1))$$

$$vt7(nxb:nxe)=c1*(w1(nxb:nxe,j+1,k)-w1(nxb:nxe,j,k))+c2*(w1(nxb:nxe,j+2,k)-w1(nxb:nxe,j-1,k))$$

$$vh1(nxb:nxe)=-vxm(nxb:nxe)*vqsa(nxb:nxe)$$

$$vtmp(nxb:nxe)=vxl(nxb:nxe)*(vt1(nxb:nxe)+vt2(nxb:nxe)+vt3(nxb:nxe))$$

$$val(nxb:nxe)=-$$

$$vqpa(nxb:nxe)*vxl(nxb:nxe)*dh1*(vt1(nxb:nxe)+vt2(nxb:nxe)+vt3(nxb:nxe))/2.$$

$$xx(nxb:nxe,j,k)=xx(nxb:nxe,j,k)+dth*(vtmp(nxb:nxe)-2.*vxm*(vt2(nxb:nxe)+vt3(nxb:nxe)))+dt*r1(nxb:nxe,j,k)$$

$$yy(nxb:nxe,j,k)=yy(nxb:nxe,j,k)+dth*(vtmp(nxb:nxe)-2.*vxm*(vt1(nxb:nxe)+vt3(nxb:nxe)))+dt*r2(nxb:nxe,j,k)$$

$$zz(nxb:nxe,j,k)=zz(nxb:nxe,j,k)+dth*(vtmp(nxb:nxe)-2.*vxm*(vt1(nxb:nxe)+vt2(nxb:nxe)))+dt*r3(nxb:nxe,j,k)$$

!use updated shear modulus for 3 tangential components

$$vxmu(nxb:nxe) = 1./(\mu\_new1(nxb:nxe,j,k))$$

$$vaas(nxb:nxe) = 0.5*(qs(nxb:nxe,j,k)+qs(nxb:nxe,j,k-1))$$

$$vh2\_r4(nxb:nxe)=-vaas(nxb:nxe)*vxmu(nxb:nxe)/2.$$

$$xy(nxb:nxe,j,k)=xy(nxb:nxe,j,k)+vxmu(nxb:nxe)*dth*vt4(nxb:nxe)+dt*r4(nxb:nxe,j,k)$$

$$vxmu(nxb:nxe) = 1./(\mu\_new2(nxb:nxe,j,k))$$

$$vaas(nxb:nxe) = 0.5*(qs(nxb:nxe,j,k)+qs(nxb:nxe,j-1,k))$$

$$vh2\_r5(nxb:nxe)=-vaas(nxb:nxe)*vxmu(nxb:nxe)/2.$$

$$xz(nxb:nxe,j,k)=xz(nxb:nxe,j,k)+vxmu(nxb:nxe)*dth*vt5(nxb:nxe)+dt*r5(nxb:nxe,j,k)$$

$$vxmu(nxb:nxe) = 1./(\mu\_new3(nxb:nxe,j,k))$$

$$vaas(nxb:nxe) = 0.5*(qs(nxb:nxe,j,k)+qs(nxb+1:nxe+1,j,k))$$

$$vh2\_r6(nxb:nxe)=-vaas(nxb:nxe)*vxmu(nxb:nxe)/2.$$

$$yz(nxb:nxe,j,k)=yz(nxb:nxe,j,k)+vxmu(nxb:nxe)*(dth*vt6(nxb:nxe)+dth*vt7(nxb:nxe))+dt*r6(nxb:nxe,j,k)$$

$$r1(nxb:nxe,j,k)=(vx2(nxb:nxe)*r1(nxb:nxe,j,k)-vh1(nxb:nxe)*(vt2(nxb:nxe)+vt3(nxb:nxe))*dh1+va1(nxb:nxe))* & vx1(nxb:nxe)$$

$$r2(nxb:nxe,j,k)=(vx2(nxb:nxe)*r2(nxb:nxe,j,k)-vh1(nxb:nxe)*(vt1(nxb:nxe)+vt3(nxb:nxe))*dh1+va1(nxb:nxe))* & vx1(nxb:nxe)$$

$$r3(nxb:nxe,j,k)=(vx2(nxb:nxe)*r3(nxb:nxe,j,k)-vh1(nxb:nxe)*(vt1(nxb:nxe)+vt2(nxb:nxe))*dh1+va1(nxb:nxe))* & vx1(nxb:nxe)$$

$$r4(nxb:nxe,j,k)=(vx2(nxb:nxe)*r4(nxb:nxe,j,k)+vh2_r4(nxb:nxe)*dh1*vt4(nxb:nxe))*vx1(nxb:nxe)$$

$$r5(nxb:nxe,j,k)=(vx2(nxb:nxe)*r5(nxb:nxe,j,k)+vh2_r5(nxb:nxe)*dh1*vt5(nxb:nxe))*vx1(nxb:nxe)$$

$$r6(nxb:nxe,j,k)=(vx2(nxb:nxe)*r6(nxb:nxe,j,k)+vh2_r6(nxb:nxe)*dh1*(vt6(nxb:nxe)+vt7(nxb:nxe)))*vx1(nxb:nxe)$$

$$xx(nxb:nxe,j,k)=xx(nxb:nxe,j,k)+dt*r1(nxb:nxe,j,k)$$

$$yy(nxb:nxe,j,k)=yy(nxb:nxe,j,k)+dt*r2(nxb:nxe,j,k)$$

$$zz(nxb:nxe,j,k)=zz(nxb:nxe,j,k)+dt*r3(nxb:nxe,j,k)$$

$$xy(nxb:nxe,j,k)=xy(nxb:nxe,j,k)+dt*r4(nxb:nxe,j,k)$$

$$xz(nxb:nxe,j,k)=xz(nxb:nxe,j,k)+dt*r5(nxb:nxe,j,k)$$

```
yz(nxb:nxe,j,k)=yz(nxb:nxe,j,k)+dt*r6(nxb:nxe,j,k)
```

```
60   continue
```

```
     enddo
```

```
  enddo
```

**4. Sensitivity analysis for finite difference seismic basin modeling: a case study for Kinburn basin, Ottawa, Canada**

## Abstract

We used a finite difference (FD) modeling method, developed by Olsen-Day-Cui, to simulate the viscoelastic propagation of seismic waves, in the spectral frequency range of 0.1 to 1 Hz, in the Kinburn bedrock topographic basin, Ottawa, Canada, for the Ladysmith earthquake ( $M_w=4.7$ ). We investigated the sensitivity of the ground motion simulation results to the main input parameters including the source model (seismic moment, strike, slip and dip angles, source function, slip duration), the regional path properties (crustal velocity and density model, crustal damping model, relaxation coefficients and relaxation of modulus for viscoelastic calculation) and the local site conditions (soil damping (Q) model, shear wave velocity ( $V_s$ ) contrast [ $V_{s\_soil}/V_{s\_rock}$ ]) for a small earthquake ( $M_w=4.7$ ). In addition, to investigate the sensitivity of simulation to source dimensions (point source model versus finite fault model), and soil behaviour (linear versus nonlinear soil) we scaled up the  $M_w=4.7$  to  $M_w=7$ .

Our sensitivity analysis of simulations for different seismic moments showed that the PGV values exponentially increased with moment magnitude, as expected. The fault type slightly influences the PGVs. Using a Gaussian source function with a short half duration increased the PGVs and the amplitude of velocity Fourier spectrum. Varying crustal velocity and density model influenced the arrival time of waves for simulation of a small earthquake. Thus, variation in crustal model also slightly affected the PGV and PSA and the amplitude of the velocity Fourier spectrum. Varying the crustal Q model did not significantly affect simulations. Relaxation times and relaxation coefficients for viscoelastic simulation could significantly increase the amplitude of later arrivals at a soil site, which, consequently, led to an increase in PGV and the amplitude of the PSA ratio and the velocity Fourier spectrum for a small earthquakes. Employing a small soil Q model damped a significant amount of energy of the

waves in the basin; thus, PGV, PSA of soil/rock ratios, and the velocity Fourier spectrum were dependent on soil Q model. Using high velocity contrast between soil and rock (which resulted from the employment of the small soil Vs model) increased PGVs and amplitude of PSA of soil/rock ratios while the frequency content of waves shifted toward lower frequency. Using finite fault model for a large earthquake ( $M_w = 7$ ) significantly reduced the PGV values relative to point source model. Using nonlinear-viscoelastic simulation for a large earthquake ( $M_w = 7$ ) reduced the amplitude of the latter arrivals and high frequency content of waves. Using nonlinear-viscoelastic simulation reduced the amplitude of PSA of soil/rock ratios and shifted the amplitude of PSA ratios to lower frequency.

#### **4.1. Introduction**

Earthquakes in eastern and central North America are felt for great distances, sometimes up to 1000 km away, due to the regional geological conditions that cause low anelastic seismic wave attenuation in the area (Atkinson and Mereu, 1992; Atkinson, 2004; Chapman and Godbee, 2012). Therefore, although a large earthquake has not been reported during the past decade, the occurrence of distant but moderate to large earthquakes may affect this area in the future. In intraplate regions like eastern North America, because of the low crustal deformation rates, the return periods of large earthquakes are longer than the time span covered by instrumental and historical records (Strasser et al., 2006). However, there are several paleo-seismic studies that identify disturbed deposits related to large earthquakes by studying the landslides within lake basins in eastern Canada (e.g., Adams, 1982; Shilts and Clague, 1992; Ouellet, 1997; Doughty et al., 2014; Brooks, 2015; Lajeunesse et al., 2017). Therefore, the risk of damaging earthquakes has become a matter of concern, and a detailed estimate of the seismic ground motion parameters is useful for risk mitigation and city planning for large cities in eastern North America.

There are three different groups of parameters that influence ground motion simulation in earthquake hazard analysis: earthquake source effects (seismic moment, slip distribution, stress drop distribution, fault geometry, rupture velocity, etc.), path effects (distance, depth, crustal velocity structure, near source effects, etc.) and site effects (soil type, thickness and heterogeneity, 3D basin effect, etc.).

Earthquake-related ground motions have previously been modeled for eastern Canada using different programs (e.g., Motazedian and Atkinson, 2005; Atkinson and Boore, 2007; Atkinson, 2009; Assatourians and Atkinson 2010; Khaheshi Banab et al., 2012; Atkinson and Adams, 2013; Crane and Motazedian, 2014; Atkinson and Assatourians, 2015; Crane et al., 2015; Hayek,

2016; Crane, 2016; Esmailzadeh et al., 2019). However, the uncertainties that influence the results of the models, related to source, path, and site parameters, have not been yet resolved for the study area.

Regarding the detailed estimate of the seismic ground motion parameters, over the last three decades, seismologists have introduced several analytical and numerical techniques to compute synthetic seismograms. These ground motion simulation approaches are increasingly applied to estimate reliably the ground shaking levels for past and future events. (Graves et al., 2008; Imperatori and Mai, 2012). In this study, we study the sensitivity of a physics-based ground motion simulation to source characteristics, regional path and site effects models for the case study of modeling the Ladysmith earthquake in the Kinburn basin, Ottawa, Canada.

#### **4.2. The Ladysmith earthquake**

On 17 May 2013 at 13:43 hours UTC, a magnitude  $M_w$  4.7 ( $M_N$  5.2) earthquake occurred about 4 km from the town of Ladysmith, Quebec, within the Western Quebec Seismic Zone (WQSZ) (Figure 4-1.a). The WQSZ is a seismically active region in eastern Canada, extending northwest from Montreal to the Lake Timiskaming region in Quebec as well as the Laurentians and the Eastern Ontario (as shown on the map of Figure 4-1.a) (Basham et al., 1979). Although the Ladysmith earthquake is moderate in size ( $M_w$  4.7,  $M_N$  5.2), it was one of the best-recorded earthquakes to occur in eastern Canada in recent years due to the density of the Canadian National Seismograph Network (CNSN) in western Quebec and eastern Ontario and the fortuitous deployment of several U.S. Transportable Array (USTA) stations in the region (Figure 4-1.b). We used Ladysmith recordings and source parameters based on Bent et al. (2015), Ma

and Audet (2014) and CMT (last modified 2011) to study the sensitivity of our simulations to source parameters.

### **4.3. Geographical location and geological features**

The Kinburn basin is located in the Ottawa region (in Figure 4-1.b, JSSS-JSBS stations are located in the Kinburn basin, and the OTT station is located in the city of Ottawa). This basin extends 6 km by 7 km for E-W and N-S respectively southwest of Kinburn, Ontario, approximately 40 km to the west of Ottawa. The Kinburn basin is made up of a series of smaller interconnected basins (Figure 4-2). In this research, we considered the part of the basin that was instrumented with identical seismometers and digitizers at rock and soil sites (Figure 4-2). The stations at soil site (JSSS) and rock site (JSBS) were installed in 2010 using identical equipment: Trillium 120p seismometers and Taurus digitizers. Thus, the stations allow us to compare our simulation with real records and study the sensitivity of simulation for rock and soil sites (Fulton, 1987; Richard, 1984; Medioli et al., 2010; Hunter et al., 2012; Hayek, 2016).

The basin is mostly filled with highly hydrated, low Vs, and a Holocene-age non-sensitive silt or silty clay deposit often referred to as Leda Clay. There is a thin layer of Pleistocene glacial deposits below the Leda clay sediments and directly above the bedrock surface in many locations. A Precambrian Shield ridge bounds the depression to the north and east while the southern and western parts of the basin appear to be underlain by Paleozoic rocks. The maximum depth of the Leda clay deposits in the study area is about 100 m, and the thickness of the till layer is about 30 m (Richard, 1984; Hunter et al., 2010; Hunter et al., 2012; Hayek, 2016; Crane, 2016).

#### 4.4. Kinburn basin model

The Kinburn basin model was developed and refined over several years. For this research, the Kinburn basin depth (Figure 4-3) was modeled based on 900 City of Ottawa water wells, 286 horizontal-to-vertical spectral ratio (HVSr) measurements, 2 high resolution Landstreamer seismic lines (Pugin, 2009), and a well-studied GSC logged borehole (Medioli et al., 2012). The velocity profile of the Kinburn basin (Figure 4-4) that was extracted from the well-studied borehole logging studies at a site near the deepest part of the basin was used to model the basin.

For this study, the borehole shear wave velocity-depth profile was arithmetically averaged within each mesh (25 m) of the velocity model (Figure 4-4) (For more information on the selected mesh size see section 4.5). Below soil layers, the bedrock was assigned measured velocities, estimated densities, and Q for modeling. Table 4-1 shows soil and rock properties that were used in the simulation.

We used an average constant value for the Q of P and S waves in both rock and soil sites for simplicity in the linear soil simulation, as it has been reported that Q in fine grained soils (clays/silts) is primarily independent of frequency over some bands (0.1–10 Hz). Further, we used half of  $Q_p$  as  $Q_s$  in rock sites (Shibuya et al., 1995; Rix and Meng, 2005; Crow et al., 2011). However, for the nonlinear behaviour of soil we used the Shear Modulus reduction curve for the Leda clay (Esmailzadeh et al., 2019).

The results of simulation are presented for two receivers (sites), JSBS located at rock site and JSSS at soil site (Figure 4-5), in the basin (Figure 4-2) to consider the effects of input parameters at both rock and soil sites and to verify the accuracy of simulation compared to the records.

#### 4.5. Physics-based finite difference modeling

In this study, for linear behaviour of soil, we used the finite difference (FD) code [Anelastic Wave Propagation (AWP)] developed and maintained by Kim B. Olsen, Steven M. Day, and Yifeng Cui (ODC) (Olsen, 1994; Olsen et al., 1995, 2003, 2006; Cui et al., 2009) that simulates the 3D propagation of spontaneous rupture. For the nonlinear behaviour of soil, we used the modified version of AWP-ODC (Esmailzadeh et al., 2019). The AWP-ODC program solves 3D velocity-stress wave equations with an explicit staggered-grid FD scheme. This method is fourth-order accurate in space and second-order accurate in time. The AWP-ODC code was developed for elastic, viscoelastic, elastoplastic, and visco-elasto-plastic behavior. In this study, we used the viscoelastic simulation with the available data on the Kinburn area.

Physics-based earthquake simulations depend on two basic models, the source model and the material ( both bedrock and soil) model, which represent the earthquake itself and the propagation media, respectively (Taborda and Roten, 2014).

The source model defines the characteristics of the applied forces in the formulation of the solution of the wave propagation problem. The kinematic source representation, which is a model that represents the source as a set of equivalent forces (or stresses) that trigger the propagation of seismic waves, is one of the most common approaches used in simulations. For small-magnitude earthquakes ( $M < 5$ ), the earthquake source can be modeled using a point source model, which uses a single set of self-balanced (double-couple) forces acting on a point. In this study we applied both point source and finite fault models. The point source model is defined in terms of its location (latitude, longitude, and depth), orientation (the strike, dip, and rake angles of the fault), and the evolution of the slip on the fault with time (Taborda and Roten, 2014).

The soil and rock material model is the second necessary component for physics-based earthquake simulations. It defines the geotechnical properties of the propagating media in the modeling domain. The 3D material model used for viscoelastic wave propagation simulation defines the material density ( $\rho$ ), crustal and soil seismic velocities for P and S waves ( $V_p$  and  $V_s$ , respectively), and rock and soil attenuation properties, which are described by damping factors of P and S waves ( $Q_p$  and  $Q_s$ , respectively) (Taborda and Roten, 2014).

The AWP-ODC program requires at least four samples per wavelength for modeling a wave. Thus, based on the minimum soil velocity used in the velocity model (178 m/s associated with the shear wave velocity at the top of the basin) and the maximum frequency of interest, 1.0 Hz, the grid size or spatial step ( $dh$ ) is 25 m. Then, based on the maximum rock wave velocity,  $V_p=6200$  m/s, in crustal model, and the Courant number for the stability of the FD method, the time step for simulation is calculated as follows:

$$dt < 0.5 * dh / V_{max} \quad (1)$$

Consequently, for simulations we used  $dt=0.0016$  to ensure about the stability of the program.

There are two options available for the boundary conditions of simulation, the Cerjan method (using the sponge zone of artificial attenuation) and the perfect match layer (PML) method. Previous studies show that the PML method is more effective than the Cerjan method in absorbing waves at the boundary of a model, particularly in 3D simulations; thus, PML is employed in this modeling (Marcinkovich and Olsen, 2003; Liu, 2013).

According to previous studies (e.g., Olsen et al., 1995, 2003, 2006; Cui et al., 2009; Roten et al., 2016), the staggered-grid FD scheme reproduces features at both short and long offsets. Thus, it can simulate normal incidence reflections and multiples, converted shear waves, head

waves, reflected head waves, and Rayleigh waves. The advantages of the staggered-grid method lie in its stability and accuracy for modeling large Poisson ratio materials and mixed acoustic-elastic media and in the ease with which sources can be inserted at and near the free surface. This code is particularly useful for modeling near-surface problems and for amplitude-offset studies in laterally varying media (Levander, 1988; Yao and Margrave, 1999).

#### 4.6. Sensitivity of the viscoelastic simulation to source parameters

To study the sensitivity of the viscoelastic simulation, we used the focal mechanisms proposed by Bent et al. (2015), Ma and Audet (2014) and CMT (last modified 2011) for the Ladysmith earthquake. Table 4-2 presents the details of the proposed focal mechanism.

In this study we use both semi-triangular and Gaussian source functions. However, in this section we focus on semi-triangular function to model the evolution of the slip with time on the point source fault. The sensitivity to Gaussian source function will be discussed in later sections. The semi-triangular function is defined as follows:

$$m(t) = M_0 \left( \frac{t}{t_p} \right) \exp\left(-\frac{t}{t_p}\right) \quad (2)$$

where  $m(t)$  is the variation of the seismic moment with time,  $M_0$  is the total seismic moment of an earthquake,  $t$  is time in second, and  $t_p$  is the time associated with the maximum of seismic moment (or half duration of an earthquake in second) (Duputel et al., 2013). We used the scaling relation (Equation 3) used in WCMT inversions to predict the half-duration of a given seismic moment  $M_0$  (in dyne-cm).

$$t_p = 1.2 * 10^{-8} * M_0^{1/3} \quad (3)$$

This equation predicts a half-duration of about  $t_p=0.6$  s. Thus, we used  $t_p=0.6$  s to model the earthquake for all simulations.

The velocity time series for simulations and the recorded values were filtered with a 12-pole casual Butterworth bandpass filter between 0.1 and 1.0 Hz, which was an acceptable frequency range for simulation according to the available computational facilities and feasibility of simulation. This filter was designed using the Signal Processing Toolbox for MATLAB (Simulink).

Comparisons of the modeled velocity time series and associated Fourier spectrum from three simulations and the real records at rock site are shown in Figure 4-6. The main objective at this step is to investigate the different focal mechanisms proposed by different researchers. The PGV of rock site in the real record was  $1.14\text{E-}4$  m/s for the east-west (E-W) component, while the PGVs of simulations with focal mechanisms proposed by Bent et al. (2015), Ma and Audet (2014) and CMT (last modified 2011) were  $7.7\text{E-}5$  m/s for the E-W component,  $1.51\text{E-}4$  m/s for vertical component, and  $1.42\text{E-}4$  m/s for the E-W component, respectively. The amplitude of the Fourier spectrum of the velocity time series for the real record at rock site was  $7.59\text{E-}2$  m at a frequency of 0.9 Hz, which is along the E-W component, while the amplitudes of the Fourier spectrum of the simulated time series were  $6.75\text{E-}2$ ,  $9.83\text{E-}2$ , and  $1.56\text{E-}1$  m for the Bent et al. (2015), Ma and Audet (2014) and CMT (last modified 2011) focal mechanisms, respectively. It should be noted that rock site receiver (JSBS) is surrounded with 10 m thickness soil thus the ringing effects in the record (Figure 4-6) might result from the surrounding soil, while the 10 m soil thickness cannot be modeled due to the mesh size (25 m). Further, the rock site is located completely over rock velocity model and therefore there is no ringing within the simulated velocity time series. The uniform rock velocity model that was used for simulation might contribute in the discrepancy between record and simulation at rock site.

Figure 4-7 compares the filtered, modeled velocity time series and related Fourier spectrum to the filtered, recorded velocity time series and associated Fourier spectrum at soil site. The difference between the modeled time series and recordings is large. Although 3D geometry was carried out in simulation, the input parameters came from the only borehole available in the basin, and that borehole only had 1D information. Consequently, there was no 3D information for  $V_s$ ,  $V_p$ ,  $Q_s$ ,  $Q_p$ , and density. Thus, the large differences between the real records and simulation could be attributed to the 3D heterogeneities in the geotechnical and geophysical parameters (including seismic velocities, density,  $Q_p$ ,  $Q_s$ ) in comparison to the simplified geometry, and a grid size of 25 m that was used in simulation that could not accurately model all of the details. These parameters cause different resonances of seismic waves in the basin, focusing/defocusing, and basin edge generated surface waves (Hunter et al., 2010). Furthermore, the comparison between velocity Fourier spectrum of records and simulations shows that the discrepancy mainly is at low frequency thus the increase of seismic moment might improve the result of simulations in comparison to records. Also, our studies showed that the source function could influence on the accuracy of simulations relative to records (are described below).

The PGV of the recording at soil site was 0.0016 m/s for the north-south (N-S) component. However, the PGVs of simulations at soil site for the focal mechanisms proposed by Bent et al. (2015), Ma and Audet (2014) and CMT (last modified 2011) were  $5.05E-4$  for the N-S component,  $6.34E-4$  for the N-S component, and  $8.4E-4$  for the E-W component, respectively. Comparing the Fourier spectrum of the real record to the simulated velocity time series using the three focal mechanisms at soil site showed that the amplitude of the Fourier spectrum of the record was 2.42 m, while the amplitude of the Fourier spectrum of simulations were  $8.48E-1$ ,

1.53, and 1.56 m for the Bent et al. (2015), Ma and Audet (2014) and CMT (last modified 2011) focal mechanisms, respectively. Although there was a difference between the amplitudes of the simulated time series and associated Fourier spectrum and those of the recorded time series for all three components in all three simulations at soil site, the focal mechanism proposed by Ma and Audet (2014) simulated the Ladysmith earthquake for the Kinburn basin for both soil and rock sites better than the others based on the predicted PGVs of simulations and the shape and amplitude of the Fourier spectrum of the velocity time series for each component. Thus, the focal mechanism of Ma and Audet (2014) was used for below simulations in this study.

#### **4.6.1. Sensitivity to M<sub>0</sub>, using a point source model**

To investigate the sensitivity of the viscoelastic simulation to the seismic moment (M<sub>0</sub>) for small and large earthquakes (using a point source model in this section), we scaled the moment magnitude of the Ladysmith earthquake to 5.0, 5.5, 6.0, 6.5, and 7 using equation 4, the relation between the moment magnitude and seismic moment (Bormann and Giacomo, 2011; IASPEI, 2005; Bormann et al., 2002):

$$M_w = (\log M_0 - 9.1)/1.5 \quad (4)$$

There are many different methods in time and frequency domains for scaling a small earthquake to a large earthquake (IASPEI, 2005; Hanks and Kanamori, 1979; etc.). For this study, we investigated the sensitivity of the viscoelastic simulation to M<sub>0</sub>, and therefore, a standard method of scaling served our purpose (Bormann and Giacomo, 2011; IASPEI, 2005; Bormann et al., 2002). Table 4-3 shows the calculated M<sub>0</sub> associated with each moment magnitude (M<sub>w</sub>).

We used the comparison of the PGVs associated with different M<sub>w</sub>. Figure 4-8 shows that the PGV increases approximately linearly as M<sub>0</sub> increases at rock site on logarithmic axes. Also,

comparing the PGVs of simulations at soil site (Figure 4-8) shows a linear increase in the PGVs as  $M_0$  increases on logarithmic axes. The relationship between  $M_w$  and the PGVs at rock and soil sites, using linear- viscoelastic simulation in this section, can be described as  $PGV_{rock} = 1E-11e^{3.4747*M_w}$  and  $PGV_{soil} = 7E-11e^{3.4695*M_w}$ , respectively.

Previous research indicates that nonlinearity is typically only identified for large earthquakes with particularly strong shaking (with threshold of approximately 100 Gal). In addition to strong shaking, a compliant medium (i.e., soil or soft rocks) is a necessary condition for a nonlinear site response (Rubinstein, 2011; Beresnev and Wen, 1996). As the nonlinear behaviour of soil is not well captured in the viscoelastic simulation (this section), a modification has been applied to the program to model the nonlinear soil, and results has been analyzed and discussed in Esmaeilzadeh et al., 2019. The sensitivity of simulations to nonlinear soil behavior will be considered in a later section (section 4.8.3) for an earthquake with moment magnitude 7.

Furthermore, using a finite fault model to simulate an earthquake with  $M_w=7$  was necessary to predict realistically the stresses and strains that were generated in the basin. Thus, we studied the sensitivity of simulations for point source versus finite fault source in a later section (section 4.6.5) for magnitude 7 as well.

Comparing the amplitudes of velocity Fourier spectrum of the simulated velocity time series at rock site for different  $M_w$  (Figure 4-9) showed that the amplitude of velocity Fourier spectrum increased as  $M_w$  increased. Also, the amplitude of the velocity Fourier spectrum occurred in the E-W component.

Figure 4-9 shows that the amplitude of the velocity Fourier spectrum of the modeled velocity time series at soil site increased as the  $M_w$  increased. In addition, the amplitude of velocity Fourier spectrum happened in the E-W component for all simulations.

The increase in amplitudes of the velocity Fourier spectrum at rock site and soil site is at almost the same rate. However, the amplitude at soil site was almost 10 times greater than the amplitude at rock site for all Mw.

The PSA ratio of soil site to rock site for different Mw (Figure 4-10) shows the amplification at soil site for all Mw and in all three components, and that the PSA ratio diagram is the same for all Mw. Thus, for all Mw, the amplitudes of the PSA ratios for the E-W, N-S, and vertical components are 18.6, 27.3, and 3.1, respectively.

It should be noted that the nonlinear soil effect is not considered in this section. Thus the effects of nonlinear soil behavior on the frequency content of waves and PSA ratios will be considered later (section 4.8.3).

#### **4.6.2. Sensitivity to strike and dip angles**

As shown in Table 4-2, there are two fault plane solutions available for the Ladysmith earthquake associated with each proposed focal mechanism. We used fault plane 1 for all previous viscoelastic simulations. To study the effects of the fault plane parameters on the viscoelastic simulation, we compared simulation from fault plane 1 with the modeled wave propagation using fault plane 2 of the Ma and Audet (2014) proposed focal mechanism for the Ladysmith earthquake. Using different strike and dip angles we studied the effects of radiation pattern on the simulations. The consideration of radiation pattern is specifically important for accurate prediction of phase and amplitude of arrivals for each component.

The simulated velocity time series (Figure 4-11.a) and associated velocity Fourier spectrum (Figure 4-11.b) resulting from fault plane 1 and fault plane 2 for Mw=4.7 showed a similar amplitude and phase at rock site, even though the PGV of all three components of fault plane 1 were slightly smaller than the PGVs of fault plane 2, and there were some small discrepancies in

later arrivals. The velocity Fourier spectrum at rock site associated with fault plane 1 and fault plane 2 were almost the same, while the amplitude of the velocity Fourier spectrum related to fault plane 2 was about 10% greater than the amplitude related to fault plane 1.

Similarly, there was a small difference between simulation results using fault plane 1 and those using of fault plane 2 at soil site (Figure 4-12). The amplitude of the velocity time series (Figure 4-12.a) decreased from 8.56E-4 m/s for fault plane 1 to 6.75E-4 m/s for fault plane 2. In addition, the amplitudes of the velocity Fourier spectrum (Figure 4-12.b) of simulations associated with fault plane 1 and fault plane 2 are at 0.8 Hz, which was the natural frequency of basin; further, the amplitude of the velocity Fourier spectrum for fault plane 1 was 26% more than the amplitude for fault plane 2. The discrepancy in soil site can be described by the differences in the components of incident waves that will be generated using different fault planes.

The PSA ratios of soil site to rock site for fault plane 1 and fault plane 2 (Figure 4-13) showed that the amplitude of the PSA of soil to rock ratio resulting from fault plane 2 was smaller than the amplitude of the PSA ratio resulting from fault plane 1 by factor of about 25% for horizontal components and 50% for vertical component.

#### **4.6.3. Sensitivity to the source functions**

An earthquake source function defines the evolution of the slip on the fault with time (Taborda and Roten, 2014). Thus, it plays an important role in simulation of an earthquake. We used a semi-triangular function (Equation 2) for all the previous simulations.

To consider the effects of the source function, we also used Gaussian function (Equation 5) to model the Ladysmith earthquake source:

$$M(t) = \frac{M_0}{\sqrt{2\pi\sigma^2}} e^{-\frac{(t-\mu)^2}{2\sigma^2}} \quad (5)$$

where  $M(t)$  is the seismic moment as a function of time,  $M_0$  is the total seismic moment,  $\mu$  is the mean of the distribution (or half duration of an earthquake, which is equal to  $4\sigma$  in the code that we used), and  $\sigma$  is the standard deviation of the distribution.

A comparison of the simulated velocity time series (Figure 4-14.a) showed that the PGV at rock site for  $M_w=4.7$  using a Gaussian source function was about nine times greater than the PGV of semi-triangular simulation, even though for both source functions, the PGV happened at the E-W component. The big difference between PGVs of simulations for Gaussian source function and semi-triangular function can be attributed to the slip duration of the source function. In Gaussian source function the total slip duration is a function of half duration (total slip duration =  $2 \times$  half duration) thus using a short half duration will significantly increase the amplitude of generated stress at source while for semi-triangular source function the half duration is only a portion of total slip duration. Our previous studies show that an increase in the half duration for Gaussian source function will reduce the PGVs of simulation to the level of the PGVs of simulation related to semi-triangular function (Esmaeilzadeh et al., 2019). As shown in Figure 4-14.b, the amplitude of the velocity Fourier spectrum associated with Gaussian source function simulation was seven times greater than the velocity Fourier spectrum related to semi-triangular function modeling. Further, the maximum velocity Fourier spectrum is in vertical component for Gaussian source function and in the E-W component for semi-triangular source function, and they happened at 0.9 Hz and 0.14 Hz for Gaussian and semi-triangular source functions, respectively.

Figure 4-15.a shows that the PGV of the simulated time series at soil site for  $M_w=4.7$  using Gaussian source function is  $9.02E-3$  m/s, while the PGV of semi-triangular source function is  $8.56E-4$  m/s. The maximum velocity Fourier spectrum related to Gaussian source function

(Figure 4-15.b) is 15.2 m and to semi-triangular source function (Figure 4-15.b) is 1.5 m, both of which is at 0.8 Hz.

Comparing the PSA ratios of soil site to rock site for  $M_w=4.7$  (Figure 4-16) shows that in all three components the amplitudes of the PSA ratios of simulation of Gaussian function are smaller than the amplitudes of the PSA ratios of simulation of semi-triangular function although the frequency of the amplitudes of the PSA ratios of simulations for both source functions are the same. In addition, the amplitudes of the PSA ratios are in the N-S component for both simulations, while the amplitude of the PSA ratio of simulation of Gaussian source function was about 15% smaller than that of simulation of semi-triangular source function.

The incident waves with long duration and large amplitude of latter arrivals that generated by semi-triangular function could be the main reasons which the amplitude of PSA ratio of simulation for semi-triangular function is greater than the amplitude of PSA ratio of the or simulation of Gaussian function.

#### **4.6.4. Sensitivity to the slip duration**

Our studies showed that the slip duration in semi-triangular source function did not significantly influence the results of simulations. However, simulations that used Gaussian source function were affected by the slip duration. Thus, we used a Gaussian source function to study the effects of the slip duration on the ground motion simulations.

As described in Equation 5, the half duration (half of the slip duration) of an earthquake in Gaussian source function is defined as  $hd = 4 * \sigma$ , where  $\sigma$  is the standard deviation of distribution. We used  $hd=0.6$ , which was the actual half duration of the Ladysmith earthquake and  $hd=1.6$ , which was based on the comparison of simulations and records and gave the best results at soil site.

The comparison of simulations using a half duration of 0.6 s and 1.6 s with Gaussian source function at rock site (Figure 4-17.a) showed that the PGV of simulation that used  $hd=1.6$  s was almost 3 times smaller than the PGV of simulation with  $hd=0.6$  s. Furthermore, using  $hd=0.6$  s increased the amplitude of the velocity Fourier spectrum (by a factor of about 3) and the frequency content of simulation for a higher frequency (Figure 4-17.b) relative to simulation that used  $hd=1.6$  s. Thus, the amplitude of the velocity Fourier spectrum for  $hd=0.6$  s and  $hd=1.6$  s are at 0.92 Hz and 0.15 Hz, respectively.

Figure 4-18.a shows that using  $hd=0.6$  s increased the PGV of simulation by a factor of 7.5 at soil site compared to simulation that used  $hd=1.6$  s. Also, the amplitude of the velocity Fourier spectrum for the source function using  $hd=1.6$  s decreased by a factor of 6 relative to simulation that used  $hd=0.6$  s (Figure 4-18.b). In addition, the frequency associated with the amplitude of the velocity Fourier spectrum slightly shifted toward a lower frequency for simulation with  $hd=1.6$  s.

Comparing the PSA ratios of soil site to rock site using half durations of 0.6 s and 1.6 s (Figure 4-19) showed that the amplitude of the PSA ratio for  $hd=1.6$  s was greater (by about 18%) than the amplitude of the PSA ratio for  $hd=0.6$  s only in N-S component, while in the other two components, the amplitude of the PSA ratio for  $hd=1.6$  s was slightly smaller than the amplitude of the PSA ratio for  $hd=0.6$  s.

#### **4.6.5. Sensitivity to geometry of source (point source versus finite fault source)**

Large earthquakes ( $M_w 7.0+$ ) occur over a finite fault and cannot be treated as a point source. Thus, to model a large earthquake using a finite fault model, the fault plane is discretized into small independently rupturing subfaults (Hartzell, 1978; Irikura, 1983; Joyner and Boore, 1986; Heaton and Hartzell, 1986; Somerville et al., 1991; Tumarkin and Archuleta, 1994; Zeng

et al., 1994; Beresnev and Atkinson, 1998a; Beresnev and Atkinson, 2002; Motazedian and Atkinson 2005).

To study the sensitivity of simulations for the point source versus finite fault source we scaled the earthquake magnitude to  $M_w=7$  using equation 4 for both simulations. For point source simulation, we used a point source semi-triangular function as it was described in equation 2. For finite fault simulation we used a fault plane equal to  $900 \text{ km}^2$  (45 km by 20 km) using Wells and Coppersmith equations, 1994. Since there was not a real large earthquake, we used a simplified finite fault model that assumed all sub faults behave similarly and simultaneously rupture; also, we assumed that the center of the fault plane was the hypocenter of the earthquake (Crouse, 1991). It should be mentioned that source directivity effects cannot be considered in this study because all sub faults rupture simultaneously, however the source dimensions effects is considered using this finite model. Figure 4-20 shows the 3D view of the sub-faults that were used for the finite fault simulations described below. Each sub-fault is 5 km by 5 km, as shown in Figure 4-20. The strike, dip, and rake associated with the focal mechanism proposed by Ma and Audit (2014) for the Ladysmith earthquake (Table 4-2) were used for both point source model and finite fault model.

Comparison between simulated velocity time series at rock site (Figure 4-21.a) shows that the PGV of the point source simulation is about 4.6 times greater than the finite fault simulation. Further, the PGV is at E-W component for both of point source simulation and finite fault simulation. Also, comparison between velocity Fourier spectrum of simulations using point source model and finite fault model (Figure 4-21.b) shows the frequency content for simulation related to finite fault model slightly shifted toward lower frequency and the amplitude of velocity

Fourier spectrum of finite fault simulation is 4.6 times smaller than the amplitude for point source simulation.

Figure 4-22.a shows that the PGV of both point source simulation and finite fault simulation for soil site is at E-W component while the PGV of point source simulation is 2.3 times greater than the PGV of finite fault simulation. In addition, Figure 4-22.b shows that the amplitude of velocity Fourier spectrum of soil site for point source simulation is 2.3 times greater than the amplitude of soil site for finite fault simulation while the amplitude is in E-W component and at the frequency of 0.8 Hz for both simulations.

Comparison between PSA ratio for point source simulation and finite fault simulation (Figure 4-23) shows that both simulations predicted similar amplitude of PSA ratios for E-W and vertical components although the PSA ratio of finite fault simulation is greater of PSA ratio of point source simulation for almost all frequencies. The amplitude of PSA ratio of N-S component for finite fault simulation is almost twice of the amplitude of PSA ratio of N-S component of point source simulation.

#### **4.7. Sensitivity to the regional path parameters**

##### **4.7.1. Sensitivity to crustal $V_s$ , $V_p$ and density model of rock**

There are many studies on crustal model for Eastern Canada using a wide variety of techniques (e.g., Motazedian et al., 2013; Ma et al., 2013). Motazedian et al. (2013) proposed a crustal shear velocity model for eastern North America using the average over many techniques (Table 4-4). Table 4-4 shows crustal model used in previous simulations, crustal model 1 (Burger et al. 1987; Hunter et al., 2010) and crustal model 2 (Burger et al. 1987; Motazedian et al., 2013), which is used in this new simulation. For crustal model 2, the primary wave (P-wave) velocity

value in each layer was calculated using Poisson's ratio ( $V_p=V_s1.732$ ). In addition, the density corresponding to the secondary wave (S-wave) velocity value in each layer was calculated following the Nafe–Drake relation ( $V_p$  is in km/s) (Ludwig et al., 1970; Motazedian et al., 2013; Ma et al., 2013):

$$\rho = 1.6612V_p - 0.4721V_p^2 + 0.0671V_p^3 - 0.0043V_p^4 + 0.000106V_p^5 \quad (6)$$

To study the sensitivity of the program to the employed crustal model for simulation, we used crustal model 1 (Burger et al. 1987; Hunter et al., 2010) and crustal model 2 (Burger et al. 1987; Motazedian et al. 2013) as described in Table 4-4. It should be noted that all crustal model parameters ( $V_s$ ,  $V_p$ , Density,  $Q_p$ , and  $Q_s$ ) in crustal model 1 (Burger et al. 1987; Hunter et al., 2010) are constant in the crust. Comparing the synthetic velocity time series at rock site (Figure 4-24.a) for  $M_w=4.7$  using crustal model 1 and crustal model 2 showed that crustal model 2 reduced the PGV of the E-W, N-S, and vertical components by factors of 42%, 29%, and 56%, respectively. Furthermore, as shown in Figure 4-24.b, the frequency related to the amplitudes of the velocity Fourier spectrum of the E-W and vertical components for simulation that used crustal model 2 shifted toward a higher frequency compared to simulation that used crustal model 1; also, the frequency associated with the amplitude of the velocity Fourier spectrum of the N-S component for simulation that used crustal model 2 was smaller than the frequency related to the amplitude of the velocity Fourier spectrum of the N-S component in simulation that used crustal model 1. Also, using crustal model 2 in simulation reduced the amplitudes of the velocity Fourier spectrum for all three components by factors of 27%, 19%, and 29% for the E-W, N-S, and vertical components, respectively, compared to simulation that used crustal model 1. The differences in the incident waves in the basin caused differences in the synthetic velocity time series in the basin. Particularly, crustal model 2 includes multiple layer compared to the

uniform rock used in crustal model 1, thus less energy reached to the basin in simulation used crustal model 2 because of the more reflections that happened at the layers boundary.

As shown in Figure 4-25.a, using crustal model 2 in simulation for  $M_w=4.7$  at soil site reduced the PGVs of the E-W and vertical components by a factor of about 50%, while the PGV of the N-S component decreased by a factor of 18% relative to simulation that used crustal model 1. Furthermore, the frequency content of simulation that used crustal model 2 shifted toward a lower frequency (Figure 4-25.b). In addition, using crustal model 2 reduced the amplitudes of the velocity Fourier spectrum at soil site (Figure 4-25.b) by a factor of 28% and 36% for the E-W and vertical components, respectively, and increased the amplitude of the velocity Fourier spectrum of the N-S component by a factor of 17%.

Moreover, in both rock (Figure 4-24.a) and soil (Figure 4-25.a) sites, the arrival times were noticeably reduced in simulation that used crustal model 2 compared to simulation that used crustal model 1. This phenomenon can be attributed to the high velocity that were used for the deep layers in crustal model 2.

Comparing the PSA ratios of simulations ( $M_w=4.7$ ) using crustal model 1 and crustal model 2 (Figure 4-26) shows that using crustal model 2 increased the PSA ratios of the E-W and vertical components by factors of 20% and 28%, respectively, while the amplitude of the PSA ratio of the N-S component decreased by a factor of 40% relative to simulation using crustal model 1.

#### **4.7.2. Sensitivity to crustal damping**

Burger et al. (1987) used smaller  $Q_s$  for shallow rock and large values for  $Q_p$  for deep rock. To study the effects of crustal damping factor ( $Q$ ) model on simulations, we used  $Q_s=500$ ,  $Q_p=1000$  (crustal  $Q$  model 1) which already were used for previous simulations and  $Q_s=475$ ,

$Q_p=2375$  (crustal Q model 2). Thus, the ratio of  $Q_p/Q_s$  increased from 2 (using crustal Q model 1) to 5 (in crustal Q model 2). Table 4-5 shows the seismic characteristics of rock site that we used in simulations.

Comparing the simulated velocity time series for the models that used crustal Q model 1 and crustal Q model 2 for  $M_w=4.7$  at rock site (Figure 4-27.a) shows that the Q models did not have any noticeable effects on the simulated time series, and thus, the synthetic time series related to simulations of crustal Q model 1 and crustal Q model 2 are almost the same. Figure 4-27.b shows that the velocity Fourier spectrum diagrams associated with simulations which used crustal Q model 1 and crustal Q model 2 at rock site are the same as well. Consequently, the simulated velocity time series (Figure 4-28.a) and associated velocity Fourier spectrum (Figure 4-28.b) for simulations that used crustal Q model 1 and crustal Q model 2 at soil site show the same results. In addition, the PSA ratios for both simulations (Figure 4-29) show the same diagram.

#### 4.7.3. Sensitivity to relaxation coefficients, and relaxation of modulus

To incorporate the effects of viscosity into the time-stepped numerical simulations of wave propagation, the AWP-ODC program solves the following stress-strain equation:

$$\sigma(t) = \mu u [\varepsilon(t) - \sum_{i=1}^N \xi_i(t)] \quad (7)$$

where  $\xi_i$ ,  $i=1 \dots N$  are internal or memory variables that evolve with time,  $N$  is the number of relaxation terms in the approximation,  $\mu u$  is the unrelaxed shear modulus,  $\sigma(t)$  is stress as a function of time, and  $\varepsilon(t)$  is strain as a function of time.  $N$  in equation 7 should be equal to 8 for a 3D simulation. The memory variables are approximated by solving the  $N$  first order of the following differential equation:

$$\tau_i = \frac{d\xi_i(t)}{dt} + \xi_i(t) = \lambda_i \frac{\delta M}{\mu u} \varepsilon(t) \quad (8)$$

To solve the differential equation, we calculate  $\tau_i$ ,  $\lambda_i$ , and  $\delta M$ , which are the relaxation times, relaxation coefficients, and the relaxation of the modulus, respectively. In the conventional memory variables approach for a 3D simulation,  $\lambda_i \frac{\delta M}{Mu}$  is assumed as the relaxation coefficient ( $\lambda_i$ ).  $2N$  values of  $\tau_i$  and  $\lambda_i$  are chosen in such a way that equation 9 is a good approximation of the target  $Q^{-1}(\omega)$ :

$$Q^{-1}(\omega) \approx \frac{\delta M}{Mu} \sum_{i=0}^N \frac{\lambda_i \omega \tau_i}{\omega \tau_i + 1} \quad (9)$$

Day (1998) set the relaxation coefficient to 1 and uniformly distributed the relaxation times over the logarithmic axis between the lower and upper absorption-band cutoffs using the below equation:

$$\ln \tau_k = \ln \tau_m + \frac{2k-1}{16} (\ln \tau_M - \ln \tau_m) \quad (10)$$

The lower and upper absorption-band cutoffs are represented by  $\tau_m$  and  $\tau_M$ , respectively, and calculated  $\tau_m = \omega_n^{-1}$  and  $\tau_M = 5N_t \omega_n^{-1}$ , where  $N_t$  is the total number of time steps in the computation (Day and Minster, 1984; Day, 1998; Day and Bradly, 2001; Graves and Day, 2003; Liu and Archuleta, 2006). This method could approximately, but not optimally, model the viscoelastic behavior of seismic waves (Day and Bradly, 2001).

There are many studies (e.g., Lanzo et al., 1997; Zekkos et al., 2006; Díaz-Rodríguez et al., 2008; El Mosallamy, 2016) that showed even small strains could cause a small modulus reduction. Furthermore, our simulation showed that the resulting strains from the Ladysmith earthquake slightly exceeded the nonlinear yielding strain level of clay ( $10^{-6}$ ) at some points in soil sites.

Thus, to consider the effect of the approximation that was used in the viscoelastic simulation, we adopted the approximation by calculating the modulus deficit ( $\delta M/Mu$ ) and relaxation coefficients ( $\lambda_i$ ) at each time step of simulation. The relaxation times were calculated using the

same method as that of the regular viscoelastic simulation. The relaxation coefficients were defined as a function of the modulus deficit so that equation 9 would be a good approximation of the target  $Q^{-1}(w)$ . The modulus deficit was calculated using a modulus reduction curve. In this research, we used the modulus reduction equation proposed by Seed et al. (1970), which was described as follows (Rollins et al., 1998):

$$\frac{M}{Mu} = \frac{1}{1+20\varepsilon(1+10^{-10\varepsilon})} \quad (11)$$

where  $M$  is the modified shear modulus calculated at each time step,  $Mu$  is the preliminary value of the shear modulus ( $Mu=Vs*\rho$ ), and  $\varepsilon$  is strain. Thus, the relaxation coefficient and modulus deficit ( $\delta M/Mu$ ) are updated at each time step. The calculated relaxation times, relaxation coefficients, and modulus deficit are used to calculate the memory variables at each time step of simulation.

Therefore, to consider the sensitivity of simulations to relaxation coefficients and relaxation of modulus, we compared simulation that used simplified approximation of viscoelastic calculation proposed by Day (1998) (memory variables model 1) with a modeling which used adopted approximation of viscoelastic calculation (memory variables model 2) as described above.

Comparing the modeled velocity time series associated with the viscoelastic simulations that used memory variables model 1 and memory variables model 2 at rock site (Figure 4-30.a) shows that the PGV and modeled velocity time series are almost the same for both simulations as there is no modulus reduction at rock site. Further, Figure 4-30.b shows that the velocity Fourier spectrum diagram at rock site for the viscoelastic simulation that used memory variables model 1 and memory variables model 2 are the same as well.

In contrast, the comparison of the simulated time series related to the viscoelastic simulations that used memory variables model 1 and memory variables model 2 at soil site (Figure 4-31.a) shows that the PGVs of the E-W and vertical components increased by a factor of about 16%, and the PGV of the N-S component increased by a factor of 45% using the memory variables model 2. Furthermore, the amplitude of later arrivals increased in the viscoelastic simulation which used memory variables model 2, particularly in horizontal components. In addition, Figure 4-31.b shows that the amplitudes of the velocity Fourier spectrum increased by factors of 12%, 10%, and 33% for the E-W, N-S, and vertical components using the memory variables model 2.

Comparing the PSA ratios for the viscoelastic simulation used the memory variables model 1 and the viscoelastic simulation used the memory variables model 2 (Figure 4-32) shows that the amplitudes of the PSA ratio of all three components increased by factors of 22%, 40%, and 5% for the E-W, N-S, and vertical components, respectively, in the viscoelastic simulation that used the memory variables model 2.

#### **4.8. Sensitivity to local soil/site conditions**

##### **4.8.1. Sensitivity to soil Q model**

The velocity model of soil site described in Table 4-1 is the best available velocity model for the Kinburn basin; however, to improve simulation, we employed a damping factor (Q factor), proposed by Crow et al. (2011), of soils associated with shear waves for the Ottawa area. Crow et al. (2011) proposed two sets of soil Q factors based on different methods. We used the greater Q factors for previous simulations (Table 4-1). To study the sensitivity of simulation to the Q factor of soil, we employed the large damping factor values (soil damping factor (Q) model 1 in Table 4-6) for soil Q model 1 and we used small damping factor (soil damping factor (Q) model 2

in Table 4-6) for soil Q model 2. Table 4-6 presents the  $Q_s$  and  $Q_p$  for soil site that were used in simulations. In addition,  $Q_p$  of each layer was assumed to be  $1.5Q_s$  for each associated layer.

Comparing the modeled velocity time series for  $M_w=4.7$  at soil site (Figure 4-33) showed that using soil Q model 2 reduced the PGVs by factors of 14%, 34%, and 20% for the E-W, N-S, and vertical components, respectively. Also, the amplitudes of the velocity Fourier spectrum decreased by factors of 25%, 35%, and 40% for the E-W, N-S, and vertical components, respectively, for simulation that used soil Q model 2. However, the frequency associated with the amplitudes of the velocity Fourier spectrum was the same for both soil Q model 1 and soil Q model 2.

As shown in Figure 4-34, using soil Q model 2 reduced the PSA in all three components. The amplitudes of the PSA ratios associated with soil Q model 2 decreased by factors of 12%, 33%, and 21% for the E-W, N-S, and vertical components, respectively, compared to the soil Q model 1.

#### **4.8.2. Sensitivity to $V_s$ contrast ( $V_{s\_soil}/V_{s\_rock}$ )**

The product of density and wave propagation velocity is the specific seismic impedance that influences the behavior of waves at the interface of the layers. The ratio of the specific seismic impedances for two mediums is called seismic impedance ratio ( $\rho_2 v_2 / \rho_1 v_1$ ) (Kramer 1996). Due to the seismic impedance contrast between the sediments in a basin and bedrock, the seismic waves that propagate in the basin are reflected back and forth between the free surface and the underlying seismic impedance boundary at soil-bedrock interface, which leads to the trapping of seismic waves in the low velocity soil zone.

The high seismic impedance contrast between the basin and the bedrock is one of the controlling factors in the amount of the trapped energy in the basin. Maximum resonance arises

when interference of these trapped reverberating waves are in phase with one another. Thus, resonance is frequency dependent and related to the density, damping and wave velocities of a soil (Kramer 1996, Hartzell et al. 2004, Pitilakis 2004, Hunter et al. 2007, Hunter and Crow 2012, Qin et al. 2012).

Past geological studies in the Ottawa area have proven the existence of soft soil with a low velocity over stiff bedrock with a high velocity; this unusual seismic impedance contrast leads to unusual soil amplification, at least for the weak motions (Hunter et al. 2007, Motazedian et al. 2010). Further, numerical computations show that the strong seismic impedance contrast between the sediments and the surrounding bedrock produces a strong amplification regardless of the basin geometry. The sensitivity of simulation to soil Q model was considered above. Here we studied the effects of the Vs contrast on the ground motion simulation. We used the relationship between average shear wave velocity ( $V_{s_{ave}}$ ) and depth (z) which was determined for the city of Ottawa to calculate the shear waves velocity in the basin (Motazedian et al., 2011):

$$V_{s_{ave}} = 123.86 + 0.88z \quad \text{for } 10 < z < 100 \quad (12)$$

Table 4-7 shows the seismic characteristics that were used for simulations. Table 4-7 shows that the shear wave velocities used in Soil Vs model 2 is smaller than the shear wave velocities used in Soil Vs model 1 for each layer.

Comparison between simulated velocity time series using Soil Vs model 1 and Soil Vs model 2 at soil site (Figure 4-35.a) shows that the amplitude of first arrivals was decreased in soil Vs model 2 while the amplitude of latter arrivals was increased for soil Vs model 2. Thus, the predicted PGVs at soil site increased by factor of 40% and 56% for E-W and Vertical component for soil Vs model 2 while the PGV of N-S component is the same for both simulations of soil Vs model 1 and soil Vs model 2.

Figure 4-35.b shows that using soil Vs model 2 shifted the frequency content of waves toward lower frequency. In addition, the amplitudes of velocity Fourier spectrum of horizontal components shifted for about 0.25 Hz and the amplitude of vertical component shifted for about 0.17 Hz toward lower frequency for soil Vs model 2 in comparison to soil Vs model 1. It should be noted that the natural frequency of a basin is calculated by:

$$f_n = \frac{V_s}{4h} \quad (13)$$

where h is the depth of the basin and Vs is the shear wave velocity of soil in the basin. Thus, using smaller Vs in soil Vs model 2 relative to soil Vs model 1 shifted the natural frequency of the basin toward lower frequency in simulation of soil Vs model 2. Using equation 13 and the average Vs of the basin for soil Vs model 1 ( $V_{s_{ave}}=248$  m/s) and soil Vs model 2 ( $V_{s_{ave}}=178$  m/s) shows that the difference between the natural frequencies of the basin for soil Vs model 1 and soil Vs model 2 is approximately equal to 0.2 Hz. Therefore, using soil Vs model 2 could shift the natural frequency of the basin for about 0.2 Hz. Furthermore, the amplitude of velocity Fourier spectrum of E-W and vertical components increased by about 32% for soil Vs model 2 while the amplitude of N-S component decreased by factor of 21% for soil Vs model 2.

Comparison between PSA ratios for soil Vs model 1 and soil Vs model 2 (Figure 4-36) shows that the amplitude of PSA ratio in all three component shifted toward lower frequency (For about 0.2 Hz) for soil Vs model 2. Further, predicted amplitude of PSA ratios of E-W and vertical components increased by factor of 18% and 11% respectively while the amplitude of PSA ratio of N-S component decreased by factor of 53% for soil Vs model 2 relative to soil Vs model 1.

### 4.8.3. Sensitivity to level of shaking and nonlinearity

Past observations have shown that both viscoelasticity and nonlinearity strongly modify the ground motion for a range of broadband frequencies but they influence on different frequency bands. This means that realistic simulations should take into consideration both viscoelasticity and nonlinear soil behavior. Although the effects of nonlinear attenuation were initially considered controversial among seismologists and engineers, it is now well accepted that soil may behave nonlinearly during large magnitude earthquakes ( $M_w \geq 7$ ) (Beresnev and Wen 1996, Restrepo et al., 2012).

The nonlinear behaviour of soil is not well captured in the viscoelastic simulation. A modification has been applied to the program to model the nonlinear soil, and results has been analyzed and discussed in Esmailzadeh et al., 2019.

To study the effects of the shaking level and nonlinearity we compared the viscoelastic simulation and nonlinear-viscoelastic simulation for  $M_w=7$ . We used the finite fault model (Figure 4-20) described in section 4.6.5 for both simulations.

Comparison between simulation velocity time series at soil site for viscoelastic simulation and nonlinear viscoelastic simulation (Figure 4-37.a) shows that the PGVs of E-W component and N-S component for nonlinear-viscoelastic simulation are smaller than the PGVs of E-W component and N-S component by factor of 3.4 and 2.5 respectively. However, the PGV of vertical component of nonlinear-viscoelastic simulation is 1.4 times greater than PGV of vertical component of viscoelastic simulation. Further, Figure 4-37.b shows that the velocity Fourier spectrum of viscoelastic simulation and nonlinear-viscoelastic simulation are the same for the frequency of  $<0.5$  Hz at soil site, while the velocity Fourier spectrum of nonlinear-viscoelastic simulation is slightly greater than the velocity Fourier spectrum of viscoelastic simulation for the

frequency range of 0.4-0.7 Hz. Also, the amplitudes of velocity Fourier spectrum of horizontal components for viscoelastic simulation is almost 5 times greater than the amplitudes of velocity Fourier spectrum of horizontal components for nonlinear-viscoelastic simulation, but the amplitude of vertical component for viscoelastic simulation is almost 18% smaller than the amplitude of vertical component for nonlinear-viscoelastic simulation. Thus using nonlinear-viscoelastic simulation shifted the frequency content of waves within the basin toward lower frequency and reduced the amplitude of velocity Fourier spectrum.

Comparison between PSA ratios for viscoelastic simulation and nonlinear-viscoelastic simulation (Figure 4-38) shows that the amplitudes of PSA ratios of E-W and N-S components for nonlinear-viscoelastic simulation decreased by factor of 3.5 and 3.8 relative to the amplitudes of PSA ratios of E-W and N-S components for viscoelastic simulation respectively, while the amplitude of PSA ratios of vertical component for nonlinear-viscoelastic simulation is 1.13 times greater than the amplitude of PSA ratios of vertical component for viscoelastic simulation. Furthermore, the amplitude of PSA ratios for nonlinear-viscoelastic simulation is at slightly lower frequency in comparison to the frequency associated with the amplitude of the PSA ratios of viscoelastic simulation.

#### **4.9. Discussion and conclusion**

In the context of physics-based ground motion simulations of the Ladysmith earthquake (Mw 4.7) for the Kinburn basin, we studied the influence of source and material models on the ground motion simulation.

Studying the sensitivity of simulations to moment magnitude showed that the PGVs increased logarithmically with  $M_0$  for both rock and soil sites at a similar rate, while the PGV of

soil site was 5.9 times greater than the PGV of rock site for all  $M_0$ . Also, the amplitude of the velocity Fourier spectrum logarithmically increased with  $M_0$ .

Using fault plane 1 and 2 to simulate small earthquakes ( $M_w=4.7$ ) showed that the fault type slightly affected rock site, while it influenced the PGV and amplitude of the velocity Fourier spectrum at soil site. Specifically, fault type 1 generated waves in soil site that increased the amplitude of later arrivals. The discrepancy between the PGVs and amplitude of the velocity Fourier spectrum at soil site for different fault planes can be attributed to differences in the components of incident waves for the two fault planes that particularly lead to different level of amplification/de-amplification in the basin.

Using a Gaussian source function to model small earthquakes ( $M_w=4.7$ ) increased the PGV by a factor of about 10 for all three components at both rock and soil sites compared to using a semi-triangular source function. A similar increase was shown for the amplitude of the velocity Fourier spectrum at both rock and soil sites. However, using a Gaussian source function reduced the amplitudes of the PSA ratios for all three components. This discrepancy is because the amplification generated in the basin by semi-triangular source function is slightly greater than the amplification for Gaussian source function.

Our study shows that slip duration mainly influenced simulation when Gaussian source function was used to model the earthquake, because the half duration in Gaussian function significantly affects the amount of energy that was generated at the source. Using a short half duration (0.6 s) in simulations significantly increased the PGVs and amplitudes of the velocity Fourier spectrum and shifted the frequency content of the simulated waves toward a higher frequency for both soil and rock sites. Furthermore, the effects of the half duration on the PGVs and amplitudes of the velocity Fourier spectrum at soil site was almost twice that at rock site.

However, the PSA ratios were not affected by the half duration except for the PSA ratio of the N-S component.

Comparison between point source simulation and finite fault simulation shows that using finite fault significantly reduced the PGV at both rock site and soil site relative to the point source simulation. Also, the amplitude of velocity Fourier spectrum significantly decreased for finite fault simulation at rock site and soil site particularly at high frequencies because using finite fault model shifted the frequency content of waves toward lower frequency. Furthermore, the amplitude of PSA ratio of both point source and finite fault simulations for E-W and vertical components are similar, while the amplitude of PSA ratio of N-S component for point source simulation is two times smaller than the amplitude of PSA ratio of N-S component for finite fault simulation.

Comparing simulations using crustal model 1 and crustal model 2 for the earthquake with  $M_w=4.7$  showed that crustal model 2 reduced arrival times (because it considered a higher crustal velocity) and decreased the PGV at both rock and soil sites. Layers used in crustal model 2 increased the reflection waves and reduced the incident waves at rock site and soil site which consequently reduced the PGVs of the simulated time series. Also, crustal model 2 reduced the amplitudes of the velocity Fourier spectrum at rock and soil sites. In addition, crustal model 2 shifted the frequency content of the waves toward a lower frequency at soil site and increased the amplitude of the PSA ratios.

Varying crustal Q model did not affect simulations of the earthquake for rock or soil sites. Thus, the PGVs of simulations for both crustal Q models are almost the same.

Simulations of the Ladysmith earthquake using the memory variables model 2 increased the PGVs and amplitudes of the velocity spectrum at soil site in all three components, while the

PGVs and amplitudes of the velocity spectrum at rock site did not change. In addition, the amplitude of later arrivals significantly increased in simulation used memory variables model 2 relative to that of simulation used memory variables model 1.

Using soil Q model 2 (small soil Q model) for simulation reduced the PGVs at soil site and amplitudes of the velocity Fourier spectrum as the energy of waves damped faster compared to when soil Q model 1 was used. Thus, the amplitudes of later arrivals were significantly reduced in simulation that used soil Q model 2. Consequently, the PSA ratios of all three components decreased in simulations that used soil Q model 2.

Using soil Vs model 2 (high velocity contrast which resulted from employed small soil Vs model) for the viscoelastic simulation increased the PGVs for E-W and vertical component at soil site and shifted the amplitude of velocity Fourier spectrum of all three components toward low frequency. Using soil Vs model 2 (or smaller soil Vs model) shifted the natural frequency of the basin toward lower frequency. Thus, the amplitude of the velocity Fourier spectrum for soil Vs model 2 is at lower frequency relative to the frequency associated with the amplitude of velocity Fourier spectrum for soil Vs model 1. It should be noted that using soil Vs model 2 decreased the amplitude of velocity time series of first arrivals at soil site because most of the first arrivals could not enter to the basin as the waves were reflected back from the edge of the basin while the amplitude of velocity time series (which is associated with latter arrivals) increased significantly because of the significant reverberation of waves and generated surface waves within the basin. Further, using soil Vs model 2, the amplitude of velocity Fourier spectrum increased in E-W and vertical components while decreased for N-S component. Also, the amplitude of PSA ratios of E-W and vertical components decreased for simulation using soil Vs model 1 while decreased for N-S component for simulation used soil Vs model 2.

Comparison between viscoelastic simulation and nonlinear-viscoelastic simulation showed that using nonlinear soil effects for modeling the large earthquake ( $M_w=7$ ) significantly damped the high frequency waves in the basin. Further, using the nonlinear-viscoelastic simulation reduced the amplitude of latter of arrivals particularly in horizontal components as the energy of waves was attenuated by the nonlinear soil effects. Thus, the predicted PGV and amplitude of velocity Fourier spectrum by viscoelastic simulation were reduced by factor of 3.4 and 4.5, respectively, using nonlinear-viscoelastic simulation. Also, the predicted amplitude of PSA ratios were reduced by a factor of 3.8 using nonlinear-viscoelastic simulation relative to the amplitude of PSA ratios of viscoelastic simulation. Also, the amplitude of PSA ratios of all three components for nonlinear-viscoelastic simulation is at lower frequency in comparison to the frequency relative to the amplitude of PSA ratios of the three components for viscoelastic simulation.

### **Data and Resources**

The Global Centroid Moment Tensor Project database: [www.globalcmt.org/CMTsearch.html](http://www.globalcmt.org/CMTsearch.html) (last accessed August 2017).

The Earthquakes Canada, Natural Resources Canada (NRCAN) database: [www.earthquakescanada.nrcan.gc.ca](http://www.earthquakescanada.nrcan.gc.ca) (last accessed October 2017).

The Geological Survey of Canada provided the seismograms and information on the Kinburn basin depth; this information cannot be released to the public.

## **Acknowledgements**

This research was supported by the Natural Sciences and Engineering Research Council of Canada under the Discovery Grant program and Collaborative Research and Development grants. This research used computational resources provided by the High Performance Computing Virtual Laboratory (HPCVL) and Calcul Québec, both under Compute Canada. We gratefully acknowledge the constructive comments, suggestions, and text revisions from reviewers and Associate Editor, \*\*\*\*. We used the AWP-ODC (Anelastic Wave Propagation, developed by Olsen-Day-Cui) program package, and we would like to show our gratitude to Professor Kim Olsen for providing us with the package. We appreciate Dr. Daniel Roten's guidance in using the AWP-ODC program. Special gratitude is given to the Geological Survey of Canada for providing us with helpful comments, suggestions, and the necessary materials, including seismograms and geological information, for this research.

## Tables and Figures

Table 4-1. Properties of modelled soil and rock (Burger et al., 1987; Hunter et al., 2010; Crow et al., 2011; Motazedian et al., 2011; Bent et al., 2015)

Type of material	Soil	Soil	Soil	Soil	Rock
Depth (m)	0-25	25-50	50-75	75-100	Out of basin
Vs (m/s)	178	219	278	320	2783
Vp (m/s)	1380	1380	1380	1380	6200
Density (kg/m <sup>3</sup> )	1600	1600	1600	1600	2650
Qp	185	185	185	185	1000
Qs	185	185	185	185	500

Table 4-2. The focal mechanisms proposed for the Ladysmith earthquake

	<b>Bent et al. (2015)</b>			<b>Ma and Audet (2014)</b>			<b>CMT (last modified 2011)</b>		
	Epicenter = 45.76, -76.32 Depth = 12 Km $M_w = 4.55$ $M_0 = 8.372e+15$ Nt-m			Epicenter = 45.74, -76.34 Depth = 14.5 Km $M_w = 4.7$ $M_0 = 1.32e+16$ Nt-m			Epicenter = 45.8, -76.41 Depth = 22.1 Km $M_w = 4.7$ $M_0 = 1.52e+16$ Nt-m		
	<b>Strike</b>	<b>Dip</b>	<b>Slip</b>	<b>Strike</b>	<b>Dip</b>	<b>Slip</b>	<b>Strike</b>	<b>Dip</b>	<b>Slip</b>
Plane1	350.40	47.91	118.03	306	41	94	143	45	79
Plane2	131.94	49.08	62.52	122	50	87	338	46	101

Table 4-3. Calculated seismic moments associated with different moment magnitudes

Moment Magnitude ( $M_w$ )	Seismic Moment ( $M_0$ ) (N.m)
4.7	1.32E16
5.5	2.2387E17
6	1.2589E18
6.5	7.0795E18
7	3.9811E19

Table 4-4. Crustal Vs, Vp and density models; Model 1 (Burger et al., 1987; Hunter et al., 2010) and Model 2 (Burger et al., 1987; Motazedian et al., 2013)

Depth(km)	Crustal model 2					Crustal model 1				
	Vs(m/s)	Vp(m/s)	Density (kg/m <sup>3</sup> )	Qp	Qs	Vs(m/s)	Vp(m/s)	Density (kg/m <sup>3</sup> )	Qp	Qs
D < 2	3400	5888	2693	1000	500	2783	6200	2650	1000	500
2 <= D < 4	3410	5906	2696							
4 <= D < 8	3420	5923	2700							
8 <= D < 12	3560	6165	2753							
12 <= D < 14	3580	6200	2761							
14 <= D < 16	3600	6235	2769							
16 <= D < 17	3620	6269	2777							
17 <= D < 17.5	3700	6408	2810							

Table 4-5. Crustal damping factor models; Crustal damping factor (Q) model 1 (Burger et al., 1987; Hunter et al., 2010.) and Crustal damping factor (Q) model 2 (Burger et al., 1987; Hunter et al., 2010) used for rock site

Depth(km)	Crustal damping factor (Q) model 2					Crustal damping factor (Q) model 1				
	Vs(m/s)	Vp(m/s)	Density (kg/m <sup>3</sup> )	Qp	Qs	Vs(m/s)	Vp(m/s)	Density (kg/m <sup>3</sup> )	Qp	Qs
Any depth	2783	6200	2650	2375	475	2783	6200	2650	1000	500

Table 4-6. Damping factor models; Soil damping factor(Q) model 1 (Burger et al., 1987; Hunter et al., 2010; Crow et al., 2011) and Soil damping factor(Q) model 2 (Burger et al., 1987; Hunter et al., 2010; Crow et al., 2011) used for soil site

Depth(km)	Soil damping factor (Q) model 2					Soil damping factor(Q) model 1				
	Vs(m/s)	Vp(m/s)	Density (kg/m <sup>3</sup> )	Qp	Qs	Vs(m/s)	Vp(m/s)	Density (kg/m <sup>3</sup> )	Qp	Qs
0-25	178	1380	1600	29	19	178	1380	1600	185	185
25-50	219	1380	1600	53	35	219	1380	1600	185	185
50-75	278	1380	1600	129	86	278	1380	1600	185	185
75-100	320	1380	1600	106	71	320	1380	1600	185	185
Rock site	2783	6200	2650	1000	500	2783	6200	2650	1000	500

Table 4-7. Vs models used for soil site; Soil Vs model 1 (Burger et al., 1987; Hunter et al., 2010; Crow et al., 2011) and Soil Vs model 2 (Burger et al., 1987; Hunter et al., 2010; Crow et al., 2011; Motazedian et al., 2011)

Depth(km)	Soil Vs model 2					Soil Vs model 1				
	Vs(m/s)	Vp(m/s)	Density (kg/m <sup>3</sup> )	Qp	Qs	Vs(m/s)	Vp(m/s)	Density (kg/m <sup>3</sup> )	Qp	Qs
0-25	145	1380	1600	185	185	178	1380	1600	185	185
25-50	167	1380	1600	185	185	219	1380	1600	185	185
50-75	189	1380	1600	185	185	278	1380	1600	185	185
75-100	211	1380	1600	185	185	320	1380	1600	185	185
Rock site	2783	6200	2650	1000	500	2783	6200	2650	1000	500

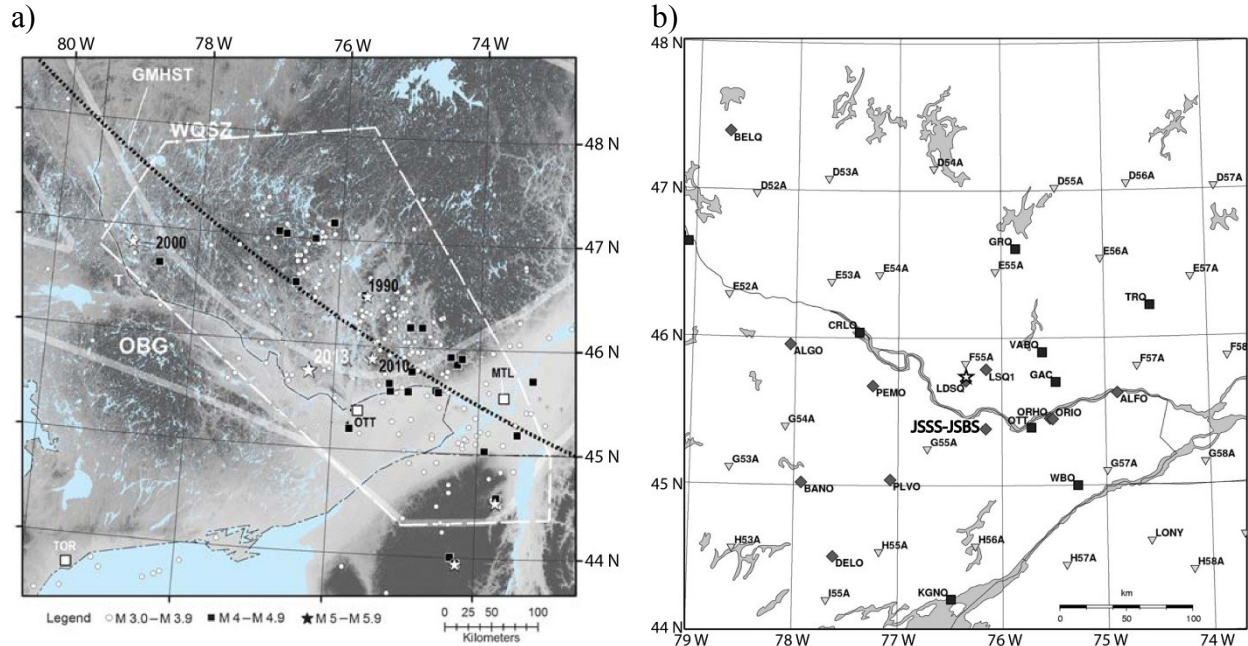


Figure 4-1. a) Location of the May 2013 Ladysmith, Quebec, earthquake (star with 2013), within the outline of the western Quebec seismic zone (WQSZ; Basham et al., 1982). The earthquakes recorded between January 1980 and May 2014 are also denoted by circles,  $m N \geq 3.0$ ; squares,  $m N \geq 4.0$ ; stars,  $m N \geq 5$  events with the year of occurrence. The other abbreviations show the approximate area of the Ottawa–Bonnechère Graben (OBG) and St. Lawrence rift system, the assumed position of the Great Meteor hot spot track (GMHST; Bleeker et al., 2011), and TOR, Toronto; OTT, Ottawa; MTL, Montréal; and T, Temiscaming. b) The open star shows the epicenter of the Ladysmith earthquake. Other symbols represent seismograph stations (diamonds: three-component broadband stations installed for research purposes; squares: permanent instruments of the Canadian National Seismograph Network; upside-down triangles: the U.S. Transportable Array stations; and JSBS–JSSS: the locations of the Kinburn basin array) for approximately the same region as (a) (Bent et al., 2015).

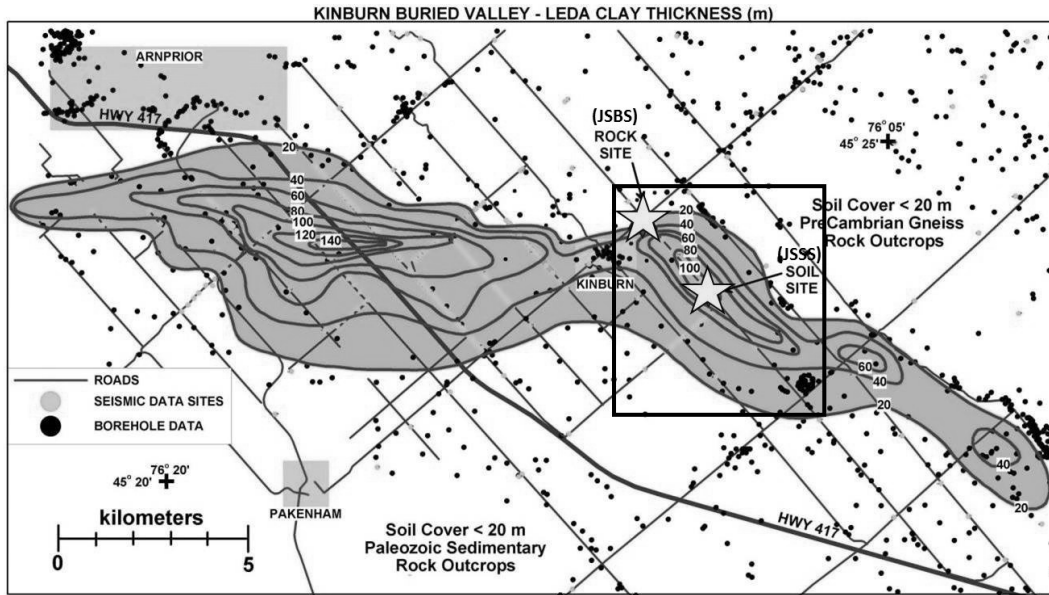


Figure 4-2. Topographic map of the Kinburn basin, as prepared by J. A. Hunter (2012). Approximate locations of seismic stations are marked with yellow stars, and the study area is outlined by a black box (Hayek, 2016).

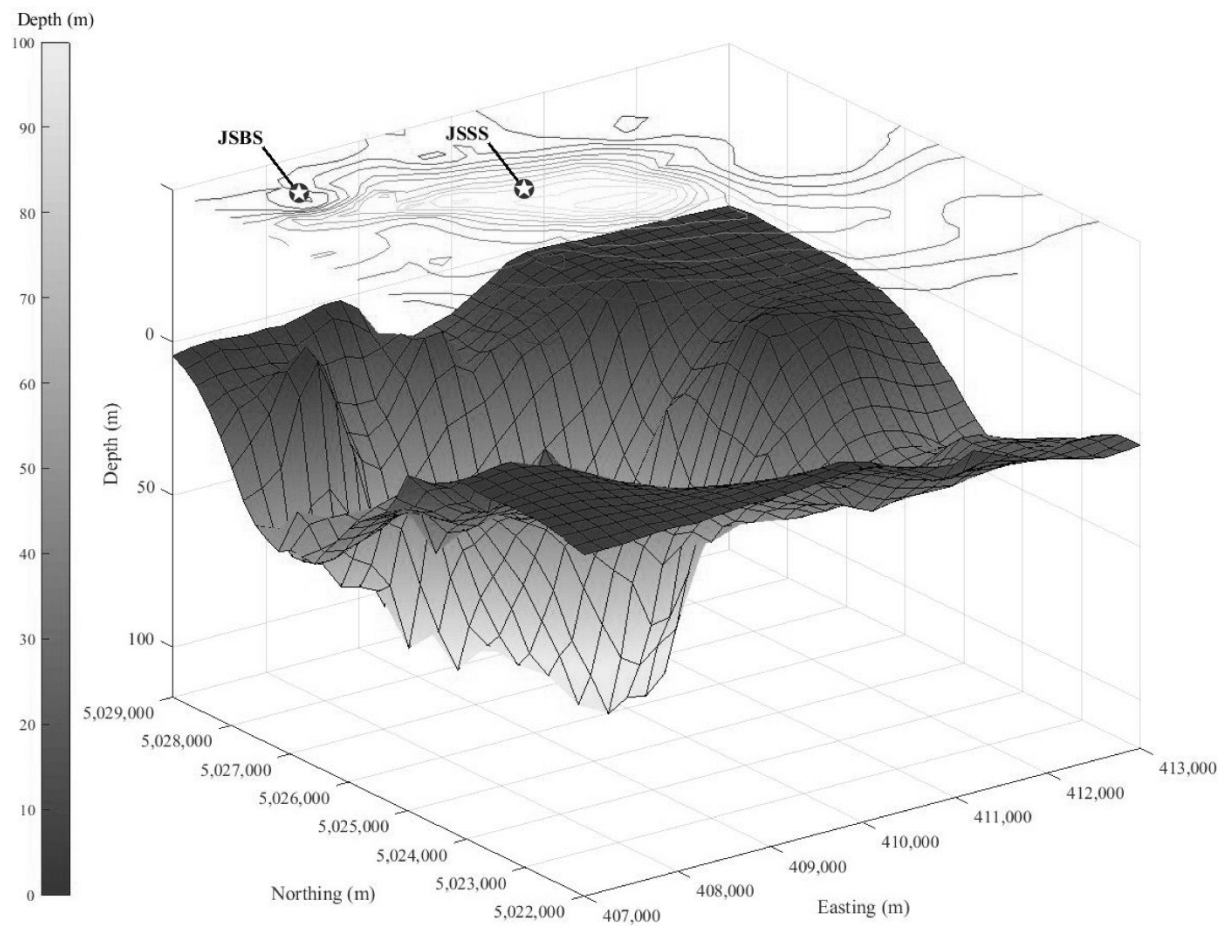


Figure 4-3. Contour map of the Kinburn basin depth showing the location of soil site (JSSS) and rock site (JSBS) and the gridded (mesh size 25 m) 3D variation of depth within the Kinburn basin.

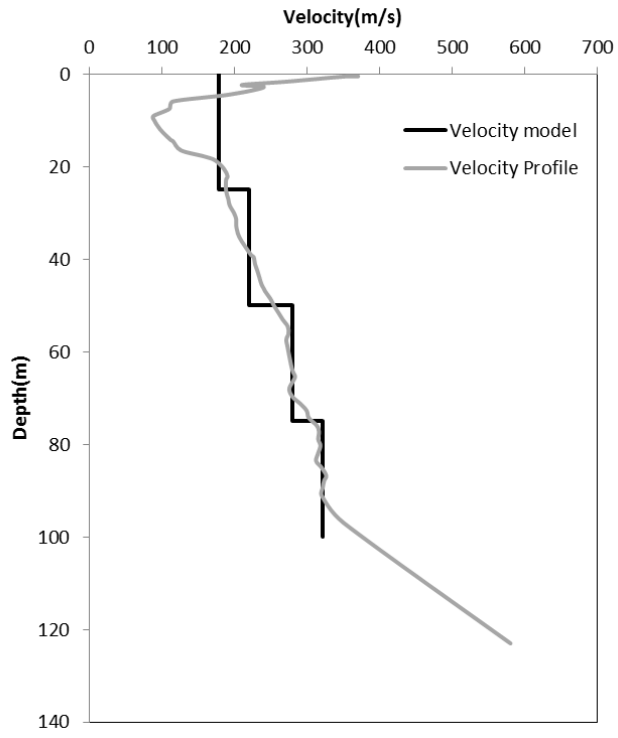


Figure 4-4. Velocity profile of the Kinburn basin.

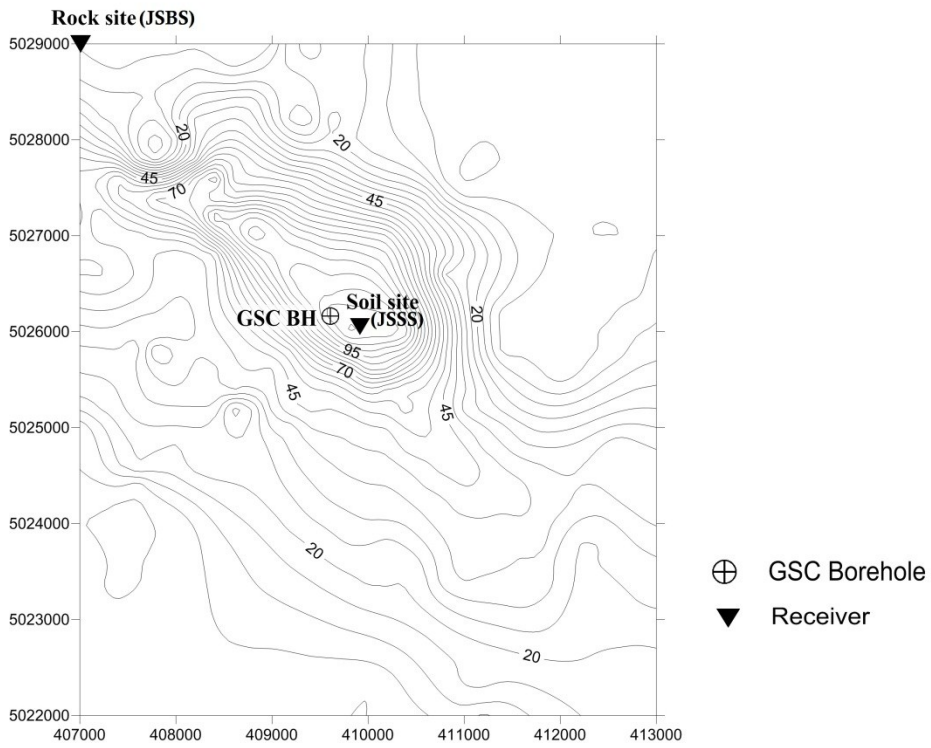
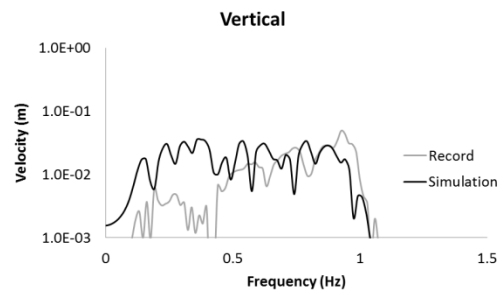
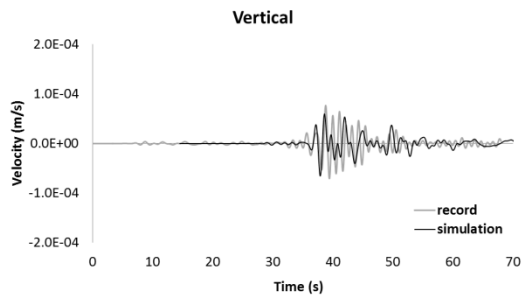
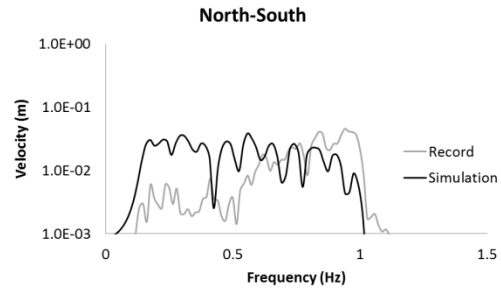
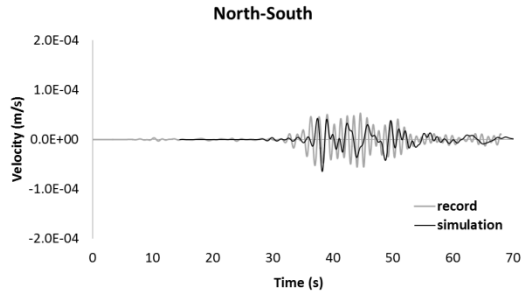
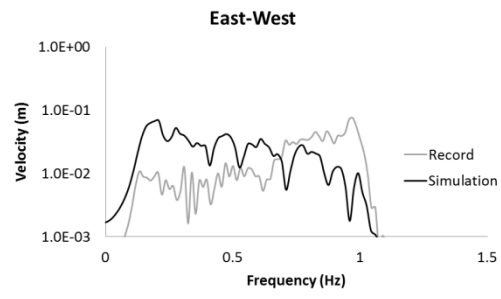
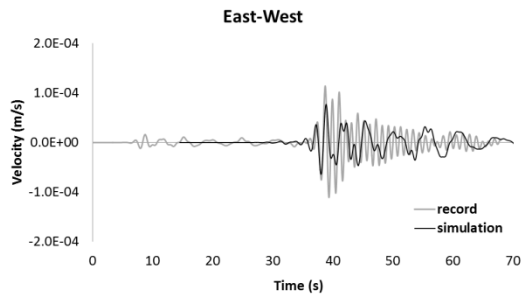
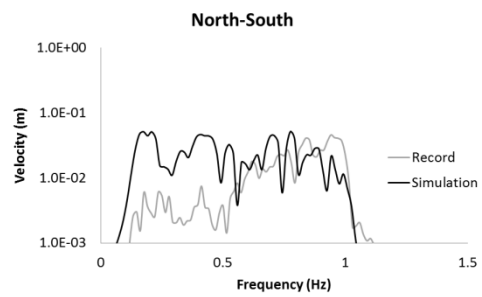
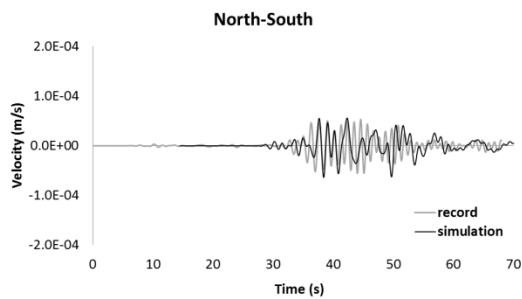
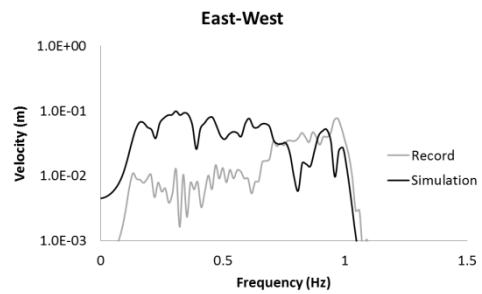
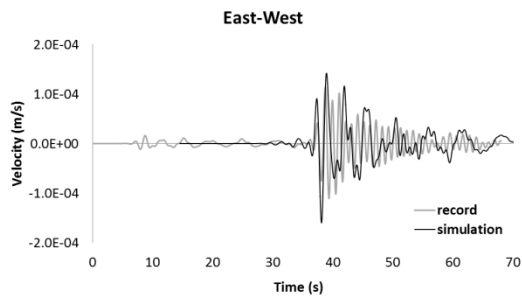


Figure 4-5. Contour map of the Kinburn basin depth and the location of the receivers at soil (JSSS) and rock sites (JSBS) and the GSC borehole in the basin.

(a)



(b)



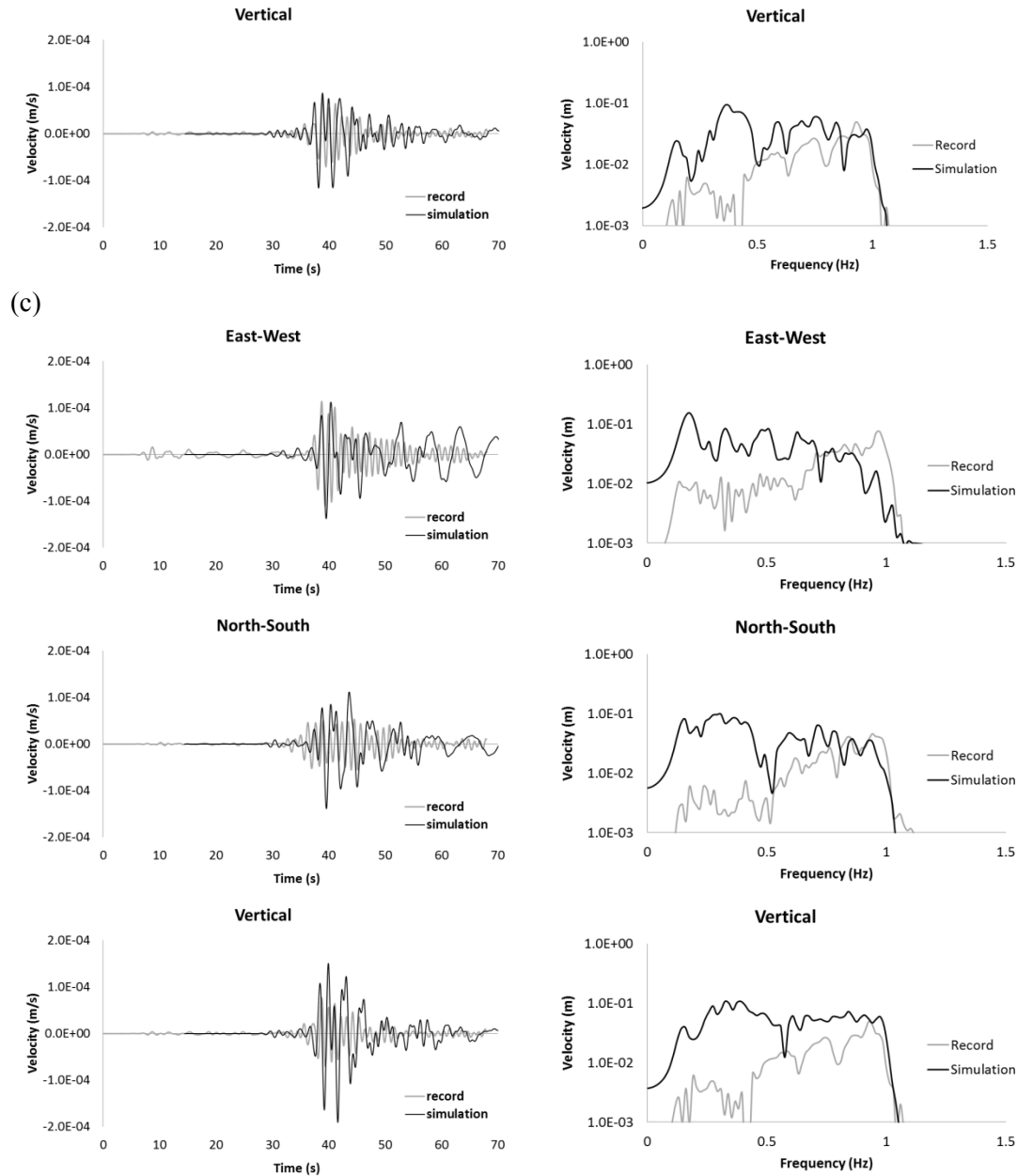
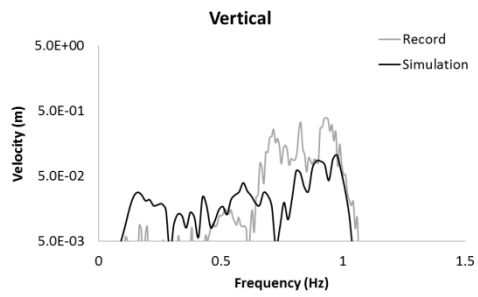
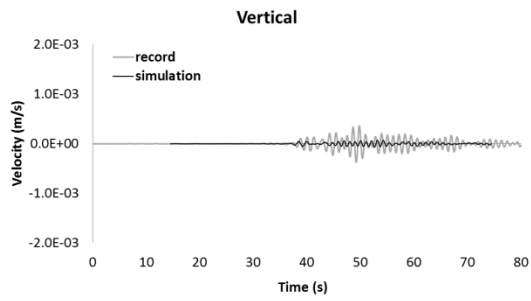
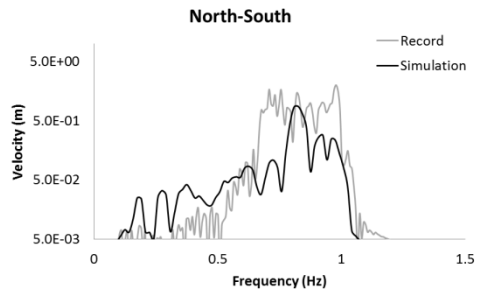
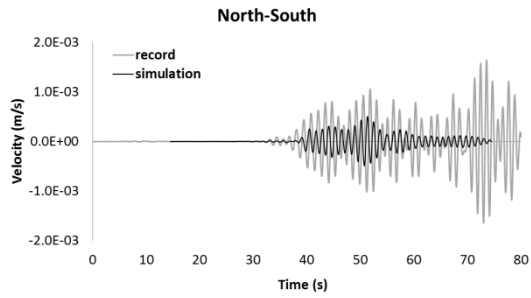
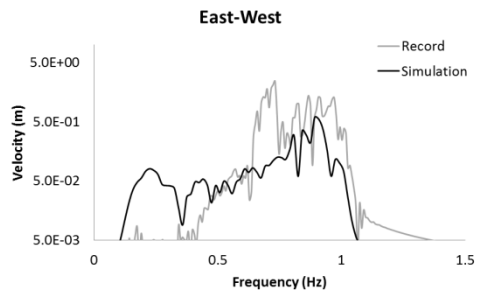
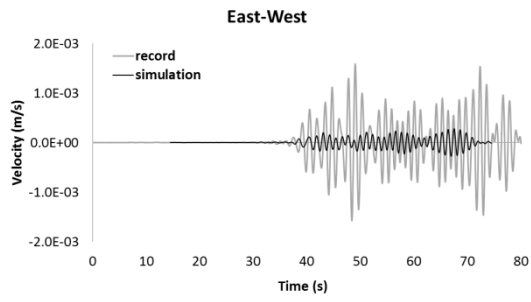
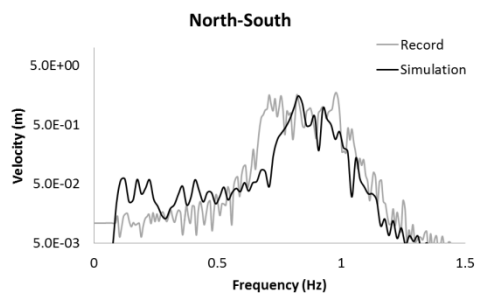
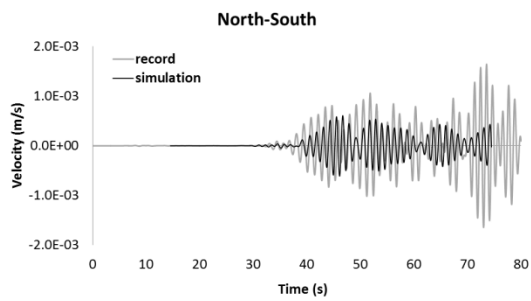
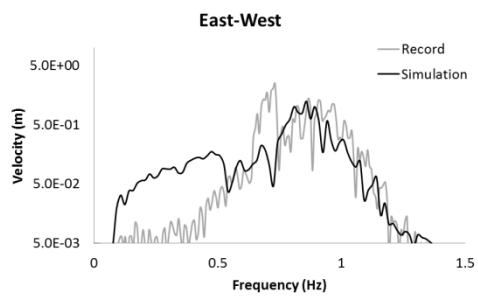
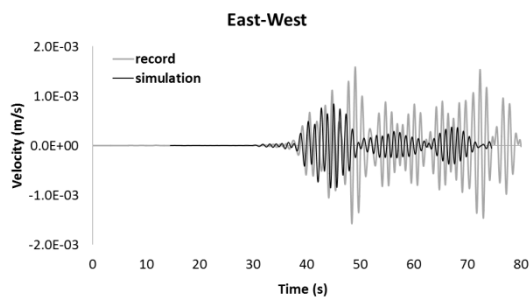


Figure 4-6. Simulated velocity time series and related Fourier spectrum versus recorded velocity time series and associated Fourier spectrum at rock site for the three proposed focal mechanisms: a) Bent et al. (2015); epicentral distance  $R=39.3$  km, depth=12 km,  $M_w=4.55$ ,  $M_0=8.372e+15$  Nt-m, b) Ma and Audet (2014); epicentral distance  $R=39.3$  km; depth=14.5 km,  $M_w=4.7$ ,  $M_0=1.32e+16$  Nt-m, and c) CMT (last modified 2011); epicentral distance  $R=39.3$  km, depth=22.1 km,  $M_w=4.7$ ,  $M_0=1.52e+16$  Nt-m

(a)



(b)



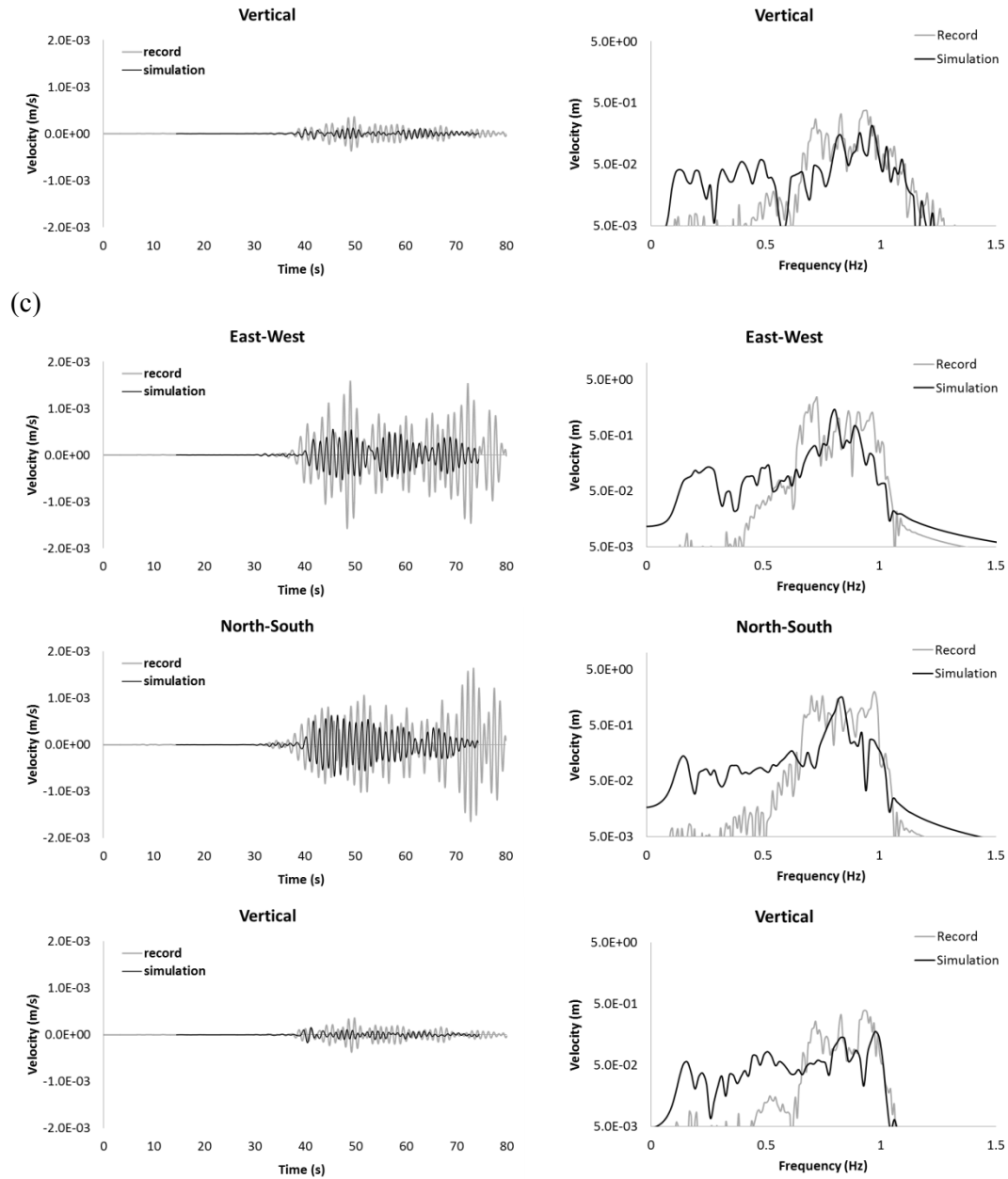


Figure 4-7. Simulated velocity time series and related Fourier spectrum versus recorded velocity time series and associated Fourier spectrum at soil site for the three proposed focal mechanisms: a) Bent et al. (2015); epicentral distance  $R=43$  km, depth=12 km,  $M_w=4.55$ ,  $M_0=8.372e+15$  Nt-m, b) Ma and Audet (2014); epicentral distance  $R=43$  km, depth=14.5 km,  $M_w=4.7$ ,  $M_0=1.32e+16$  Nt-m, and c) CMT (last modified 2011); epicentral distance  $R=43$  km, depth=22.1 km,  $M_w=4.7$ ,  $M_0=1.52e+16$  Nt-m

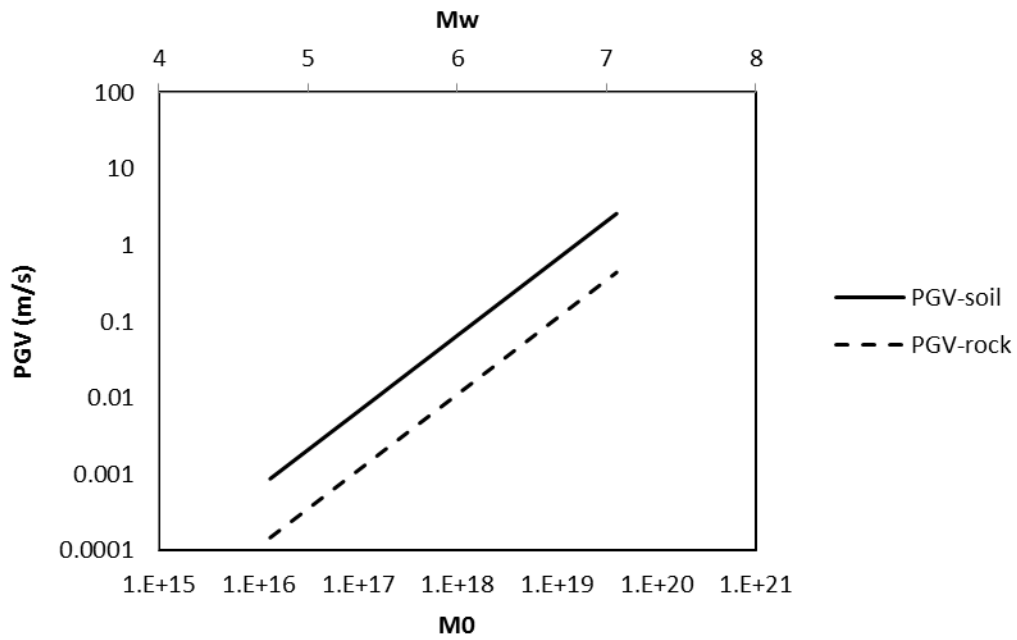


Figure 4-8. PGVs of the viscoelastic simulations associated with seismic moment and seismic magnitude, using a point source model.  $PGV_{rock} = 1E-11e^{3.4747 \cdot M_w}$  and  $PGV_{soil} = 7E-11e^{3.4695 \cdot M_w}$  represents the equations related to plots.

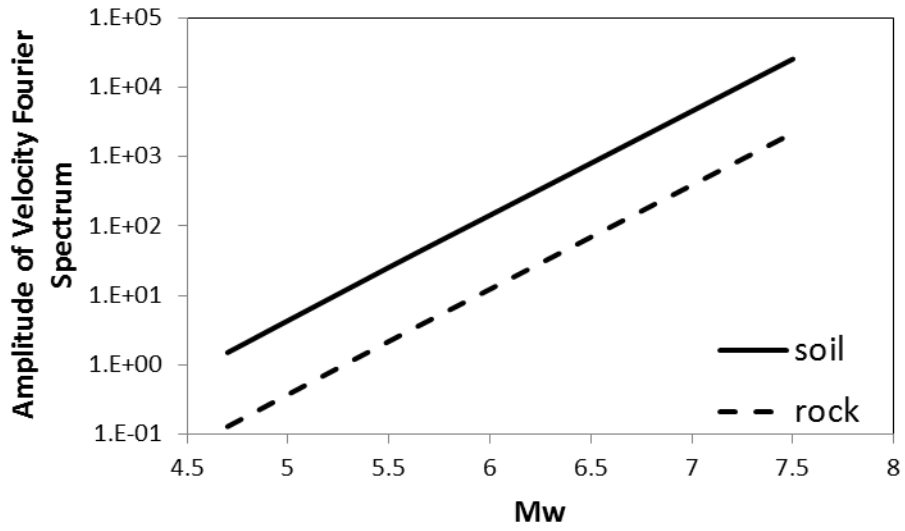


Figure 4-9. Amplitude of Velocity Fourier spectrum of the modeled velocity time series for the rock site and soil site associated with different moment magnitudes.

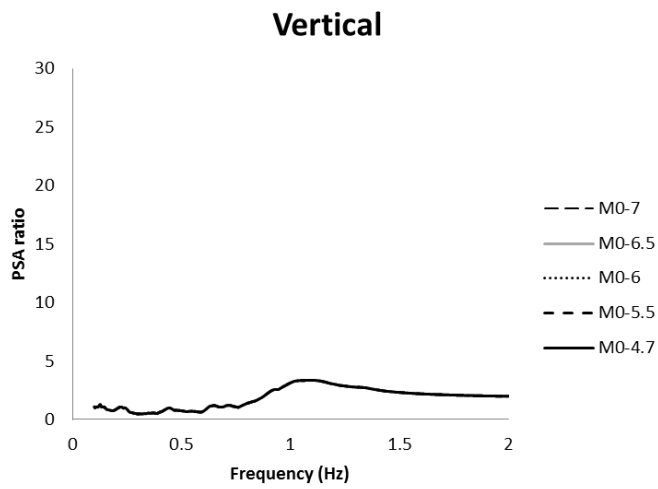
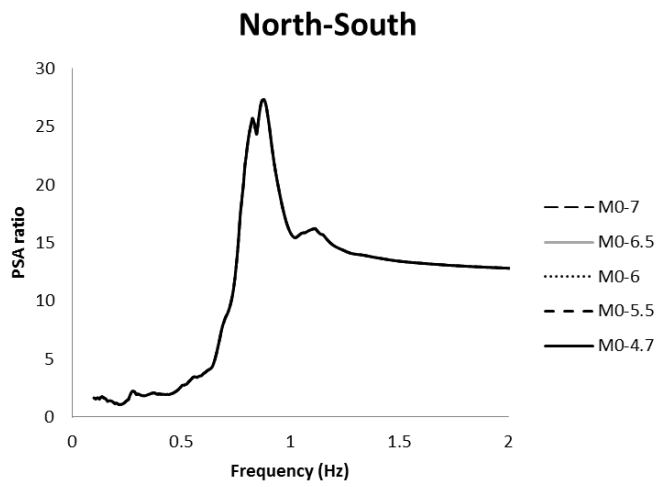
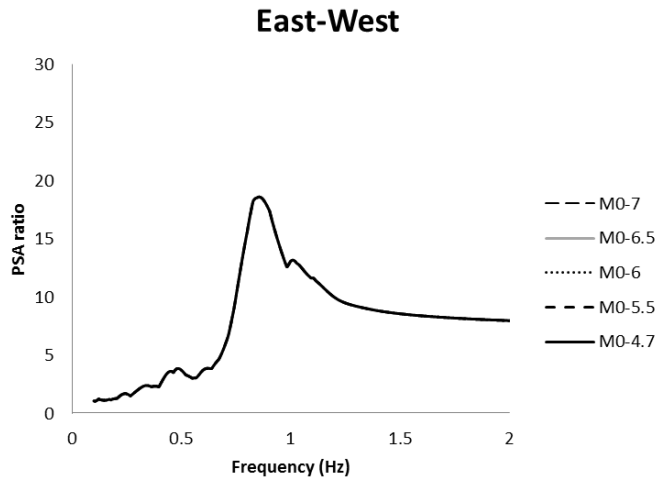
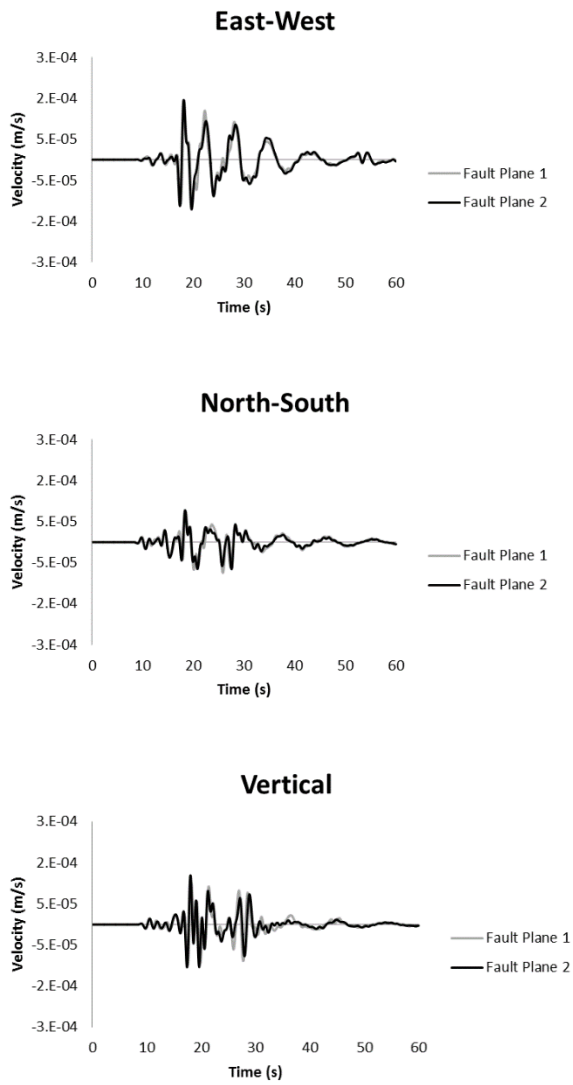


Figure 4-10. PSA ratio of soil site to rock site associated with different moment magnitudes.

a.



b.

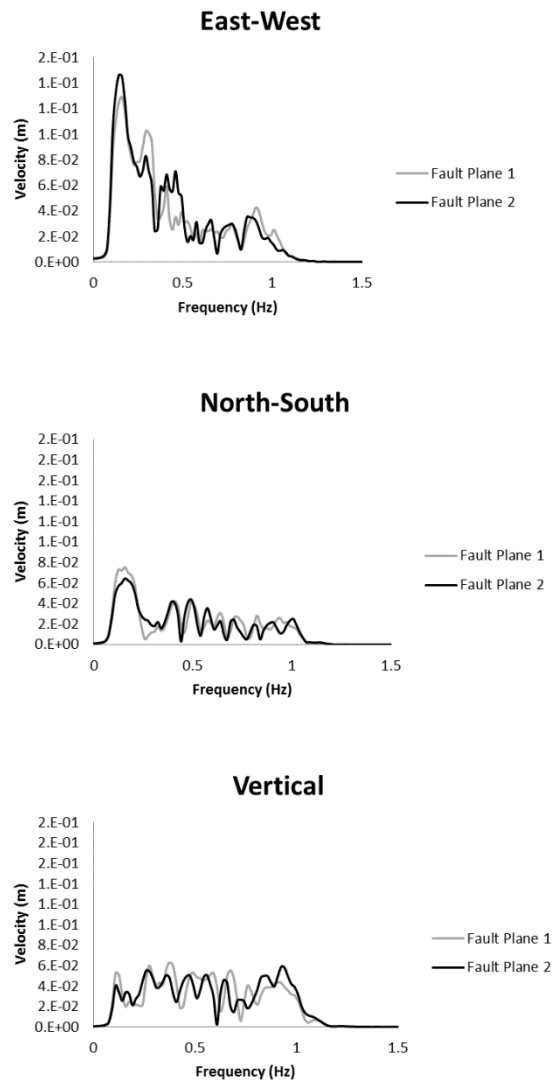
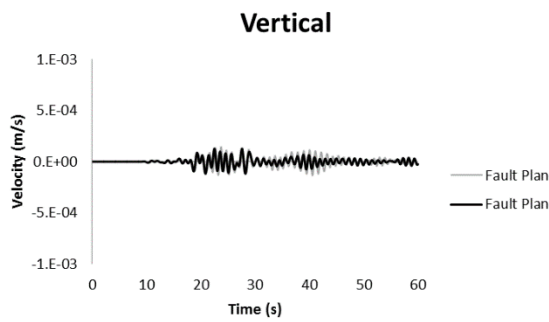
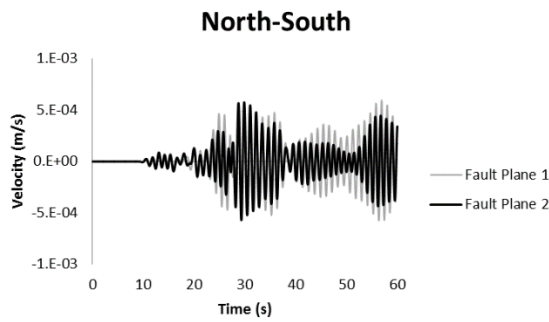
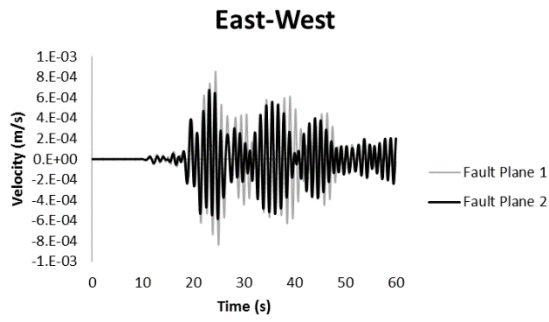


Figure 4-11. Simulated a) velocity time series and b) Fourier spectrum of rock site for  $M_w=4.7$  using fault plane 1: 306 (strike), 41 (dip), 94 (slip); and fault plane 2: 122 (strike), 50 (dip), 87 (slip).

a.



b.

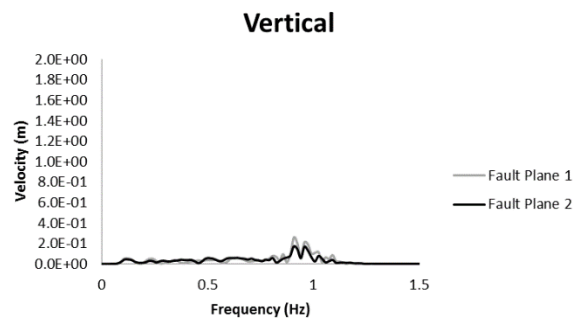
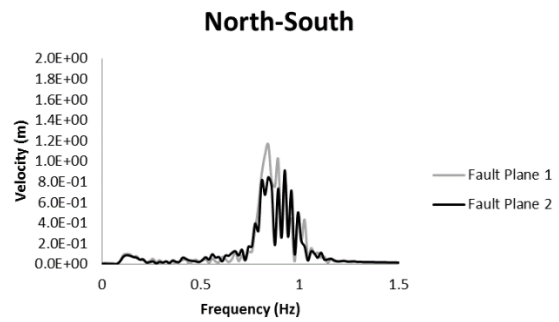
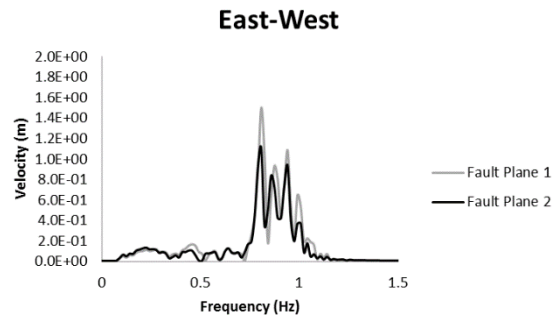


Figure 4-12. Simulated a) velocity time series and b) Fourier spectrum of soil site for Mw=4.7 using fault plane 1: 306 (strike), 41 (dip), 94 (slip); and fault plane 2: 122 (strike), 50 (dip), 87 (slip).

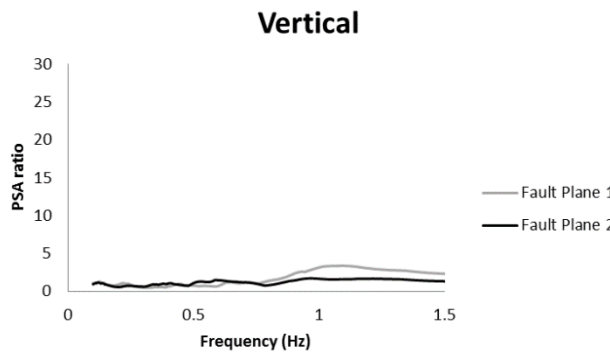
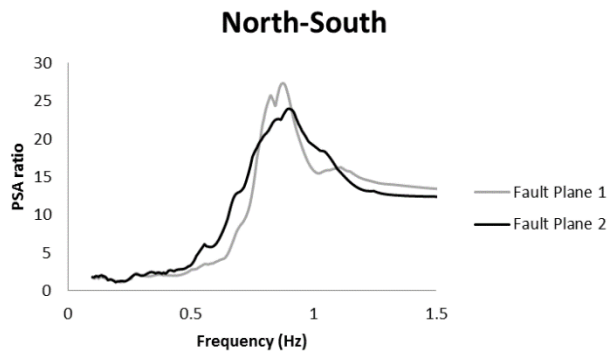
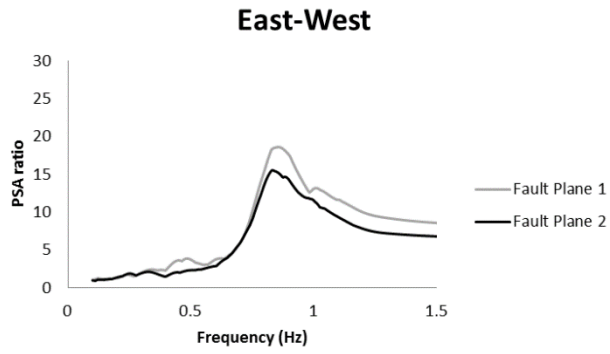
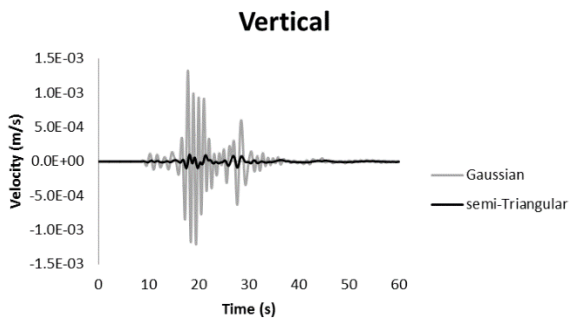
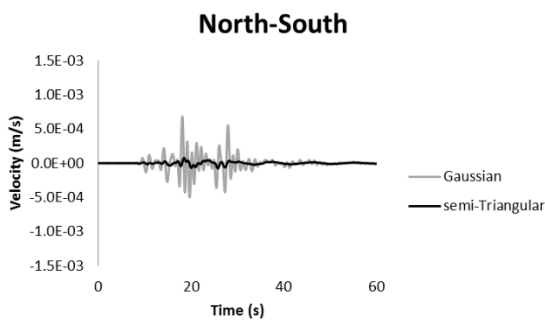
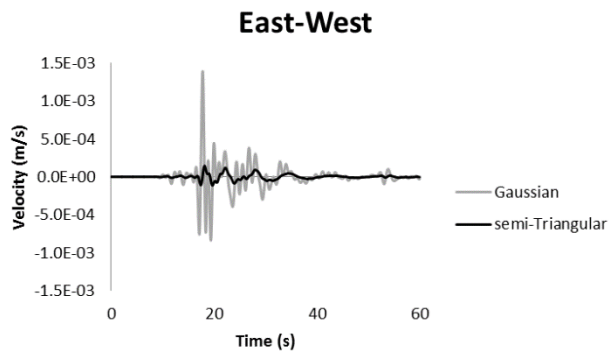


Figure 4-13. Comparison of PSA ratios of soil site to rock site for Mw=4.7 using fault plane 1: 306 (strike), 41 (dip), 94 (slip); and fault plane 2: 122 (strike), 50 (dip), 87 (slip).

a.



b.

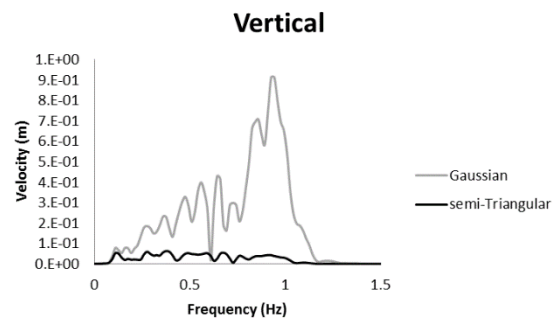
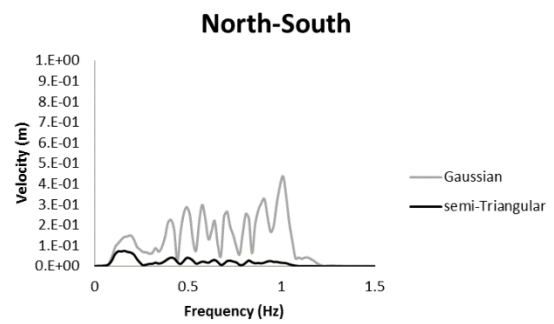
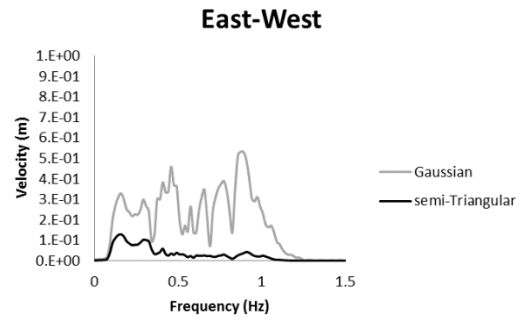


Figure 4-14. Simulated a) velocity time series and b) Fourier spectrum of rock site for Mw=4.7 using Gaussian and semi-triangular source functions.

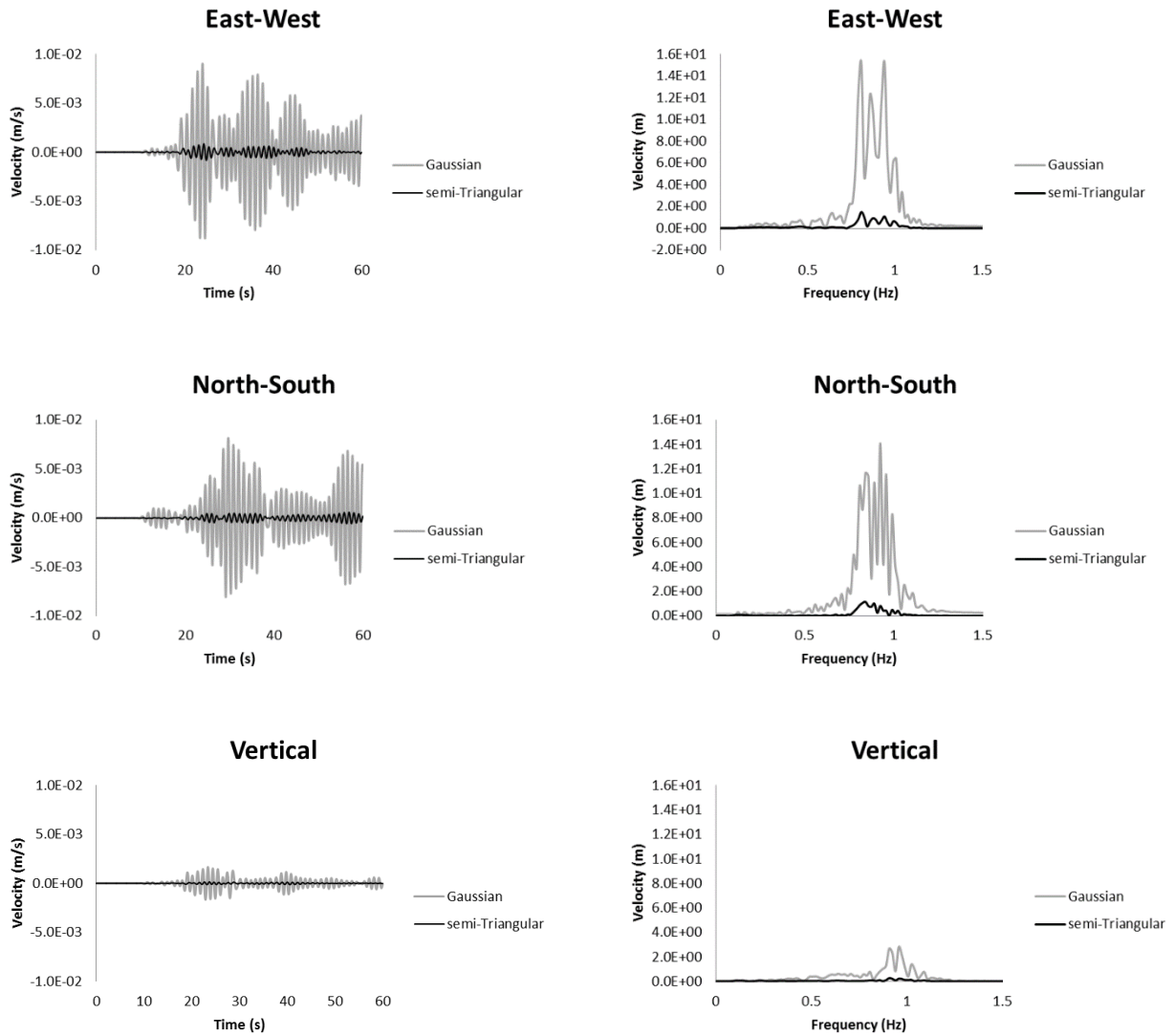


Figure 4-15. Simulated a) velocity time series and b) Fourier spectrum of soil site for  $M_w=4.7$  using Gaussian and semi-triangular source functions.

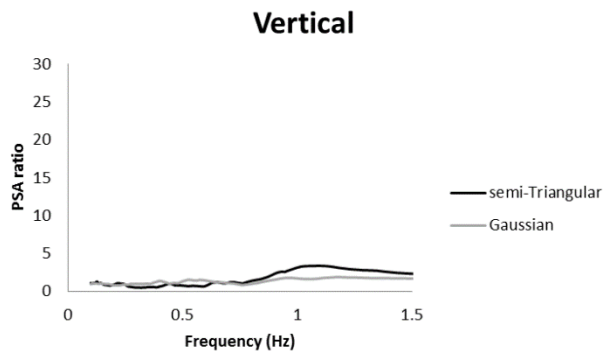
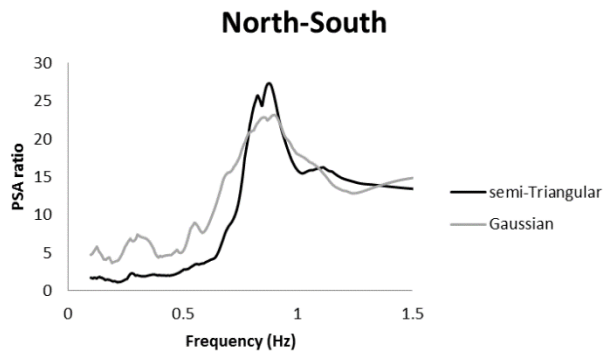
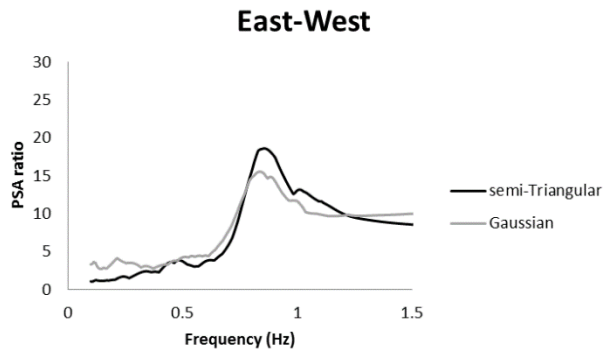
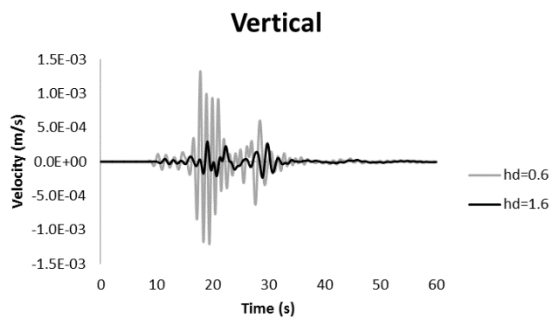
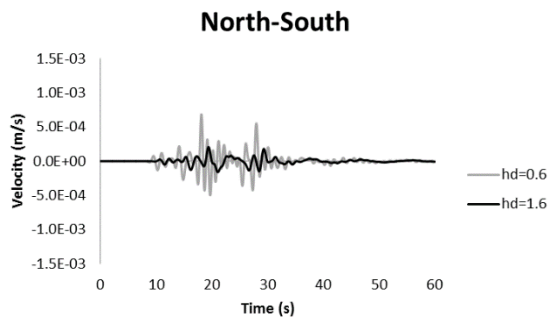
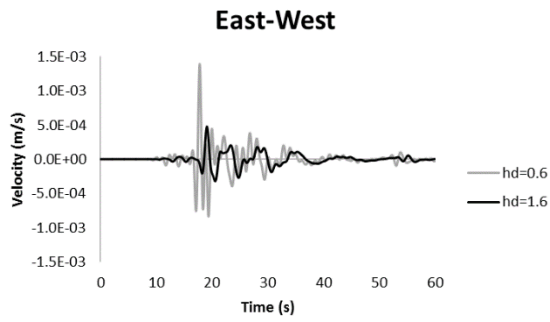


Figure 4-16. Comparison of PSA ratios of soil site to rock site for  $M_w=4.7$  using Gaussian and semi-triangular source functions.

a.



b.

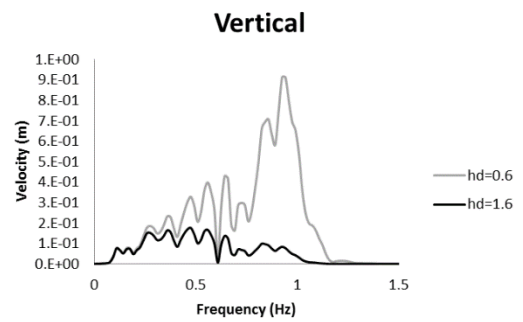
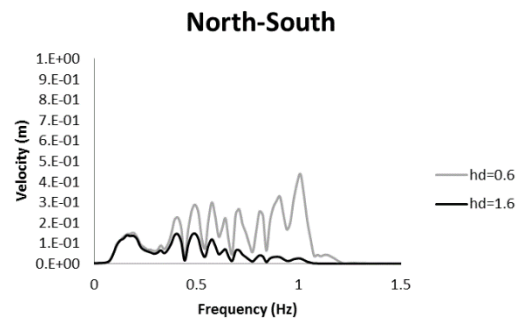
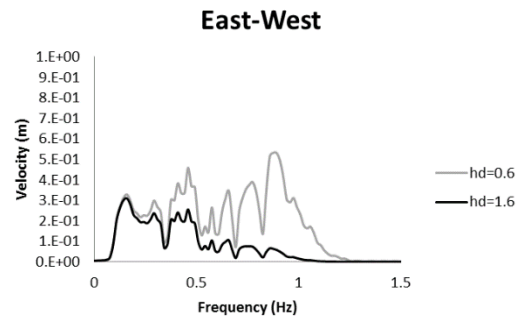
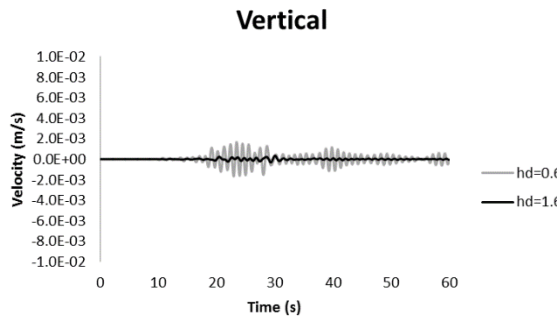
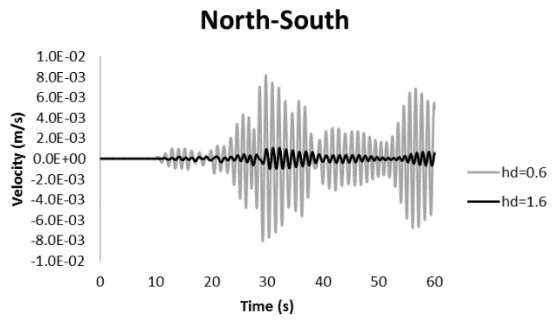
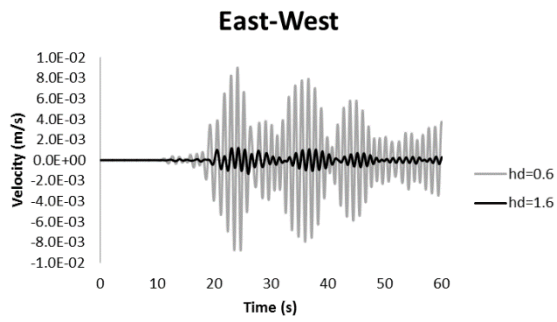


Figure 4-17. Simulated a) velocity time series and b) Fourier spectrum of rock site for Mw=4.7 using half durations of 0.6 s and 1.6 s for Gaussian source function.

a.



b.

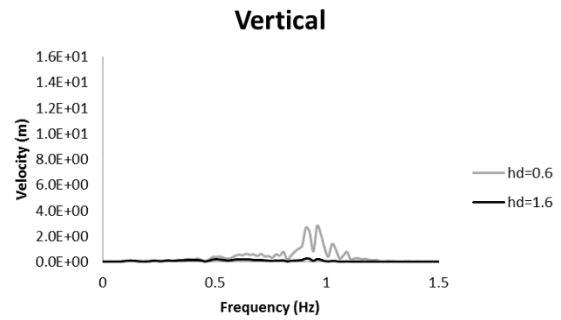
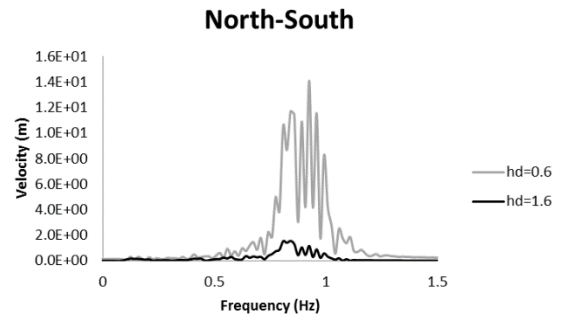
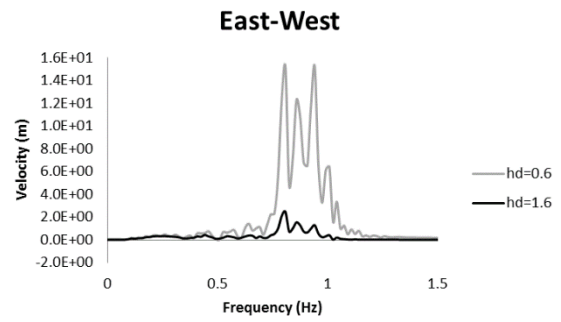


Figure 4-18. Simulated a) velocity time series and b) Fourier spectrum of soil site for Mw=4.7 using half durations of 0.6 s and 1.6 s for Gaussian source function.

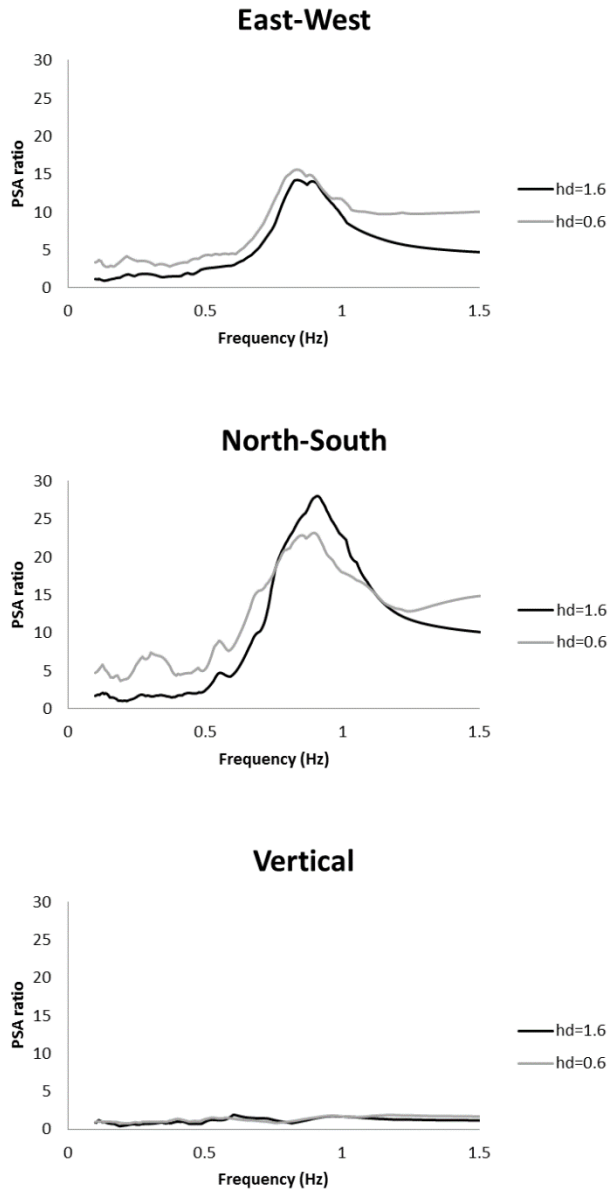


Figure 4-19. Comparison of PSA ratios of soil site to rock site for  $M_w=4.7$  using half durations of 0.6 s and 1.6 s for Gaussian source function.

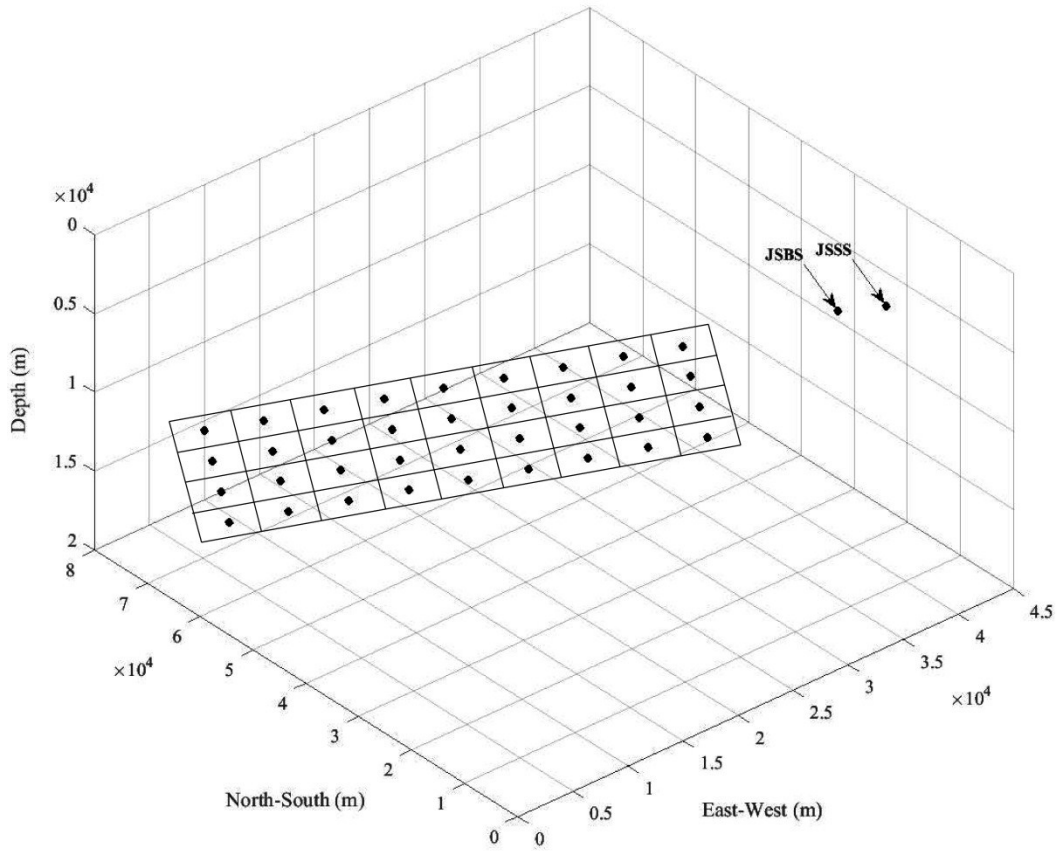
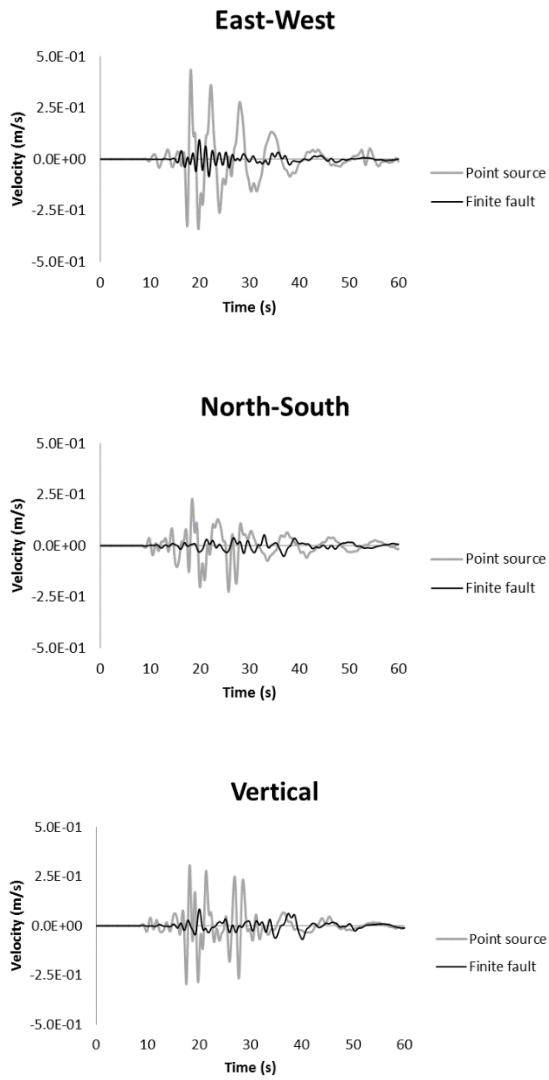


Figure 4-20. 3D view of sub-faults of the finite fault plane used for simulation.

a.



b.

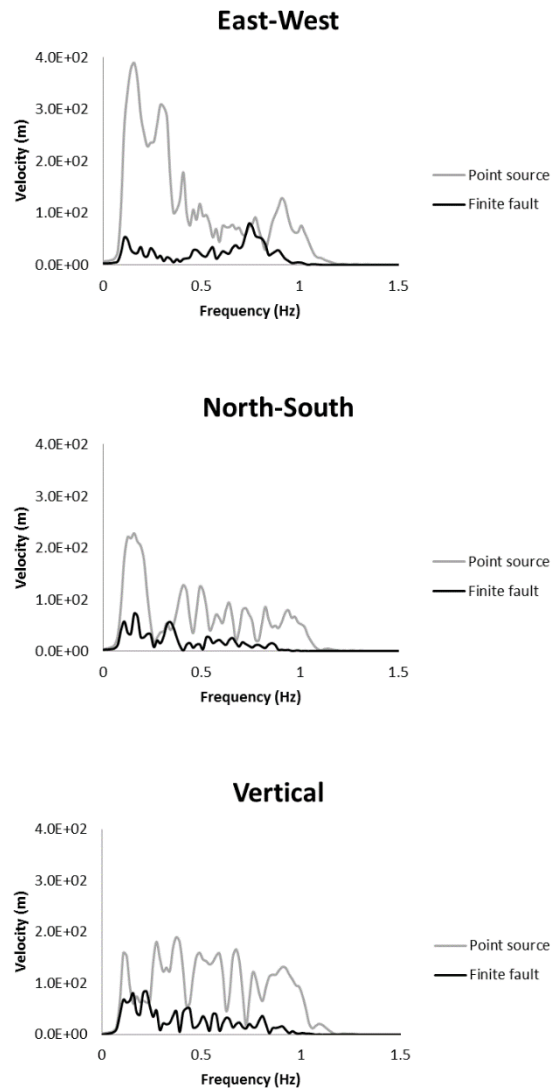
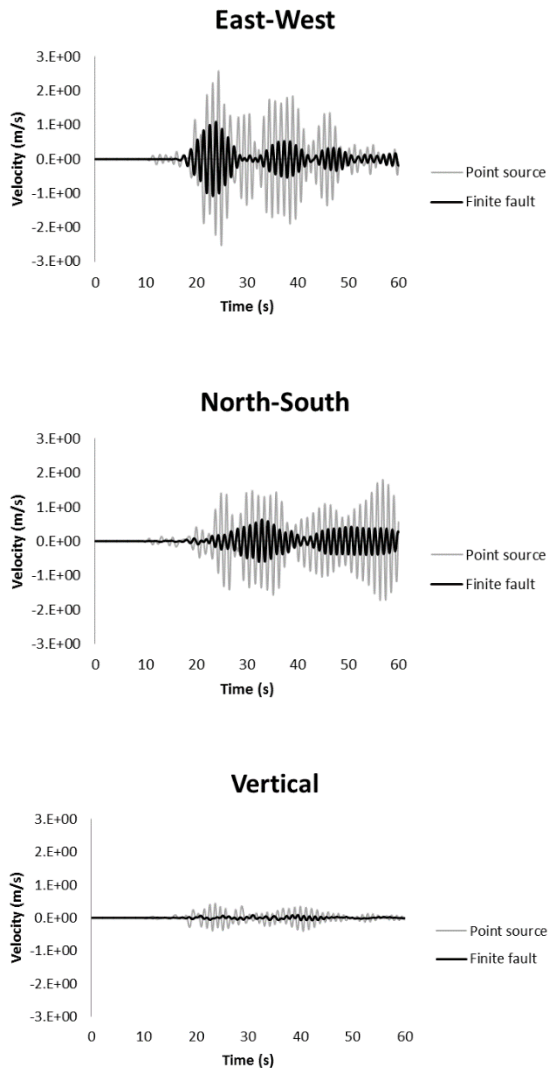


Figure 4-21. Simulated a) velocity time series and b) Fourier spectrum of rock site for Mw=7 using point source model and finite fault model.

a.



b.

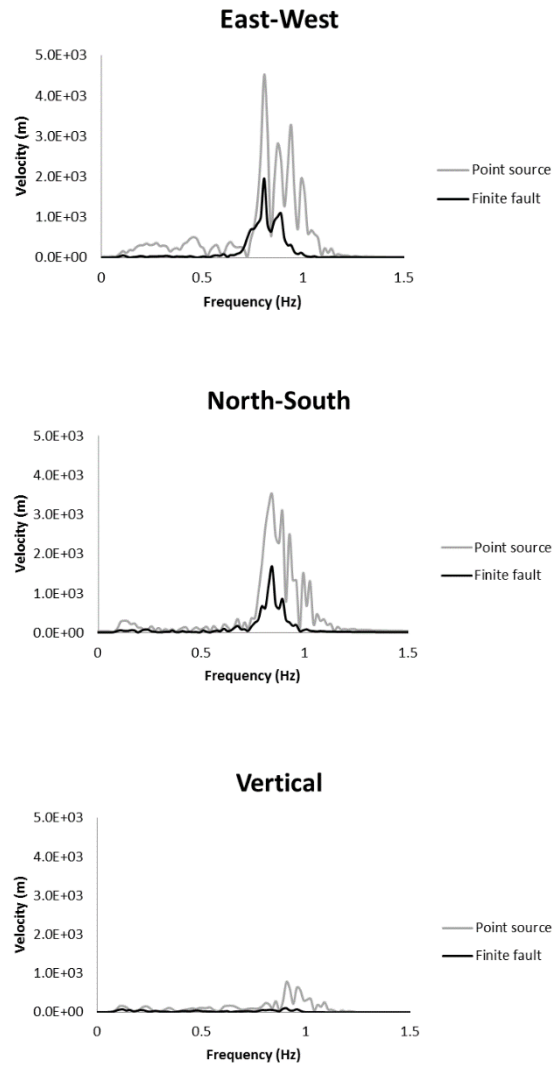


Figure 4-22. Simulated a) velocity time series and b) Fourier spectrum of soil site for  $M_w=7$  using point source model and finite fault model.

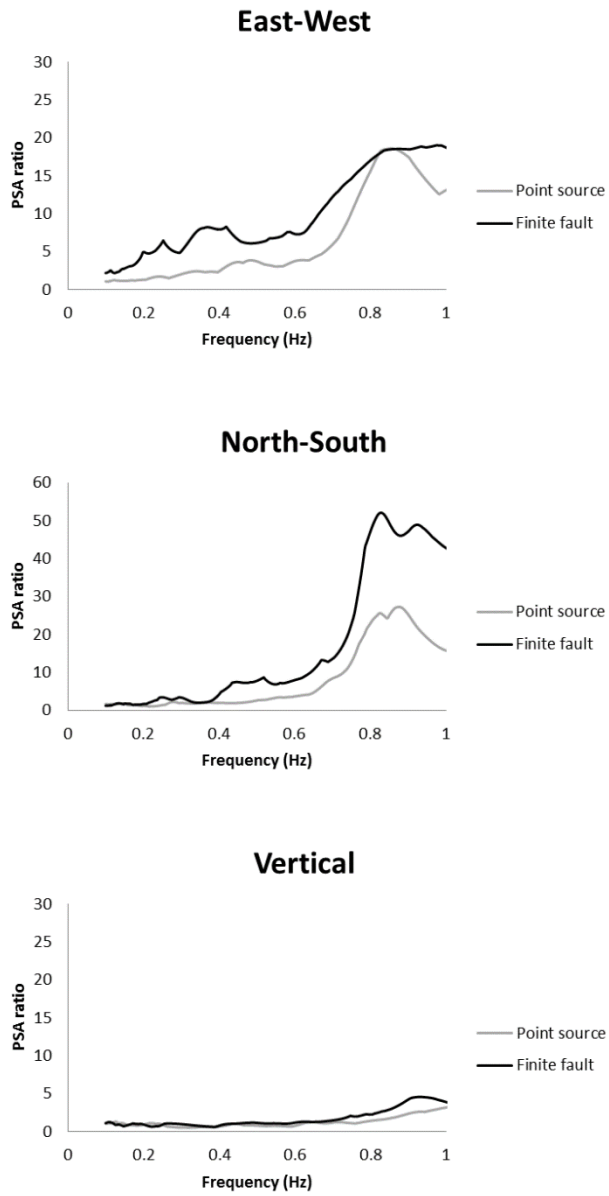
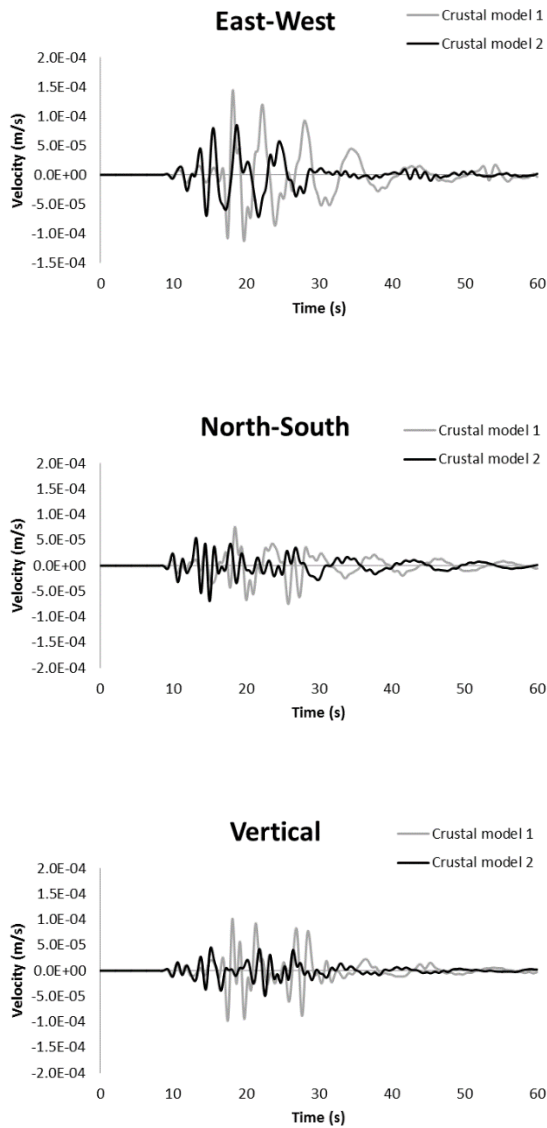


Figure 4-23. Comparison of PSA ratios of soil site to rock site for Mw=7 using point source model and finite fault model.

a.



b.

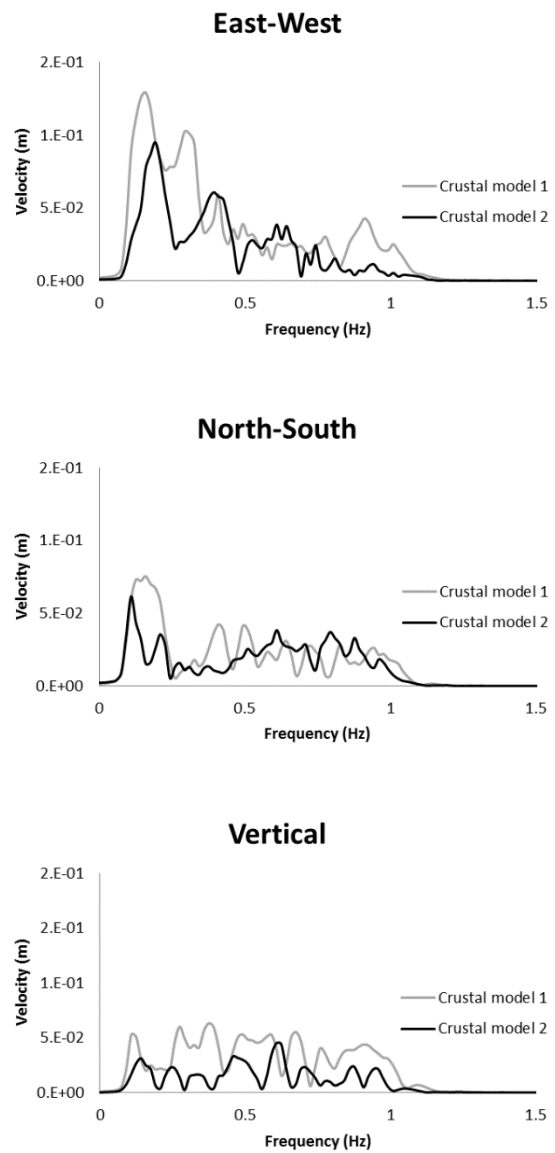
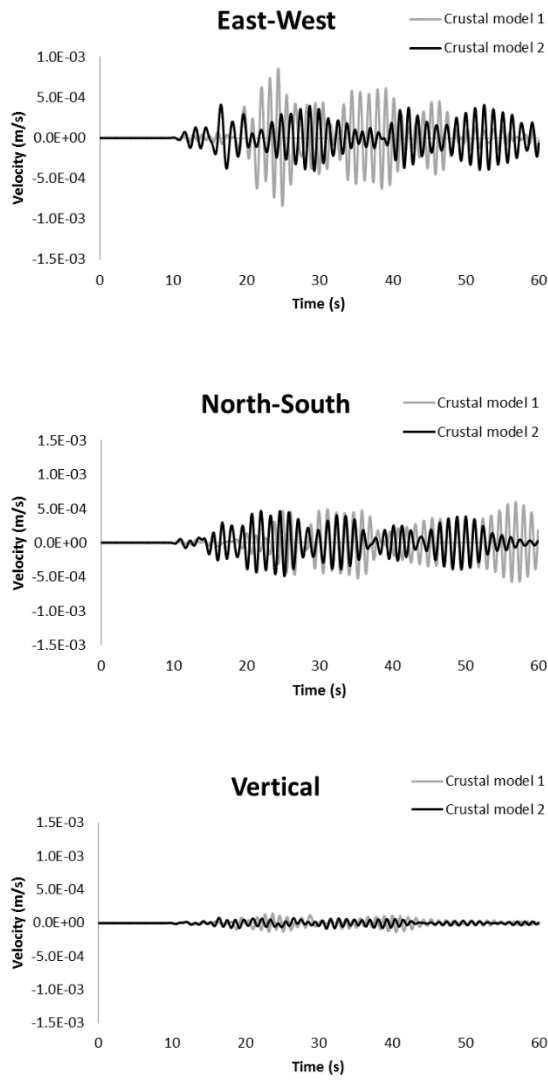


Figure 4-24. Simulated a) velocity time series and b) Fourier spectrum of rock site for Mw=4.7 using crustal model 1 and crustal model 2.

a.



b.

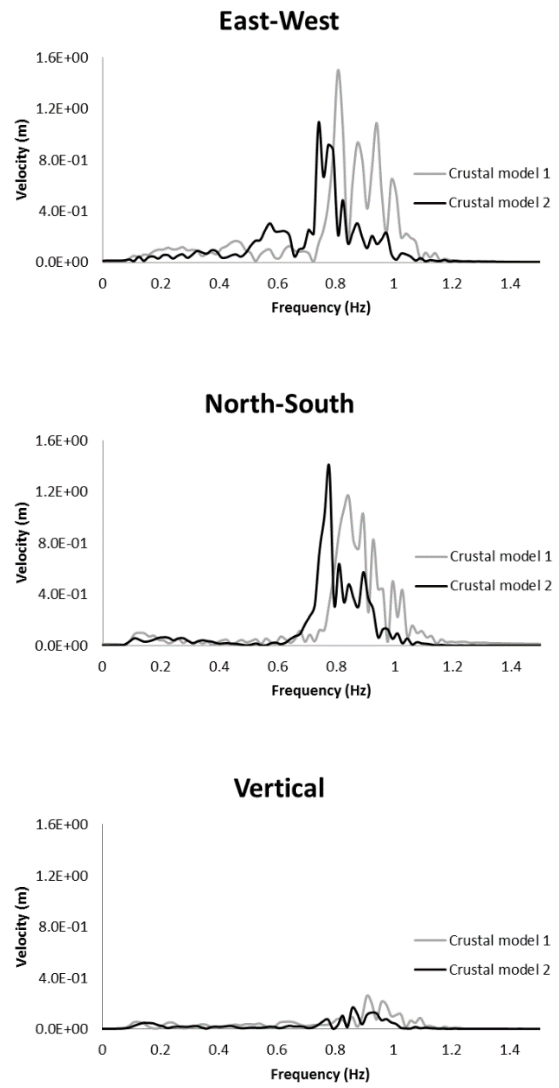


Figure 4-25. Simulated a) velocity time series and b) Fourier spectrum of soil site for Mw=4.7 using crustal model 1 and crustal model 2.

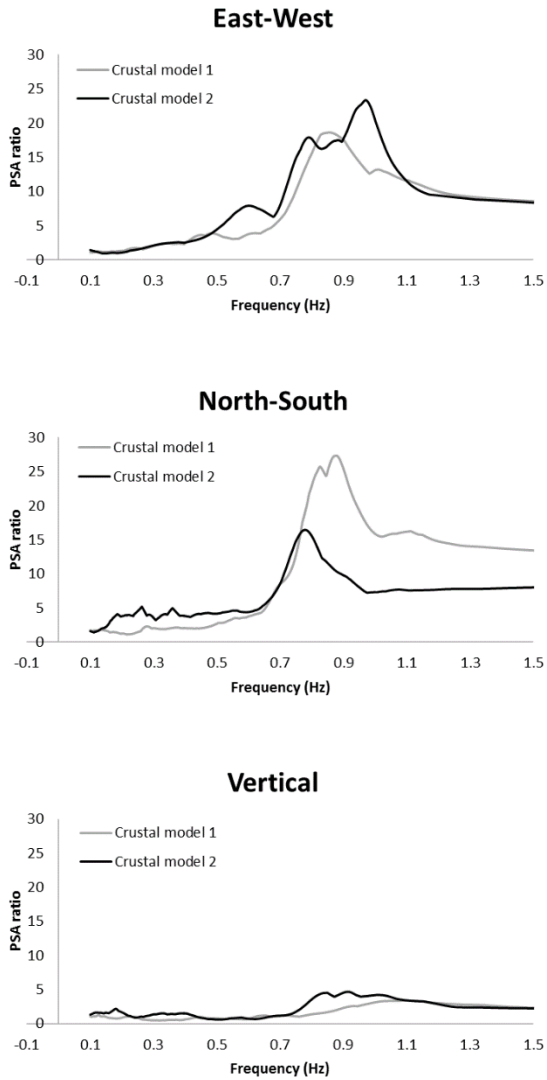
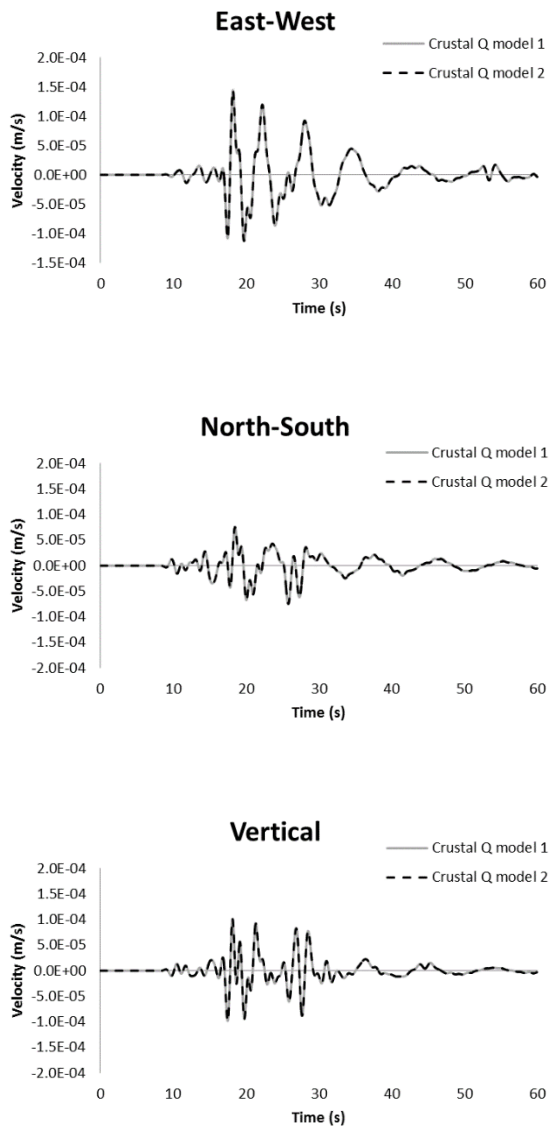


Figure 4-26. Comparison of PSA ratios of soil site to rock site for Mw=4.7 using crustal model 1 and crustal model 2.

a.



b.

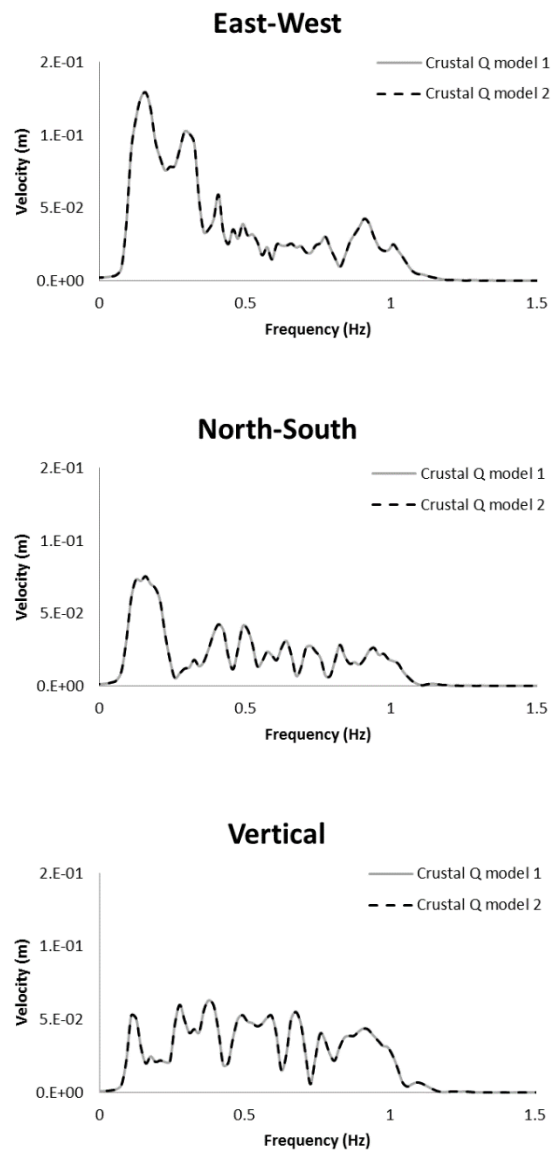
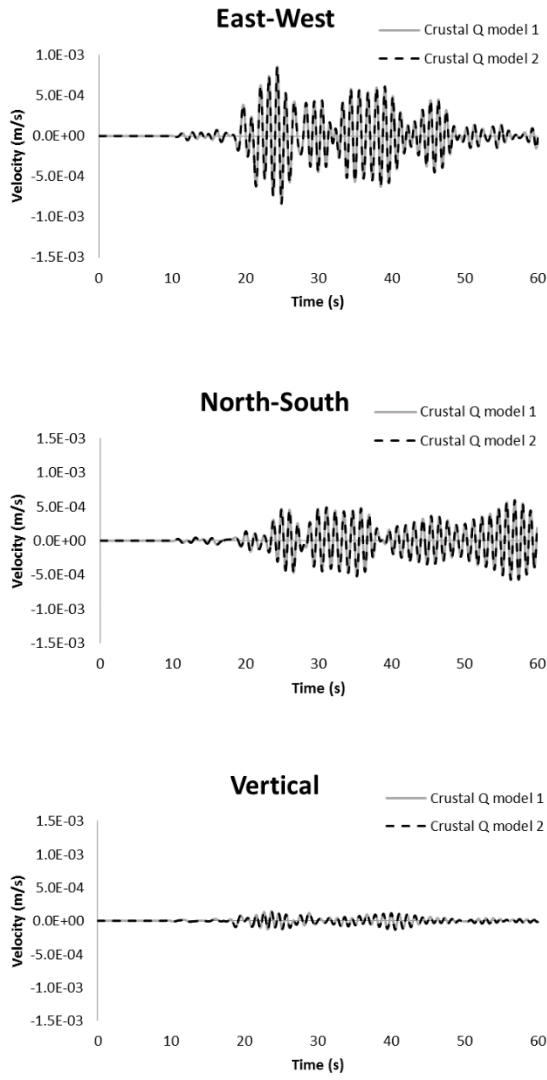


Figure 4-27. Simulated a) velocity time series and b) Fourier spectrum of rock site for  $M_w=4.7$  using crustal Q model 1 and crustal Q model 2.

a.



b.

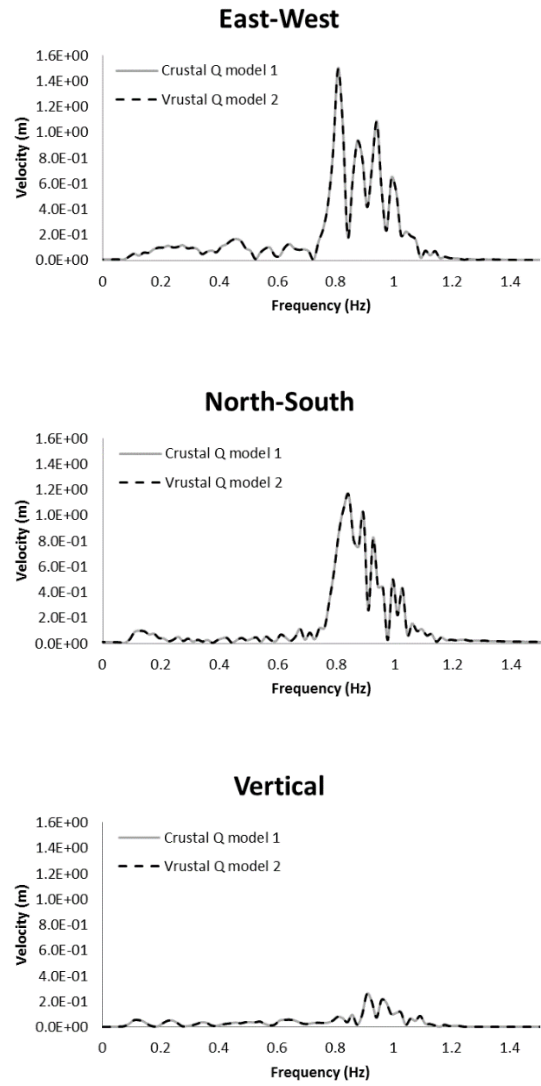


Figure 4-28. Simulated a) velocity time series and b) Fourier spectrum of soil site for Mw=4.7 using crustal Q model 1 and crustal Q model 2.

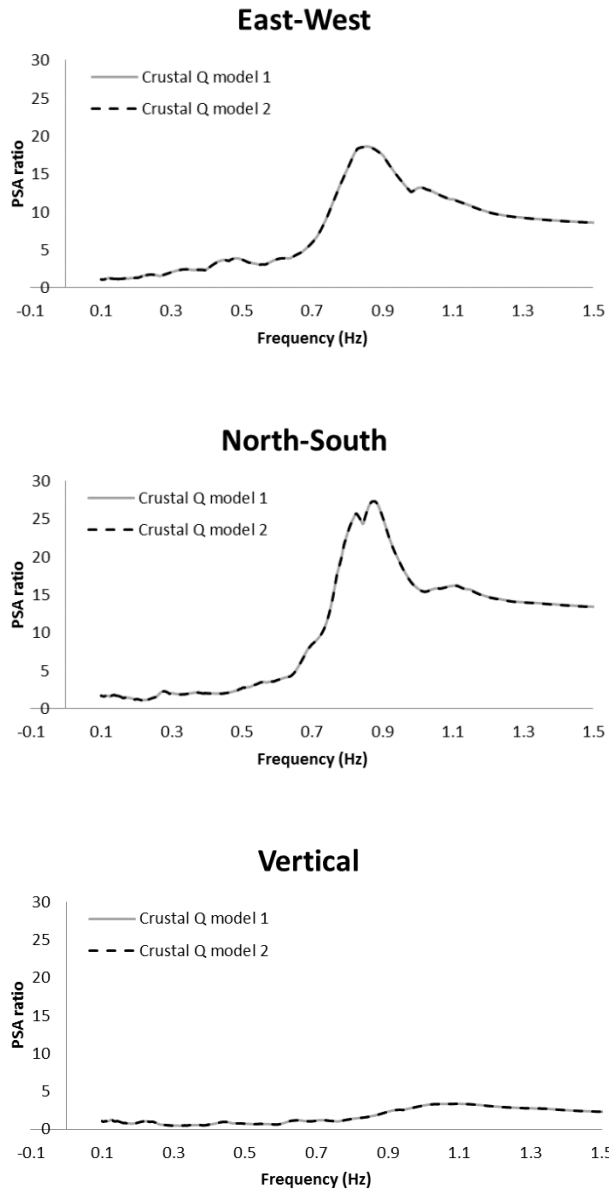
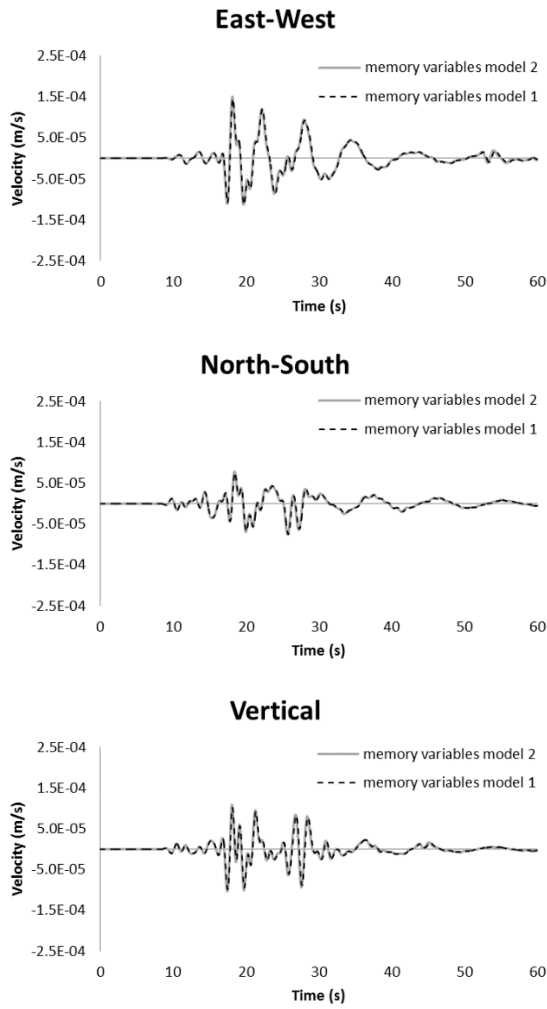


Figure 4-29. Comparison of PSA ratios of soil site to rock site for Mw=4.7 using crustal Q model 1 and crustal Q model 2.

a.



b.

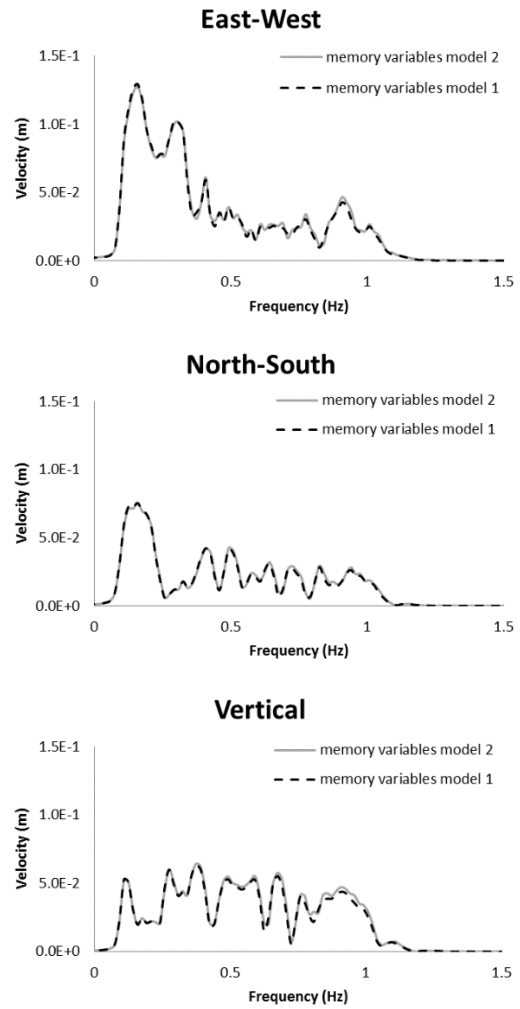
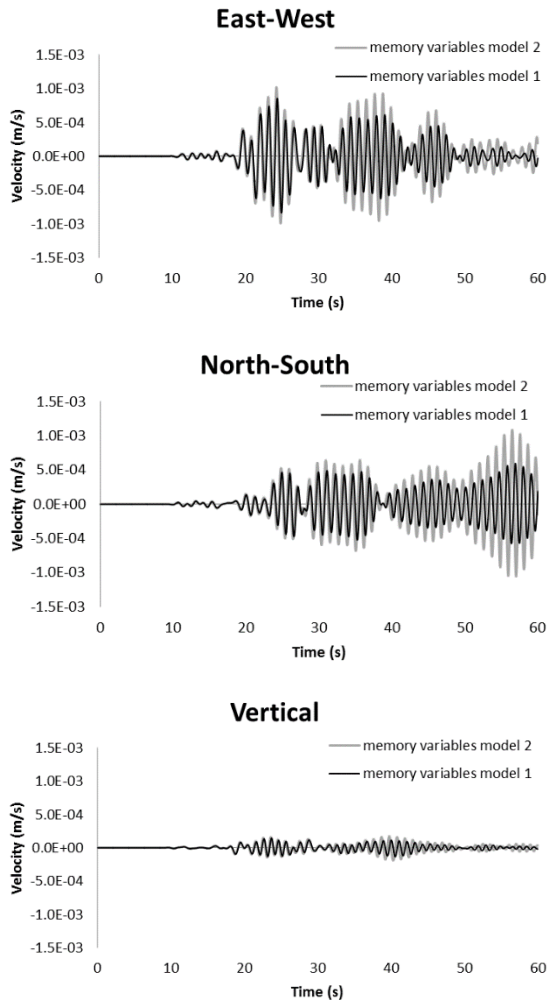


Figure 4-30. Simulated a) velocity time series and b) Fourier spectrum of rock site for Mw=4.7 using the memory variables model 1 and the memory variables model 2.

a.



b.

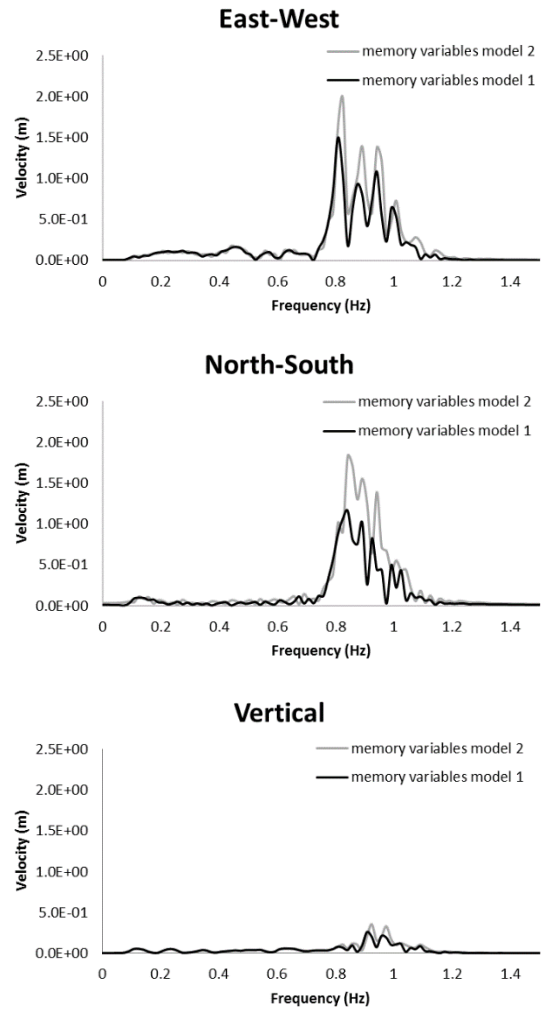


Figure 4-31. Simulated a) velocity time series and b) Fourier spectrum of soil site for Mw=4.7 using the memory variables model 1 and the memory variables model 2.

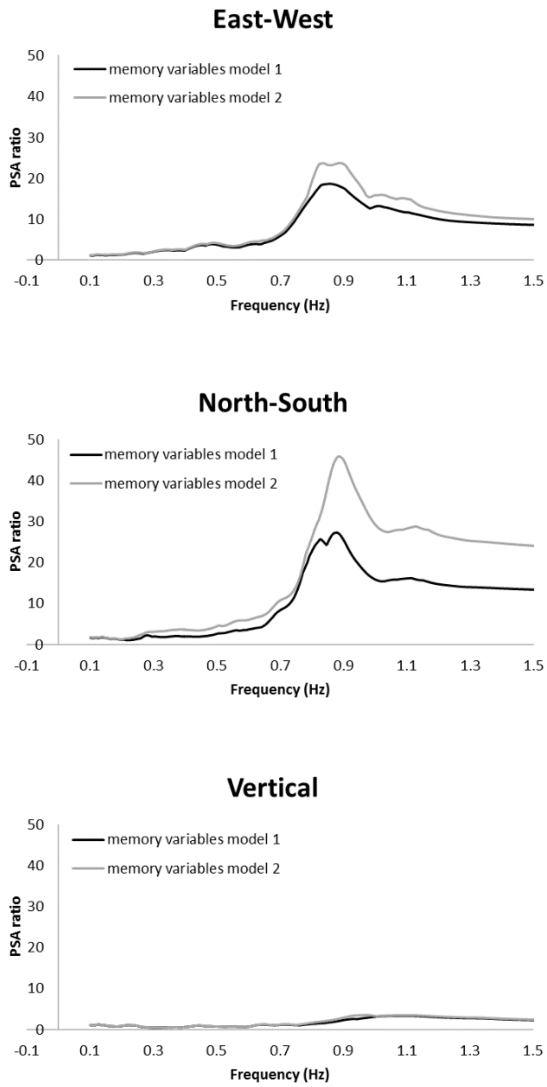
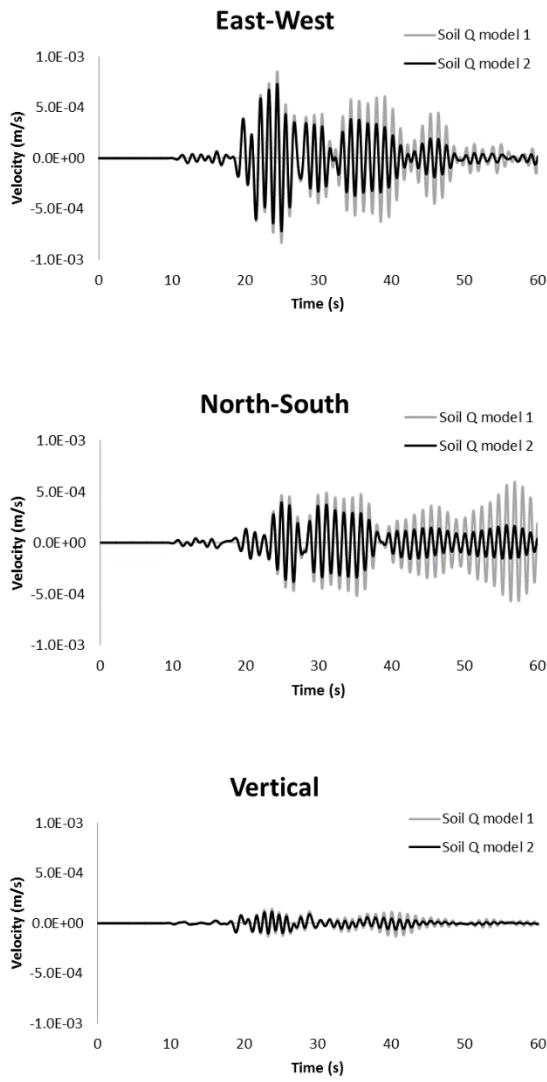


Figure 4-32. Comparison of PSA ratios of soil site to rock site for Mw=4.7 using the memory variables model 1 and the memory variables model 2.

a.



b.

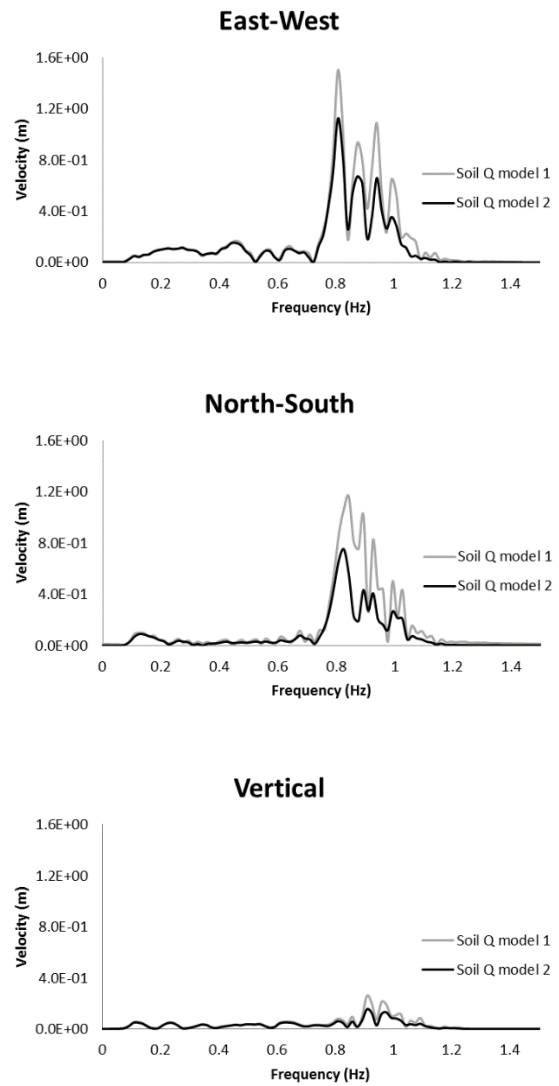


Figure 4-33. Simulated a) velocity time series and b) Fourier spectrum of soil site for Mw=4.7 using soil Q model 1 and soil Q model 2.

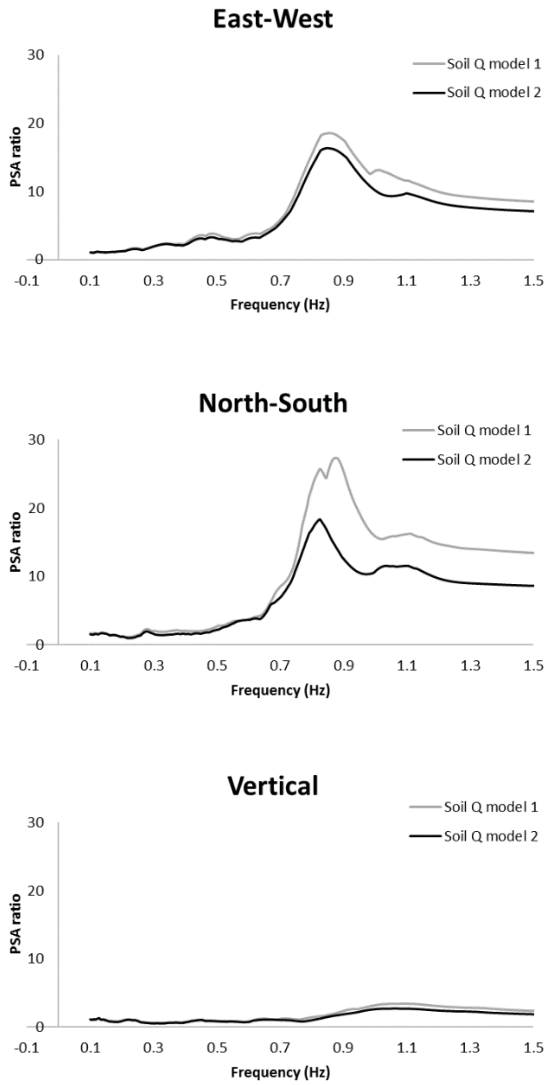
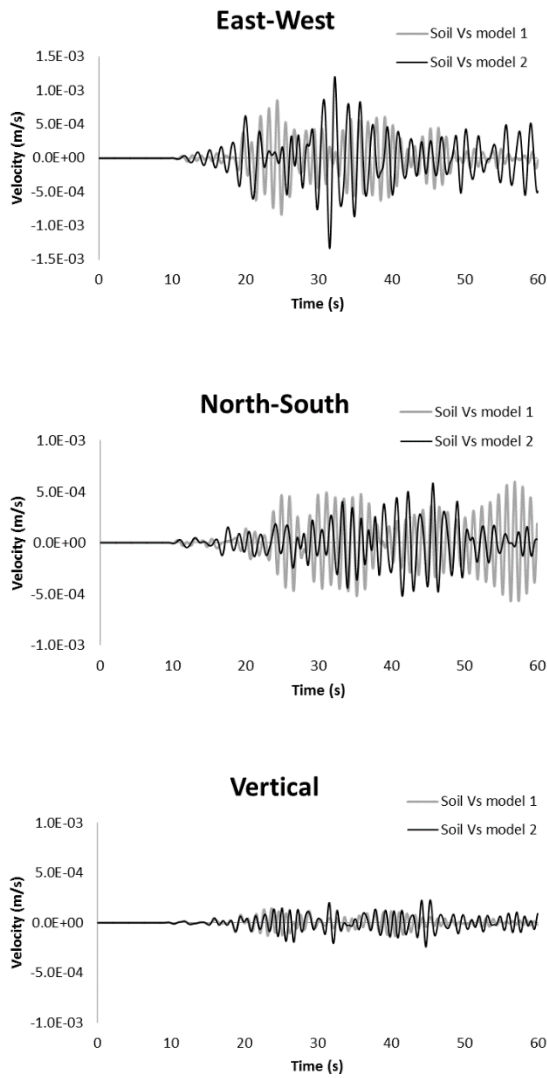


Figure 4-34. Comparison of PSA ratios of soil site to rock site for Mw=4.7 using soil Q model 1 and soil Q model 2.

a.



b.

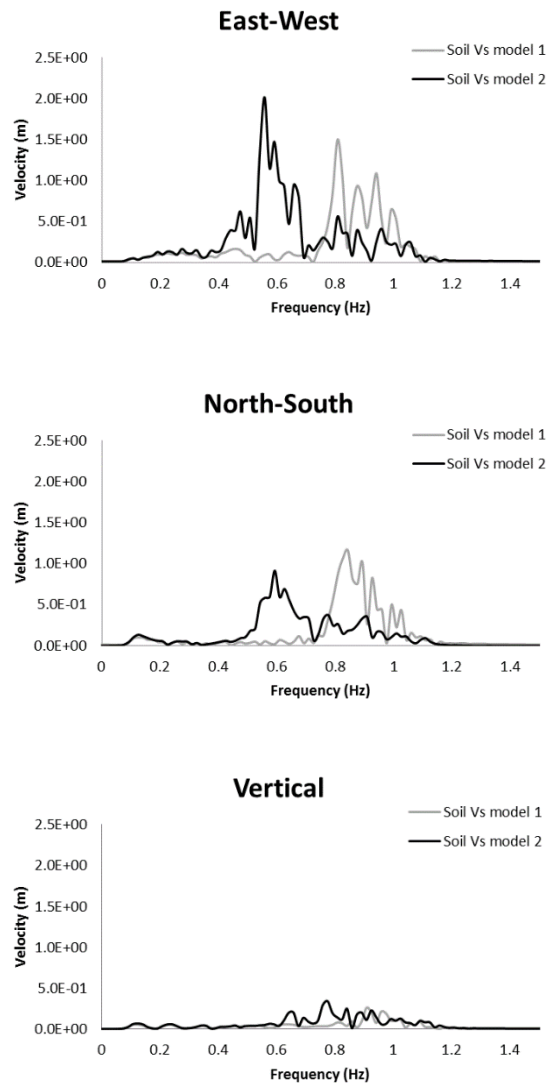


Figure 4-35. Simulated a) velocity time series and b) Fourier spectrum of soil site for Mw=4.7 using soil Vs model 1 and soil Vs model 2.

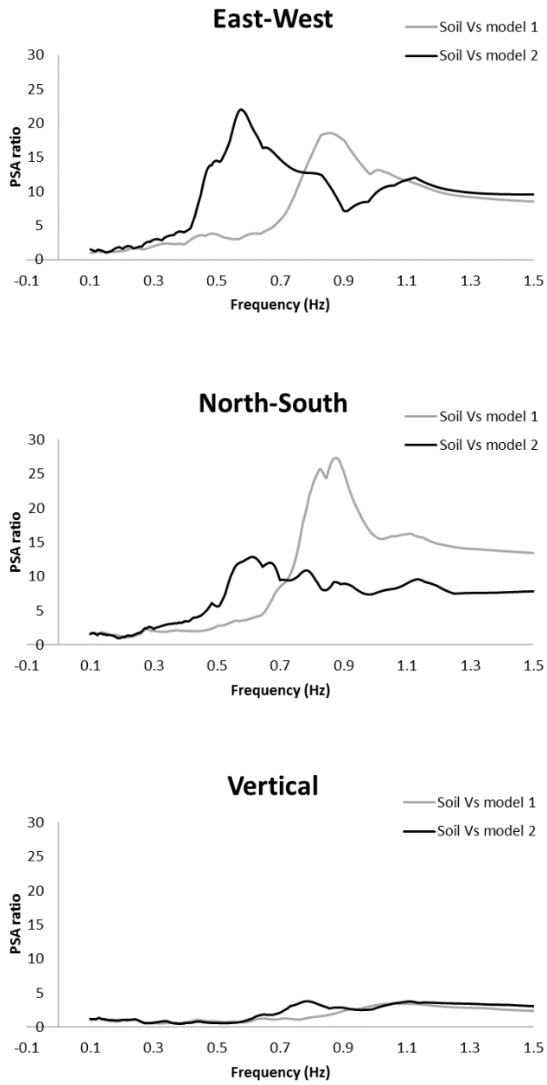
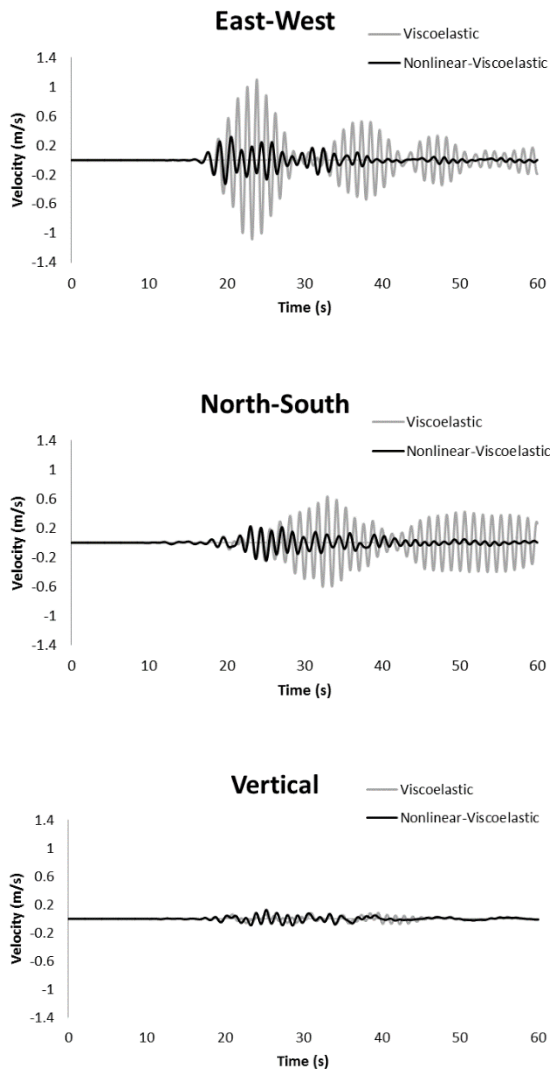


Figure 4-36. Comparison of PSA ratios of soil site to rock site for Mw=4.7 using soil Vs model 1 and soil Vs model 2.

a.



b.

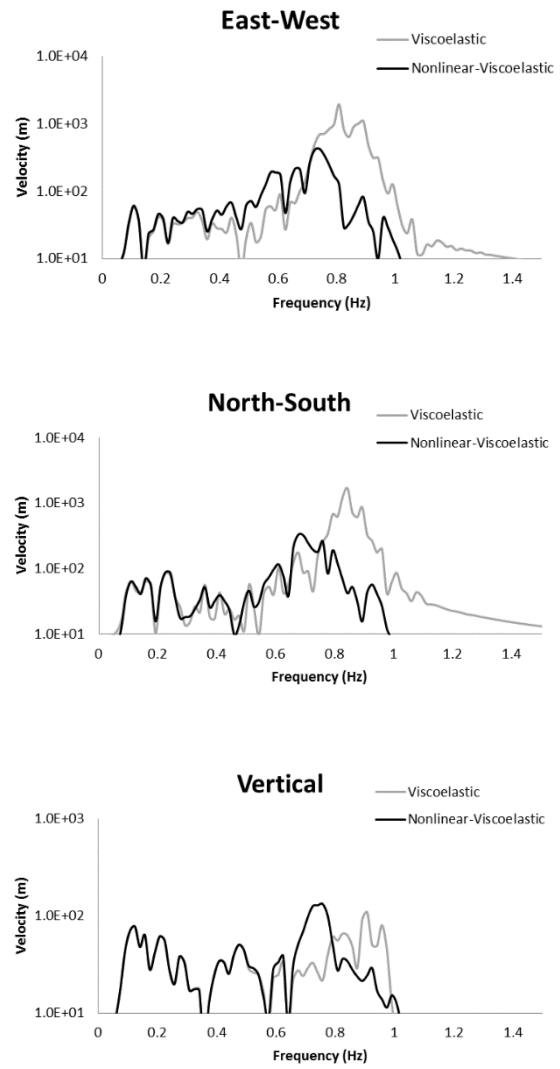


Figure 4-37. Simulated a) velocity time series and b) Fourier spectrum of soil site for  $M_w=7$  using viscoelastic simulation and nonlinear-viscoelastic simulation.

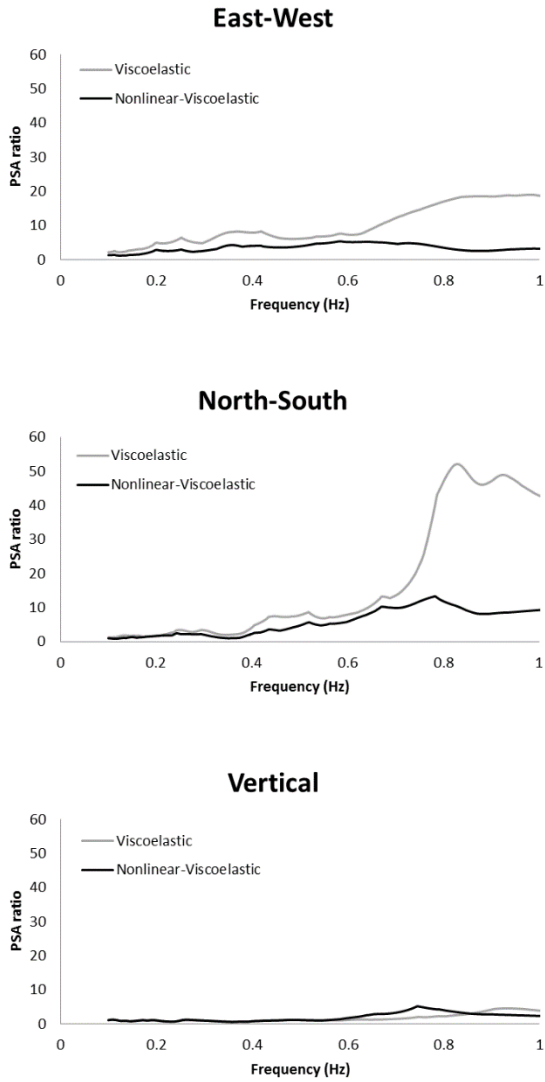


Figure 4-38. Comparison of PSA ratios of soil site to rock site for Mw=7 using viscoelastic simulation and nonlinear-viscoelastic simulation.

**5. Increasing the maximum frequency to 2.5 Hz in finite difference modeling  
using a dual grid size method for basins in Ottawa, Canada**

## **Abstract**

We applied a single grid size for a frequency range of 0.1 Hz to 1.0 Hz and a dual grid size for a frequency range of 0.1 Hz to 2.5 Hz in finite difference (FD) modeling to simulate ground motions in the Kinburn and Orleans basins in Ottawa, Canada. Comparing recorded and simulated velocity time series showed that viscoelastic simulations were capable of modeling the ground motions at rock and soil sites in both basins for the Ladysmith earthquake, a local earthquake that occurred on 17 May 2013 with  $M_w$  4.7 ( $M_N$  5.2). The dual grid size method more accurately predicted the PGVs in all three components and modeled soil amplification in the Kinburn basin although there were large differences between the amplitude of the velocity Fourier spectrum of simulations and the amplitude of the recordings. The simulated velocity time series from the dual grid size method provided the spectrum at higher frequencies compared to that of the single grid size and the velocity Fourier spectrum of the recordings and simulations showed a similar variation versus frequency. Further, using the dual grid size method increased the PGVs and amplitudes of the velocity Fourier spectrum for the Kinburn basin compared to the results of simulations for the single grid size method. Comparing the PSA ratios of simulations and recordings showed that the broadband ground motion simulation reasonably predicted the amplitude of the PSA ratios for the horizontal components, while the amplitude of the PSA ratio for the vertical component was not accurately predicted. Furthermore, the frequency associated with the amplitude of the PSA ratios for the horizontal components in the broadband ground motion simulation for Orleans basin was slightly smaller than the frequency of the amplitude of the PSA ratios in the recordings.

## 5.1. Introduction

Time domain Finite Difference (FD) modeling has become a popular technique for ground motion simulation in heterogeneous media because of its flexibility in representing complex models and its computational efficiency. Mostly, the modeled area is discretized on a numerical grid with a single grid size. Simulating seismic waves with a single grid size in heterogeneous high-velocity contrast media, such as sedimentary basins with very low seismic wave velocity over a very high seismic wave velocity bedrock, requires small-grid spacing that is determined by the minimum shear wave velocity of soil in the sedimentary basin. Thus, the high velocity contrast between soil in the sedimentary basin and the bedrock leads to unnecessary oversampling of the bedrock. In contrast, simulating wave propagation, which does not include the low seismic velocity of soil in basins, produces inaccurate results.

Thus, the discretization of small-scale heterogeneities, such as basins, needs a dense sampling with a small grid size, which causes an extensive oversampling of the bedrock. Therefore, simulating high-frequency ground motions in a large-scale, geologically realistic, 3D structure needs a large number of grids, which is still a computational challenge (Köhn and Bohlen, 2000; Wu and Harris, 2004; Zhang et al., 2012; Nie et al., 2017). For example, increasing the highest simulated frequency in the FD method by a factor of  $N$  (or decreasing the shear wave velocity by  $N$ ) reduces the grid size by  $N$ , which increases the necessary memory for simulation by  $N^3$  and increases the computational time by  $N^4$  (Aoi and Fujiwara, 1999). Thus, a single grid size is not practical for frequencies above 1 Hz and a dual grid size is necessary to achieve optimal computational efficiency for higher frequencies (Wang, 2000).

There are many techniques that implement dual grid sizes in time domain FD modeling. While some approaches use dual grid sizes in one direction only (e.g., Jastram and Tessmer,

1994; Falk et al., 1996; Pitarka, 1999), others employ dual grid sizes in all dimensions (e.g., Jastram and Behle, 1991; Wang and Schuster, 1996; Köhn and Bohlen, 2000; Wang et al., 2001; Nie et al., 2017).

One simple method to implement dual grid sizes in ground motion simulations is to continuously decrease spacing in low-velocity regions and thin layers and increase grid spacing in the other parts of the model (Moczo, 1989; Pitarka, 1999; Zhang et al., 2008; Zhang et al., 2012a). Although using a dual grid size method can reduce computational cost, it is more efficient to use dual grid sizes in which grid spacing does not continuously vary but rapidly changes. Thus, dual grid size methods, which discretized media using a large grid size for the bedrock and a small grid size for the basin, provide a more convenient way to overcome computational efficiency issues (Aoi and Fujiwara, 1999; Tessmer, 2000; Hayashi et al., 2001; Wang et al., 2001; Bielak et al., 2003; Kristek et al., 2010; Zhang et al., 2012; Nie et al., 2017).

In contrast, most of the all-in-one source-path-site computational methods that implement dual grid sizes suffer from instability in long-time simulations. This instability arises from numerical noise generated at the overlap basin-bedrock boundary with different grid sizes. In addition, there are some limitations associated with the number of grids in the transition zone, which is the basin-bedrock boundary. At least 7–8 grid points per minimum S wavelength inside the grid overlap zone are required. Further, the ratio of the coarse grid size to fine grid size, and the boundary conditions used in simulation are the limitations that should be considered for the stability of the program (Hayashi et al., 2001; Kristek et al., 2010; Zhang et al., 2012; Nie et al., 2017).

Other two-step methods are available and are applied in 2D FE-FE (finite element) modeling, 3D FE-FE modeling, 2D FD-FD hybrid simulations, and 3D FD-FD hybrid simulations (eg.,

Bielak and Christiano, 1984; Cremonini et al., 1988; Oprsal and Zahradnik, 1999; Oprsal and Zahradnik, 2002; Bielak et al., 2003; Yoshimura et al., 2003). There are also other various methods in seismic modeling; those methods refer to the combination of deterministic low-frequency (LF) ground motion simulations (for frequencies of 0.5-1 Hz) and a stochastic high-frequency (HF) component to generate synthetic seismograms for the entire frequency range of engineering interest (0-10 Hz) (Hartzell et al., 1999; Pitarka et al., 2000; Oprsal and Zahradnik, 2002; Hartzell et al., 2005; Liu et al., 2006; Mai et al., 2010; Olsen, 2011).

In this study, we develop a dual grid size method, which is a two-step technique, to model seismic waves for a broad frequency range (0.1 Hz to 2.5 Hz) and overcomes the instability issue. Our new dual grid size method combines two FD models (one for soil and one for rock) where each model uses a specific grid size based on the velocity model that is used in each simulation (Oprsal and Zahradnik, 2002).

## **5.2. Study sites**

The study basins are situated along the southern edge of the Western Quebec Seismic Zone (WQSZ) (Figure 5-1), which has experienced several moderate to large earthquakes, including a  $M_w=6.1$  in 1935 in the Temiscamingue region and a  $M_w=5.8$  in 1944 in the Cornwall-Massena region (Cassidy et al., 2010). Because of the regional population and seismic hazards, Montreal and Ottawa are ranked second and third, respectively, behind Vancouver, in terms of seismic risk in Canada.

The two studied basins, the Kinburn and Orleans basins, are located in the Ottawa region as shown in Figure 5-2 [Vs30 map of the Ottawa region (Motazedian et al., 2011; Hunter et al., 2012)]. The geotechnical and geological features of these two basins are unique: loose,

postglacial sediments with very low shear wave velocities ( $\sim 150$  m/s on average overlying very firm bedrock with high shear wave velocities ( $\sim 2700$  m/s on average).

In this study, we used the Ladysmith earthquake, which occurred at 09:43 EDT (13:43 UTC) on 17 May 2013 measuring  $M_w$  4.7 (MN 5.2). The epicentre of the earthquake was located 18 km northeast of Shawville in southwestern Quebec and 4 km from the small community of Ladysmith (Figure 5-3) (Bent et al., 2015). The earthquake occurred in the WQSZ, a broad region of moderate earthquake activity extending northwest from Montreal to the Lake Timiskaming region in Quebec. The Ladysmith earthquake was recorded by two strong motion stations, JSBS (rock site) and JSSS (soil site), in the Kinburn basin (Figure 5-4). Also, the Orleans basin was instrumented with soil site (ORHO) and rock site (ORIO) seismometers (Figure 5-5). A comparison of the recordings at rock and soil sites for the Kinburn basin (Figure 5-6.a) and Orleans basin (Figure 5-6.b) showed significant amplification within the basins. The recordings from both basins were later used to verify the simulated time series at rock and soil sites.

### **5.2.1. The Kinburn Basin**

The Kinburn basin consists of a series of smaller interconnected basins. For this study, one of these basins is referred to as the Kinburn basin (Figure 5-2). This Kinburn basin (lat.  $45^{\circ}22'59.5''N$ , long.  $76^{\circ}09'16.5''W$ ) is located 2.8 km southeast of the hamlet of Kinburn, Ontario (Fulton, 1987). The basin is roughly 7 km long from northwest to southeast and about 5 km long southwest to northeast. The prepared Landstreamer seismic section in the Kinburn basin shows that the northern and eastern portions of the basin are surrounded by Precambrian rocks, which can be seen in outcrops beyond the basin (Hunter et al., 2010; Pugin et al., 2013; Crane,

2016). Based on seismic and borehole data, a Paleozoic carbonate bedrock ridge bounds the depression to the south and west, and a Precambrian Shield ridge bounds the depression to the north and east (Richard, 1984). The maximum depth of soil in basin is approximately 100 m. The basin is mostly filled with high water content (low shear wave velocity) Holocene age silts or silty clay deposits, often referred to as Leda Clay. This material was deposited in the Champlain Sea during the last retreat of glaciers in the region. The seismic velocity of near surface soils (between 0-6 m) generally increases sharply as depth increases to a maximum depth of approximately 5 m, which may be caused by over consolidation of the clay from successive freeze-thaw cycles (Eden and Crawford, 1957). The Holocene sediments overlie a thin layer of Pleistocene glacial deposits, which directly overlie the bedrock in many locations. The Pleistocene glacial deposits are thicker in the deeper portions of the basin, while there is no evidence of their presence close to the bedrock outcrops (Hunter et al., 2012; Hayek, 2016; Crane, 2016).

For this research, the Kinburn basin depth (Figure 5-4) was modeled based on 900 City of Ottawa water wells, 286 horizontal-to-vertical spectral ratio (HVSR) measurements (Hunter et al., 2007; Hunter et al., 2010), 2 high resolution Landstreamer seismic lines (Pugin et al, 2013), and a GSC logged borehole (Medioli et al., 2012). The velocity profile of the Kinburn basin that was extracted from the borehole logging studies at a site near the deepest part of the basin was used to model the basin.

### **5.2.2. The Orleans Basin**

The Orleans basin is small and bowl-shaped, and the Kinburn basin is large and elongated. Both basins are oriented in a northeast to southwest direction (Hayek, 2016). The Orleans basin

is located in a residential area around Heritage Park in the eastern part of Ottawa. It is approximately 9 km by 10 km with steep sides (Motazedian and Hunter, 2008). There is a broad opening to the northwest, and a narrow one to the southwest (Kolaj, 2010).

The Orleans basin was inundated by the Champlain Sea approximately 10,000 – 12,000 years ago. The underlying bedrock is composed of Paleozoic sedimentary limestone, dolostone, shale, and sandstone, which overlie Precambrian crystalline basement rock. The depth to the bedrock is extremely variable; however, much of the Orleans basin has a depth to the bedrock of greater than 10 m. Late Quaternary deposits, which consist of glacialigenic gravel diamicton (till), overlie the bedrock. The layers of till, glaciofluvial gravel, and sand are relatively thin (1–3 m) in most areas, but they may be thicker (~5 m or more) within the topographic lows of the bedrock. Glaciomarine silty clays and pro-delta silts are deposited on top of all other layers within the former Champlain Sea. The Champlain Sea deposits (Leda clay) consist of glacially-ground, non-clay minerals held together in a loose structural framework (Torrance, 1988). These materials are geotechnically sensitive as the water content is quite high, which can result in reduced overall shear. Furthermore, the replacement of the original saline pore water with fresh water in these sediments can cause a loss of strength and collapse leading to flow-sliding along escarpments and river banks. The thickness of post-glacial sediment in the Orleans basin ranges from < 1 m thick to over 100 m thick where it has accumulated in bedrock depressions and valleys. In addition, a thin, high-velocity surface layer exists in the upper few metres of the Champlain Sea sediments throughout the Ottawa area. This layer could have been caused by natural over consolidation (Crow et al., 2007; Motazedian and Hunter, 2008; Motazedian et al., 2011; Hayek, 2016). The Orleans depth (Figure 5-5) was modeled using information from the borehole database, sixty-three additional seismic sites, and 3 landstreamer lines (Crow et al.,

2007).

### **5.3. Uniform grid size finite difference simulations for a frequency range of 0.1-1 Hz**

In this step, we used the FD code (Anelastic Wave Propagation - AWP), developed and maintained by Kim B. Olsen, Steven M. Day, and Yifeng Cui (ODC) (Olsen, 1994; Olsen et al., 1995, 2003, 2006; Cui et al., 2009), which simulated the 3D propagation of a spontaneous rock rupture. This program solves 3D velocity-stress wave equations with an explicit staggered-grid FD scheme. This method, which is fourth-order in space and second-order in time, can be used for elastic, viscoelastic, elastoplastic, and visco-elastoplastic behavior (Cui et al., 2010; Narayan, 2010).

We used 200 computer cores and 258.2 gigabytes (GB) of memory for the Kinburn basin simulations in a 3D block of 21 km by 50 km by 17.5 km with an earthquake epicentral distance=43 km for East-West\*North-South\*Vertical directions. The computational time for each time step of simulations was 1.427 s, and the whole running time was 16.82 hrs.

We used 300 computer cores and 387.3 GB of memory for the Orleans basin simulations in a 3D block of 71.25 km by 37 km by 15 km with an earthquake epicentral distance=70.4 km for East-West\*North-South\*Vertical directions. The computational time for each time step of simulations was 1.899 s, and the whole running time was approximately 36.6 hrs.

#### **5.3.1. Main input parameters for simulations**

*Maximum frequency, grid size, and time step:* The FD method requires at least four samples per wavelength to model a wave. Thus, the grid size or spatial step ( $\Delta h$ ) is based on the minimum velocity in the average velocity model (associated with the minimum shear wave velocity in a velocity model) and the maximum frequency of interest. Then, because of the maximum wave

velocity in the velocity model and the Courant number for the stability of the FD method, the time step for simulation is calculated as follows:

$$dt < 0.5 * dh / V_{max} \quad (1)$$

In the single grid size simulation for the Kinburn and Orleans basins (using a frequency range of 0.1-1 Hz), we used a spatial step (grid size) of 25 m because the minimum velocities in the velocity model were 178 m/s and 138 m/s for Kinburn basin and Orleans basin, respectively. Further, we used  $dt = 0.0016$  s as the time step for simulations based on the Courant number for the stability of the FD method and the maximum velocities of the velocity models (6200 m/s and 6408 m/s for the Kinburn and Orleans basins, respectively). We used  $dt = 0.0016$  s, which is smaller than the calculated  $dt$  from equation 1, to ensure the stability of simulation.

In the dual grid size method, we used 136 m and 7 m grid sizes for the high velocity and low velocity zones in the Kinburn basin modeling, respectively. The large and small grid sizes for the Orleans basin were 272 m and 10 m, respectively.

*Boundary conditions:* There are two options available for the boundary conditions of simulation: the Cerjan et al. (1985) method and the perfectly matched layer (PML) method (Berenger, 1994; Rappaport, 1995; Chew and Liu, 1996). Previous studies showed that the PML method was more effective than the Cerjan method for absorbing waves at the boundary of a model, particularly in 3D simulations (Marcinkovich and Olsen, 2003; Liu, 2013); thus, PML was employed for this modeling.

*Regional crustal velocity model:* There are many studies that propose crustal shear wave velocity models for Eastern Canada using a wide variety of techniques (e.g., Motazedian et al., 2013; Ma et al., 2013). Motazedian et al. (2013) proposed a crustal shear velocity model for southeastern North America using an average of many techniques. Table 5-1 shows the regional

crustal velocity model used for the Ottawa area (Motazedian et al., 2013; Ma et al., 2013). The primary wave (P-wave) velocity value in each layer was calculated using Poisson's ratio ( $V_p = V_s 1.732$ ). In addition, the density corresponding to the secondary wave (S-wave) velocity value in each layer was calculated following the Nafe–Drake relation ( $V_p$  is in km/s) (Ludwig et al., 1970; Motazedian et al., 2013; Ma et al., 2013):

$$\rho = 1.6612V_p - 0.4721V_p^2 + 0.0671V_p^3 - 0.0043V_p^4 + 0.000106V_p^5 \quad (2)$$

*Geotechnical characteristics of soil in the Kinburn basin:* The borehole shear wave velocity-depth profile was arithmetically averaged within each grid in the velocity model. Below soil layers, we assumed bedrock with a constant velocity, density, and Q for modeling (Hunter et al., 2010; Motazedian et al., 2011; Hunter et al., 2012). Table 5-2 presents the properties of the seismic velocity model, which uses a grid size of 25 m, used in our simulation. In addition, we used an average value of 185 for  $Q_p$  and  $Q_s$  for the whole basin. Also, Q in fine grained soils (clays/silts) was found to be primarily independent of the frequency over some bands (0.1–10 Hz). Further, we used the  $Q_p$  and  $Q_s$  of the regional studies for rock site where  $Q_s$  was equal to half of  $Q_p$  (out of the basin) (Shibuya et al., 1995; Rix and Meng, 2005; Crow et al., 2011).

*Geotechnical characteristics of soil in the Orleans basin:* Motazedian and Hunter (2008) proposed equation 3 (below) as the average shear wave velocity-depth equation for the late post-glacial sediments based on the  $V_s$  measurements obtained from the post-glacial sediments in the Orleans area.

$$V_s = 138 + 0.01205Z^2 \pm 39.6 \quad (3)$$

We used equation 3 to calculate the shear wave velocity (in m/s) of soil within the Orleans basin velocity model. Further, the measured  $V_p$  and density for the Kinburn basin was also used for the Orleans basin. For the  $Q_s$  in the Orleans basin, we used the  $Q_s$  values proposed by Crow

et al. (2011) for soft soil in the Ottawa area. Then, the  $Q_p$  was calculated as  $1.5 Q_s$ . Table 5-3 shows the seismic properties of the Orleans basin.

*The Ladysmith earthquake focal mechanism:* We used two different focal mechanisms, one proposed by Ma and Audet (2014) and one by Bent et al. (2015), for the Ladysmith earthquake to model ground motions in the Kinburn and Orleans basins. Table 5-4 presents the details of the proposed focal mechanisms. Further, our study shows that using the focal mechanism of Ma and Audet (2014) predict the closest PGVs relative to the recordings in simulations (Esmailzadeh et al. 2019). Thus, we used the Ma and Audet (2014) focal mechanism to run the dual grid size simulations for Kinburn and Orleans basins.

*Source function for Ladysmith earthquake:* We used a semi-triangular function to model the evolution of the slip with time on the point source fault for all single grid size simulations. The semi-triangular function is defined as follows:

$$m(t) = M_0 \left( \frac{t}{t_p} \right) \exp\left(-\frac{t}{t_p}\right) \quad (4)$$

where  $m(t)$  is the variation of the seismic moment with time,  $M_0$  is the total seismic moment of an earthquake,  $t$  is time, and  $t_p$  is the time associated with the maximum seismic moment (or the half duration of an earthquake) (Duputel et al., 2013).

Further, we used a Gaussian source function to model the evolution of the slip with time on the point source fault for all dual grid size simulations because our study showed that using the Gaussian source function for simulations predicts the closest PGVs relative to the recordings.

The Gaussian function is defined as follows:

$$M(t) = \frac{M_0}{\sqrt{2\pi\sigma^2}} e^{-\frac{(t-\mu)^2}{2\sigma^2}} \quad (5)$$

where  $M(t)$  is the seismic moment as a function of time,  $M_0$  is the total seismic moment,  $\mu$  is

the mean of the distribution, and  $\sigma$  is the standard deviation of the distribution.

In addition, the half duration of rupture used in simulations was 0.6 s based on the proposed half duration of the Ladysmith earthquake used in the CMT method. Also, this value was verified using other empirical equations (Dziewonski et al., 1981; Duputel et al., 2012; Ekström et al., 2012; Duputel et al., 2013).

*Signal processing:* The velocity time series for simulations and recorded values were filtered with a 12-pole casual Butterworth bandpass filter between 0.1-1.0 Hz, which was an acceptable frequency range for simulation according to the available computational facilities and feasibility of simulation. This filter was designed using the Signal Processing Toolbox for MATLAB (Simulink).

### **5.3.2. Application of single grid size method for a frequency range of 0.1-1 Hz for the Kinburn basin**

A comparison of simulations and recordings at rock site (Figure 5-7) for the Kinburn basin showed that both focal mechanisms reasonably modeled the time series at rock site because the PGV at rock site for the recordings was  $1.14\text{E-}4$  m/s related to the east-west (E-W) component. In addition, the PGVs of simulations were  $7.7\text{E-}5$  m/s and  $1.42\text{E-}4$  m/s for the E-W components for the Bent et al. (2015) and Ma and Audet (2014) proposed focal mechanisms, respectively.

In contrast, a comparison of simulations and recordings at soil site (Figure 5-8) showed differences between the amplitudes of the simulated time series and recorded time series for all three components in both simulations at soil site. However, there was reasonable consistency between the recordings and simulations in the frequency domain between 0.5 Hz to 1.0 Hz. The PGV of the recordings at soil site was 0.0016 m/s for the north-south (N-S) component, but the

PGVs of simulations at soil site were  $5.05\text{E-}4$  m/s for the N-S component and  $8.4\text{E-}4$  m/s for the E-W component for the Bent et al. (2015) and Ma and Audet (2014) proposed focal mechanisms, respectively.

The amplitude of the PSA ratios of the recordings was 28.7 for the N-S component, and the amplitudes of the PSA ratios of simulations were 25.7 and 27.3 for the N-S components for the Bent et al. (2015) and Ma and Audet (2014) proposed focal mechanisms, respectively (Figure 5-9). There was reasonable consistency between the predicted amplitudes of the PSA ratio from the Ma and Audet (2014) simulations and the recordings, even though the frequency associated with the amplitude of the PSA ratio in the recordings was smaller than that in simulation.

### **5.3.3. Application of single grid size method for a frequency range of 0.1-1 Hz for the Orleans basin**

For recorded velocity time series at rock site (Figure 5-10), the PGVs are  $8.5\text{E-}5$  m/s,  $1.2\text{E-}4$  m/s, and  $5.69\text{E-}5$  m/s for the E-W, N-S, and vertical (V) components, respectively. For the modeled velocity time series at rock site (Figure 5-10), the PGVs are  $4.9\text{E-}5$  m/s,  $1\text{E-}4$  m/s, and  $1.5\text{E-}5$  m/s (E-W, N-S, and V components, respectively) for the Bent et al. (2015) focal mechanism and  $8.8\text{E-}5$  m/s,  $2.9\text{E-}4$  m/s, and  $3.1\text{E-}5$  m/s for the E-W, N-S, and V components, respectively, for the Ma and Audet (2014) focal mechanism. In contrast, comparing simulations and recordings in the frequency domain (Figure 5-10) shows a large difference between simulations and recordings, particularly for low frequencies ( $<0.6$  Hz) and for both focal mechanisms.

Figure 5-11 shows that there is reasonable consistency between recorded and modeled velocity time series at soil site, particularly for simulation that uses the Ma and Audet (2014)

focal mechanism. The PGVs of the recordings at soil site are  $1\text{E-}3$  m/s,  $1.1\text{E-}3$  m/s, and  $9.9\text{E-}5$  m/s for the E-W, N-S, and V components. The PGVs are  $4.9\text{E-}4$  m/s,  $7.9\text{E-}4$  m/s, and  $1\text{E-}4$  m/s for the E-W, N-S, and V components of simulation that uses the Bent et al. (2015) focal mechanism (Figure 5-11.a) and  $9.8\text{E-}4$  m/s,  $1.6\text{E-}3$  m/s, and  $2.5\text{E-}4$  m/s for the E-W, N-S, and V components of simulation that uses the Ma and Audet (2014) focal mechanism (Figure 5-11.b). Further, the amplitude of the velocity Fourier spectrum of simulations shifted toward a lower frequency relative to the amplitude of the velocity Fourier spectrum of the recordings in all three components and for both focal mechanisms.

As shown in Figure 5-12, the PSA ratios of soil site to rock site for the recordings are 52.1, 26.7, and 6.5 for the E-W, N-S, and V components. In comparison, simulation using the Bent et al. (2015) focal mechanism predicted PSA ratios of 47.1, 22.9, and 23.9 for the E-W, N-S, and V components, respectively, and simulation using the Ma and Audet (2014) focal mechanism predicted PSA ratios of 43.2, 18.9, and 19.6 for the E-W, N-S, and V components, respectively.

#### **5.4. Dual grid size method for a frequency range of 0.1-2.5 Hz**

Using a single grid size method for ground motion simulations of the Kinburn and Orleans basins for a broadband frequency range (more than 1 Hz) is not feasible as simulations require large computational resources (computational time and memory). The required running time for a simulation of 60 s of wave propagation for a frequency range of 0.1-1 Hz is 16.82 hrs and 36.6 hrs for the Kinburn basin and Orleans basin, respectively. Further, we used 200 computer cores and 258.2 GB of memory for the Kinburn basin simulations and 300 computer cores and 387.3 GB of memory for the Orleans basin simulations.

Thus, we implemented a dual grid size method. For this method, we divided the entire area

(from earthquake source to basin) into two zones: a high velocity zone with a larger grid size and a low velocity zone with a smaller grid size (Figure 5-13). The high velocity zone included a source and regional path from the source to the edge of the basin, and the low velocity zone included the sedimentary basin. The size of the grid in each zone depended on the frequency range of simulation and the stability conditions of the FD simulation.

The developed dual grid size method has two steps: 1) The 3D simulation is used for the high velocity zone to model the source and regional path from the source to the edge of basin. At the end of first step, the evolution of stress over time is recorded and saved around the boundary between high and low velocity zones in three perpendicular planes (X-Y, X-Z, and Y-Z planes); the evolution of stress over time values are then used as input stresses for the low velocity zone in the second step. The location and size of the planes at the boundary between the high and low velocity zones should be defined based on the location of the source relative to the low velocity zone and the size of the low velocity zone. 2) The stress evolution from the first step is used as input for a separate 3D simulation that models ground motion within low velocity zones. Further, the stress evolution is entered into the second step through a special coupling (described later). We use the same time step in both simulations to reduce the number of calculations required for interpolating recorded stress from the course grid size to a fine grid size.

Implementing the dual grid size method speed up modeling; the second step in the computational model that was discretized using a small grid size was a small spatial fraction of the original source-path-site model (Opsal and Zahradnik, 2002).

#### **5.4.1. Implementation of the dual grid size method**

In this section, we explain the linear technique used to interpolate recorded stresses into the

defined planes around the low velocity zone for small grids and for each time step. The linear functions used for the interpolation are defined as follows:

$$\begin{cases} a^0(x) = 1 - x \\ a^1(x) = x \end{cases} \quad (0 \leq x \leq 1) \quad (6)$$

If the ratio of the large grid size (dH) to small grid size (dh) is equal to n (the grid reduction factor), the weights related to the points are  $x=0, 1/n, 2/n, \dots$  and 1. Further, recorded stresses of the big grid size simulation are divided by the grid reduction factor to scale them for the small grid size. Therefore, interpolating the 4 nearest points in a defined plane using the large grid size simulation, we obtain the stress for the points within the same plane in the small grid size simulation (Aoi and Fujiwara, 1999):

$$\begin{cases} \tau_{ij} = \frac{1}{n} \sum_1^n \alpha_{ij}^{IJ} \tau^{IJ} \\ \alpha_{ij}^{IJ} = a_i^I * a_j^J \end{cases} \quad (i,j = 0,1,2, \dots,n; I,J = 0,1) \quad (7)$$

Figure 5-14 shows the grid point locations for a simple case where the grid reduction factor (dH/dh) is equal to 3 (Aoi and Fujiwara, 1999). In our simulation for the Kinburn and Orleans basins, the grid reduction factor is 19 and 27, respectively.

### 5.5. Application of the dual grid size method for a frequency range of 0.1-2.5 Hz

We used crustal velocity model described in Table 5-1 to simulate the Ladysmith earthquake for the Kinburn and Orleans basins for a frequency range of 0.1-2.5 Hz. We used the focal mechanism of Ma and Audet (2014) for the dual grid size simulations using a Gaussian source function. We used spatial steps (dH) of 136 m and 272 m to discretize the high velocity zones of the Kinburn basin and Orleans basin simulations, respectively, as the minimum velocity in crustal velocity model (high velocity zone) was 2783 m/s.

Table 5-5 shows the velocity model used for the low velocity zone of the Kinburn basin. The

minimum velocity used in the low velocity zone of the Kinburn basin simulation is 96 m/s, and therefore, the  $dh$  required to model a frequency range of 0.1-2.5 Hz is equal to 7 m. Furthermore, based on the Courant number for the stability of the FD method (equation 1), the time step ( $dt$ ) of the ground motion simulation is 0.0005 s for both the high and low velocity zones of the Kinburn basin for a frequency range of 0.1-2.5 Hz.

The velocity model of soil in the low velocity zone of the Orleans basin simulation is calculated using equation 3; thus, the minimum velocity in the low velocity zone is 139.205 m/s. Therefore,  $dh=10$  m is sufficient to model the ground motion of waves for a frequency range of 0.1-2.5 Hz. Further,  $dt=0.0008$  s is used for the ground motion simulation of both high and low velocity zones, according to the Courant number for the stability of the FD method (equation 1). Table 5-6 shows the seismic properties used for the low velocity zone simulation of the Orleans basin.

The time steps for the high velocity zones of both basin simulations could be larger than what was used here, but to reduce the interpolation calculation in the low velocity zones, we used the same time steps for both low and high velocity zone simulations.

For the Kinburn basin, we used 2 cores for the large grid size simulations (epicentral distance=43 km; input velocity model: 21\*50\*17.5 km for E-W\*N-S\*Vertical directions), and the computational time for every time step of simulations was 0.801 s. Further, we used 40 cores for the small grid size simulations (input velocity model: 6.5\*7.5\*0.4 km for E-W\*N-S\*Vertical directions), and the computational time for every time step was 0.376 s.

For the Orleans basin, we used 4 cores for the large grid size simulation (epicentral distance=70.4 km; input velocity model: 81\*46.7\*21.7 km for E-W\*N-S\*Vertical directions), and the computational time for every time step of simulation was 0.285 s. For the small grid size

simulations, we used 50 cores (input velocity model: 12.7\*9.7\*0.75 km for E-W\*N-S\*Vertical directions), and the computational time for every time step was 0.371 s.

### **5.5.1. Application of the dual grid size method to the Kinburn basin**

Comparing the velocity time series of simulation and the recording for rock site (Figure 5-15) shows that using the Ma and Audet (2014) focal mechanism properly models the velocity time series at rock site (Figure 5-15), particularly for the horizontal components as the PGV of the simulated velocity time series is  $4.8E-4$  m/s and the PGV of recorded velocity time series is  $6.7E-4$  m/s for the E-W component. Further, comparing the velocity Fourier spectrum from the Ma and Audet (2014) focal mechanism with recorded velocity Fourier spectrum (Figure 5-15) shows that simulation properly models the velocity Fourier spectrum for high frequency values ( $>0.8$  Hz) in all three components, but large differences occur at low frequencies ( $<0.8$  Hz).

Comparing the simulated velocity time series for the single grid size simulation (frequency range of 0.1-1 Hz) and the dual grid size simulation (frequency range of 0.1-2.5 Hz) for the Kinburn basin at rock site (Figure 5-16) shows that the PGVs of the simulated time series for the dual grid size simulation is 3 times larger than the PGVs for the single grid size simulation. Further, the simulated velocity Fourier spectrum for the single grid size simulation is consistent with those for the dual grid size simulation for vertical components for a frequency range of 0.1-1 Hz (Figure 5-16). However, the simulated velocity Fourier spectrum for the single grid size simulation for horizontal components is larger than those for the dual grid size simulation because of the different source functions which has been used for simulations.

Using the Ma and Audet (2014) focal mechanism models the velocity time series at soil site (Figure 5-17) as the PGVs of simulation are  $6.4E-3$  m/s,  $4.9E-3$  m/s, and  $2.1E-3$  m/s for the E-W,

N-S, and V components, respectively, and the PGVs of the recordings are 3.8E-3 m/s, 3.5E-3 m/s, and 1.6E-3 m/s for the E-W, N-S, and V components, respectively. However, Figure 5-17 shows that the simulated velocity Fourier spectrum is larger than recorded velocity Fourier spectrum, particularly in a frequency range <1.5 Hz.

Comparing the results of the single grid size and dual grid size simulations for the Kinburn basin at soil site (Figure 5-18) shows that the PGV of the single grid size simulation is about 8 times smaller than the PGV of the dual grid size simulation. Also, the amplitude of the velocity Fourier spectrum for the single grid size simulation is about 24 times smaller than that of the dual grid size simulation.

Figure 5-19 shows that, with the Ma and Audet (2014) focal mechanism, the predicted PSA ratios of simulation are 26, 67, and 181 for the E-W, N-S, and V components, respectively, while the PSA ratios of the recordings are 17.2, 22.5, and 7.3 for the E-W, N-S, and V components, respectively. Thus, simulation properly predicts the PSA ratios of the E-W component.

Figure 5-20 shows that using the dual grid size simulation predicts PSA ratios that are slightly larger than the PSA ratios of the single grid size simulation for the horizontal components. However, there are large differences between the PSA ratio predicted by the dual grid size simulation and the PSA ratios predicted by the single grid size simulation for the vertical components.

### **5.5.2. Application of the dual grid size method to the Orleans basin**

For the velocity time series of simulation at rock site for the Orleans basin, with the Ma and Audet (2014) focal mechanism (Figure 5-21), the predicted PGVs are 6.5E-5 m/s, 1E-4 m/s, and 2.1E-5 m/s for the E-W, N-S, and V components, respectively. For recorded velocity time series,

the PGVs are  $1.7\text{E-}4$  m/s,  $2.1\text{E-}4$  m/s, and  $1\text{E-}4$  m/s for the E-W, N-S, and V components, respectively. Therefore, the predicted PGVs of the horizontal components are more accurate compared to the vertical component. Comparing the velocity Fourier spectrum of the recording and simulation (Figure 5-21) shows that there is good consistency between the velocity Fourier spectrum of simulation and the velocity Fourier spectrum of the recording in the frequency domain, particularly in the vertical component.

For the Orleans basin at rock site (Figure 5-22), the predicted PGV of the dual grid size simulation are almost 2.8 times smaller than the PGV of the single grid size simulation for the Ma and Audet (2014) focal mechanism. Further, the simulated velocity Fourier spectrum for the single grid size simulation is consistent with those for the dual grid size simulation for a frequency range of 0.1-1 Hz, although the amplitude of the velocity Fourier spectrum for the dual grid size simulation is smaller than the amplitude of the velocity Fourier spectrum for the single grid size simulation.

Comparing the modeled velocity time series and recorded velocity time series at soil site (Figure 5-23) shows that, with the Ma and Audet (2014) focal mechanism, the predicted PGVs are  $5.5\text{E-}4$  m/s,  $3.7\text{E-}4$  m/s, and  $2\text{E-}4$  m/s for the E-W, N-S, and V components, respectively (Figure 5-23), while recorded PGVs are  $1.8\text{E-}3$  m/s,  $1.5\text{E-}3$  m/s, and  $6.8\text{E-}4$  m/s for the E-W, N-S, and V components, respectively. Further, as shown in Figure 5-23, the amplitudes of the first arrivals in simulation are more consistent with the amplitudes of the first arrivals in the recordings compared to the amplitudes of later arrivals, particularly for the horizontal components. Also, there are good consistencies between the amplitudes of the velocity Fourier spectrum of simulation and the recordings in all three components (Figure 5-23), particularly in a frequency range  $>1\text{Hz}$ .

For the Orleans basin at soil site, using the Ma and Audet (2014) focal mechanism for the single grid size simulation predicts a PGV that is almost 3 times larger than the predicted PGV for the dual grid size simulation (Figure 5-24). Figure 5-24 also shows that the predicted amplitude of the velocity Fourier spectrum for the single grid size simulation for all three components are almost the same as those for the dual grid size simulation.

Figure 5-25 shows that the predicted PSA ratios of soil site to rock site for simulation are equal to 39, 13, and 27 for the E-W, N-S, and V components, respectively. In comparison, the recordings show that the PSA ratios are 45, 27.8, and 9.1 for the E-W, N-S, and V components, respectively. Thus, simulation properly predicts the amplitude of the PSA ratio for the E-W component.

Comparing the PSA ratios for the single grid size simulation and the dual grid size simulation (Figure 5-26) shows that the PSA ratio of the E-W components for both simulations predicts similar values for frequencies  $< 1$  Hz. Further, the PSA ratios of the N-S components for both the single and the dual grid size simulations predicts similar values for frequencies  $< 0.6$  Hz. However, the PSA ratio of the N-S component for the single grid size simulation is larger than the PSA ratio of the N-S component for the dual grid size simulation for a frequency range of 0.6-1 Hz. Finally, the PSA ratios of the vertical components for the single grid size simulation are smaller than those for the dual grid size simulation.

## **5.6. Discussion and conclusion**

Using the Ladysmith earthquake as a point source to model the ground motion in the Kinburn basin for a frequency range of 0.1-1 Hz shows that simulation that uses the Ma and Audet (2014) focal mechanism more accurately predicts the PGVs and PSAs compared to simulation that uses

the Bent et al. (2015) focal mechanism. The predicted PGVs at soil site are 70% and 48% less than the PGV of the recordings at soil site for simulations that use the Bent et al. (2015) and the Ma and Audet (2014) focal mechanisms, respectively. Furthermore, there are large discrepancies between the amplitudes of the velocity Fourier spectrum of simulations and the recordings for the Kinburn basin, particularly at low frequencies ( $<0.5$ ). However, the amplitudes of the PSA ratios for the Bent et al. (2015) and Ma and Audet (2014) focal mechanisms are only 10% and 5% less, respectively, than the amplitude of the PSA ratios of the recordings although the frequency associated with the amplitudes of the PSA ratios in simulations is slightly less than that of the recordings.

In addition, the ground motion simulation of the Orleans basin for a frequency range of 0.1-1 Hz for the point source Ladysmith earthquake shows that simulation that using the Bent et al. (2015) focal mechanism predicts an amplitude of the PGVs at soil site at 30% less than the amplitude of the PGVs of the recordings at soil site. In contrast, the predicted amplitude of the PGVs using the Ma and Audet (2014) focal mechanism is 30% more than that of the recordings at soil site. Further, there are large differences between the amplitudes of the velocity Fourier spectrum of both simulations and the recordings. Lastly, the predicted amplitude of the PSA ratios for the Bent et al. (2015) focal mechanism is 10% less than the amplitude of the PSA ratios of the recordings for the Orleans basin and 17% less when the Ma and Audet (2014) focal mechanism is used.

A comparison of recorded velocity time series and the velocity time series of the broadband ground motion simulation for the Kinburn basin at soil site shows that using the Ma and Audet (2014) focal mechanism properly models the velocity time series for all three components: the PGVs of simulation are 43%, 28% and 23% more than the PGVs of the recordings for the E-W,

N-S and vertical components, respectively. However, there are discrepancies between the amplitudes of the velocity Fourier spectrum of simulations and of the recordings, particularly at low frequencies ( $<1.5$  Hz). Further, simulation only predicts reasonable PSA ratios for the horizontal components. For the E-W and N-S components, with the Ma and Audet (2014) focal mechanism, the predicted amplitudes of the PSA ratios are 1.4 and 2.9 times more than the amplitude of the PSA ratios of the recordings.

Ground motion simulations of waves with frequencies of  $>1$  Hz need a large amount of computational time and facilities; thus, we need to use the dual grid size method to model the ground motion of the Ladysmith earthquake for the Kinburn and Orleans basins for the frequency range of 0.1-2.5 Hz.

Comparing the recordings and the broadband ground motion simulation at soil site for the Orleans basin shows that, with the Ma and Audet (2014) focal mechanism, the predicted PGVs at soil site are 75% smaller than recorded PGVs for all three components. Further, there are good consistencies between the amplitudes of the velocity Fourier spectrum of the recordings and of simulations particularly at high frequencies ( $>1$  Hz). In addition, simulation predicts reasonable PSA ratios for the horizontal components; the amplitude of the PSA ratios of simulation is 10% more than the amplitude of the PSA ratios of the recordings for the E-W component.

For the Kinburn basin at soil site, using the dual grid size simulation increases the predicted PGVs and the amplitudes of the velocity Fourier spectrum for the horizontal components compared to the results using the single grid size simulation. Further, using the dual grid size simulation for the Orleans basin decreases the predicted amplitudes of the velocity Fourier spectrum of soil site for the horizontal components relative to that for the single grid size simulation for soil site. The decrease in the PGVs and the amplitude of the velocity Fourier

spectrum of the horizontal components for the dual grid size simulation can be attributed to the ratio of grids sizes used in the dual grid size simulation. Our study shows that using a small ratio for the grids sizes used in the dual grid size simulation can increase the accuracy of the dual grid size simulation.

In conclusion, using the developed dual grid size method, we modeled the ground motion for the Kinburn and Orleans basins for a broadband frequency (0.1-2.5 Hz) in a time domain; this ground motion simulation was not possible using a single grid size method because of the extensive computational facilities and computational time required for single grid size simulations. In contrast, using the dual grid size method, we significantly reduced the computational time and computational cost that was usually necessary for broadband ground motion simulations. Furthermore, the discrepancies between the amplitudes of the velocity Fourier spectrum of simulations and the recordings could be attributed to the seismic moment that was proposed in the focal mechanisms because the same differences occurred in the single grid size simulation, particularly at low frequencies (i.e., both methods were dependent on this seismic moment). Also, the amplitude of the PSA ratio for the vertical component was not properly predicted because the vertical component of the waves at rock site was not modeled accurately.

## **Data and Resources**

Earthquakes Canada, Natural Resources Canada (NRCan) database:  
[www.earthquakescanada.nrcan.gc.ca](http://www.earthquakescanada.nrcan.gc.ca) (last accessed October 2017).

The Geological Survey of Canada provided the seismograms and information on the depths of the Kinburn and Orleans basins; this information cannot be released to the public.

## **Acknowledgements**

This research was supported by the Natural Sciences and Engineering Research Council of Canada under the Discovery Grant program and Collaborative Research and Development grants. This research used computational resources provided by the High Performance Computing Virtual Laboratory (HPCVL) and Calcul Québec, both under Compute Canada. We gratefully acknowledge the constructive comments, suggestions, and text revisions from the reviewers and Associate Editor. We used the AWP-ODC [Anelastic Wave Propagation, developed by Olsen-Day-Cui) program package, and we would like to show our gratitude to Professor Kim Olsen for providing us with the package. We appreciate Dr. Daniel Roten's guidance in using the AWP-ODC program. Special gratitude is given to the Geological Survey of Canada for providing us with helpful comments, suggestions, and the necessary materials, including seismograms and geological information, for this research.

## Tables and Figures

Table 5-1. Crustal velocity models used for rock sites in the Ottawa area (Burger et al., 1987; Motazedian et al., 2013)

Depth(km)	Vs(m/s)	Vp(m/s)	Density (kg/m <sup>3</sup> )	Qp	Qs
D < 2	3400	5888	2693	1000	500
2 <= D < 4	3410	5906	2696		
4 <= D < 8	3420	5923	2700		
8 <= D < 12	3560	6165	2753		
12 <= D < 14	3580	6200	2761		
14 <= D < 16	3600	6235	2769		
16 <= D < 17	3620	6269	2777		
17 <= D < 17.5	3700	6408	2810		

Table 5-2. Properties of the seismic velocity model of the Kinburn basin (Burger et al., 1987; Hunter et al., 2010; Crow et al., 2011; Motazedian et al., 2011)

Type of material	Soil	Soil	Soil	Soil	Rock
Depth (m)	0-25	25-50	50-75	75-100	Out of basin
Vs (m/s)	178	219	278	320	2783
Vp (m/s)	1380	1380	1380	1380	6200
Density (kg/m <sup>3</sup> )	1600	1600	1600	1600	2650
Qp	185	185	185	185	1000
Qs	185	185	185	185	500

Table 5-3. Properties of the seismic velocity model of the Orleans basin (Motazedian and Hunter, 2008; Hunter et al., 2010; Crow et al., 2011)

Type of material	Soil	Soil	Soil	Soil
Depth (m)	0-25	25-50	50-75	75-100
Vs (m/s)	145	168	205	258
Vp (m/s)	1380	1380	1380	1380
Density (kg/m <sup>3</sup> )	1600	1600	1600	1600
Qp	172.5	300	298	288
Qs	115	200	199	192

Table 5-4. Two focal mechanisms proposed for the Ladysmith earthquake

	<b>Bent et al. (2015)</b>			<b>Ma and Audet (2014)</b>		
	Epicenter = 45.76, -76.32 Depth = 12 Km $M_w = 4.55$ $M_0 = 8.372e+15 \text{ Nt-m}$			Epicenter = 45.74, -76.34 Depth = 14.5 Km $M_w = 4.7$ $M_0 = 1.32e+16 \text{ Nt-m}$		
	<b>Strike</b>	<b>Dip</b>	<b>Slip</b>	<b>Strike</b>	<b>Dip</b>	<b>Slip</b>
Plane1	350.40	47.91	118.03	306	41	94
Plane2	131.94	49.08	62.52	122	50	87

Table 5-5. Velocity model used for the low velocity zone in the Kinburn basin simulation  
 (Burger et al., 1987; Hunter et al., 2010; Crow et al., 2011; Motazedian et al., 2011)

Depth (m)	Vs(m/s)	Vp(m/s)	Density (kg/m <sup>3</sup> )	Qp	Qs
D < 7	232	1380	1600	172.5	115
7 <= D < 14	96				
14 <= D < 21	151				
21 <= D < 28	190				
28 <= D < 35	203			300	200
35 <= D < 42	226				
42 <= D < 49	241			298.5	199
49 <= D < 56	266				
56 <= D < 63	275				
63 <= D < 70	279				
70 <= D < 77	304			288	192
77 <= D < 84	315				
84 <= D < 91	322				
91 <= D < 98	350			5888	2693
Out of basin	3400				

Table 5-6. Velocity model used for the low velocity zone in the Orleans basin simulation (Burger et al., 1987; Motazedian and Hunter, 2008; Hunter et al., 2010; Crow et al., 2011; Motazedian et al., 2013)

Depth (m)	Vs(m/s)	Vp(m/s)	Density (kg/m <sup>3</sup> )	Qp	Qs
D < 10	139	1380	1600	172.5	115
10 <= D < 20	142				
20 <= D < 30	148				
30 <= D < 40	157				
40 <= D < 50	168			300	200
50 <= D < 60	181				
60 <= D < 70	197			298.5	199
70 <= D < 80	215				
80 <= D < 90	235			288	192
90 <= D < 100	258				
Out of basin	3400			5888	2693

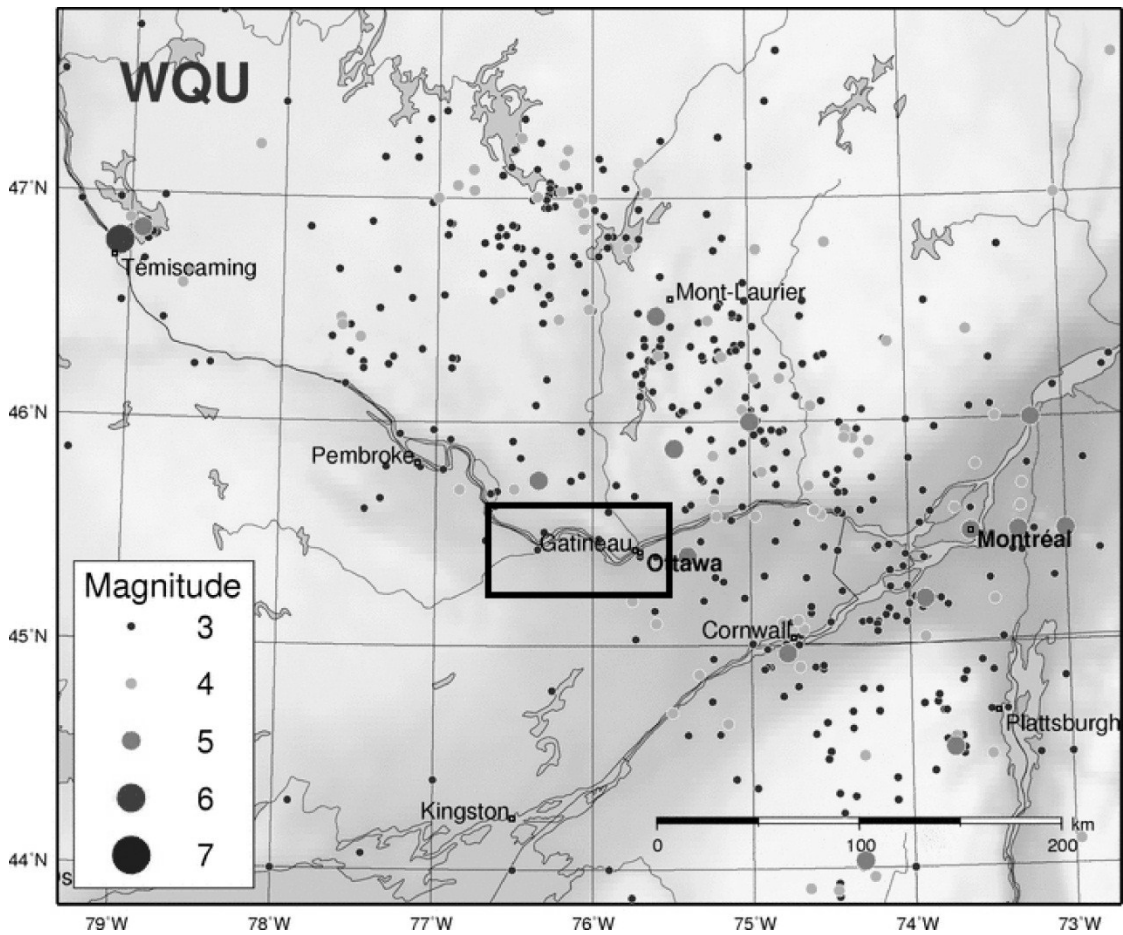


Figure 5-1. Recorded earthquakes by the Canadian seismograph network since the beginning of the century in the Western Quebec Seismic Zone. The approximate study region is outlined by a black rectangle. The studied basins are located in the black box ([www.earthquakescanada.nrcan.gc.ca](http://www.earthquakescanada.nrcan.gc.ca)).

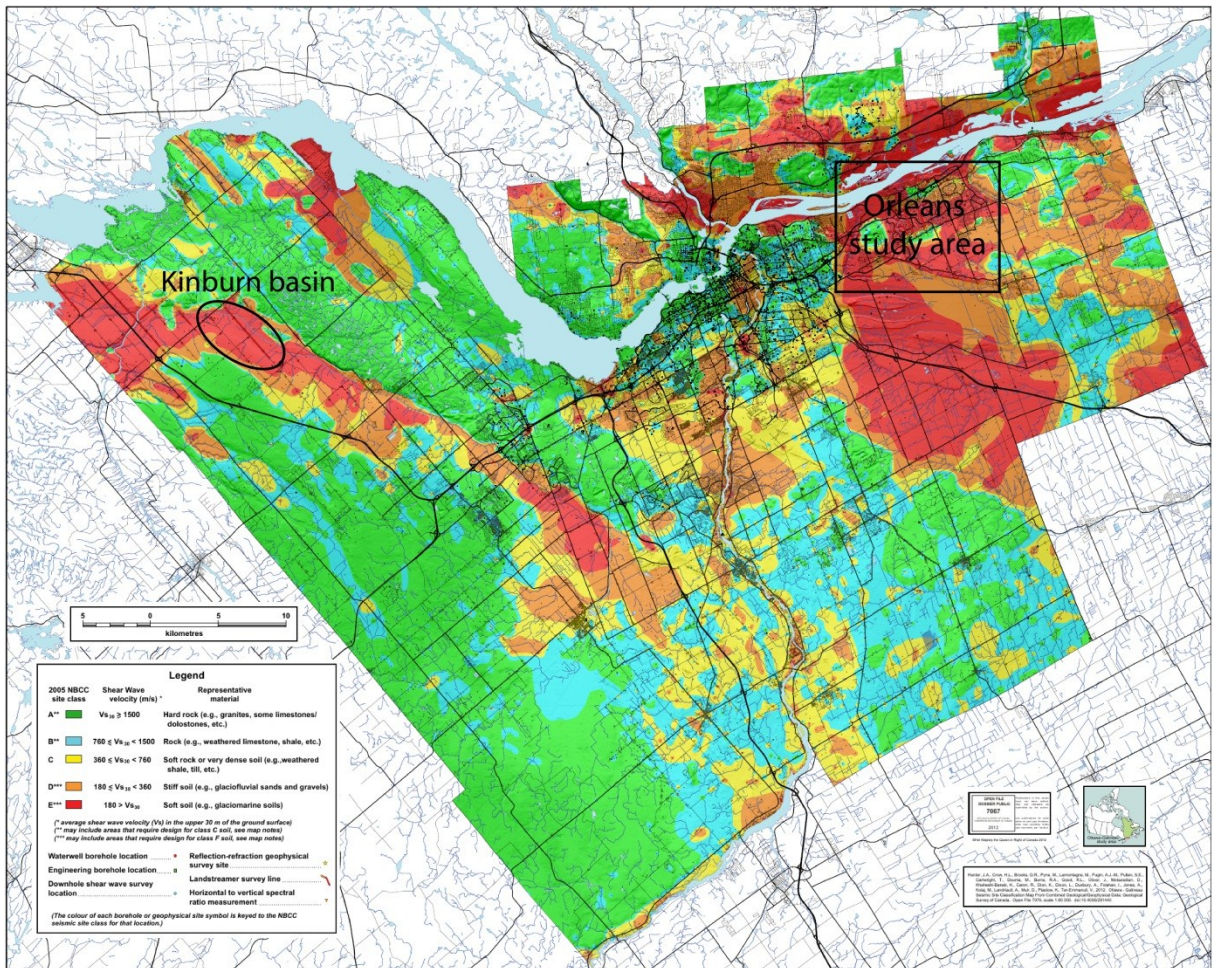


Figure 5-2. Vs30 map of the Ottawa region (Motazedian et al., 2011; Hunter et al., 2012). The locations of the Kinburn basin and Orleans basin are indicated by the black circle and black box, respectively.

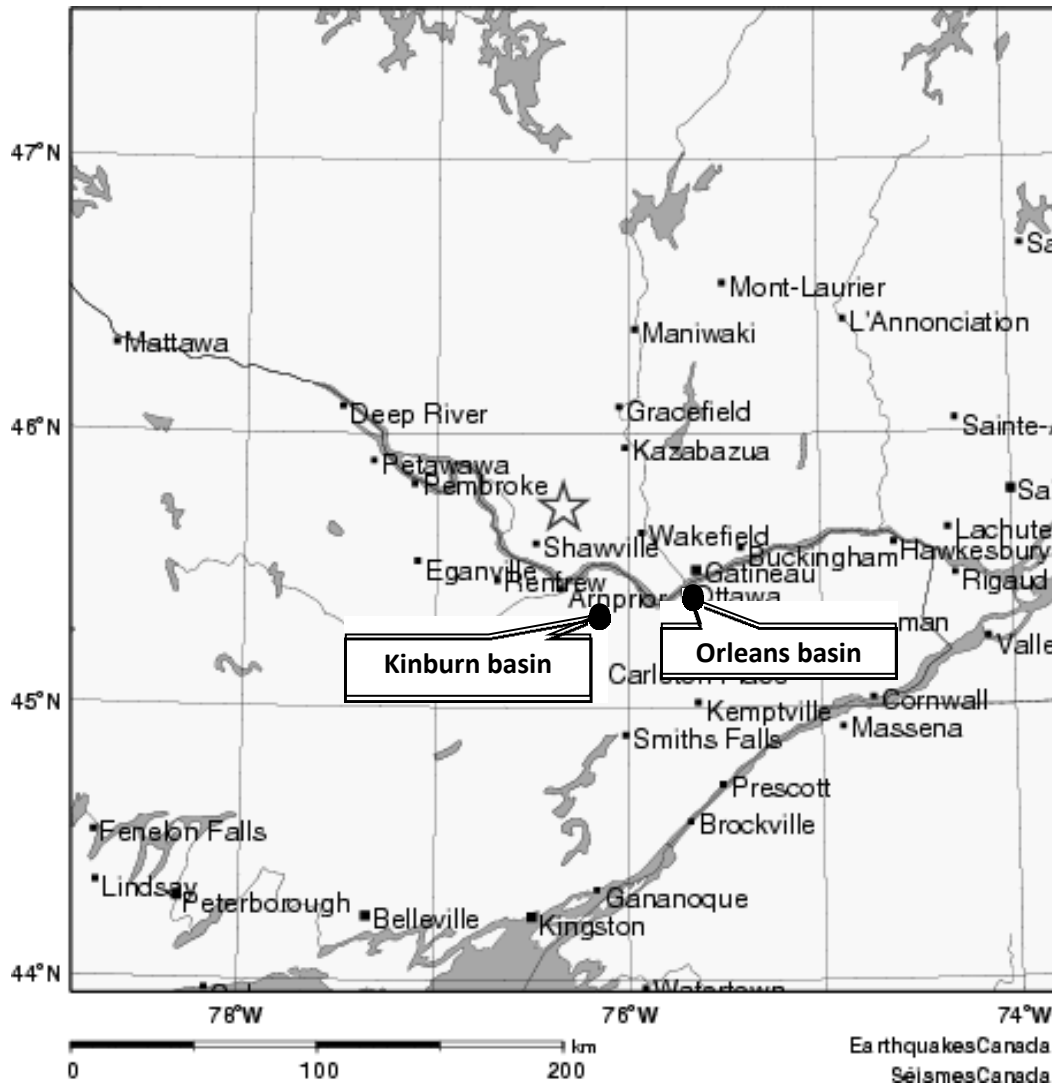


Figure 5-3. Location of the Ladysmith earthquake (the star) and the locations of Kinburn and Orleans basins (NRCan webpage).

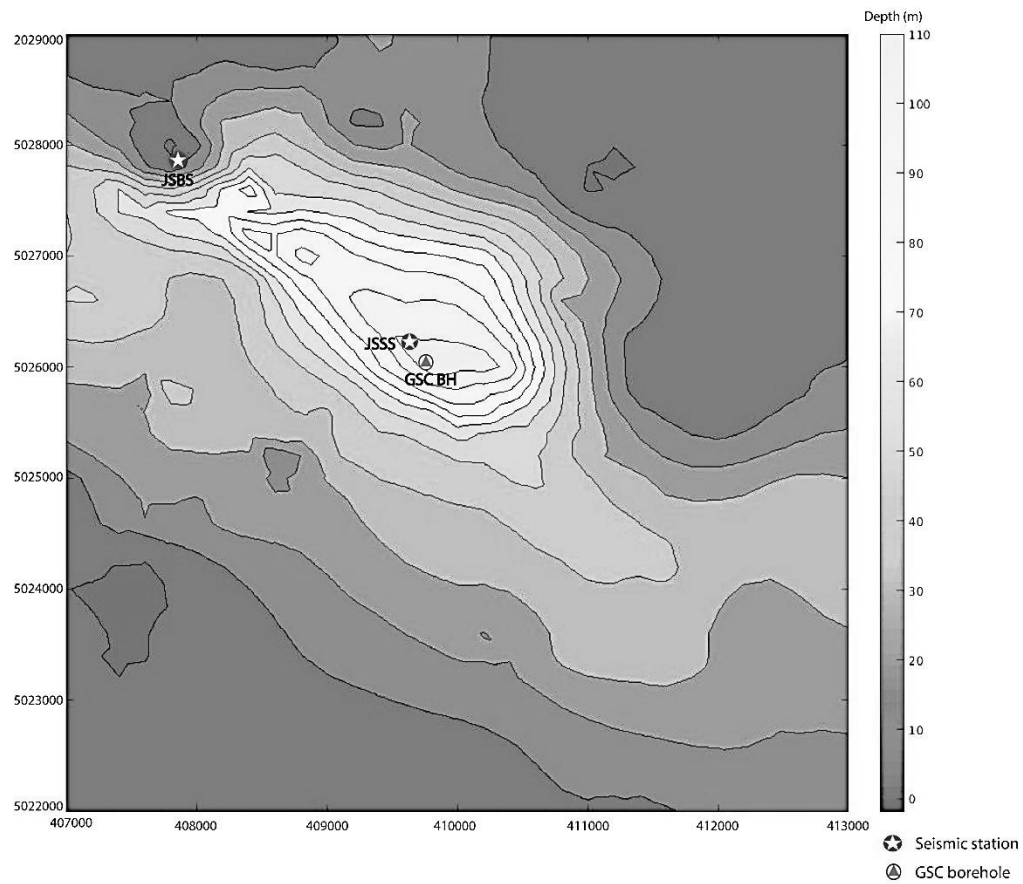


Figure 5-4. Kinburn basin depth model and locations of seismic stations and GSC boreholes.

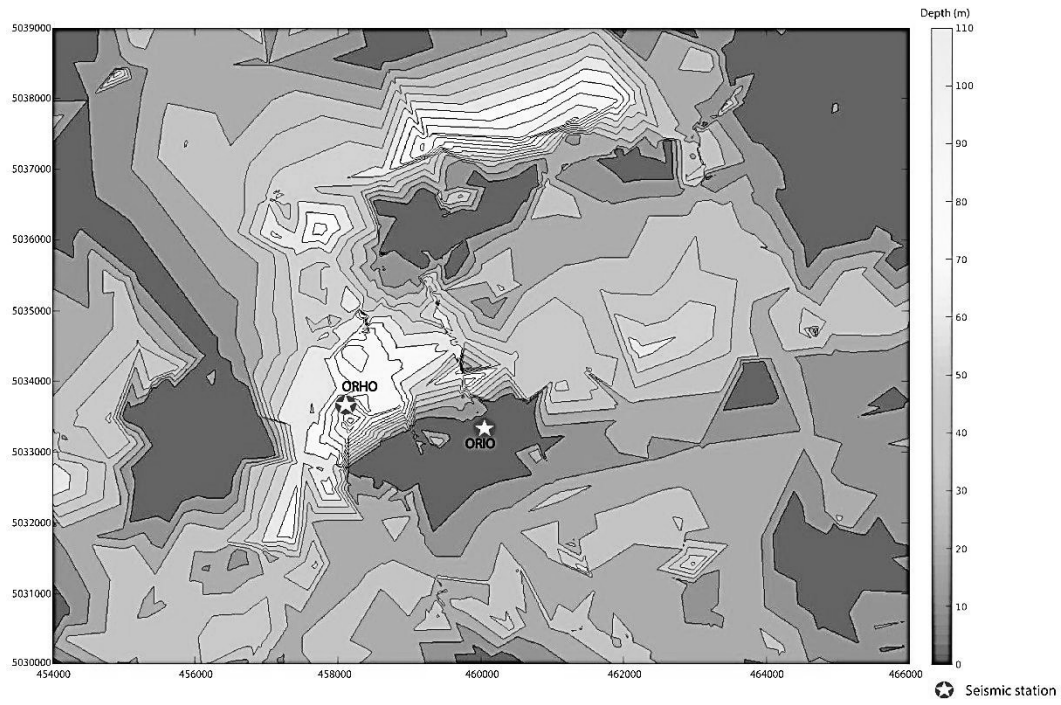
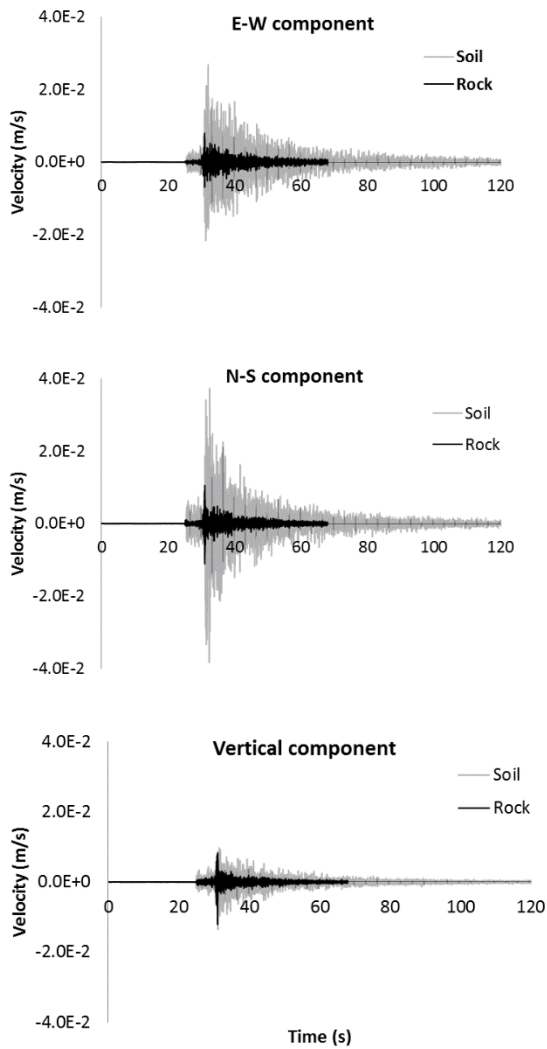


Figure 5-5. Orleans basin depth model and seismic stations.

a. Kinburn basin (recordings)



b. Orleans basin (recordings)

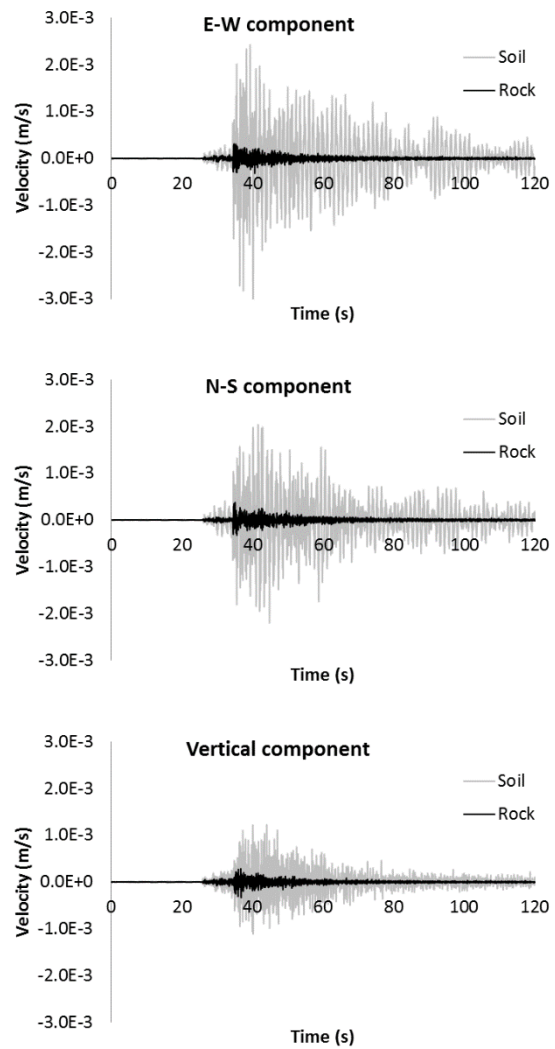
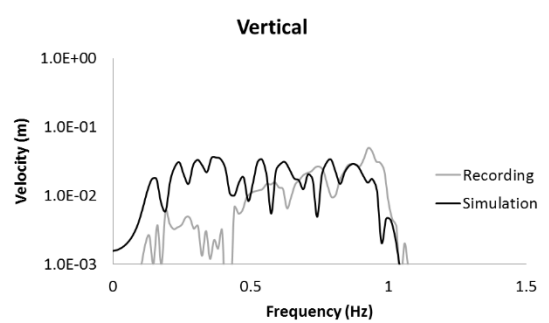
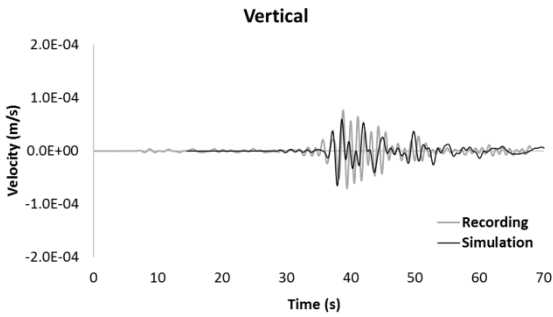
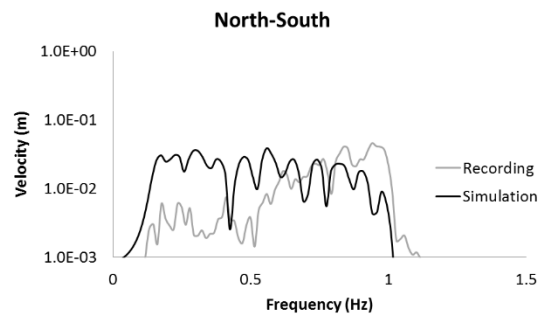
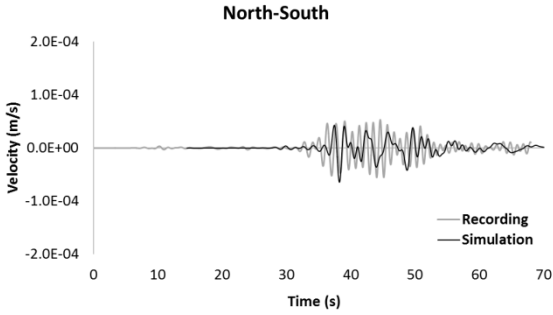
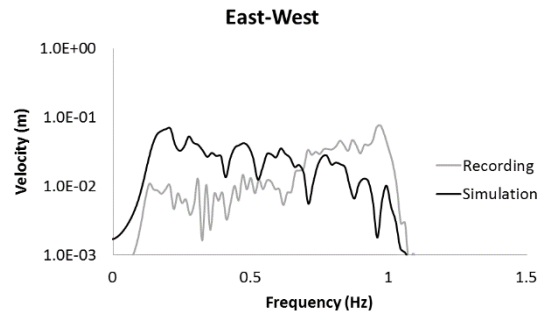
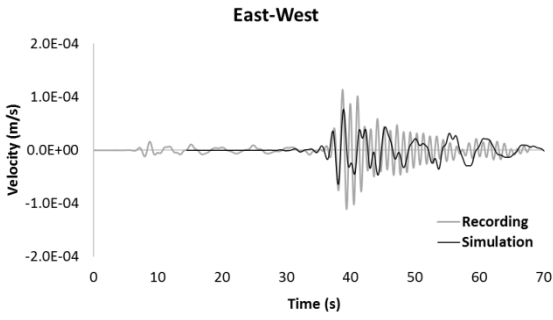
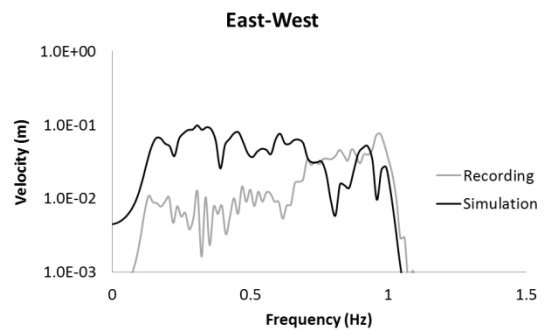
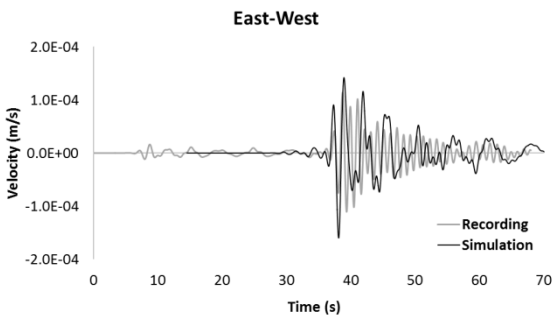


Figure 5-6. Recorded velocity time series associated with the Ladysmith earthquake at a) rock site (JSBS) and soil site (JSSS) in the Kinburn basin and b) rock site (ORHO) and soil site (ORIO) in the Orleans basin.

a. Bent et al. (2015) focal mechanism (single grid size)



b. Ma and Audet (2014) focal mechanism (single grid size)



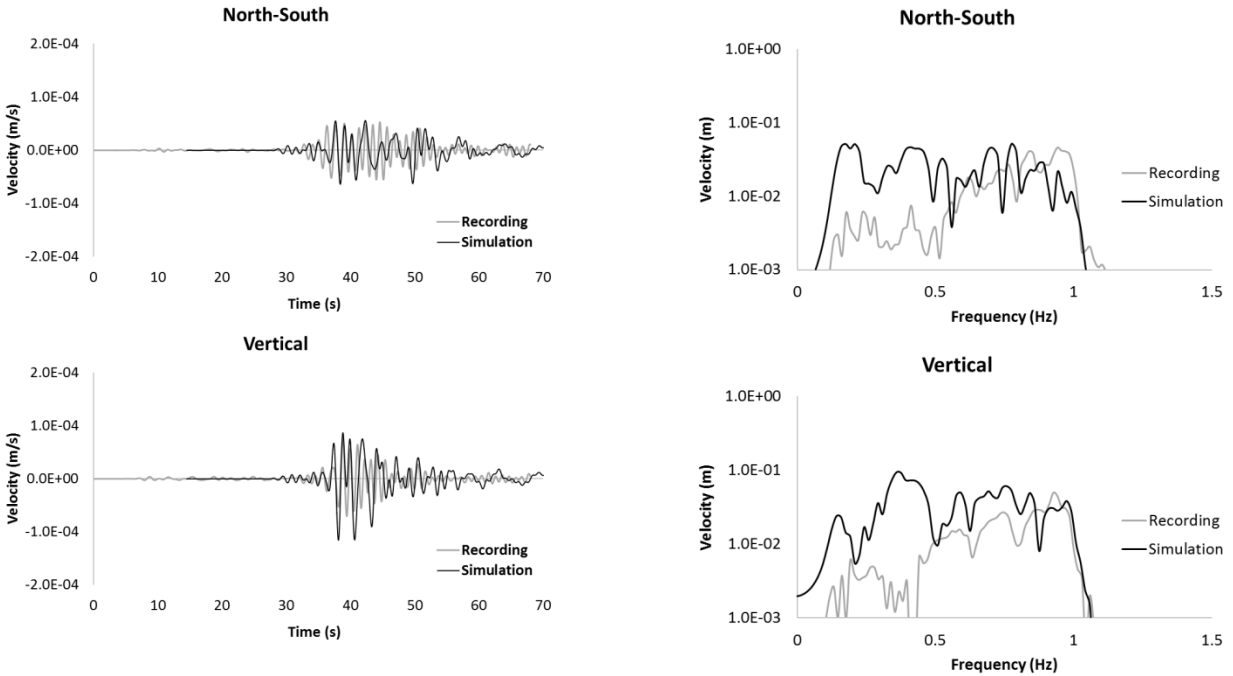
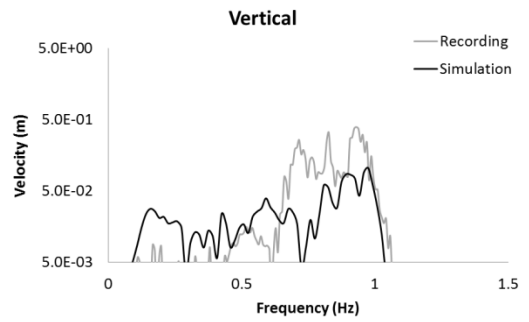
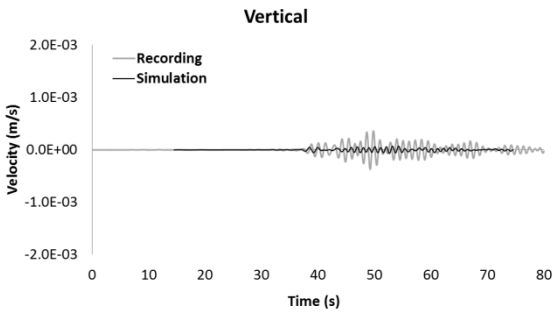
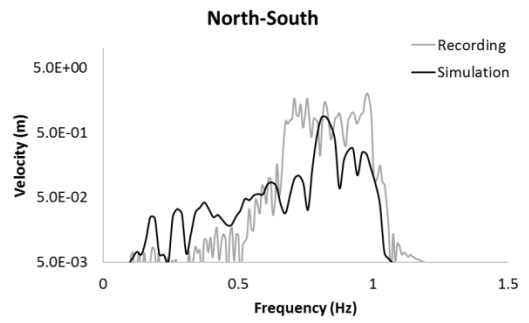
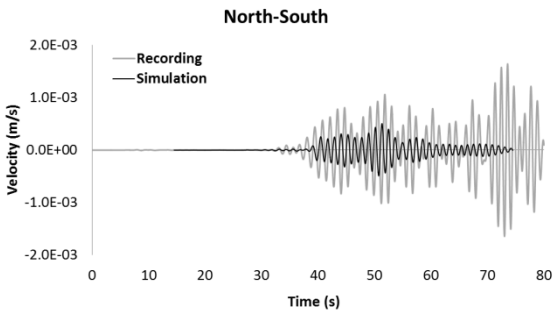
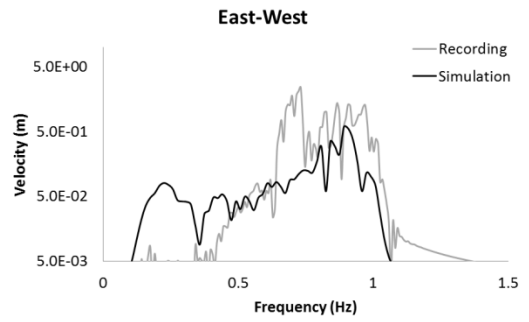
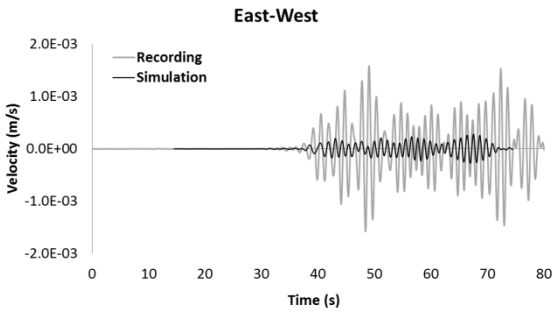
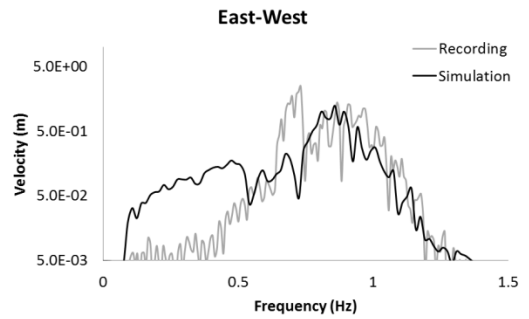
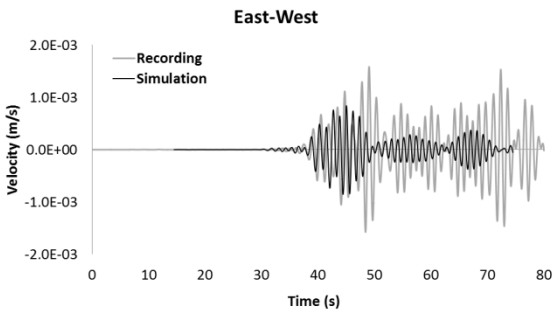


Figure 5-7. Simulated velocity time series and related Fourier spectrum versus recorded velocity time series and associated Fourier spectrum at rock site for the two proposed focal mechanisms: a) Bent et al. (2015); epicentral distance  $R=39.3$  km, depth=12 km,  $M_w=4.55$ ,  $M_0=8.372e+15$  Nt-m, frequency range=0.1-1 Hz and b) Ma and Audet (2014); epicentral distance  $R=39.3$  km, depth=14.5 km,  $M_w=4.7$ ,  $M_0=1.32e+16$  Nt-m, frequency range=0.1-1 Hz.

a. Bent et al. (2015) focal mechanism (single grid size)



b. Ma and Audet (2014) focal mechanism (single grid size)



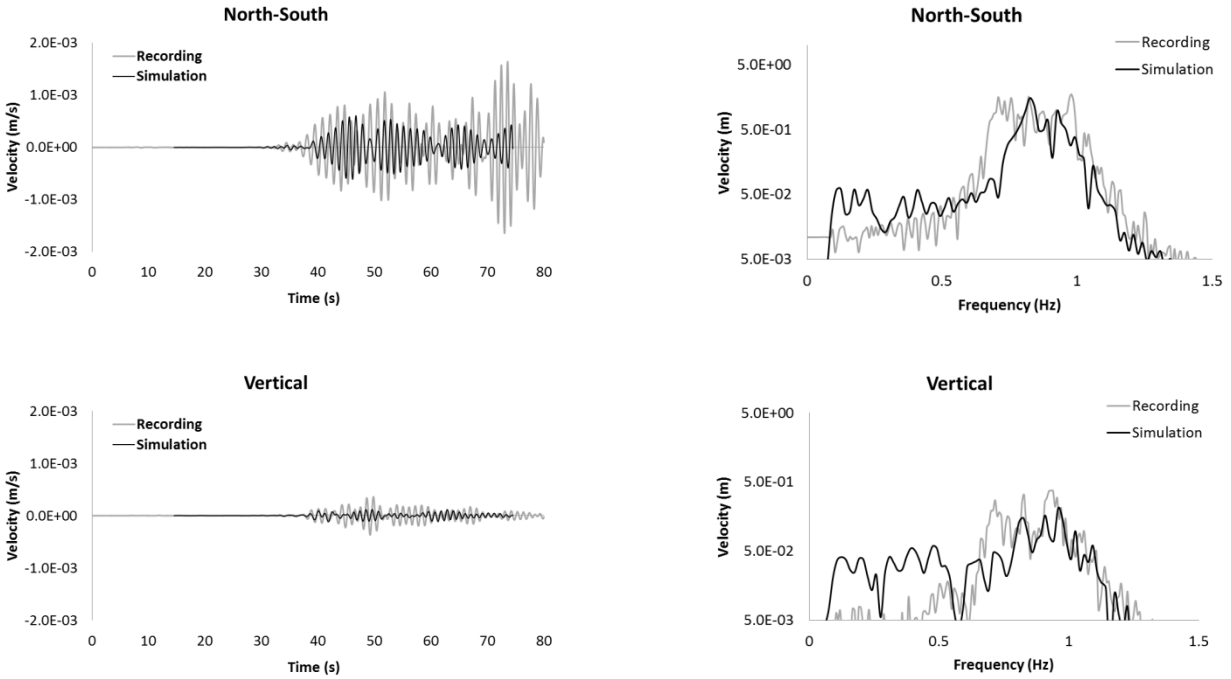


Figure 5-8. Simulated velocity time series and related Fourier spectrum versus recorded velocity time series and associated Fourier spectrum at soil site for the two proposed focal mechanisms: a) Bent et al. (2015); epicentral distance  $R=43$  km, depth=12 km,  $M_w=4.55$ ,  $M_0=8.372e+15$  Nt-m, frequency range=0.1-1 Hz and b) Ma and Audet (2014); epicentral distance  $R=43$  km, depth=14.5 km,  $M_w=4.7$ ,  $M_0=1.32e+16$  Nt-m, frequency range=0.1-1 Hz.

a. Bent et al. (2015) focal mechanism (single grid size)

b. Ma and Audet (2014) focal mechanism (single grid size)

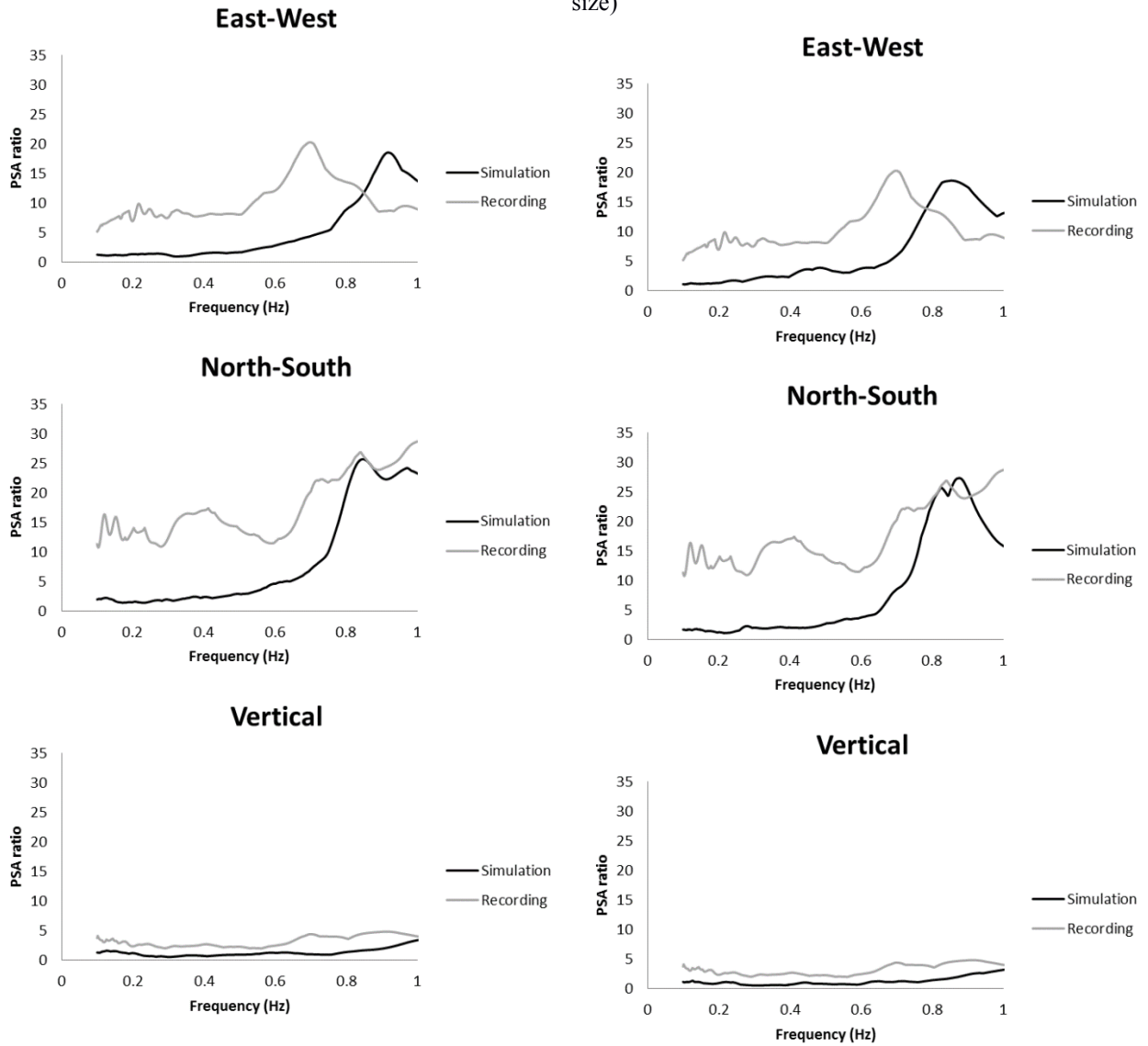
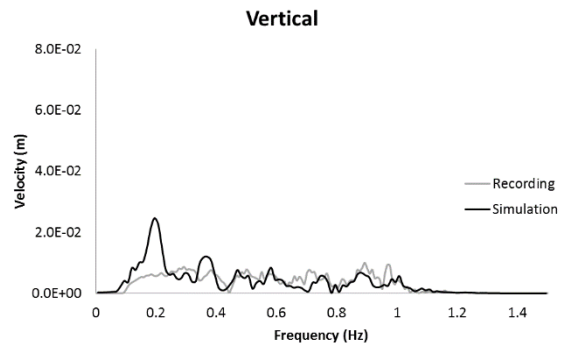
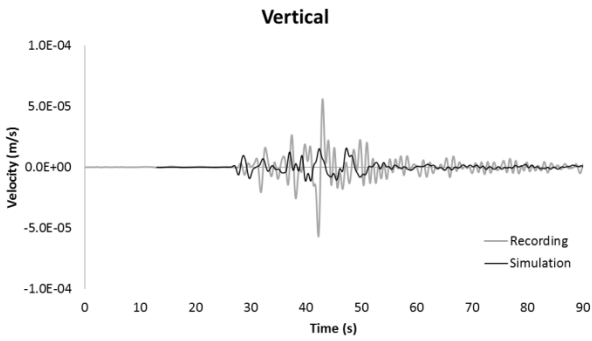
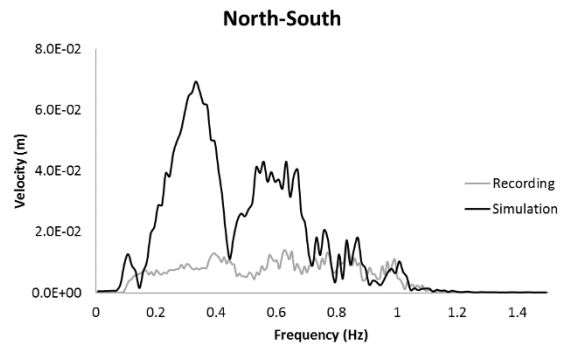
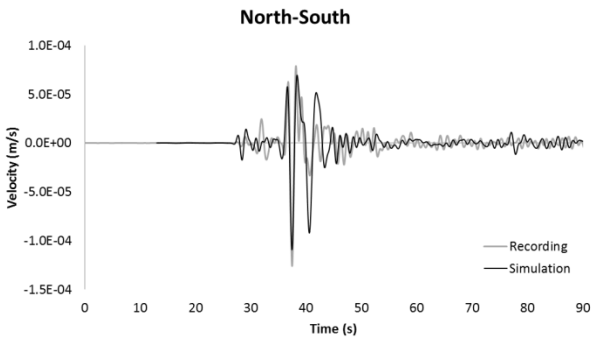
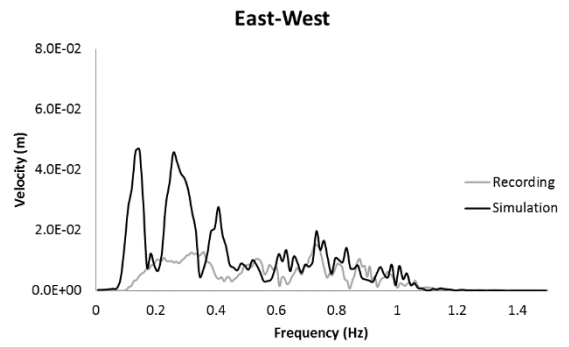
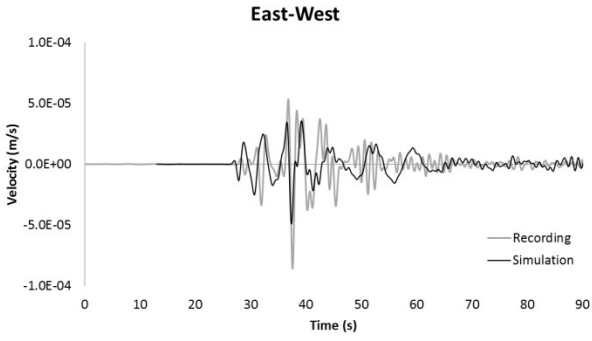
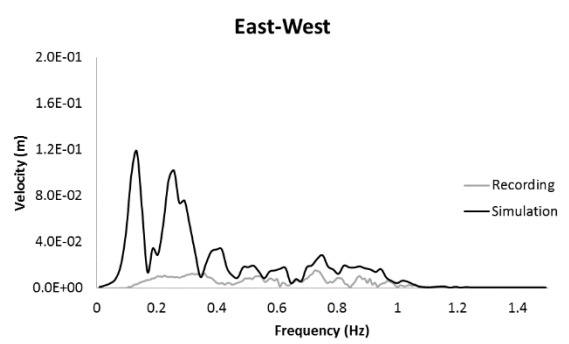
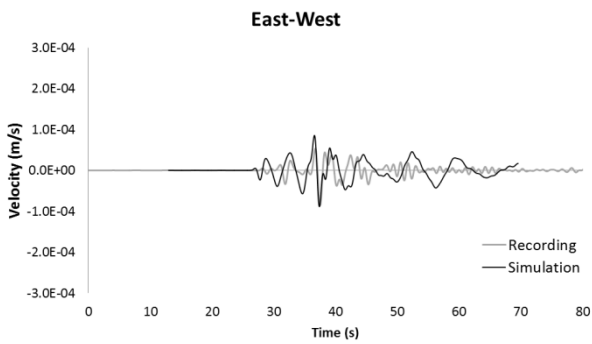


Figure 5-9. PSA ratios of soil site to rock site for recorded velocity time series versus PSA ratios of the simulated velocity time series for the Kinburn basin for the two proposed focal mechanisms: a) Bent et al. (2015); epicentral distance=43 km, depth=12 km, MW=4.55,  $M_0=8.372 \times 10^{15}$  Nt-m, frequency range=0.1-1 Hz and b) Ma and Audet (2014); epicentral distance=43 km, depth=14.5 km, MW=4.7,  $M_0=1.32 \times 10^{16}$  Nt-m, frequency range=0.1-1 Hz.

a. Bent et al. (2015) focal mechanism (single grid size)



b. Ma and Audet (2014) focal mechanism (single grid size)



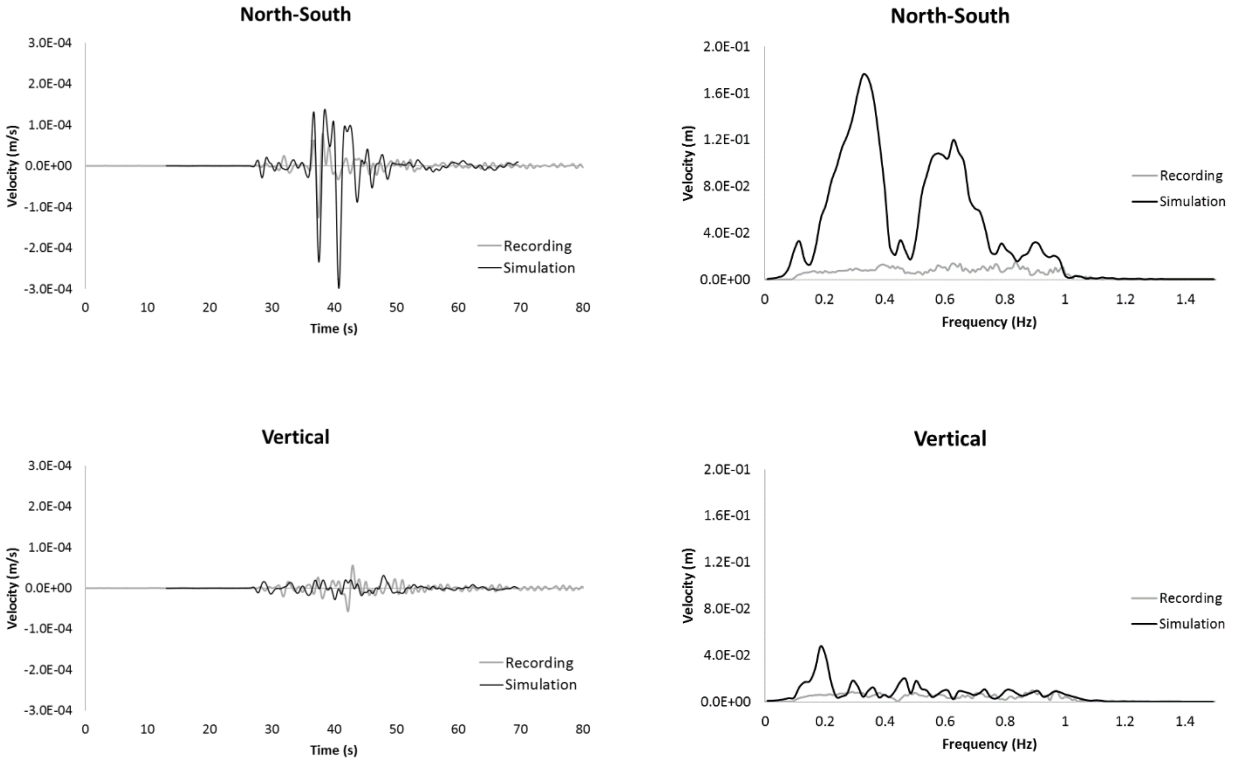
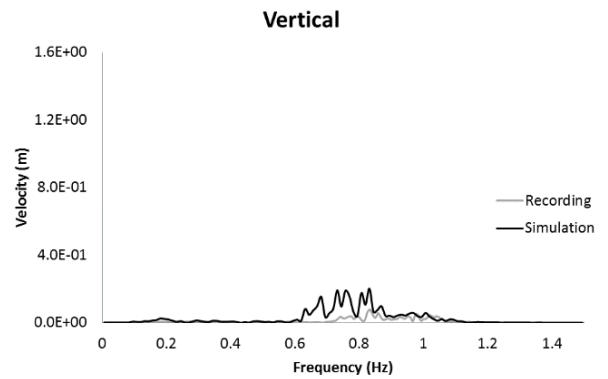
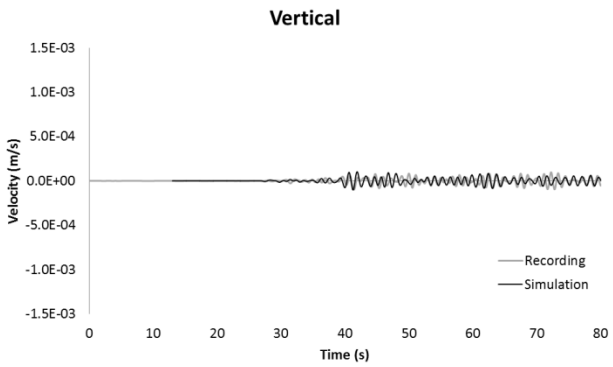
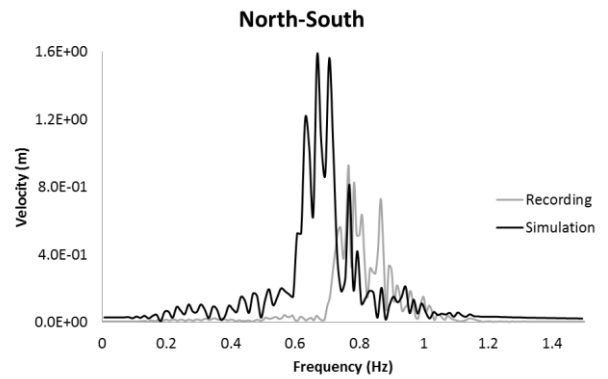
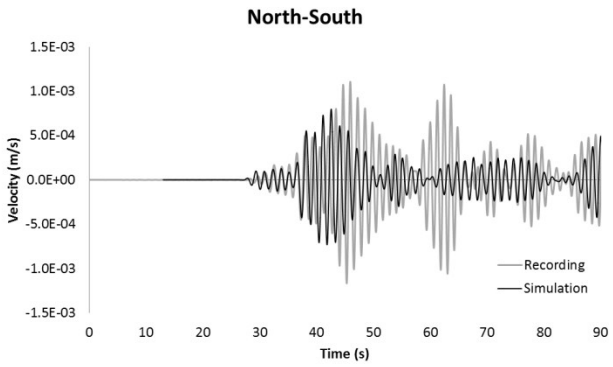
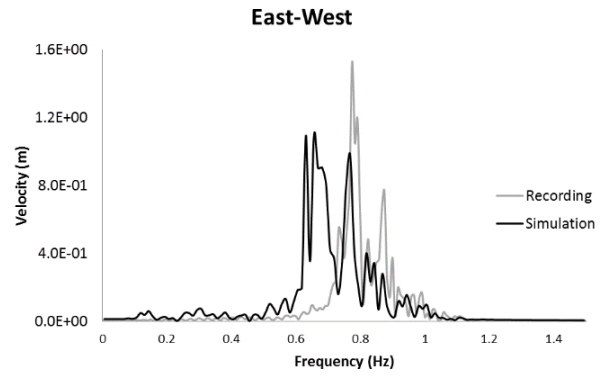
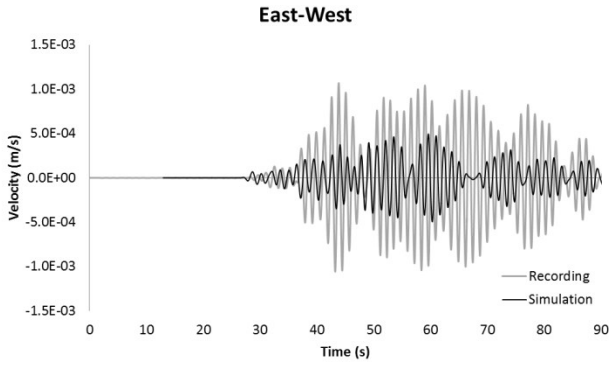
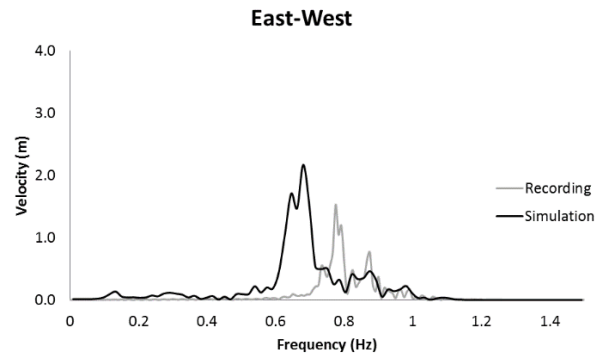
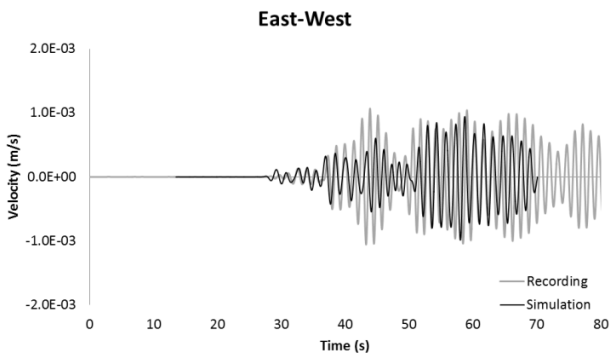


Figure 5-10. Simulated velocity time series and associated velocity Fourier spectrum versus recorded velocity time series and related velocity Fourier spectrum for the Orleans basin at rock site for the two proposed focal mechanisms: a) Bent et al. (2015); epicentral distance=72.2 km, depth=12 km, MW=4.55,  $M_0=8.372e+15$  Nt-m, frequency range=0.1-1 Hz and b) Ma and Audet (2014); epicentral distance=72.2 km, depth=14.5 km, MW=4.7,  $M_0=1.32e+16$  Nt-m, frequency range=0.1-1 Hz.

a. Bent et al. (2015) focal mechanism (single grid size)



b. Ma and Audet (2014) focal mechanism (single grid size)



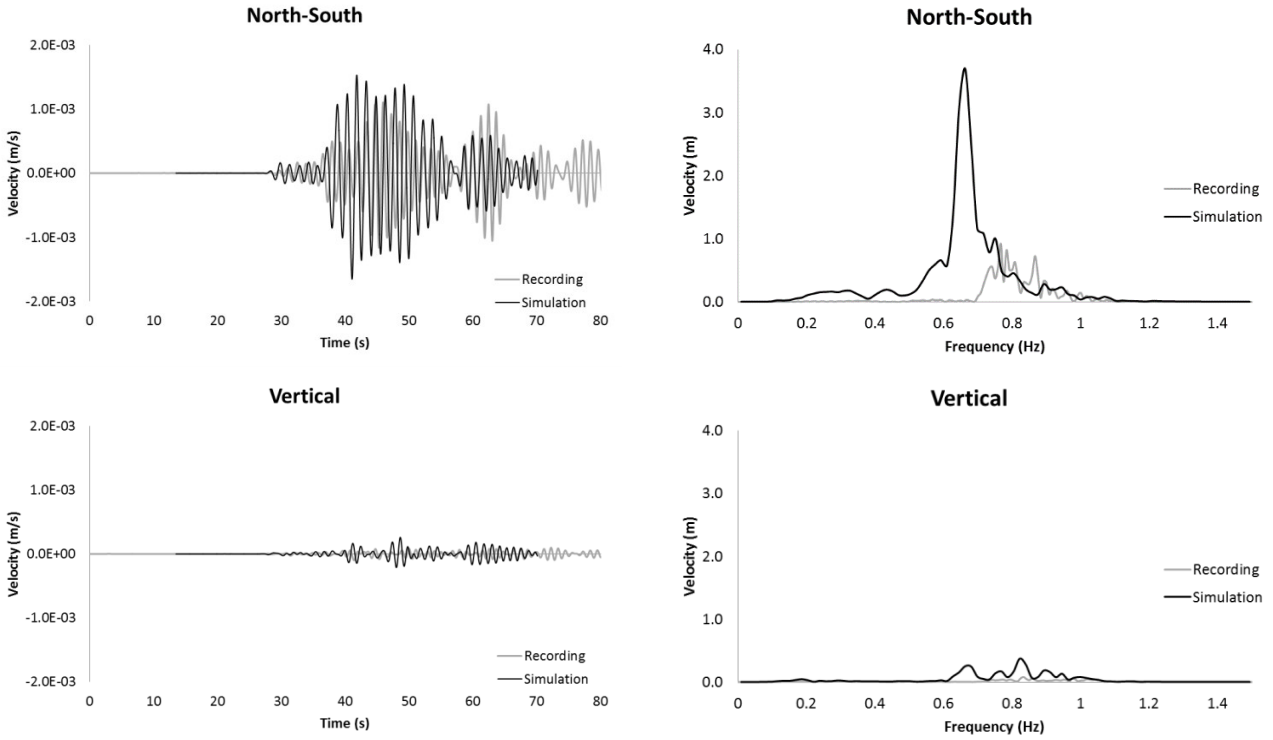


Figure 5-11. Simulated velocity time series and associated velocity Fourier spectrum versus recorded velocity time series and related velocity Fourier spectrum for the Orleans basin at soil site for the two proposed focal mechanisms: a) Bent et al. (2015); epicentral distance=70.4 km, depth=12 km, MW=4.55,  $M_0=8.372e+15$  Nt-m, frequency range=0.1-1 Hz and b) Ma and Audet (2014); epicentral distance=70.4 km, depth=14.5 km, MW=4.7,  $M_0=1.32e+16$  Nt-m, frequency range=0.1-1 Hz.

a. Bent et al. (2015) focal mechanism (single grid size)      b. Ma and Audet (2014) focal mechanism (single grid size)

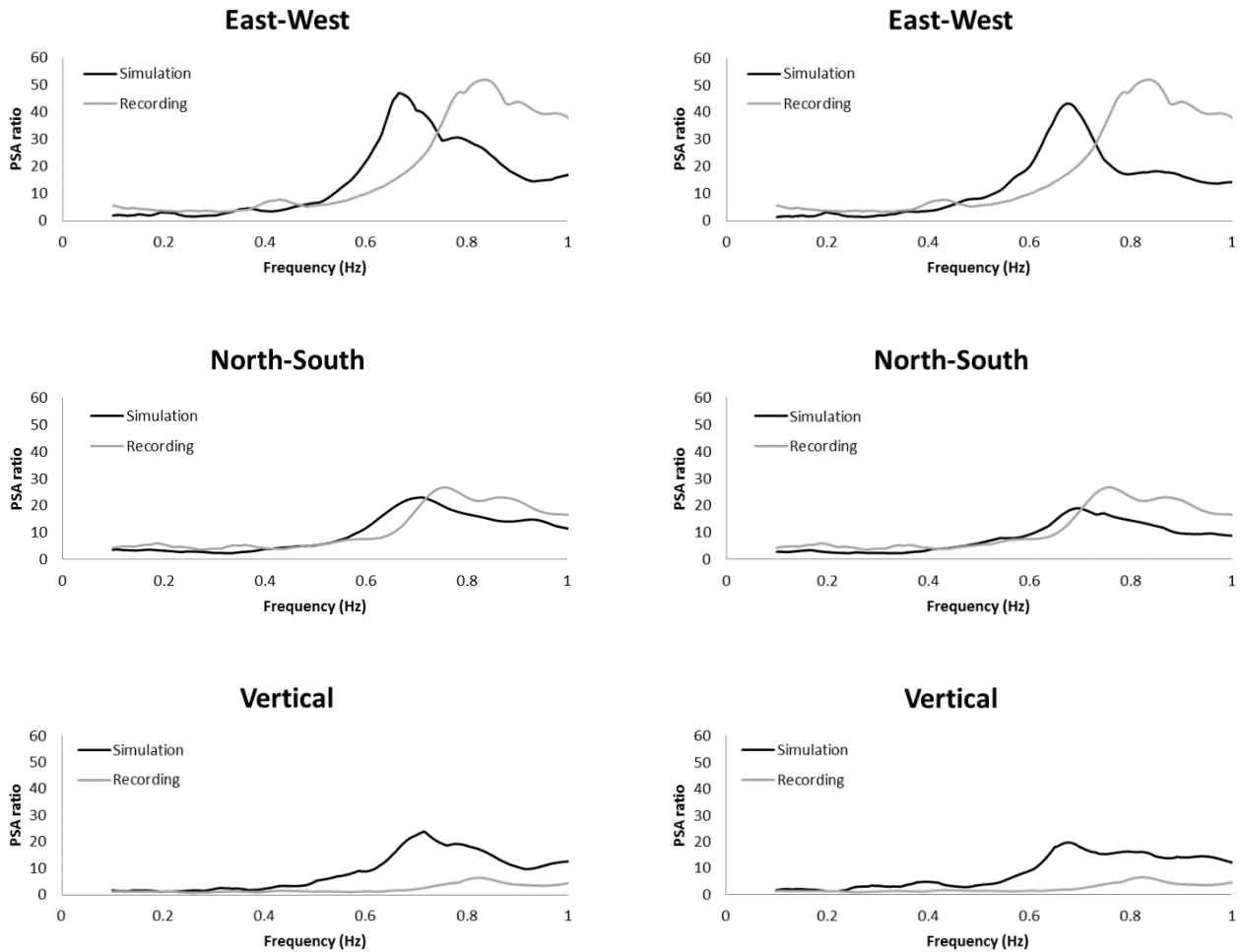


Figure 5-12. PSA ratios of soil site to rock site for recorded velocity time series versus PSA ratios of the simulated velocity time series for the Orleans basin for the two proposed focal mechanisms: a) Bent et al. (2015); epicentral distance=70.4 km, depth=12 km, MW=4.55,  $M_0=8.372e+15$  Nt-m, frequency range=0.1-1 Hz and b) Ma and Audet (2014); epicentral distance=70.4 km, depth=14.5 km, MW=4.7,  $M_0=1.32e+16$  Nt-m, frequency range=0.1-1 Hz.

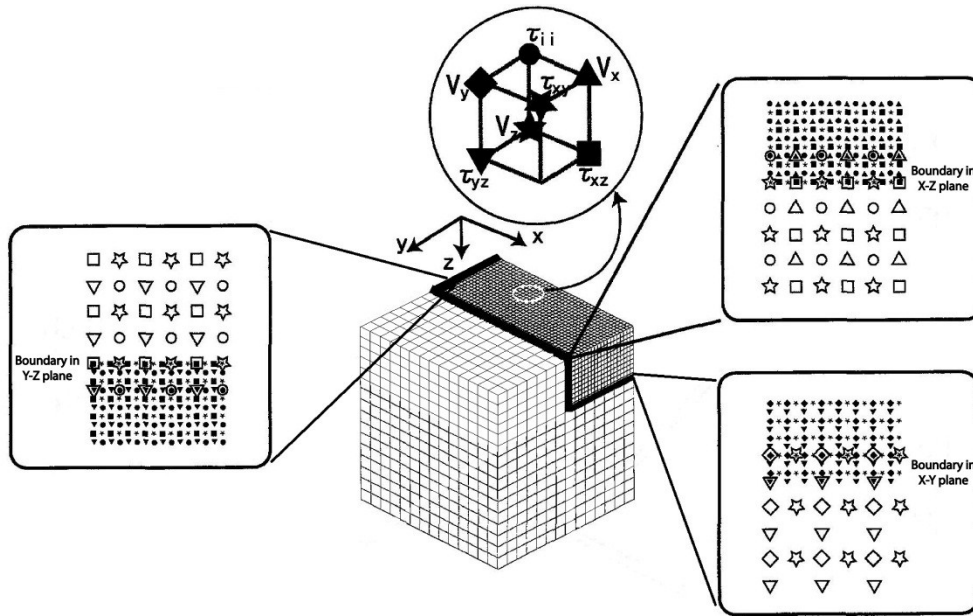


Figure 5-13. Schematic figure of 3D grid system that shows the boundary between the high velocity zone (large grids) and low velocity zone (small grids) (Aoi and Fujiwara, 1999).

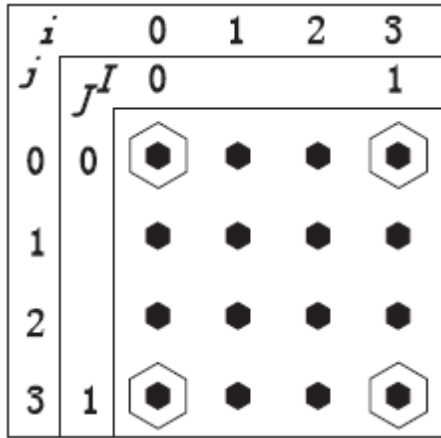


Figure 5-14. Grid point locations on a plane for interpolation, where the large white hexagons show grid points in the large grid (high velocity zone) simulation, and the small black hexagons are grid points in the small grid (low velocity zone) simulation (Aoi and Fujiwara, 1999).

Ma and Audet (2014) focal mechanism (dual grid size)

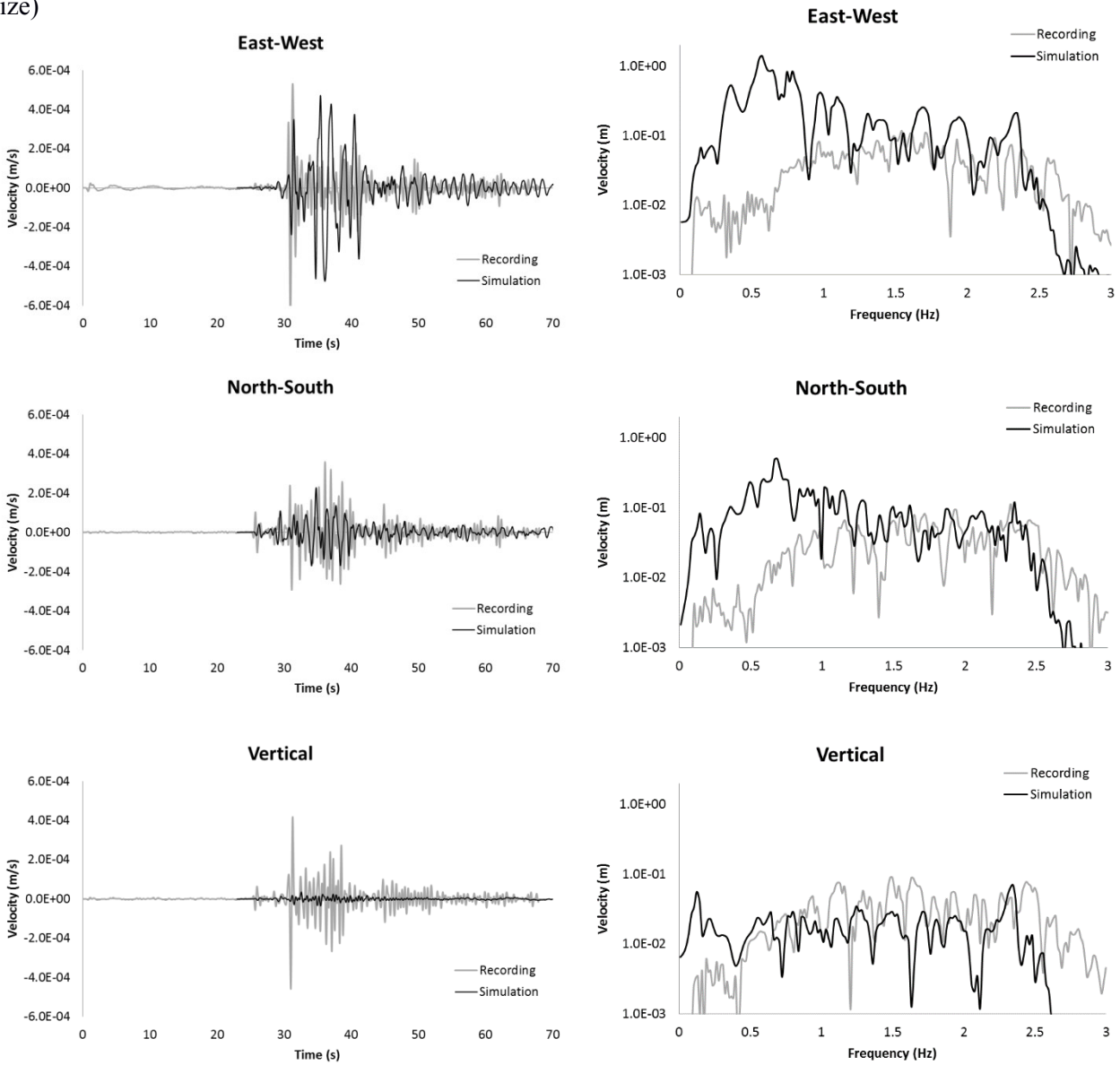


Figure 5-15. Simulated velocity time series and associated velocity Fourier spectrum versus recorded velocity time series and related velocity Fourier spectrum for the Kinburn basin at rock site for the Ma and Audet (2014); epicentral distance=39.3 km, depth=14.5 km, MW=4.7,  $M_0=1.32e+16$  Nt-m, frequency range=0.1-2.5 Hz.

Ma and Audet (2014) focal mechanism

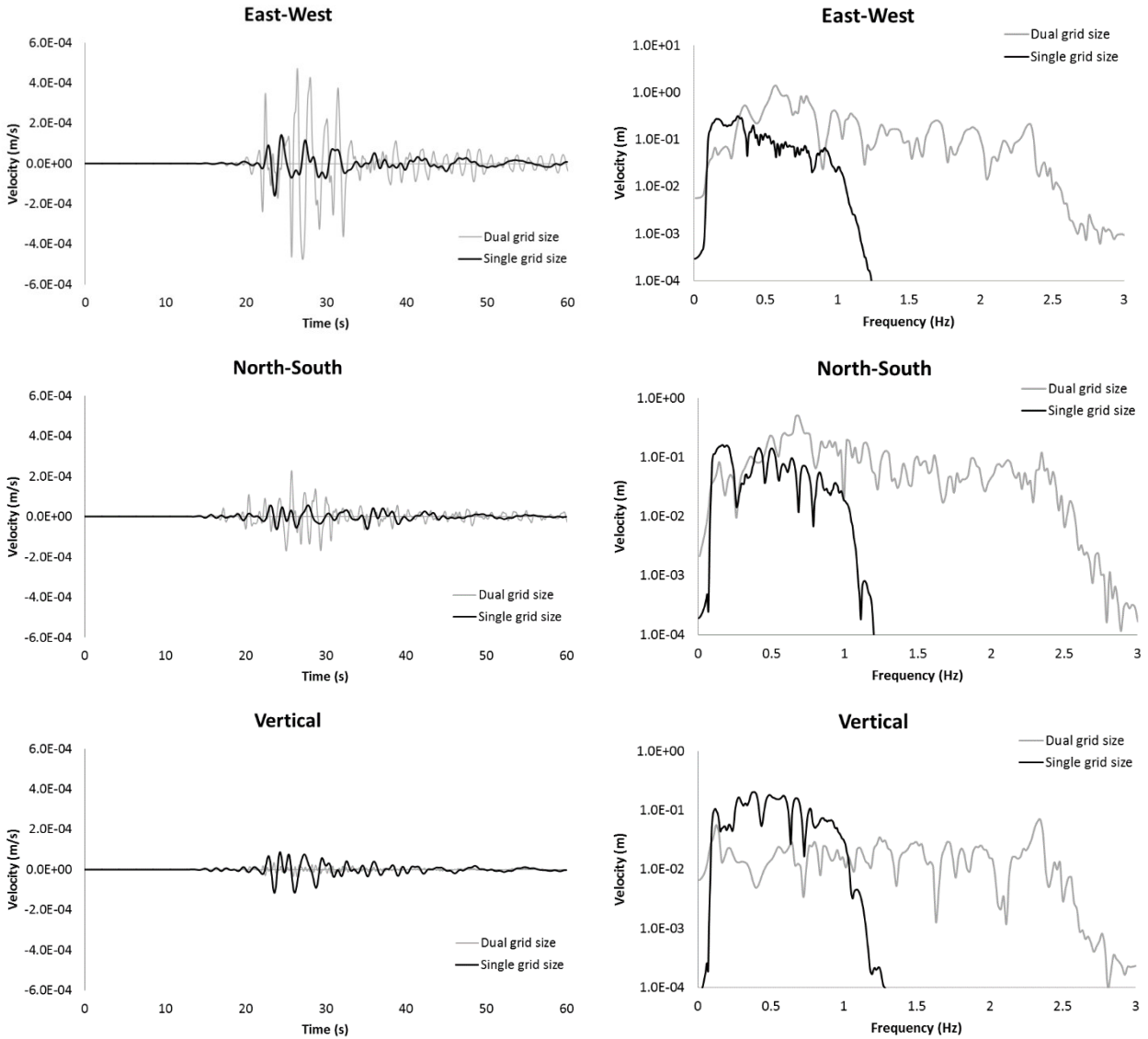


Figure 5-16. Simulated velocity time series and associated velocity Fourier spectrum for the single grid size simulation (frequency range of 0.1-1 Hz) versus modeled velocity time series and related velocity Fourier spectrum for the dual grid size simulation (frequency range of 0.1-2.5 Hz) for the Kinburn basin at rock site for the Ma and Audet (2014); epicentral distance=39.3 km, depth=14.5 km, MW=4.7, M0=1.32e+16 Nt-m.

Ma and Audet (2014) focal mechanism (dual grid size)

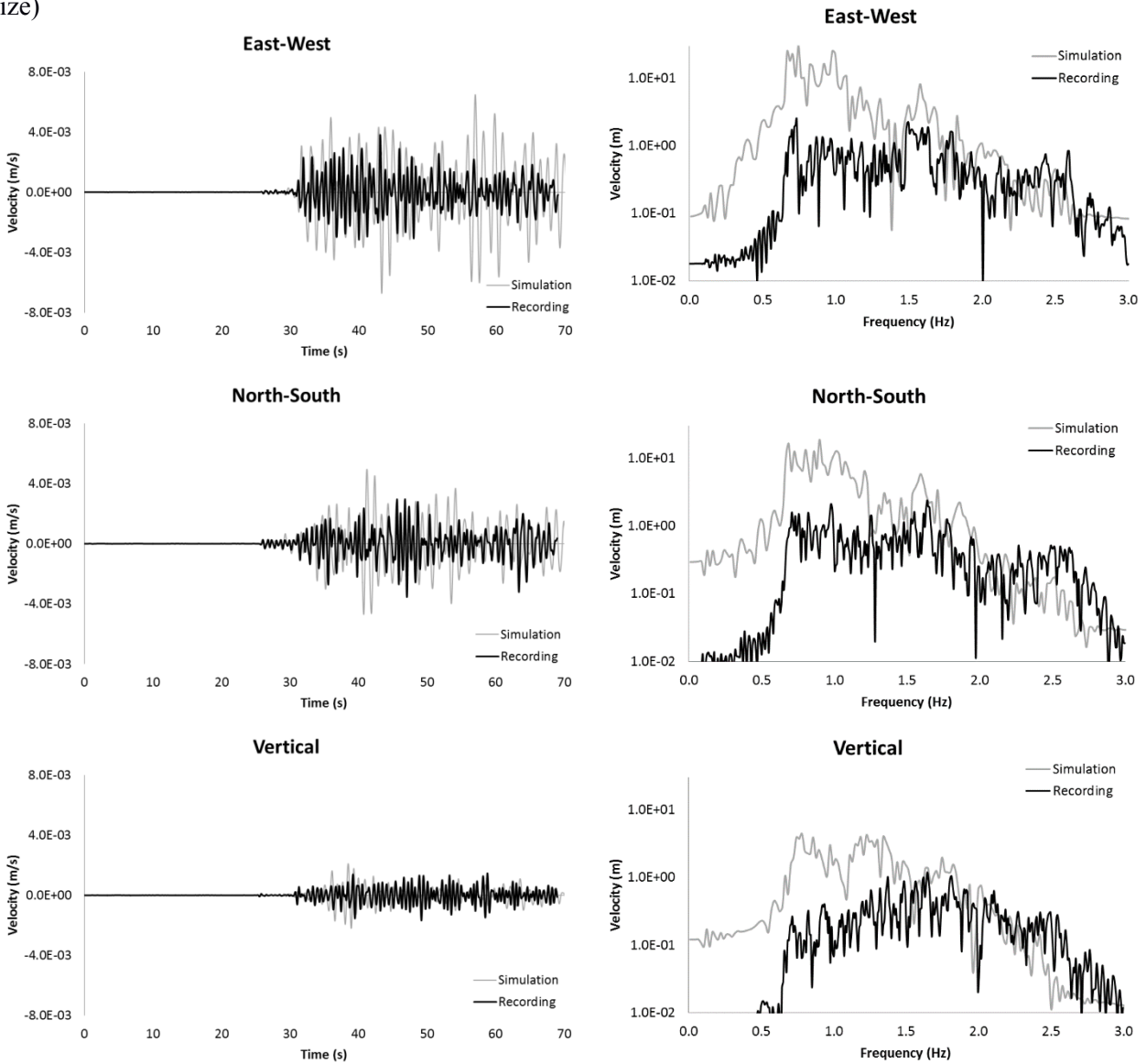


Figure 5-17. Simulated velocity time series and associated velocity Fourier spectrum versus recorded velocity time series and related velocity Fourier spectrum for the Kinburn basin at soil site for the Ma and Audet (2014); epicentral distance=43 km, depth=14.5 km, MW=4.7,  $M_0=1.32e+16$  Nt-m, frequency range=0.1-2.5 Hz.

Ma and Audet (2014) focal mechanism

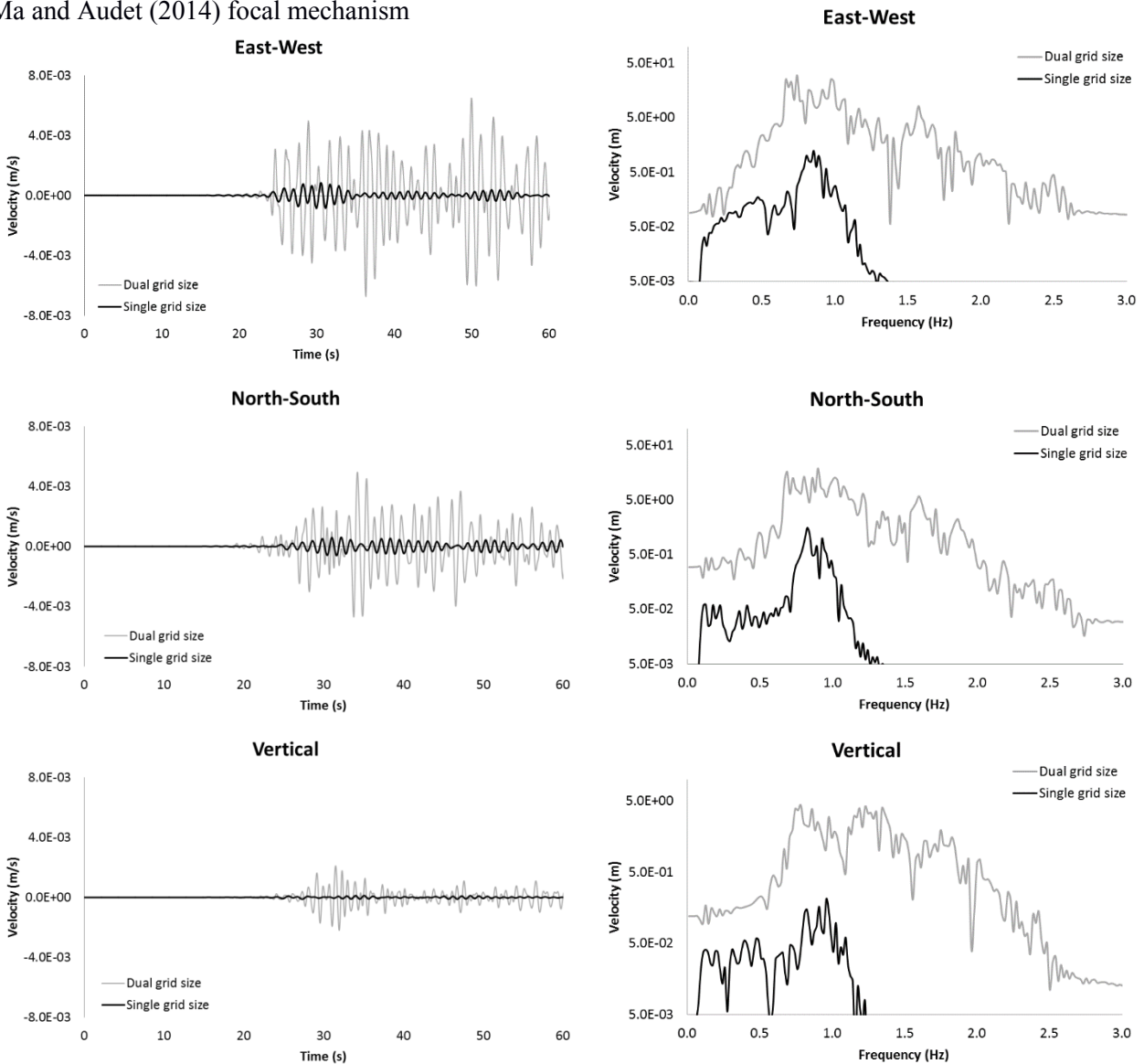


Figure 5-18. Simulated velocity time series and associated velocity Fourier spectrum for the single grid size simulation (frequency range of 0.1-1 Hz) versus modeled velocity time series and related velocity Fourier spectrum for the dual grid size simulation (frequency range of 0.1-2.5 Hz) for the Kinburn basin at soil site for the Ma and Audet (2014); epicentral distance=43 km, depth=14.5 km, MW=4.7, M0=1.32e+16 Nt-m.

Ma and Audet (2014) focal mechanism (dual grid size)

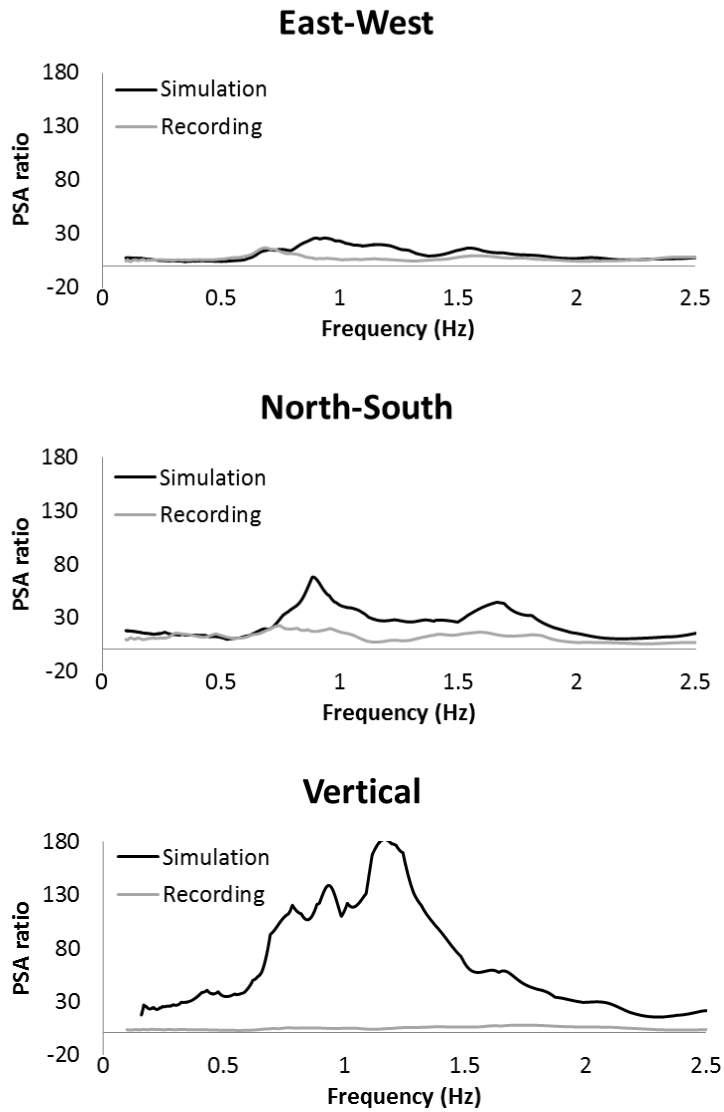


Figure 5-19. PSA ratios of soil site to rock site for recorded velocity time series versus PSA ratios of the simulated velocity time series for the Kinburn basin for the Ma and Audet (2014); epicentral distance=43 km, depth=14.5 km, MW=4.7, M0=1.32e+16 Nt-m, frequency range=0.1-2.5 Hz.

Ma and Audet (2014) focal mechanism

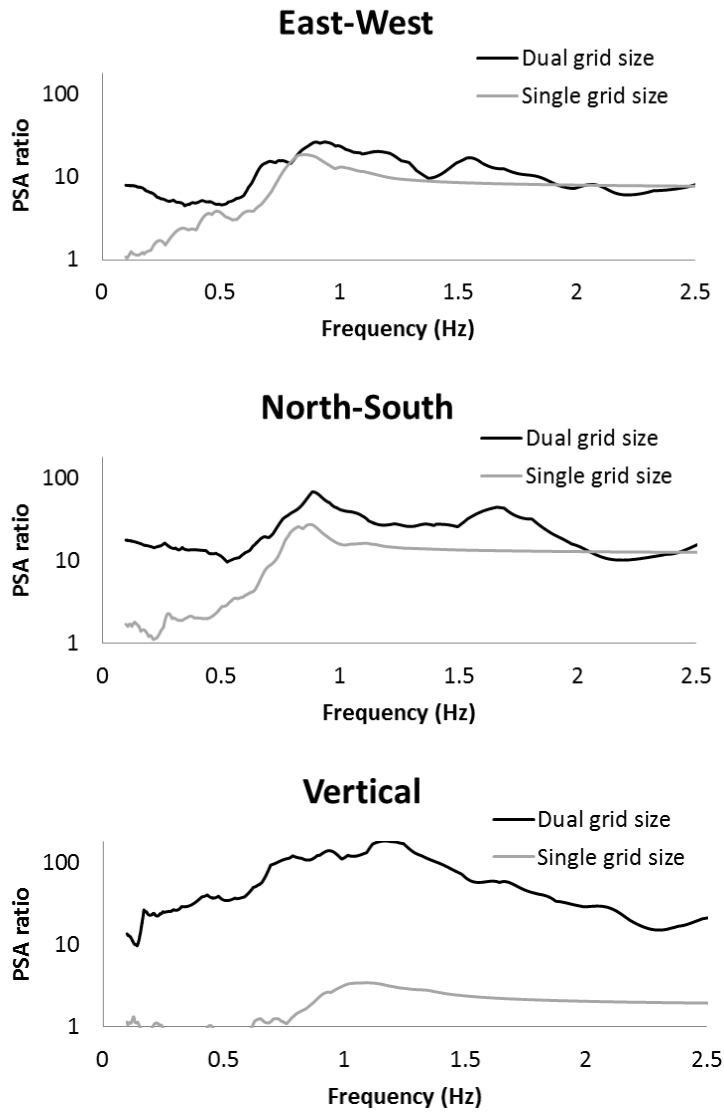


Figure 5-20. PSA ratios of soil site to rock site for the simulated velocity time series of the single grid size simulation (frequency range of 0.1-1 Hz) and the dual grid size simulation (frequency range of 0.1-2.5 Hz) for the Kinburn basin for the Ma and Audet (2014); epicentral distance=43 km, depth=14.5 km, MW=4.7, M0=1.32e+16 Nt-m.

Ma and Audet (2014) focal mechanism (dual grid size)

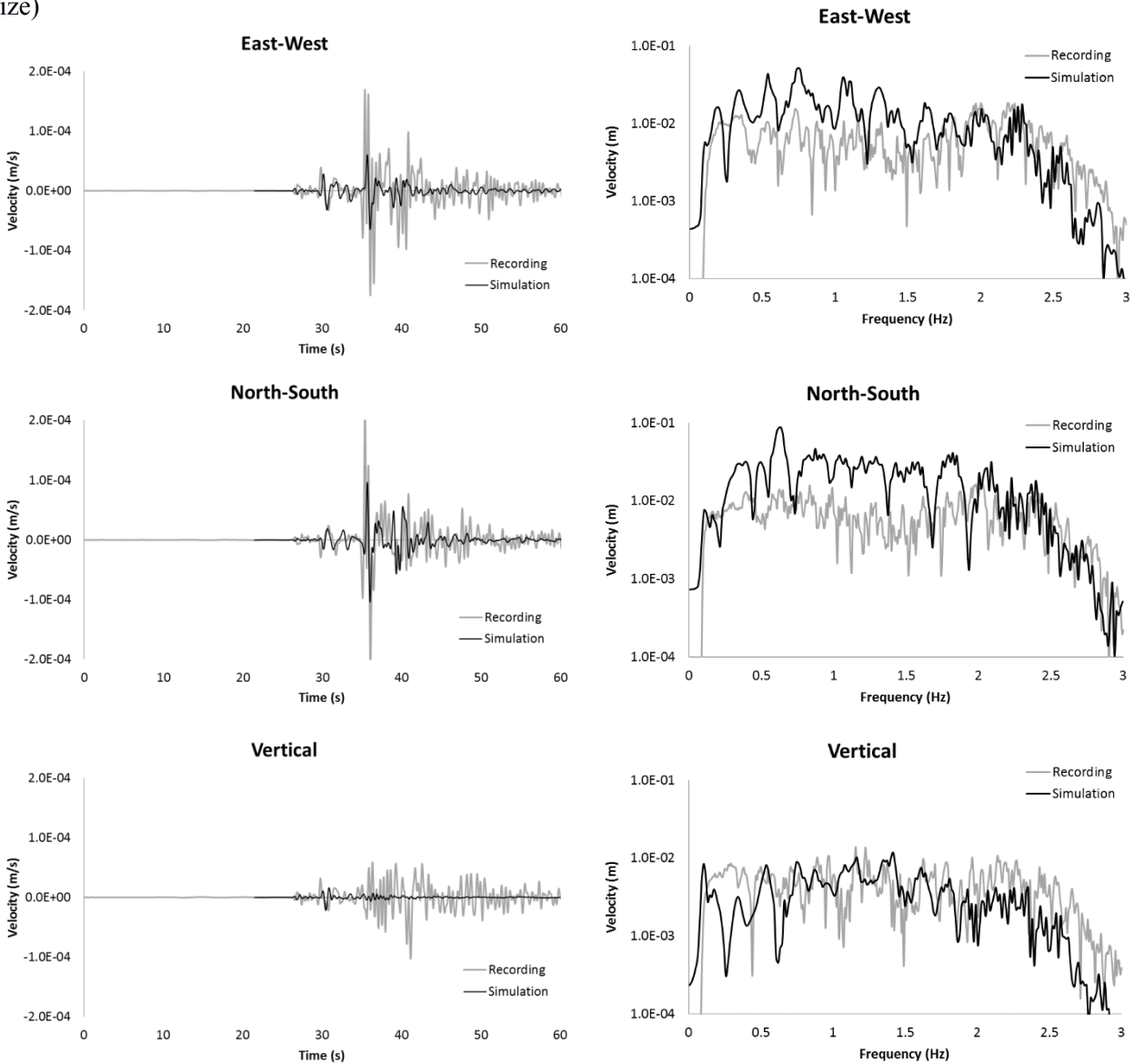


Figure 5-21. Simulated velocity time series and associated velocity Fourier spectrum versus recorded velocity time series and related velocity Fourier spectrum for the Orleans basin at rock site for the Ma and Audet (2014); epicentral distance=72.2 km, depth=14.5 km, MW=4.7,  $M_0=1.32e+16$  Nt-m, frequency range=0.1-2.5 Hz.

Ma and Audet (2014) focal mechanism

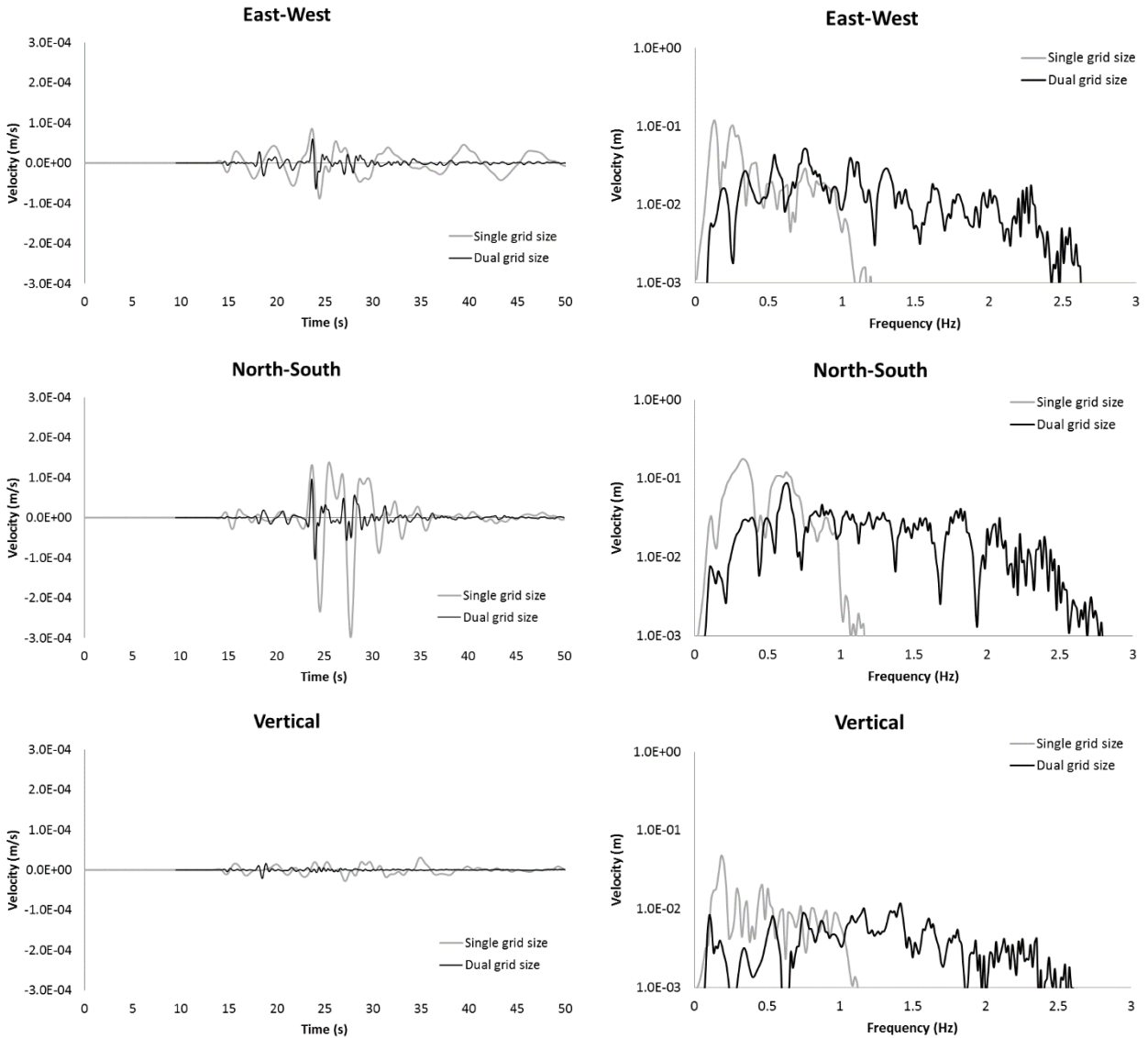


Figure 5-22. Simulated velocity time series and associated velocity Fourier spectrum for the single grid size simulation (frequency range of 0.1-1 Hz) versus modeled velocity time series and related velocity Fourier spectrum for the dual grid size simulation (frequency range of 0.1-2.5 Hz) for the Orleans basin at rock site for the Ma and Audet (2014); epicentral distance=72.2 km, depth=14.5 km, MW=4.7, M0=1.32e+16 Nt-m.

Ma and Audet (2014) focal mechanism (dual grid size)

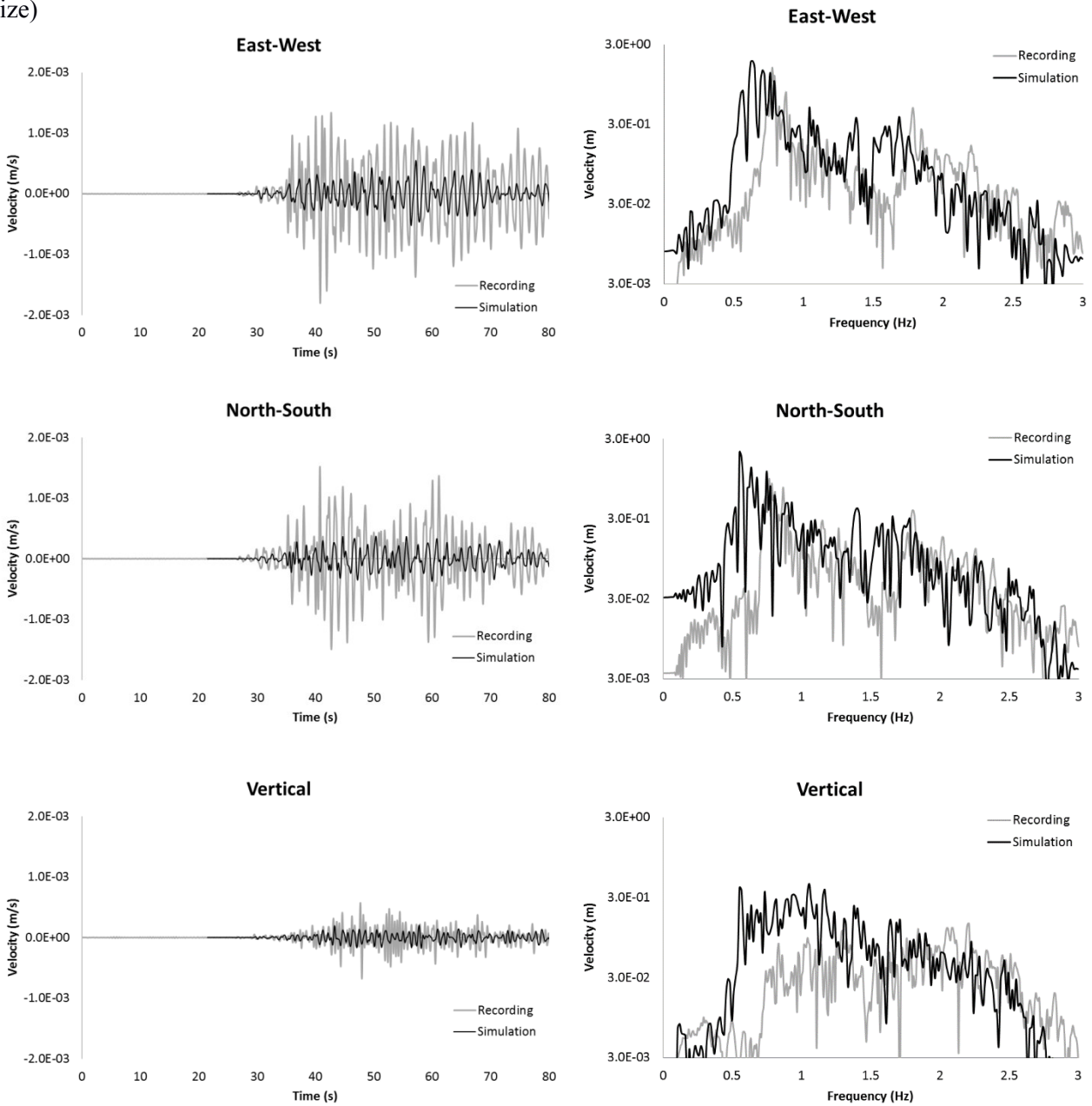


Figure 5-23. Simulated velocity time series and associated velocity Fourier spectrum versus recorded velocity time series and related velocity Fourier spectrum for the Orleans basin at soil site for the Ma and Audet (2014); epicentral distance=70.4 km, depth=14.5 km, MW=4.7,  $M_0=1.32e+16$  Nt-m, frequency range=0.1-2.5 Hz.

Ma and Audet (2014) focal mechanism

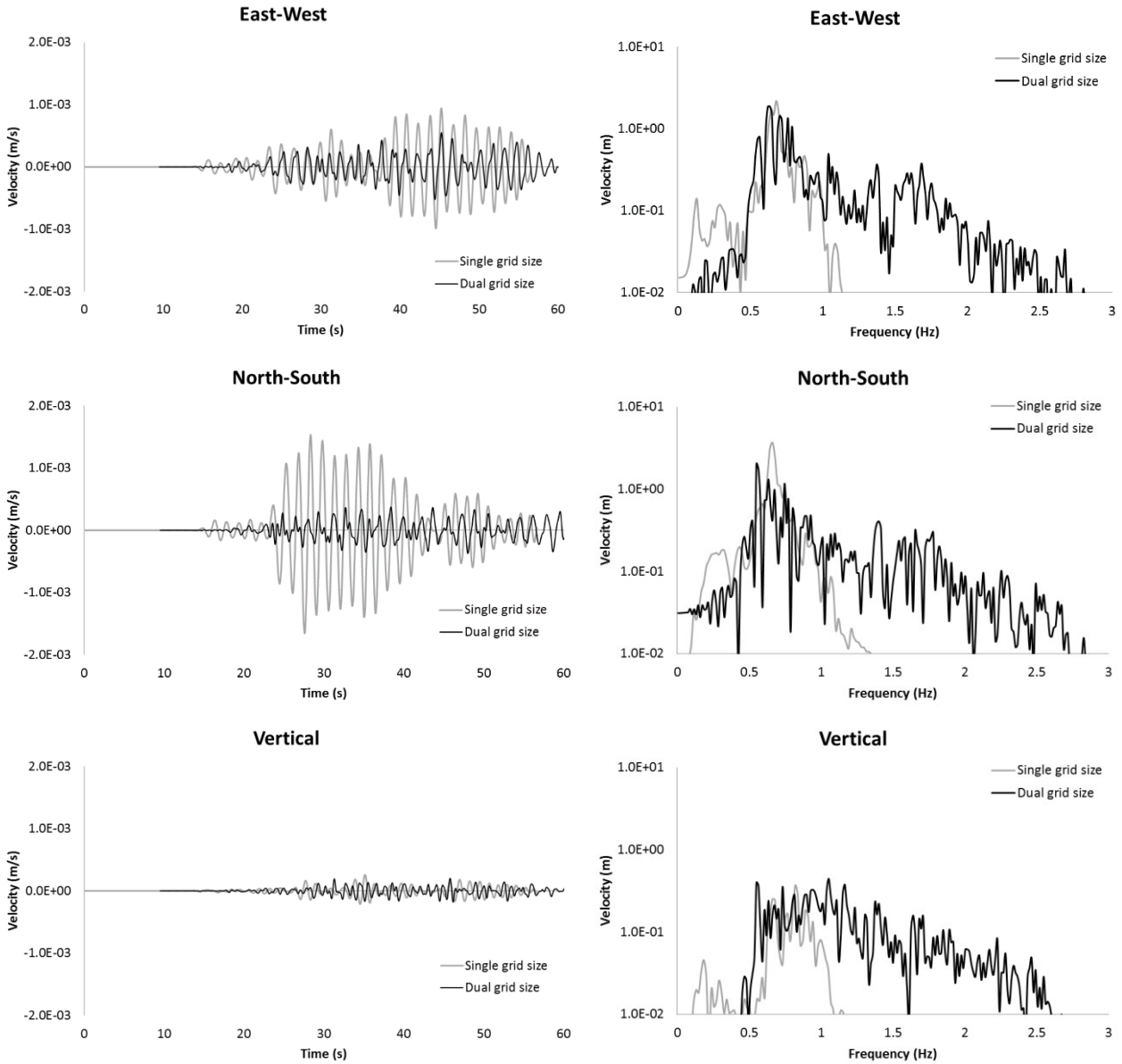


Figure 5-24. Simulated velocity time series and associated velocity Fourier spectrum for the single grid size simulation (frequency range of 0.1-1 Hz) versus modeled velocity time series and related velocity Fourier spectrum for the dual grid size simulation (frequency range of 0.1-2.5 Hz) for the Orleans basin at soil site for the Ma and Audet (2014); epicentral distance=70.4 km, depth=14.5 km, MW=4.7, M0=1.32e+16 Nt-m.

Ma and Audet (2014) focal mechanism (dual grid size)

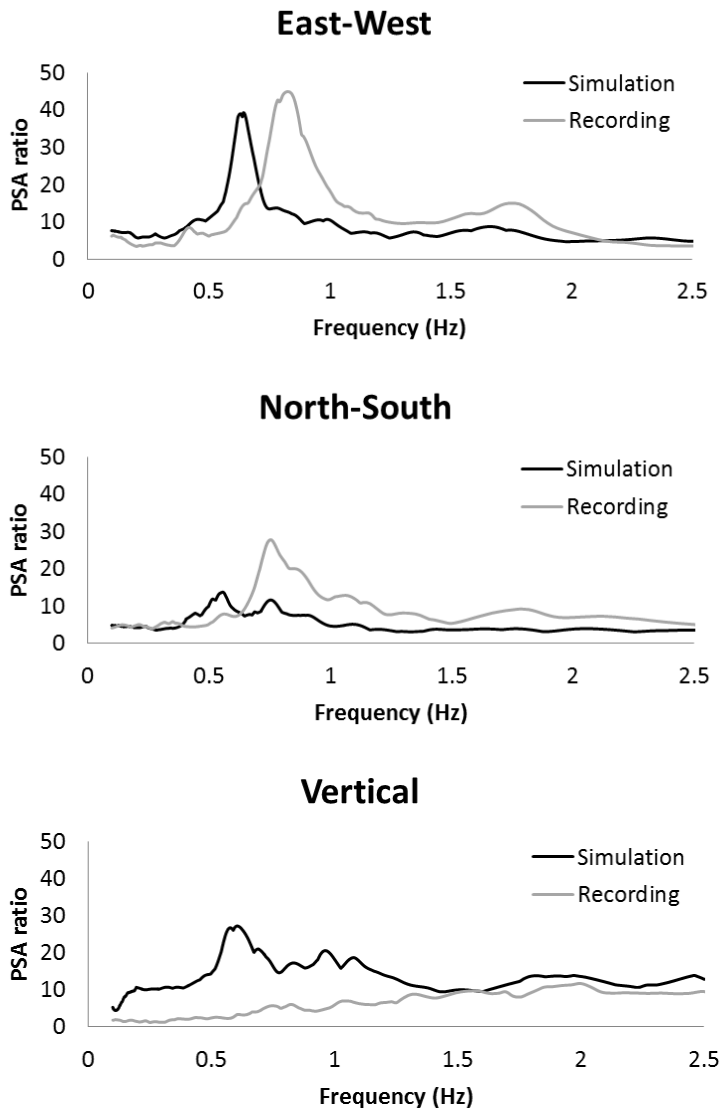


Figure 5-25. PSA ratios of soil site to rock site for recorded velocity time series versus PSA ratios of the simulated velocity time series for the Orleans basin for the Ma and Audet (2014); epicentral distance=70.4 km, depth=14.5 km, MW=4.7, M0=1.32e+16 Nt-m, frequency range=0.1-2.5 Hz.

Ma and Audet (2014) focal mechanism

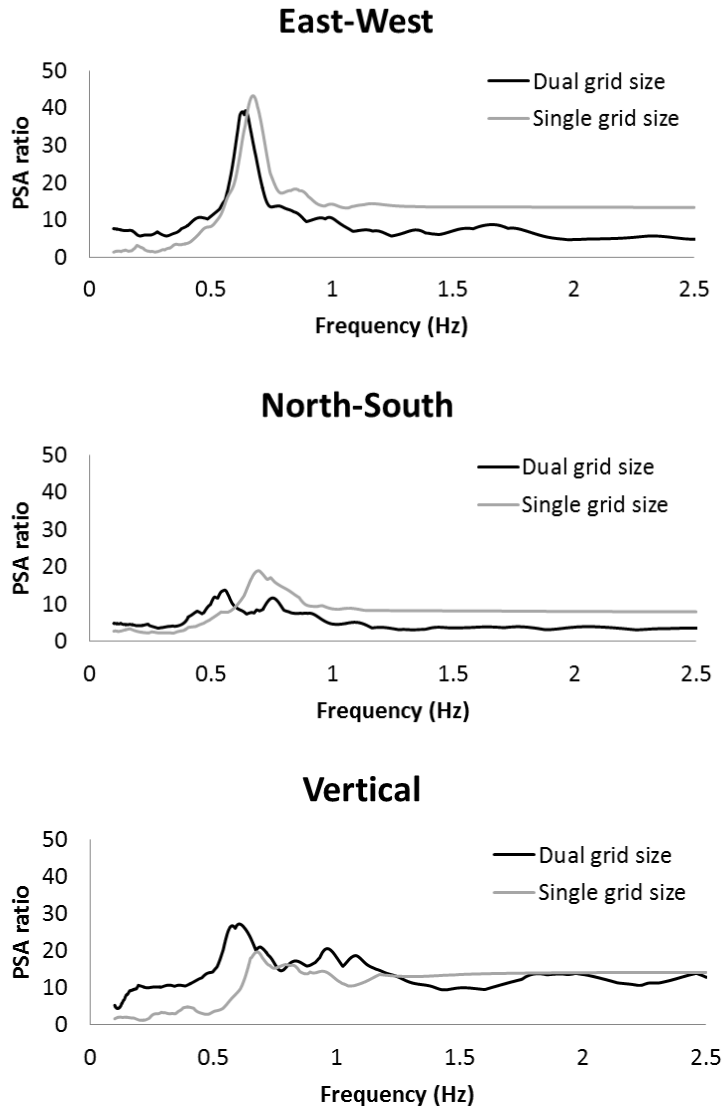


Figure 5-26. PSA ratios of soil site to rock site for the simulated velocity time series of the single grid size simulation (frequency range of 0.1-1 Hz) and the dual grid size simulation (frequency range of 0.1-2.5 Hz) for the Orleans basin for Ma and Audet (2014); epicentral distance=70.4 km, depth=14.5 km, MW=4.7, M0=1.32e+16 Nt-m.

## **6. Conclusion**

### **6.1. Summary**

We used a finite difference (FD) modeling method, developed by Olsen-Day-Cui, to simulate nonlinear-viscoelastic basin effects; a new nonlinear-viscoelastic subroutine was added to the program in a spectral frequency range of 0.1 to 1 Hz in the Kinburn bedrock topographic basin, Ottawa, Canada, for large earthquakes. Considering nonlinear soil behavior in ground motion simulations significantly reduced the predicted PSA, PGA, and PGV values of materials with low strength that were subjected to high intensity incident wave-fields, lowered the frequency content of waves, reduced the resonant frequency amplitudes of the velocity Fourier spectral ratio, damped the energy of waves and, consequently, decreased the predicted amplification. Thus, ignoring nonlinear soil behavior in ground motion simulations can significantly increase the motion parameter values and using the modulus reduction equation or curve is necessary to have a more realistic simulation.

Also, using a finite fault source for nonlinear-viscoelastic simulations caused a slight amplification in the vertical component (trapping more energy in the basin because of the increase of the impedance contrast) and de-amplification in the horizontal components (due to the increase of damping in the basin) compared to viscoelastic simulations.

Studying the sensitivity of the simulations to the source model (seismic moment, strike, slip and dip angles, source function and slip duration) showed that the source function and slip duration can significantly influenced the PGVs. Further, simulations for different seismic moments showed that the PGVs of the earthquake simulations exponentially increased with moment magnitude. In addition, the sensitivity analysis of the regional path properties (crustal velocity and density model, crustal damping model, relaxation coefficients, and relaxation of

modulus for viscoelastic calculations) showed that the crustal velocity and density model influenced the arrival times and slightly affected the PGVs and PSAs; the relaxation coefficients and relaxation of modulus significantly increased the PGVs, particularly for later arrivals. Further, the local site conditions [soil damping (Q) model, Vs contrast ( $V_{s\_soil}/V_{s\_rock}$ )] for a small earthquake ( $M_w=4.7$ ) significantly affected the PGVs, PSAs, and the amplitude of the velocity Fourier spectrum. Lastly, the soil Vs model influenced the frequency content of waves in the basin.

Our results also showed that using a finite fault model to simulate a large earthquake ( $M_w=7$ ) significantly reduced the PGV and the amplitude of the velocity Fourier spectrum at both the rock and soil sites, particularly at high frequencies relative to the point source simulation, because using a finite fault model shifted the frequency content of waves toward lower frequencies. Also, the nonlinear-viscoelastic simulation for modeling a large earthquake ( $M_w=7$ ) significantly damped the high frequency waves in the basin. Thus, the predicted PGV, PSA, and amplitude of the velocity Fourier spectrum were reduced using nonlinear soil effects. In addition, the amplitude of the PSA ratios for the nonlinear-viscoelastic simulation occurred at lower frequencies compared to the frequency of the amplitude of the PSA ratios for the viscoelastic simulation.

Furthermore, using the hybrid non-uniform mesh size finite difference (FD) modeling method, we simulated the ground motion in a spectral frequency range of 0.1 to 2.5 Hz in the Kinburn and Orleans bedrock topographic basins in Ottawa, Canada for the Ladysmith earthquake. Comparing the simulations and records showed that the Bent et al. (2015) focal mechanism properly modeled the velocity time series for all three components for the Kinburn basin at the soil site; however, there were discrepancies between the amplitudes of the velocity

Fourier spectrums of the simulations and of the records, particularly at low frequencies ( $<1.5$  Hz). Further, the simulation only predicted reasonable PSA ratios for the horizontal components. In contrast, the Ma and Audet (2014) focal mechanism predicted accurate PGVs of the horizontal and vertical components at the soil site for the Orleans basin, but there were large differences between the amplitudes of the velocity Fourier spectrums of the simulations and of the records although the differences were less at high frequencies ( $>1$  Hz). Also, the PSA ratios of the simulation using the Ma and Audet (2014) focal mechanism correlated well with the PSA ratios of the records in the horizontal components. Consequently, using the hybrid non-uniform mesh size method, we properly modeled the ground motion for the Kinburn and Orleans basins for a broadband frequency (0.1-2.5 HZ) in a time domain. Further, using the hybrid method, we significantly reduced the computational time (about 40%) and computational cost (about 80%) usually required for regular broadband ground motion simulations.

## **6.2. Future work**

- 1- Inclusion of stochastic finite fault modeling in the hybrid FD method for higher frequencies.
- 2- Application of the modified FD method for the large paleo-earthquakes in Alfred basin.
- 3- Application of the modified method for large and well-recorded earthquakes worldwide.
- 4- Inclusion of the heterogeneity of fault surface (different slip vector, stress drop, etc.). In this study, a simplified homogenous finite fault model was used.
- 5- Improving of the dual grid size simulation to higher frequencies (i.e. 5 Hz or 10 Hz).
- 6- Development of a multi-step multi-grid size simulation method for higher frequencies (i.e. 5 Hz or 10 Hz).

7- Development of a set of ground motion prediction equations for nonlinear soil amplification in eastern Canada based on simulations of scenario earthquakes with different magnitudes and distances following the de-aggregation studies for cities in eastern Canada.

8- Studying the near field ground motion behavior (i.e. directivity and seismic radiation pattern) while using heterogeneous finite fault modeling at higher frequencies

## 7. References

- Adams, J. (1982). Deformed lake sediments record prehistoric earthquakes during the deglaciation of the Canadian Shield (abstract). EOS, Transactions. American Geophysical Union 63, 436.
- Aki, K. & Richards, P. G. (2002). Quantitative Seismology, Second Edition. University Science Books.
- Anderson, J. G., Bodin, P., Brune, J. N., Prince, J., Singh, S. K., Quaas, R., & Onate, M. (1986). Strong ground motion from the Michoacan, Mexico, Earthquake. Science, 233(4768), 1043-1049.
- Aoi, S. & Fujiwara, H. (1999). 3D finite-difference method using discontinuous grids. Bulletin of the Seismological Society of America, 89(4), 918-930.
- Assatourians K and Atkinson G (2010). Database of processed time series and response spectra data for Canada: An example application to study of 2005 MN 5.4 Riviere du Loup, Quebec, earthquake, Seismological Research, 1013-1031, doi: 10.1785/gssrl.81.6.1013
- Atkinson G and Assatourians K (2015). Implementation and validation of EXSIM (a stochastic finite fault ground motion simulation algorithm) on the SCEC broadband platform, Seismological Research, 48-60, doi: 10.1785/0220140097
- Atkinson GM, 2009, Earthquake time histories compatible with 2005 National Building Code of Canada uniform hazard spectrum. Canadian Journal of Civil Engineering, 36: 991-1000.
- Atkinson, G. M. & Adams, J. (2013). Ground motion prediction equations for application to the 2015 Canadian national seismic hazard maps. Canadian Journal of Civil Engineering, 40(10), 988-998.

- Atkinson, G. M. & Adams, J. (2013). Ground motion prediction equations for application to the 2015 Canadian national seismic hazard maps. *Canadian Journal of Civil Engineering*, 40(10), 988-998.
- Atkinson, G. M. & Boore, D. M. (2007). Earthquake ground-motion prediction equations for Eastern North America. *Bulletin of the Seismological Society of America*, 97(3), 1032-1032.
- Atkinson, G. M. & Mereu, R. F. (1992). The shape of ground motion attenuation curves in southeastern Canada. *Bulletin of the Seismological Society of America*, 82(5), 2014-2031.
- Atkinson, G. M. (2004). Empirical attenuation of ground-motion spectral amplitudes in southeastern Canada and the northeastern United States. *Bulletin of the Seismological Society of America*, 94(3), 1079-1095.
- Atkinson, G. M., Assatourians, K., & Lamontagne, M. (2014). Characteristics of the 17 May 2013 M 4.5 Ladysmith, Quebec, Earthquake. *Seismological Research Letters*, 85(3), 755-762.
- Banks, H. T., Hu, S., & Kenz, Z. R. (2011). A brief review of elasticity and viscoelasticity for solids. *Advances in Applied Mathematics and Mechanics*, 3(1), 1-51.
- Basham, P. W., D. H. Weichert, F. M. Anglin, and M. J. Berry (1982). New probabilistic strong seismic ground motion map of Canada: A compilation of earthquake source zones, methods and results, Earth Physics Branch Open File 82-33, 205.
- Basham, P. W., Weichert, D. H., & Berry, M. J. (1979). Regional assessment of seismic risk in eastern Canada. *Bulletin of the Seismological Society of America*, 69(5), 1567-1602.
- Benites, R. & Olsen, K. B. (2005). Modeling strong ground motion in the Wellington metropolitan area, New Zealand. *Bulletin of the Seismological Society of America*, 95(6), 2180-2196.

- Bent, A. L., Lamontagne, M., Peci, V., Halchuk, S., Brooks, G. R., Motazedian, D., ... & Hayek, S. (2015). The 17 May 2013 M 4.6 Ladysmith, Quebec, Earthquake. *Seismological Research Letters*, 86(2A), 460-476.
- Berenger, J. P. (1994). A perfectly matched layer for the absorption of electromagnetic waves. *Journal of Computational Physics*, 114(2), 185-200.
- Beresnev, I. A. & Atkinson, G. M. (2002). Source parameters of earthquakes in eastern and western North America based on finite-fault modeling. *Bulletin of the Seismological Society of America*, 92(2), 695-710.
- Beresnev, I. A. & Wen, K. L. (1996). Nonlinear soil response—A reality? *Bulletin of the Seismological Society of America*, 86(6), 1964-1978.
- Beresnev, I. A. (2002). Nonlinearity at California generic soil sites from modeling recent strong-motion data. *Bulletin of the Seismological Society of America*, 92(2), 863-870.
- Beresnev, I. A., & K.-L. Wen (1996). Nonlinear soil response—A reality?, *Bull. Seismol. Soc. Am.* 86, 1964–1978.
- Beresnev, I. A., Wen, K. L., & Tein Yeh, Y. (1995). Nonlinear soil amplification: its corroboration in Taiwan. *Bulletin of the Seismological Society of America*, 85(2), 496-515.
- Bielak, J. & Christiano, P. (1984). On the effective seismic input for non-linear soil-structure interaction systems. *Earthquake engineering & structural dynamics*, 12(1), 107-119.
- Bielak, J., Loukakis, K., Hisada, Y., & Yoshimura, C. (2003). Domain reduction method for three-dimensional earthquake modeling in localized regions, Part I: Theory. *Bulletin of the Seismological Society of America*, 93(2), 817-824.
- Bonilla, L. F. (2000). Computation of linear and nonlinear site response for near field ground motion. Ph.D. Thesis, University of California, Santa Barbara, CA, USA.

- Bonilla, L. F., Liu, P. C., & Nielsen, S. (2006, August). 1D and 2D linear and nonlinear site response in the Grenoble area. In Proc. 3rd Int. Symp. on the Effects of Surface Geology on Seismic Motion (ESG2006).
- Bonilla, L.F. (2000). Computation of linear and nonlinear site response for near field ground motion. Ph.D. Thesis, University of California, Santa Barbara, CA, USA.
- Bormann, P. & Di Giacomo, D. (2011). The moment magnitude  $M_w$  and the energy magnitude  $M_e$ : common roots and differences. *Journal of Seismology*, 15(2), 411-427.
- Bormann, P., Baumbach, M., Bock, G., Grosser, H., Choy, G. L., & Boatwright, J. (2002). Seismic sources and source parameters. *IASPEI New Manual of Seismological Observatory Practice*, 1, 1-94.
- Brinkgreve, R. B. (2005). Selection of soil models and parameters for geotechnical engineering application. In *Soil constitutive models: Evaluation, selection, and calibration*, 69-98.
- Brooks, G.R. (2015). An Integrated Stratigraphic Approach to Investigating Evidence of Paleearthquakes in Lake Deposits of Eastern Canada. *Geoscience Canada*, 42(2).
- Brooks, G.R. (2015). Evidence of paleoseismicity within the West Quebec Seismic Zone, eastern Canada, from the age and morphology of sensitive clay landslides. 6th INQUA International Workshop on Active Tectonics Paleoseismology and Archaeoseismology, Pescara, IT, April 19-24.
- Burger, R. W., Somerville, P. G., Barker, J. S., Herrmann, R. B., & Helmberger, D. V. (1987). The effect of crustal structure on strong ground motion attenuation relations in eastern North America. *Bulletin of the Seismological Society of America*, 77(2), 420-439.
- Cerjan, C., Kosloff, D., Kosloff, R., & Reshef, M. (1985). A non-reflecting boundary condition for direct acoustic and elastic wave equations. *Geophysics*, 50, 705-708.

- Chandra, J., Guéguen, P., Steidl, J. H., & Bonilla, L. F. (2015). In situ assessment of the  $G-\gamma$  curve for characterizing the nonlinear response of soil: Application to the Garner Valley downhole array and the wildlife liquefaction array. *Bulletin of the Seismological Society of America*, 105(2A), 993-1010.
- Chang, C. Y., Power, M. S., Tang, Y. K., & Mok, C. M. (1989). Evidence of nonlinear soil response during a moderate earthquake. 12<sup>th</sup> International Conference on Soil Mechanics and Foundation Engineering, vol. 3, Rio de Janeiro, Brazil, 13–18 August 1989, 1927–1930.
- Chapman, M. C. & Godbee, R. W. (2012). Modeling geometrical spreading and the relative amplitudes of vertical and horizontal high-frequency ground motions in eastern North America. *Bulletin of the Seismological Society of America*, 102(5), 1957-1975.
- Chew, W. C. & Liu, Q. H. (1996). Perfectly matched layers for elastodynamics: A new absorbing boundary condition. *Journal of Computational Acoustics*, 4(04), 341-359.
- Chin, B. H. & Aki, K. (1991). Simultaneous study of the source, path, and site effects on strong ground motion during the 1989 Loma Prieta earthquake: a preliminary result on pervasive nonlinear site effects. *Bulletin of the Seismological Society of America*, 81(5), 1859-1884.
- Choi, Y. & Stewart, J. P. (2005). Nonlinear site amplification as a function of 30 m shear wave velocity. *Earthquake Spectra*, 21(1), 1-30.
- Choi, Y. & Stewart, J.P. (2003). Nonlinear Site Amplification as Function of 30 m Shear Wave velocity. *Earthquake Spectra*, 21: 1–30.
- Crane, S. & Motazedian, D. (2014). Low-frequency scaling applied to stochastic finite-fault modeling. *Journal of Seismology*, 18(1), 109-122.
- Crane, S. (2017). Numerical modelling of seismic wave propagation through a soft-sediment filled basin near Kinburn, ON (Doctoral dissertation, Carleton University).

- Crane, S., Motazedian, D., & Hunter, J. (2015). 2D Modelling of Seismic Wave Propagation through a Soft Soil Basin: Kinburn, Canada. Proceedings of the 11<sup>th</sup> Canadian Conference on Earthquake Engineering, in press.
- Cremonini, M. G., Christiano, P., & Bielak, J. (1988). Implementation of effective seismic input for soil-structure interaction systems. *Earthquake engineering & structural dynamics*, 16(4), 615-625.
- Crouse, C. B. (1991). Ground-motion attenuation equations for earthquakes on the Cascadia subduction zone. *Earthquake Spectra* 7, 201–235, and 506.
- Crouse, C. B. (1991). Ground-motion attenuation equations for earthquakes on the Cascadia subduction zone. *Earthquake Spectra* 7, 201–235, and 506.
- Crow, H., Hunter, J. A., & Motazedian, D. (2011). Monofrequency in situ damping measurements in Ottawa area soft soils. *Soil Dynamics and Earthquake Engineering*, 31(12), 1669-1677.
- Crow, H., Pyne, M., Hunter, J. A., Pullan, S. E., Motazedian, D., & Pugin, A. (2007). Shear wave measurements for earthquake response evaluation in Orleans, Ontario. Geological Survey of Canada. Open-File, 5579, 192.
- Cui, Y., Olsen, K. B., Jordan, T. H., Lee, K., Zhou, J., Small, P., ... & Levesque, J. (2010). Scalable earthquake simulation on petascale supercomputers. Proceedings of the 2010 ACM/IEEE International Conference for High Performance Computing, Networking, Storage and Analysis (1-20). IEEE Computer Society.
- Cui, Y., Olsen, K., Chourasia, A., Moore, R., Maechling, P., & Jordan, T. (2009). The terashake computational platform for large-scale earthquake simulations. *Advances in Geocomputing*. Springer, Berlin, Heidelberg, 229-277.

- Cui, Y., Poyraz, E., Olsen, K. B., Zhou, J., Withers, K., Callaghan, S., ... & Shi, Z. (2013). Physics-based seismic hazard analysis on petascale heterogeneous supercomputers. High Performance Computing, Networking, Storage and Analysis (SC), 2013 International Conference for (1-12). IEEE.
- Darragh, R. B. & Shakal, A. F. (1991). The site response of two rock and soil station pairs to strong and weak ground motion. *Bulletin of the Seismological Society of America*, 81(5), 1885-1899.
- Day, S. M. & Bradley, C. R. (2001). Memory-efficient simulation of anelastic wave propagation. *Bulletin of the Seismological Society of America*, 91(3), 520-531.
- Day, S. M. & Minster, J. B. (1984). Numerical simulation of attenuated wavefields using a Padé approximant method. *Geophysical Journal International*, 78(1), 105-118.
- Day, S. M. (1998). Efficient simulation of constant Q using coarse-grained memory variables. *Bulletin of the Seismological Society of America*, 88(4), 1051-1062.
- Díaz-Rodríguez, J. A. & López-Molina, J. A. (2008). Strain thresholds in soil dynamics. *Proceedings of the 14<sup>th</sup> World Conference on Earthquake Engineering*, 12-17.
- Doughty, M., Eyles, N., Eyles, C.H., Wallace, K., & Boyce, J. I. (2014). Lake sediments as natural seismographs: earthquake-related deformations (seismites) in central Canadian lakes. *Sedimentary Geology*, 313, 45-67.
- Dupros, F., Martin, F. D., Foerster, E., Komatitsch, D., & Roman, J. (2010). High-performance finite-element simulations of seismic wave propagation in three-dimensional non-linear inelastic geological media. *Parallel Computing*, 36: 308–325.

- Duputel, Z., Rivera, L., Kanamori, H., & Hayes, G. (2012). W phase source inversion for moderate to large earthquakes (1990–2010). *Geophysical Journal International*, 189(2), 1125-1147.
- Duputel, Z., Tsai, V. C., Rivera, L., & Kanamori, H. (2013). Using centroid time-delays to characterize source durations and identify earthquakes with unique characteristics. *Earth and Planetary Science Letters*, 374, 92-100.
- Dziewonski, A. M., Chou, T. A., & Woodhouse, J. H. (1981). Determination of earthquake source parameters from waveform data for studies of global and regional seismicity. *Journal of Geophysical Research: Solid Earth*, 86(B4), 2825-2852.
- Eaton, D. W., Dineva, S., & Mereu, R. (2006). Crustal thickness and V P/V S variations in the Grenville orogen (Ontario, Canada) from analysis of teleseismic receiver functions. *Tectonophysics*, 420(1), 223-238.
- Eden, W. J. & Crawford, J. B. (1957). *Geotechnical Properties of Leda Clay in the Ottawa Area*; National Research Council of Canada, Research Paper No. 37 of the Division of Building Research, Ottawa, ON.
- Ekström, G., Nettles, M., & Dziewoński, A. M. (2012). The global CMT project 2004–2010: Centroid-moment tensors for 13,017 earthquakes. *Physics of the Earth and Planetary Interiors*, 200, 1-9.
- El Mosallamy, M., El Fattah, T. T. A., & El Khouly, M. (2016). Experimental study on the determination of small strain-shear modulus of loess soil. *HBRC Journal*, 12(2), 181-190.
- Esmaeilzadeh, A., Brooks, G.R., Samson, C. (2017), Evidence of synchronous mass transport deposits from sub-bottom profiling at Lac de l'Argile, Quebec, CGU and CSAFM joint Annual Scientific Meeting, Vancouver, BC, Canada.

- Esmaeilzadeh, A., Motazedian, D., Hunter J. (2019). 3-D nonlinear ground motion simulation using a physics-based method for the Kinburn basin. *Bulletin of the Seismological Society of America*, submitted for publication.
- Falk, J., Tessmer, E., & Gajewski, D. (1996). Tube wave modeling by the finite-difference method with varying grid spacing. *Pure and Applied Geophysics*, 148(1-2), 77-93.
- Field, E. H., Johnson, P. A., Beresnev, I. A., & Zeng, Y. (1997). Nonlinear ground-motion amplification by sediments during the 1994 Northridge earthquake. *Nature*, 390(6660), 599-602.
- Fratta, D., Puppala, A. J., & Munhunthan, B. (2010). *Proceedings of GeoFlorida 2010: advances in analysis, modeling and design*, West Palm Beach, Florida, USA, American Society of Civil Engineers (ASCE).
- Gélis, C. & Bonilla, L. F. (2012). 2-DP–SV numerical study of soil–source interaction in a non-linear basin. *Geophysical Journal International*, 191(3), 1374-1390.
- Gélis, C. & Bonilla, L. F. (2014). Influence of a sedimentary basin infilling description on the 2-DP–SV wave propagation using linear and non-linear constitutive models. *Geophysical Journal International*, 198(3), 1684-1700.
- Gélis, C., Bonilla, F., & Peng-Cheng, L. (2011). Effect of Material Rheology When Modeling Wave Propagation in Complex Media: A 2D P-SV Case Study. 4<sup>th</sup> IASPEI / IAEE International Symposium, Santa Barbara, CA, USA.
- Graves, R. W. & Day, S. M. (2003). Stability and accuracy analysis of coarse-grain visco-elastic simulations. *Bulletin of the Seismological Society of America*, 93(1), 283-300.
- Graves, R. W., Aagaard, B. T., Hudnut, K. W., Star, L. M., Stewart, J. P., & Jordan, T. H. (2008). Broadband simulations for Mw 7.8 southern San Andreas earthquakes: Ground motion

- sensitivity to rupture speed. *Geophysical Research Letters*, 35(22).
- Guéguen, P. (2016). Predicting nonlinear site response using spectral acceleration vs PGV/VS30: a case history using the Volvi-test site. *Pure and Applied Geophysics*, 173(6), 2047-2063.
- Hanks, T. C. & Kanamori, H. (1979). A moment magnitude scale. *Journal of Geophysical Research: Solid Earth*, 84(B5), 2348-2350.
- Hardin, B. O. & Drnevich, V. P. (1972). Shear modulus and damping in soils: measurement and parameter effects. *Journal of Soil Mechanics and Foundations Division*, 98(sm6), 603–624.
- Hartzell, S., Bonilla, L. F., & Williams, R. A. (2004). Prediction of nonlinear soil effects. *Bulletin of the Seismological Society of America*, 94(5), 1609-1629.
- Hartzell, S., Guatteri, M., Mai, P. M., Liu, P. C., & Fisk, M. (2005). Calculation of broadband time histories of ground motion, Part II: Kinematic and dynamic modeling using theoretical Green's functions and comparison with the 1994 Northridge earthquake. *Bulletin of the Seismological Society of America*, 95(2), 614-645.
- Hartzell, S., Harmsen, S., Frankel, A., & Larsen, S. (1999). Calculation of broadband time histories of ground motion: Comparison of methods and validation using strong-ground motion from the 1994 Northridge earthquake. *Bulletin of the Seismological Society of America*, 89(6), 1484-1504.
- Hayashi, K., Burns, D. R., & Toksöz, M. N. (2001). Discontinuous-grid finite-difference seismic modeling including surface topography. *Bulletin of the Seismological Society of America*, 91(6), 1750-1764.
- Hayek, S. J. (2016). Seismic basin effects over soft-sediment filled basins in Ottawa, Canada (Master dissertation, Carleton University).

- Hisada, Y. & Yamamoto, S. (1996). One, two and three dimensional site effects in the sediment-filled basins. Proceedings of the 11<sup>th</sup> World Conference on Earthquake Engineering, Acapulco, Mexico, Paper No. 2040.
- Holzer, T. L. (1994). Loma Prieta damage largely attributed to enhanced ground shaking. EOS, Transactions - American Geophysical Union, 75: 299-301.
- Hunter, J. A. & Crow, H. L. (2012). Shear Wave Velocity Measurement Guidelines for Canadian Seismic Site Characterization in Soil and Rock. Geological Survey of Canada, Open File #7078.
- Hunter, J. A., Burns, R. A., Good, R. L., Aylsworth, J. M., Pullan, S. E., Perret, D., & Douma, M. (2007). Borehole shear wave velocity measurements of Champlain Sea sediments in the Ottawa-Montreal region. Geological Survey of Canada, Open File #5345.
- Hunter, J. A., Crow, H. L., Brooks, G. R., ... & Ter-Emmanuil, V. (2012). Ottawa-Gatineau seismic site classification map from combined geological/geophysical data. Geological Survey of Canada, Open File #7067.
- Hunter, J. A., Crow, H. L., Brooks, G. R., Pyne, M., Motazedian, D., Lamontagne, M., ... & Burns, R. A. (2010). Seismic site classification and site period mapping in the Ottawa area using geophysical methods. Geological Survey of Canada, Open File #6273(1).
- Hunter, J. A., Crow, H. L., Brooks, G. R., Pyne, M., Motazedian, D., Lamontagne, M., Pugin, A. J. M., Pullan, S. E., Cartwright, T., Douma, M., Burns, R. A., Good, R. L., Kaheshi-Banab, K., Caron, R., Kolaj, M., Folahan, I., Dixon, L., Dion, K., Duxbury, A., Landriault, A., Ter-Emmanuil, V., Jones, A., Plastow, G., & Muir, D. (2010). Seismic site classification and site period mapping in the Ottawa area using geophysical methods. Geological Survey of Canada. Open File #6273.

- IASPEI (2005). Summary of Magnitude Working Group recommendations on standard procedures for determining earthquake magnitudes from digital data, Procedures as adopted by the IASPEI Commission on Seismological Observation and Interpretation (CoSOI), Santiago, Chile,
- Imperator, W. & Mai, P. M. (2012). Sensitivity of broad-band ground-motion simulations to earthquake source and Earth structure variations: an application to the Messina Straits (Italy). *Geophysical Journal International*, 188(3), 1103-1116.
- Ishihara, Kenji. (1996). *Soil Behaviour in Earthquake Geotechnics*. Oxford University Press.
- Iwan, W. D. (1967). On a class of models for the yielding behavior of continuous and composite systems. *Journal of Applied Mechanics*, 34(3), 612-617.
- Jastram, C. & Behle, A. (1991). Elastic modeling by finite-difference and the rapid expansion method (REM). In *SEG Technical Program Expanded Abstracts 1991*. Society of Exploration Geophysicists, 1573-1576.
- Jastram, C. & Tessmer, E. (1994). Elastic modelling on a grid with vertically varying spacing 1. *Geophysical prospecting*, 42(4), 357-370.
- Kawase, H. (2003). *International Handbook of Earthquake and Engineering Seismology*, Chapter 'Site Effects on Strong Ground Motions.' Volume 81B, San Diego, CA, USA.
- Kawase, H. (2003). Site effects on strong ground motions. *International Geophysics Series*, 81(B), 1013-1030.
- Khaheshi Banab, K., Kolaj, M., Motazedian, D., Sivathayalan, S., Hunter, J. A., Crow, H. L., ... & Pyne, M. (2012). Seismic site response analysis for Ottawa, Canada: A comprehensive study using measurements and numerical simulations. *Bulletin of the Seismological Society of America*, 102(5), 1976-1993.

- Köhn, D. & Bohlen, T. (2000). On the numerical stability of spatial variable finite-difference grids in seismic modelling. *Geophysical Journal International*, 142, 000-000.
- Kolaj, M. (2010). Ottawa bedrock shear wave classification and weak motion earthquake site amplifications for the Orleans buried valley. Bachelor of Science, Honours thesis, Carleton University.
- Konder, R. L. & Zelasko, J. S. (1963). Hyperbolic stress-strain formulation of sands. Second Pan American Conference on soil mechanics and foundation engineering, Sao Paulo, Brazil.
- Konno, K. & Ohmachi, T. (1998). Ground-motion characteristics estimated from spectral ratio between horizontal and vertical components of microtremor. *Bulletin of the Seismological Society of America*, 88(1), 228-241.
- Kramer, S. L. (1996). *Geotechnical Earthquake Engineering*. Prentice Hall, Upper Saddle River, NJ, USA.
- Kristek, J., Moczo, P., & Galis, M. (2010). Stable discontinuous staggered grid in the finite-difference modelling of seismic motion. *Geophysical Journal International*, 183(3), 1401-1407.
- Lajeunesse, P., Sinkunas, B., Morissette, A., Normandeau, A., Joyal, G., St-Onge, G., & Locat, J. (2017). Large-scale seismically-induced mass-movements in a former glacial lake basin: Lake Témiscouata, northeastern Appalachians (eastern Canada). *Marine Geology*, 384, 120-130.
- Lanzo, G., Vucetic, M., & Doroudian, M. (1997). Reduction of shear modulus at small strains in simple shear. *Journal of Geotechnical and Geoenvironmental Engineering*, 123(11), 1035-1042.

- Levander, A. R. (1988). Fourth-order finite-difference P-SV seismograms. *Geophysics*, 53(11), 1425-1436.
- Li, W. (2010). Nonlinear effects in ground motion simulations: modeling variability, parametric uncertainty and implications in structural performance predictions (Doctoral dissertation, Georgia Institute of Technology).
- Liam Finn, W. D., Lee, K. W., & Martin, G. R. (1977). An effective stress model for liquefaction. *Electronics Letter*, 103(ASCE 13008 Proceeding).
- Liu, B. (2013). Absorption of Boundary Reflection on Simulation of Elastic Waves in Heterogeneous Medium. 2013 International Conference on Information Science and Technology Applications (ICISTA-2013). Atlantis Press.
- Liu, P. & Archuleta, R. J. (2006). Efficient modeling of Q for 3D numerical simulation of wave propagation. *Bulletin of the Seismological Society of America*, 96(4A), 1352-1358.
- Liu, P., Archuleta, R. J., & Hartzell, S. H. (2006). Prediction of broadband ground-motion time histories: Hybrid low/high-frequency method with correlated random source parameters. *Bulletin of the Seismological Society of America*, 96(6), 2118-2130.
- Ludwig, W. J., Nafe, J. E., & Drake, C. L. (1970). Seismic refraction, in *The Sea*, A. E. Maxwell (Editor), Vol. 4, Wiley-Interscience, New York, 53-84.
- Ma, K. F., Lee, C. T., Tsai, Y. B., Shin, T. C., & Mori, J. (1999). The Chi-Chi, Taiwan earthquake: Large surface displacements on an inland thrust fault. *Eos, Transactions American Geophysical Union*, 80(50), 605-611.
- Ma, S. & Audet, P. (2014). The 5.2 magnitude earthquake near Ladysmith, Quebec, 17 May 2013: implications for the seismotectonics of the Ottawa–Bonnechere Graben. *Canadian Journal of Earth Sciences*, 51(5), 439-451.

- Ma, S. & Audet, P. (2014). The 5.2 magnitude earthquake near Ladysmith, Quebec, 17 May 2013: implications for the seismotectonics of the Ottawa–Bonnechere Graben. *Canadian Journal of Earth Sciences*, 51(5), 439-451.
- Ma, S., Motazedian, D., & Corchete, V. (2013). Shear wave velocity models retrieved using Rg wave dispersion data in shallow crust in some regions of southern Ontario, Canada. *Journal of seismology*, 17(2), 683-705.
- Mai, P. M., Imperatori, W., & Olsen, K. B. (2010). Hybrid broadband ground-motion simulations: Combining long-period deterministic synthetics with high-frequency multiple S-to-S backscattering. *Bulletin of the Seismological Society of America*, 100(5A), 2124-2142.
- Marcinkovich, C. & Olsen, K. (2003). On the implementation of perfectly matched layers in a three-dimensional fourth-order velocity-stress finite difference scheme. *Journal of Geophysical Research: Solid Earth*, 108(B5).
- Martin, F. D. (2010). Influence of the nonlinear behaviour of soft soils on strong ground motions. *Engineering Sciences*. Ph.D. Thesis. Ecole Centrale, Paris.
- Masing, G. (1926). Eigenspannungen und Verfestigung beim Messing. *Proceedings of 2<sup>nd</sup> International Congress of Applied Mechanics*, Zurich, Switzerland, 332–335.
- McBryan, O. A. & Trottenberg, U. (1989). Multigrid methods on parallel computers. *Gesellschaft für Mathematik und Datenverarbeitung mbH*.
- Medioli, B. E., Alpay, S., Crow, H. L., Cummings, D. I., Hinton, M. J., Knight, R. D., ... & Sharpe, D. R. (2012). Integrated data sets from a buried valley borehole, Champlain Sea basin, Kinburn, Ontario. *Current Research*, 3.

- Moczo, P. (1989). Finite-difference technique for SH-waves in 2-D media using irregular grids application to the seismic response problem. *Geophysical Journal International*, 99(2), 321-329.
- Molnar, S., Cassidy, J. F., Olsen, K. B., Dosso, S. E., & He, J. (2014). Earthquake ground motion and 3D Georgia basin amplification in southwest British Columbia: Shallow blind-thrust scenario earthquakes. *Bulletin of the Seismological Society of America*, 104(1), 321-335.
- Motazedian, D. & Hunter, J. (2008). Development of an NEHRP map for the Orleans suburb of Ottawa, Ontario. *Canadian Geotechnical Journal*, 45(8), 1180-1188.
- Motazedian, D. and G.M. Atkinson (2005). "Stochastic Finite-Fault Modelling Based on a Dynamic Corner Frequency", *Bulletin of the Seismological Society of America*, 95, pp. 995-1010. [NSERC]. Download [EXSIM Beta \(May, 26, 2009\)](#).
- Motazedian, D., Hunter, J. A., Belvaux, M., Sivathayalan, S., Pugin, A., Chouinard, L., Khaheshi Banab, K., Crow, H., Tremblay, M., Perret, D., & Rosset, P.H. (2010). Seismic microzonation of Montreal and Ottawa, Canada. 9<sup>th</sup> U.S. National and 10<sup>th</sup> Canadian Conference on Earthquake Engineering (9USN/10CCEE).
- Motazedian, D., Hunter, J. A., Pugin, A., & Crow, H. (2011). Development of a VS30 (NEHRP) map for the city of Ottawa, Ontario, Canada. *Canadian Geotechnical Journal*, 48(3), 458-472.
- Motazedian, D., Hunter, J. A., Pugin, A., Khaheshi Banab, K., & Crow, H. L. (2011). Development of a Vs30 (NEHRP) Map for the City of Ottawa, Ontario, Canada. *Canadian Geotechnical Engineering Journal*. doi:10.1139/T10-081.
- Motazedian, D., Hunter, J.A., Belvaux, M., Sivathayalan, S., Pugin, A., Chouinard, L., Khaheshi Banab, K., Crow, H., Tremblay, M., Perret, D., and Rosset, Ph. (2010). Seismic

microzonation of montreal and ottawa, canada, 9th U.S. National and 10th Canadian Conference on Earthquake Engineering (9USN/10CCEE).

Motazedian, D., Khaheshi Banab, K., Hunter, J. A., Sivathayalan, S., Crow, H., & Brooks, G. (2011). Comparison of Site Periods Derived from Different Evaluation Methods, BSSA, v 101, 2942-2954.

Motazedian, D., Ma, S., & Crane, S. (2013). Crustal shear wave velocity models retrieved from Rayleigh wave dispersion data in northeastern North America. Bulletin of the Seismological Society of America, 103(4), 2266-2276.

Narayan, J. P. (2010). Effects of Impedance Contrast and Soil Thickness on Basin-Transduced Rayleigh Waves and Associated Differential Ground Motion. Pure and Applied Geophysics, 167: 1485-1510

Nie, S., Wang, Y., Olsen, K. B., & Day, S. M. (2017). Fourth Order Staggered Grid Finite Difference Seismic Wavefield Estimation Using a Discontinuous Mesh Interface (WEDMI). Bulletin of the Seismological Society of America, 107(5), 2183-2193.

Olsen, K. B. & Schuster, G. T. (1995). Causes of low-frequency ground motion amplification in the Salt Lake Basin: the case of the vertically incident P wave. Geophysical Journal International, ASCE, 122(3): 1045-1061.

Olsen, K. B. (1994). Simulation of three-dimensional wave propagation in the Salt Lake Basin. Doctoral dissertation, Department of Geology and Geophysics, University of Utah.

Olsen, K. B. (2000). Site amplification in the Los Angeles basin from three-dimensional modeling of ground motion. Bulletin of the Seismological Society of America, 90(6B), S77-S94.

- Olsen, K. B. (2011). 3D Broadband Ground Motion Estimation for Large Earthquakes on the New Madrid Seismic Zone, Central United States. Final Report – NEHRP.
- Olsen, K. B., Archuleta, R. J., & Matarrese, J. R. (1995). Three-dimensional simulation of a magnitude 7.75 earthquake on the San Andreas Fault. *Science*, 270(5242), 1628-1632.
- Olsen, K. B., Day, S. M., & Bradley, C. R. (2003). Estimation of Q for long-period (> 2 sec) waves in the Los Angeles basin. *Bulletin of the Seismological Society of America*, 93(2), 627-638.
- Olsen, K. B., Day, S. M., Minster, J. B., Cui, Y., Chourasia, A., Faerman, M., Moore, R., Maechling, P., & Jordan, T. (2006). TeraShake: Strong shaking in Los Angeles expected from southern San Andreas earthquake. *Seismology Research Letters*, 77: 281–282.
- Olsen, K. B., Day, S. M., Minster, J. B., Cui, Y., Chourasia, A., Faerman, M., ... & Jordan, T. (2006). Strong shaking in Los Angeles expected from southern San Andreas earthquake. *Geophysical Research Letters*, 33(7).
- Oprsal, I. & Zahradnik, J. (1999). Elastic finite-difference method for irregular grids. *Geophysics*, 64(1), 240-250.
- Opršal, I. & Zahradnik, J. (1999). From unstable to stable seismic modelling by finite-difference method. *Physics and Chemistry of the Earth, Part A: Solid Earth and Geodesy*, 24(3), 247-252.
- Oprsal, I. & Zahradnik, J. (2002). Three dimensional finite difference method and hybrid modeling of earthquake ground motion. *Journal of Geophysical Research: Solid Earth*, 107(B8).
- Ouellet, M. (1997). Lake sediments and Holocene seismic hazard assessment within the St. Lawrence Valley, Québec. *Geological Society of America Bulletin*, 109(6), 631-642.

- Panzer, F. (2012). Approaches to earthquake scenarios validation using seismic site response. Ph.D. Thesis. University of Catania, Catania, Italy.
- Pitarka, A. (1999). 3D elastic finite-difference modeling of seismic motion using staggered grids with nonuniform spacing. *Bulletin of the Seismological Society of America*, 89(1), 54-68.
- Pitarka, A., Somerville, P., Fukushima, Y., Uetake, T., & Irikura, K. (2000). Simulation of near fault strong ground motion using hybrid Green's functions. *Bulletin of the Seismological Society of America*, 90, 566-586.
- Pitilakis, K. (2004). Recent Advances in Earthquake Geotechnical Engineering and Microzonation, *Geotechnical, Geological, and Earthquake Engineering*, 1: 139-197.
- Pugin, A. M., Brewer, K., Cartwright, T., Pullan, S. E., Perret, D., Crow, H., & Hunter, J. A. (2013). Near surface S-wave seismic reflection profiling—new approaches and insights. *First Break*, 31(2), 49-60.
- Puzrin, A. (2012). Constitutive modelling in geomechanics: introduction. Springer Science and Business Media.
- Pyke, R. M. (1980). Nonlinear soil models for irregular cyclic loadings. *Journal of Geotechnical and Geoenvironmental Engineering*, 106(ASCE 15829).
- Qin, Y., Wang, Y., Takenaka, H., Zhang, X. (2012). Seismic ground motion amplification in a 3D sedimentary basin: the effect of the vertical velocity gradient, *Journal of Geophysical and Engineering*, 9: 761-772.
- Ranalli, G. (1995). *Rheology of the Earth*. Springer Science and Business Media.
- Rappaport, C. M. (1995). Perfectly matched absorbing boundary conditions based on anisotropic lossy mapping of space. *IEEE Microwave and Guided Wave Letters*, 5(3), 90-92.

- Régnier, J., Cadet, H., Bonilla, L. F., Bertrand, E., & Semblat, J. F. (2013). Assessing nonlinear behavior of soils in seismic site response: Statistical analysis on KiK-net strong-motion data. *Bulletin of the Seismological Society of America*, 103(3), 1750-1770.
- Restrepo, D., Taborda, R., & Bielak, J. (2012). Three-dimensional nonlinear earthquake ground motion simulation in the salt lake basin using the wasatch front community velocity model. Final technical report, USGS Award G10AP00077.
- Rix, G. J. & Meng, J. (2005). A non-resonance method for measuring dynamic soil properties. *Geotechnical Testing Journal*, 28(1), 1-8.
- Rollins, K. M., Evans, M. D., Diehl, N. B., & III, W. D. D. (1998). Shear modulus and damping relationships for gravels. *Journal of Geotechnical and Geoenvironmental Engineering*, 124(5), 396-405.
- Roten, D., Cui, Y., Olsen, K. B., Day, S. M., Withers, K., Savran, W. H., ... & Mu, D. (2016). High-frequency nonlinear earthquake simulations on petascale heterogeneous supercomputers. In *Proceedings of the International Conference for High Performance Computing, Networking, Storage and Analysis (82)*. IEEE Press.
- Roten, D., Fäh, D., Bonilla, L. F., Alvarez-Rubio, S., Weber, T. M., & Laue, J. (2009). Estimation of non-linear site response in a deep Alpine valley. *Geophysical Journal International*, 178(3): 1597–1613.
- Rubinstein, J. L. & Beroza, G. C. (2004). Nonlinear strong ground motion in the ML 5.4 Chittenden earthquake: Evidence that preexisting damage increases susceptibility to further damage. *Geophysical research letters*, 31(23).
- Rubinstein, J. L. (2011). Nonlinear site response in medium magnitude earthquakes near Parkfield, California. *Bulletin of the Seismological Society of America*, 101(1), 275-286.

- Seed, H. B. & Idriss, I. M. (1969). Influence of soil conditions on ground motions during earthquakes. *Journal of the Soil Mechanics and Foundations Division*, 95(1), 99-138.
- Seed, H. B. & Idriss, I. M. (1970). Soil moduli and damping factors for dynamic response analyses. Technical Report EERRC -70-10, University of California, Berkeley, CA, USA.
- Semblat, J. F., Duval, A. M., & Dangla, P. (2000). Numerical analysis of seismic wave amplification in Nice (France) and comparisons with experiments. *Soil Dynamics and Earthquake Engineering*, 19(5), 347-362.
- Shearer, P. M. (2009). *Introduction to seismology*. Cambridge University Press.
- Shibuya, S., Mitachi, T., Fukuda, F., & Degoshi, T. (1995). Strain rate effects on shear modulus and damping of normally consolidated clay. *Geotechnical testing journal*, 18(3), 365-375.
- Shilts, W. W. & Clague, J. J. (1992). Documentation of earthquake-induced disturbance of lake sediments using subbottom acoustic profiling: *Canadian Journal of Earth Sciences*, 29, 1018–1042.
- Stein, S. & Wysession, M. (2003). *An introduction to seismology, earthquakes, and earth structure*. John Wiley & Sons.
- Strasser, M., Anselmetti, F. S., Fäh, D., Giardini, D., & Schnellmann, M. (2006). Magnitudes and source areas of large prehistoric northern Alpine earthquakes revealed by slope failures in lakes. *Geology*, 34, 1005–1008.
- Taborda, R. & Roten, D. (2014). Physics-based ground-motion simulation. *Encyclopedia of Earthquake Engineering*, 1-33.
- Taborda, R., Bielak, J., & Restrepo, D. (2012). Earthquake ground motion simulation including nonlinear soil effects under idealized conditions with application to two case studies. *Seismological Research Letters*, 83(6), 1047-1060.

- Tessmer, E. (2000). Seismic finite-difference modeling with spatially varying time steps. *Geophysics*, 65(4), 1290-1293.
- Torrance, J. K. (1988). Mineralogy, pore water chemistry and geotechnical behaviour of Champlain Sea and related sediments. The late Quaternary development of the Champlain Sea basin, 259-275.
- Trifunac, M. D. & Todorovska, M. I. (1996). Nonlinear soil response—1994 Northridge, California, earthquake. *Journal of geotechnical engineering*, 122(9), 725-735.
- Vucetic, M. (1990). Normalized behavior of clay under irregular cyclic loading. *Canadian Geotechnical Journal*, 27(1), 29-46.
- Wang, Y. & Schuster, G. T. (1996). Finite-difference variable grid scheme for acoustic and elastic wave equation modeling. In *SEG Technical Program Expanded Abstracts 1996*. Society of Exploration Geophysicists, 674-677.
- Wang, Y. (2000). Variable grid-size and time-step finite difference method for seismic forward modeling and reverse-time migration. UT (Doctoral dissertation, The University of Utah).
- Wang, Y., Xu, J., & Schuster, G. T. (2001). Viscoelastic wave simulation in basins by a variable-grid finite-difference method. *Bulletin of the Seismological Society of America*, 91(6), 1741-1749.
- Wells, D. L., & Coppersmith, K. J. (1994). New empirical relationships among magnitude, rupture length, rupture width, rupture area, and surface displacement. *Bulletin of the seismological Society of America*, 84(4), 974-1002.
- Wen, K. L. (1994). Nonlinear soil response in ground motions. *Earthquake Engineering & Structural Dynamics*, 23(6), 599-608.

- Wu, C. & Harris, J. M. (2004). An optimized variable-grid finite-difference method for seismic forward modeling. *Journal of Seismic Exploration*, 12(4), 343-353.
- Yamada, M., Yamada, M., Hada, K., Ohmi, S., & Nagao, T. (2010). Spatially dense velocity structure exploration in the source region of the iwate-miyagi nairiku earthquake. *Seismological Research Letters*, 81(4), 597-604.
- Yang, X. (2008). Simulation of Seismic Real and Virtual Data Using the 3D Finite-Difference Technique and Representation Theorem. Texas A&M University, Texas, TX, USA.
- Yao, Z. & Margrave, G. F. (1999). Fourth-order finite-difference scheme for P and SV wave propagation in 2D transversely isotropic media (Vol. 11). CREWES Research Report.
- Yoshimura, C., Bielak, J., Hisada, Y., & Fernández, A. (2003). Domain reduction method for three-dimensional earthquake modeling in localized regions, part II: Verification and applications. *Bulletin of the Seismological Society of America*, 93(2), 825-841.
- Zekkos, D. P., Bray, J. D., & Riemer, M. F. (2006). Shear modulus reduction and material damping relations for municipal solid-waste. Proceedings of the 8<sup>th</sup> US national conference on earthquake engineering, San Francisco, USA, 18-22.
- Zhang, W., Shen, Y., & Chen, X. (2008). Numerical simulation of strong ground motion for the Ms 8.0 Wenchuan earthquake of 12 May 2008. *Science in China Series D: Earth Sciences*, 51(12), 1673-1682.
- Zhang, W., Shen, Y., & Zhao, L. (2012). Three-dimensional anisotropic seismic wave modelling in spherical coordinates by a collocated-grid finite-difference method. *Geophysical Journal International*, 188(3), 1359-1381.

Zhang, Z., Zhang, W., Li, H., & Chen, X. (2012). Stable discontinuous grid implementation for collocated-grid finite-difference seismic wave modelling. *Geophysical Journal International*, 192(3), 1179-1188.